OECD/MCCI-2010-TR04

OECD MCCI Project

Category 4 Integral Test to Validate Severe Accident Codes: Core-Concrete Interaction Test Six (CCI-6) Final Report

Rev. 2 - Final

November 2010

by:

M. T. Farmer, D. J. Kilsdonk, R. W. Aeschlimann, and S. Lomperski

Nuclear Engineering Division
Argonne National Laboratory
9700 S. Cass Avenue
Argonne, IL 60439 USA

Table of Contents

1. INTRODUCTION 1
1.1 Background 1
1.2 Objectives and Approach 2

2. FACILITY DESCRIPTION 4
2.1 Test Apparatus 4
2.2 Basemat Water Supply System 11
2.3 Test Section Top Flooding Water Supply System 14
2.4 Quench System 15
2.5 Test Section Pressure Relief System 16
2.6 Off Gas System 17
2.7 Cover Gas System 18
2.8 Power Supply 19
2.9 Corium Composition 19
2.10 Concrete Composition 21
2.11 Instrumentation and Data Acquisition 22

3. TEST PROCEDURES 31
3.1 Pretest Preparations 31
3.2 Test Operations 33

4. RESULTS 40
4.1 Electric Power 40
4.2 Melt Temperatures 43
4.3 Concrete Ablation 48
4.4 Crust Lance Data 50
4.5 Corium Top-Flooding Quench Rate 53
4.6 Posttest Examinations 56

5. REFERENCES.....65
APPENDIX A: Data Acquisition System Channel Assignments.....66
APPENDIX B: Power Supply Constant Voltage Operating Method 79
APPENDIX C: Test Data 81
APPENDIX D: Evaluation of Debris-Water Heat Flux 111

List of Figures

Figure **Page**

2-1 Schematic of CCI-6 Test Facility 5
2-2 Top View of Lower Test Section 5
2-3 Side View of Lower Test Section Showing Concrete Sidewall Sections....6
2-4 Details of the Basemat Nozzle Design 7
2-5 Nozzle Configuration on the Test Section Basemat Bottom Support Plate 7
2-6 Basemat Form Showing Nozzle Array Prior to Concrete Placement....8
2-7 Photograph Showing Electrode Installation 9
2-8 Details of the Top Test Section Showing Water Weirs....10
2-9 Illustration of CCI-6 Test Section Mounted on ZPR-9 Reactor Bed. 11
2-10 Illustration of CCI-6 Crust Lance Assembly Mounted in Test Section 12
2-11 Basemat Water Nozzle Water Supply System 13
2-12 CCI-6 Test Section Top Flooding Water Supply System....14
2-13 CCI-6 Quench and Overflow Tanks....15
2-14 CCI-6 Spray Tank System....16
2-15 CCI-6 Test Section Pressure Relief System 17
2-16 CCI-6 Off Gas System....18
2-17 CCI-6 Cover Gas System 19
2-18 Thermite Reaction Temperature Measured by Ignition of a 1 kg Sample 21
2-19 Data Acquisition System Setup for CCI-6. 23
2-20 Plan View of Basemat Instrumentation Layout....25
2-21 Elevation View of Basemat Type C Thermocouple Locations 26
2-22 CCI-6 Test Section Sidewall Instrumentation (view from west) 27
2-23 CCI-6 Test Section Sidewall Instrumentation (view from south) 28
2-24 CCI-6 Test Section Pressure Transducer Layout. 29
3-1 Illustration of Thermite Sample Train Installed in Test Section. 32
3-2 Voltage Across Thermite Igniter Shunt....36
3-3 Test Section Upper Plenum Gas Temperature during the Initial Interaction. 37
3-4 Concrete Surface Temperatures over the First 10 Minutes of the Interaction....37

List of Figures (Contd.)

Figure **Page**

3-5 Bulk Melt Temperature Data over the First 7 Minutes of the Interaction. 38
4-1 Power Supply Voltage. 41
4-2 Power Supply Current. 41
4-3 Total DEH Input Power. 42
4-4 Power Supply Voltage and Power: Expanded Timescale. 42
4-5 Melt Temperature Data from Basemat Type C “WCL” Array. 44
4-6 Melt Temperature Data from Basemat Type C “WNW” Array. 44
4-7 Melt Temperature Data from Basemat Type C “WSE” Array. 45
4-8 Melt Temperature Data from North Side Wall Type C “WN” Array. 45
4-9 Melt Temperature Data from South Side Wall Type C “WS” Array. 46
4-10 Data from all Melt Temperature Thermocouples. 46
4-11 Melt Temperature Data from “WS” Array: Expanded Scale. 47
4-12 Thermal Response of the Concrete Basemat at the Centerline (“A” Array). 48
4-13 North Concrete Sidewall Thermal Response at +12.5 cm (“SWI” Array). 49
4-14 South Concrete Sidewall Thermal Response at +12.5 cm (“SWJ” Array). 49
4-15 Basemat Axial Ablation Front Location. 50
4-16 South Sidewall Radial Ablation Front Location. 51
4-17 Comparison of Axial and Radial Ablation Depth Data versus Time. 51
4-18 Load Force Exerted on Crust vs. Time. 52
4-19 Cumulative Steam Flowrate from Debris-Water Interaction. 54
4-20 CCI-6 Debris-Water Heat Flux (Top Flooding). 55
4-21 Integrated Heat Removal to Water and Heat Input to Melt from DEH. 55
4-22 Photographs of Holes in the Main Steamline at (a) the Test Section Tee, and (b) the Bellows Downstream of the Tee 57
4-23 Photograph of the Interior of the Steamline Tee Showing Entrained Corium Solidified on the Pipe Interior Surface. 57
4-24 Top View of Posttest Debris after Removal of Test Section Lid 58

List of Figures (Contd.)

Figure **Page**

4-25 Top View of Particle Bed After Removal of Upper Sidewall Sections 58

4-26 Closeup Photograph of Material Removed fro m Particle Bed Over Fractured Crust 59

4-27 Views of the Debris After Particle Bed Removal (a) from the Top and (b) Closeup of the Volcanic Mound in the North-Central Region of the Debris as Viewed from the South 60

4-28 Face-on Views of (a) North and (b) South Concrete Sidewalls After Removal 61

4-29 Views of Corium Debris Remaining Over the Basemat as Viewed from (a) North and (b) South.....62

4-30 Closeup Photograph of Fractured Crust Material after Removal from Test Section 63

4-31 Rendering of Posttest Debris Configuration.....64

List of Tables

Table **Page**

1-1 Specifications for CCI-6 3

2-1 Post-Reaction Bulk Composition for CCI-6 Thermite 20

2-2 Detailed Pre- and Post-Reaction Compositions for CCI-6 Thermite 20

2-3 Engineering Composition of CCI-6 Siliceous Concrete 22

2-4 Chemical Composition of Siliceous Concrete 22

2-5 Type K Thermocouple Locations Used to Determine the Timing of Water Addition to the Test Section 24

3-1 CCI-6 Event Sequence 35

1.0 INTRODUCTION

1.1 Background

Ex-vessel debris coolability is an important light water reactor (LWR) technical challenge. For existing plants, resolution of this challenge will confirm the technical basis for severe accident management guidelines (SAMGs). For new reactors, understanding this challenge will help confirm the effectiveness of the design and implementation of new accident mitigation features and severe accident management design alternatives (SAMDAs). The first OECD-MCCI program conducted reactor material experiments focused on achieving the following technical objectives: i) provide confirmatory evidence and data for various cooling mechanisms through separate effect tests for severe accident model development, and ii) provide long-term 2-D core-concrete interaction data for code assessment and improvement.

Debris cooling mechanisms investigated as part of the first MCCI program included: i) water ingression through cracks/fissures in the core debris, ii) melt eruption caused by gas sparging, and iii) large-scale crust mechanical failure leading to renewed bulk cooling. The results of this testing and associated analysis provided an envelope (principally determined by melt depth) for debris coolability. However, this envelope does not encompass the full range of potential melt depths for all plant accident sequences. Cooling augmentation by additional means may be needed at the late stage to assure coolability for new reactor designs as well as for various accident sequences for existing reactors. In addition, the results of the CCI tests showed that lateral/axial power split is a function of concrete type. However, the first program produced limited data sets for code assessment. In light of significant differences in ablation behavior for different concrete types, additional data would be useful in reducing uncertainties and gaining confidence in code predictions.

Based on these findings, a broad workscope was defined for the follow-on MCCI program. The workscope can be divided into the following four categories:

1. Combined effect tests to investigate the interplay of different cooling mechanisms, and to provide data for model development and code assessment purposes.
2. Tests to investigate new design features to enhance coolability, applicable particularly to new reactor designs.
3. Tests to generate two-dimensional core-concrete interaction data.
4. Integral tests to validate severe accident codes.

In addition to the experimental work, an analysis task was defined to develop and validate coolability models to form the basis for extrapolating the experiment findings to plant conditions.

As one of the steps required to satisfy these objectives, the Management Board (MB) approved the conduct of the first Category 4 Test. In particular, the following PRG recommendation was approved at the 5th PRG meeting which contains specifications for this test:

> The PRG recommends that the OA design a 70 cm x 70 cm test, with two concrete side walls, using CEA siliceous concrete, 6 wt% concrete composition, early top flooding

initiated when ablation is established and melt temperature has stabilized. The melt depth shall be 30 cm. The test will be designed for two specific phases. The first phase will provide for 30 cm for radial ablation and 25 cm for vertical ablation. In the event that the melt is not cooled down by top flooding during the first phase, a second and separate test phase will begin involving bottom flooding. This second phase will be initiated when axial ablation depth reaches 25 cm. The design should be mindful of the curing time of the concrete. The instrumentation should be refined to provide data on the water injection characteristics and melt temperature near the lateral walls.

1.2 Objectives and Approach

In response to the PRG mandate, a summary test plan for this sixth Core-Concrete Interaction (CCI-6) experiment was prepared [1], reviewed by the PRG, and subsequently approved for test conduct. Detailed specifications that were developed as part of the test planning process are provided in Table 1-1. The experiment approach was to incorporate an array of water nozzles into the core-concrete interaction test apparatus. The test section was enlarged to incorporate a 70 cm x 70 cm basemat. The initial melt depth was increased to 28 cm,[1] which corresponds to a thermite charge mass of 900 kg. The melt depth is noted to be slightly less than the 30 cm level requested by the PRG. The thermite charge was redesigned to include a reduced amount of concrete decomposition products (i.e., 6 wt %) relative to the previously performed CCI tests. The concrete sidewalls allow for 24 cm of lateral erosion, and the sidewall design was modified to include refractory MgO with a UO_2 pellet and U_3O_8 powder liner to stop the ablation if the 24 cm ablation depth was reached. The basemat and sidewalls also included an array of 45 concrete nozzles that were arranged on a 14 cm lateral pitch and were located at a uniform depth of 27.5 cm below the initial concrete basemat surface elevation. The nozzles were originally sealed at the top, and were fed with water from a common water supply tank that provided a static water head of nominally 10 kPa measured at the upper surface of the nozzles.

The planned operating sequence was to ignite the thermite and then provide 210 kW Direct Electrical Heating (DEH) to simulate decay heat. The concrete would then heat up and begin erosion. At this point, the cavity would be flooded from the top. If the melt did not cool, then the core-concrete interaction would continue until the 27.5 cm axial ablation depth was reached. At this point, the nozzles would open by erosion and thus initiate cooling by bottom water injection. The test would continue to operate until the melt was quenched, or the maximum axial ablation depth of 32.5 cm was reached. The experiment would then be terminated.

The CCI-6 experiment was carried out on 18 March 2010. The balance of this report documents the facility, actual test operating procedure, and results from this experiment.

[1]The 28 cm melt depth is less than the 30 cm requested by the PRG. However, to achieve this depth the metal reaction byproduct in the melt would exceed that which, when oxidized, would produce sufficient H_2 to exceed 80 % of the lower flammability limit (LFL) in the test cell volume. This is one of the current safety limitations for the tests. Thus, the 28 cm melt depth (viz. 900 kg melt mass) was adopted to conform to the safety limitation and thereby minimize scheduling risks related to safety plan approvals.

Table 1-1. Specifications for CCI-6.

Parameter	Specification
Corium	100 % oxidized PWR with 6 wt % siliceous concrete (CEA type)
Test section cross-sectional area	70 cm x 70 cm
Initial melt mass (depth)	900 kg (28 cm)[a]
Test section sidewall construction	24 cm thick concrete followed by MgO protected with a 2.5 cm thick layer of crushed UO_2 pellets and powder.
Test section basemat construction	48.1 cm thick concrete with an array of water injection nozzles embedded at a depth of 27.5 cm from the concrete top surface. Nozzles are uniformly pitched at a lateral spacing of 14.0 cm.
Sidewall maximum ablation depth	24.0 cm
Basemat maximum ablation depth	32.5 cm
System operating pressure	Atmospheric
Melt formation technique	Chemical reaction (~30 second reaction time)
Initial melt temperature	~2300 ºC
Melt heating technique	Direct Electrical (Joule) Heating
Melt heating method under dry cavity conditions	Constant power at 210 kW[b]
Melt heating method after cavity flooding	Constant voltage (preserves melt specific power density established prior to cavity flooding)
Criteria for top cavity flooding	Any combination of two different thermocouples located 2.5 cm within the concrete indicate arrival of the ablation front
Top flooding water inlet conditions	Inlet water temperature: 15 ºC Inlet water flowrate: ~ 2 liters/sec Sustained[c] water depth over melt: 25 ± 5 cm
Criterion for bottom water injection	Passive opening of nozzles once the axial ablation depth reaches 27.5 cm
Bottom injection water inlet conditions	Inlet water temperature: ~ 15 ºC Inlet water flowrate: 3.8 g/sec per nozzle, or 170 g/sec maximum if all 45 basemat nozzles are opened[d] Inlet water pressure at nozzle opening: 10±5 kPad
Test termination criteria	1) melt is quenched, or 2) maximum axial ablation depth of 32.5 cm is reached.

[a]Based on a calculated melt density of 6640 kg/m^3.

[b]Based on 150 kW/m^2 design heat flux to top, bottom, and two sidewall concrete surfaces (1.37 m^2 area), plus an additional 5 kW to compensate for a long-term heat losses of 10 kW/m^2 to MgO sidewalls (0.5 m^2 area).

[c]The water depth over the melt will be maintained in the indicated range until the nozzles open. Additional water will not be added from the top unless the test section plenum temperature climbs above saturation, indicating that the cavity has completely dried out.

[d]The 3.8 g/sec water injection flowrate limit corresponds to a local debris cooling rate of 500 kW/m^2 g/sec over the 14 cm x 14 cm surface area covered by one nozzle, assuming injection of room temperature water. The 170 g/sec injection flowrate limit would be reached if all 45 nozzles opened.

2.0 FACILITY DESCRIPTION

The overall facility design and test operating procedures for CCI-6 contained many elements that were similar to those used in the previous five tests [2-4]. However, several changes were made so that the test could serve as an integral experiment for validation of severe accident codes. In particular, the design was modified to include a 70 cm x 70 cm siliceous concrete basemat with two concrete side walls. Also, in contrast to the previous CCI tests, this test focused on coolability and therefore the cavity was flooded from above soon after the melt was produced. The initial melt depth was also modestly increased from the 25 cm level used previously to 28 cm.

Finally, the test was designed for operation in two distinct phases. The first phase consisted of a conventional 2-D core concrete interaction experiment that provided for 24 cm of lateral ablation and 27.5 cm of axial ablation. In the event that the melt did not cool down by top flooding during this first cavity ablation phase, a second and separate test phase would begin that involved bottom flooding. This phase would be initiated when the axial ablation depth reached 27.5 cm. The instrumentation was refined to provide data on the water injection characteristics, as well as the melt temperature near the concrete walls.

Additional details regarding the facility modifications are provided in the balance of this section. Specifications for the experiment were provided previously in Table 1-1.

2.1 Test Apparatus

The CCI test facility consisted of a test apparatus, a power supply for Direct Electrical Heating (DEH) of the corium, a water supply system, two steam condensation (quench) tanks, a ventilation system to complete filtration and exhaust the off-gases, and a data acquisition system. A schematic illustration of the overall setup for CCI-6 is provided in Figure 2-1. The apparatus consisted of three rectilinear sidewall sections and a lid. The overall structure was 3.4 m tall. The two upper sidewall sections had a square internal cross sectional area of 50 cm x 50 cm.

The test section for containment of the core melt was located at the bottom of the apparatus. A top view of this component is shown in Figure 2-2, while a cross-sectional view of the non-electrode sidewalls is provided in Figures 2-3. The test section was enlarged to incorporate a 70 cm x 70 cm basemat. The concrete sidewalls allowed for 24 cm of lateral erosion, and the sidewall design was modified to include refractory MgO with a UO_2 pellet and U_3O_8 powder liner. This is the same inert sidewall design that was successfully used behind the tungsten electrodes in all previous CCI tests. Thus, the sidewall design was intended to allow for continued test operations after the maximum lateral ablation depth of 24 cm was reached. In this manner, the lateral erosion could be stabilized and allowed to proceed downwards to expose the water injection nozzles in the event that the melt did not successfully cool by top flooding in the early part of the experiment, and/or rapid sidewall erosion was experienced early in the test.

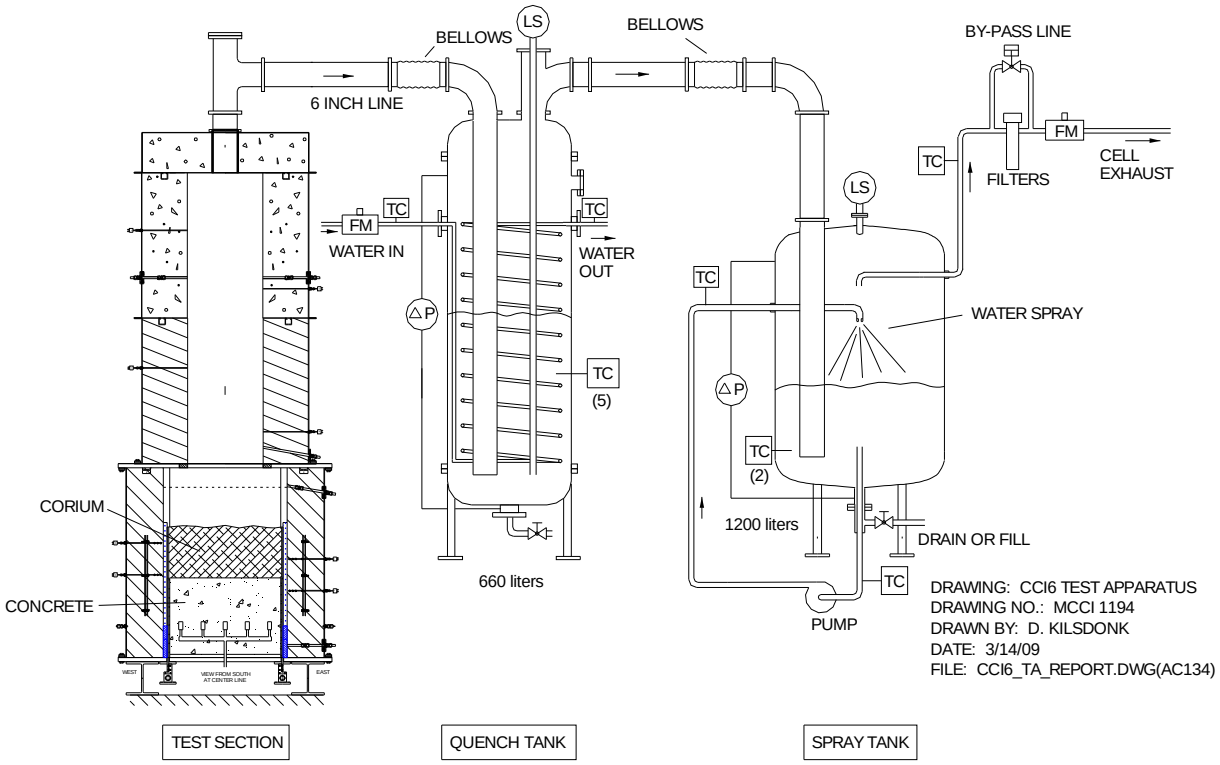

Figure 2-1. Schematic of CCI-6 Test Facility.

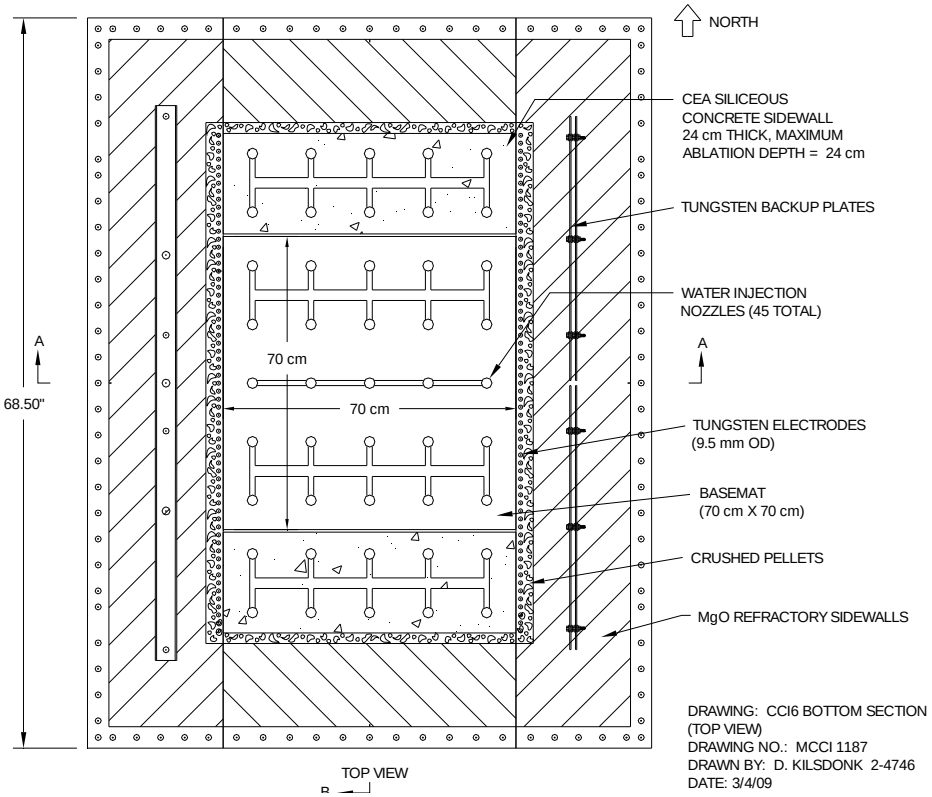

Figure 2-2. Top View of Lower Test Section.

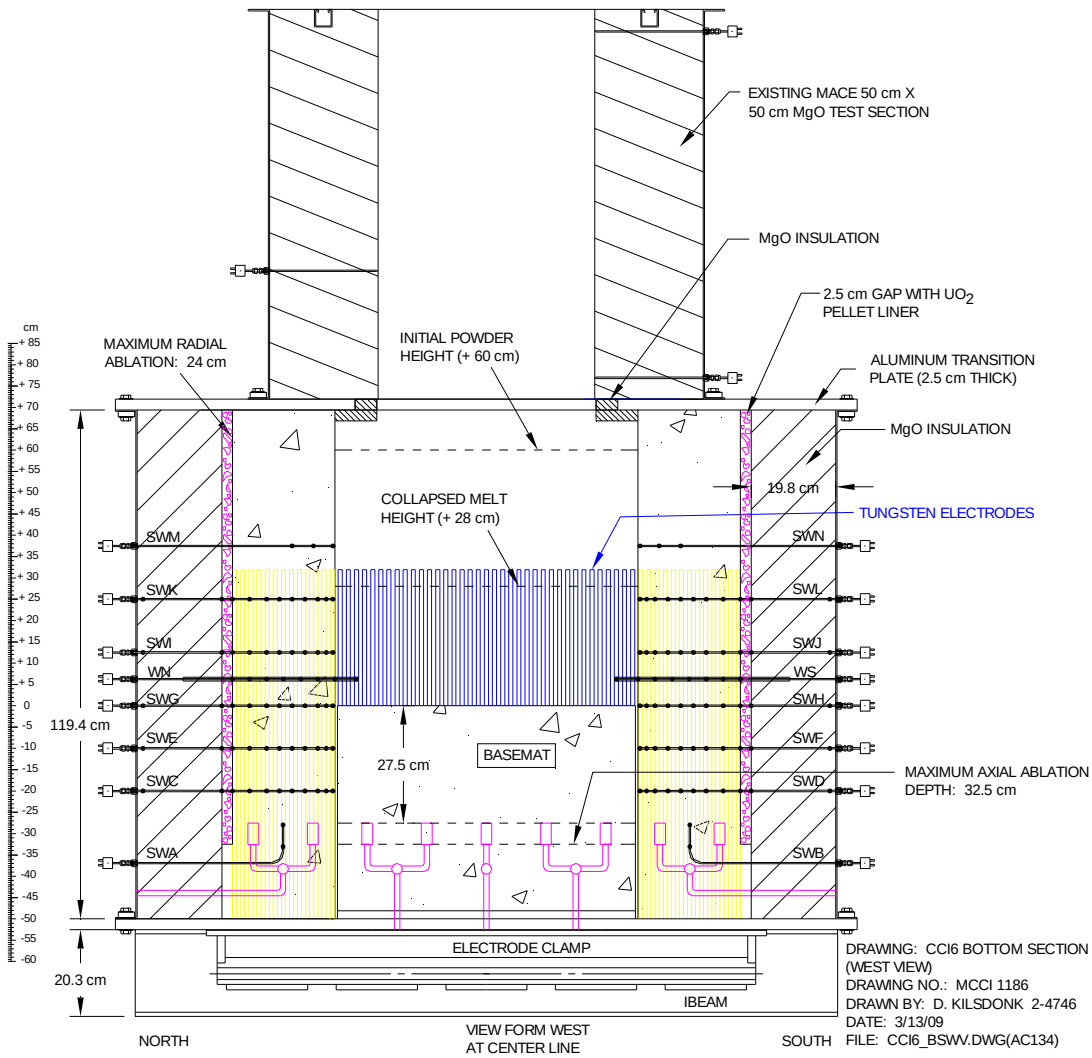

Figure 2-3. Side View of Lower Test Section Showing Concrete Sidewall Sections.

As shown in Figures 2-2 and 2-3, the basemat and sidewall designs were also modified to include an array of 45 concrete nozzles that were arranged on a 14 cm lateral pitch. Twenty five of the nozzles were configured in the basemat, while ten nozzles were configured in each of the two concrete sidewalls. The nozzle design details are shown in Figure 2-4, while the nozzle configuration on top of the basemat bottom support plate is shown in Figure 2-5. A photograph showing the concrete basemat form with the nozzles and a few of the basemat instruments installed prior to concrete placement is provided in Figure 2-6. The nozzles were all located at a depth of 27.5 cm below the initial concrete basemat surface elevation. The nozzles were sealed at the top with a PVC pipe caps, and all were fed with water from a common header tank that provided a static net pressure of nominally 10 kPa measured at the upper surface elevation of the nozzles. Once the corium melt reached the 27.5 cm axial ablation depth, the tops of the nozzles would be eroded through, thereby allowing passive water injection from below to begin the second phase of the experiment. At this point, the melt could be stabilized, or depending upon the extent of cooling, axial ablation could continue. If ablation continued, then the experiment would be terminated once the 32.5 cm axial erosion depth was reached. The porous concrete

used in the nozzles was identical to that used in the SSWICS-12 test [5]; the formulation for this material was developed by Forschungszentrum Karlsruhe (FZK). However, as shown in Figure 2-4, the nozzle design was more robust compared to SSWICS-12 to ensure that these components could survive the concrete pouring process intact. Design robustness was not an issue in terms of whether or not the nozzles would open once the melt front arrives since the melt was continuously heated. Each nozzle was electrically isolated from the test section so that an electrical shorting path could not develop once the melt contacted two or more nozzles.

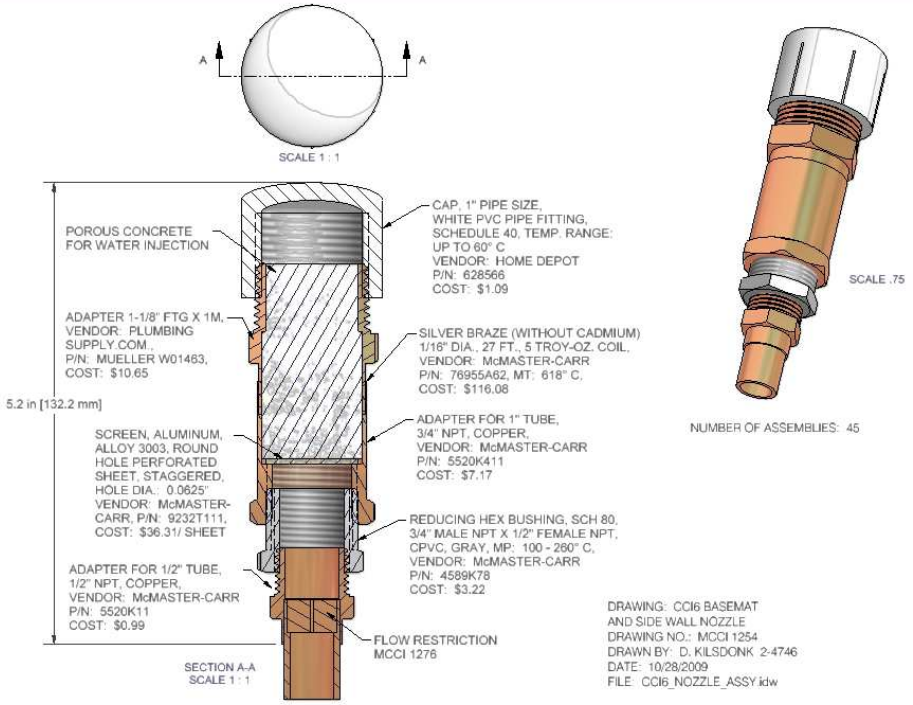

Figure 2-4. Details of the Basemat Nozzle Design.

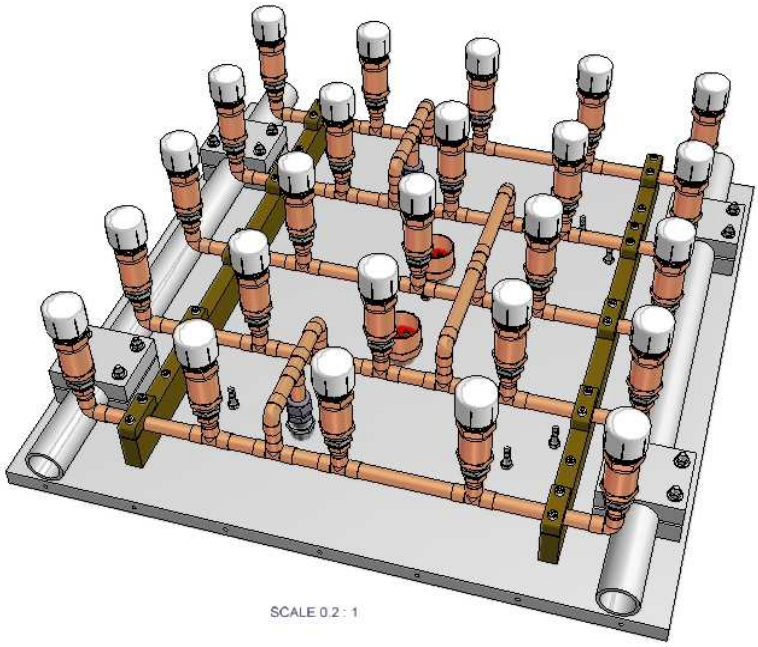

Figure 2-5. Nozzle Configuration on the Test Section Basemat Bottom Support Plate.

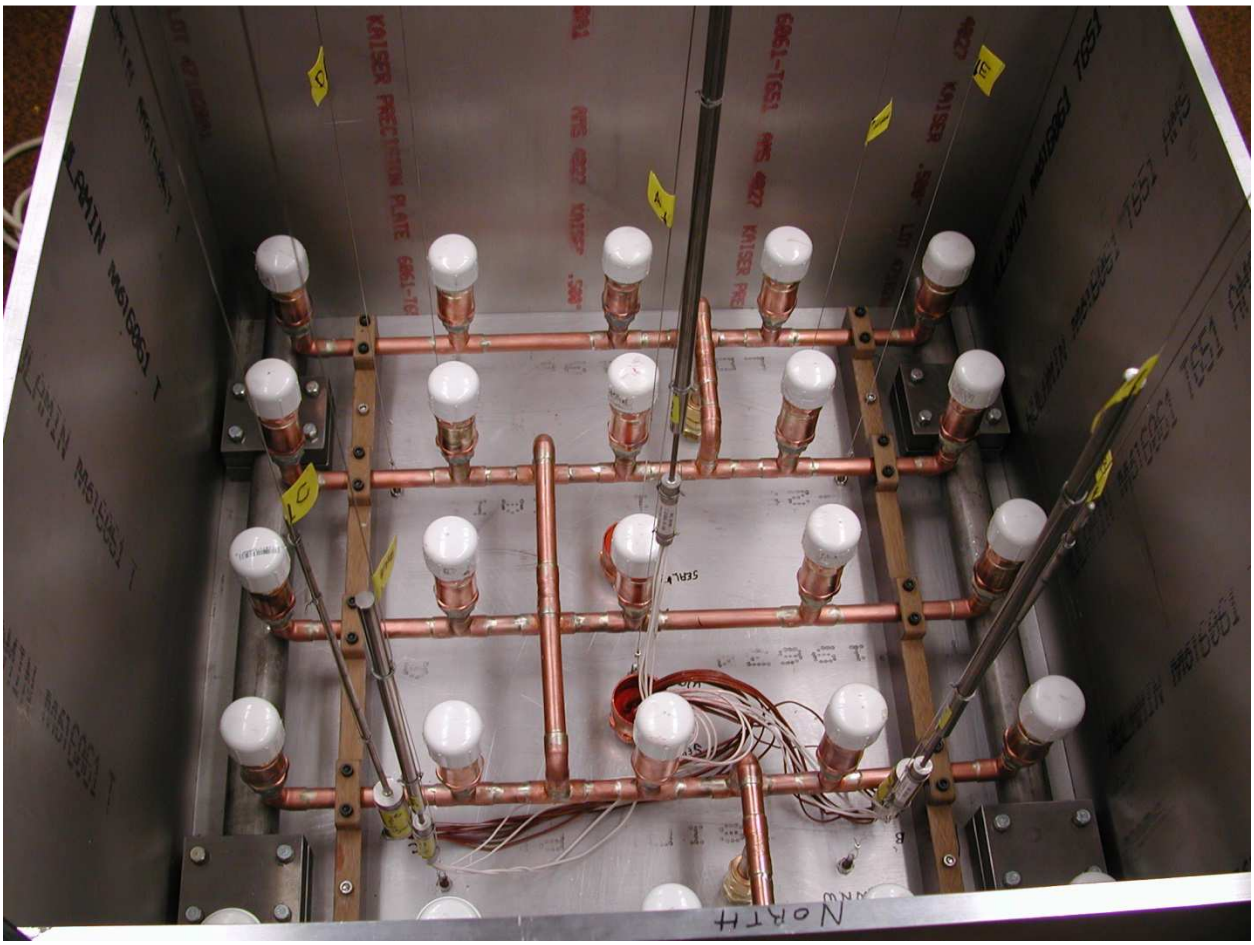

Figure 2-6. Basemat Form Showing Nozzle Array Prior to Concrete Placement.

As shown in Figures 2-2 and 2-3, the sidewalls of the lower test section were contained within a flanged steel form that was used to secure the section to the balance of the existing test section components with an aluminum transition plate. The flanges allowed the lower sidewalls to be disassembled to reveal the solidified corium following the test. As previously noted, a layer of crushed UO_2 pellets and U_3O_8 powder was used to protect the interior surface of the MgO sidewalls against thermo-chemical attack by the corium. For the electrode sidewalls, molybdenum and tungsten plates were embedded in the MgO to stop erosion in the event that the UO_2/U_3O_8 protection layer failed. Multi-junction Type C thermocouple assemblies were cast within the sidewalls so that the time-dependent heat loss from the melt could be calculated from the local temperature gradient and the thermal conductivity of the MgO.

The melt was produced through an exothermic chemical reaction yielding the target mass over a timescale of ~ 30 seconds. After the chemical reaction, DEH simulating decay heat was applied through two banks of tungsten electrodes. As shown in Figure 2-2, the electrodes lined the interior surfaces of the two opposing MgO sidewalls. A photograph showing the electrode installation around the concrete basemat and sidewalls but before placement of the inert MgO walls is provided in Figure 2-7. The electrodes were 9.5 cm in diameter and aligned in a row with a pitch of 1.9 cm. They were attached by copper clamps and water-cooled buss bars to a

560 kW AC power supply. The electrodes spanned a total width of 120 cm on each sidewall of the lower section. At the start of the experiment, the electrical current was drawn through the center, 70 cm-wide section of electrodes that were in direct contact with the melt. As the test progressed and the concrete sidewalls eroded, additional electrodes were exposed to the corium. Current was drawn through these newly exposed heating elements, thereby maintaining a uniform internal heating pattern in the melt over the course of the experiment. With the overall electrode span of 120 cm, the entire 24 cm of lateral sidewall erosion could be accommodated on both sides of the test section while ensuring that the entire melt cross-sectional area was in contact with the electrodes.

A few minutes after the melt was formed, ablation of the concrete basemat and sidewalls would commence. As shown in Figure 2-1 a large (15 cm diameter) gas line was used to vent the helium cover gas and the various gas species arising from the core-concrete interaction (i.e., CO, CO_2, H_2O, and H_2) into two adjacent quench tanks that were partially filled with water (see Figure 2-1). In the early initial phase of the experiment when the cavity was dry, the tanks served to cool the off-gases and filter aerosols generated from the core-concrete interaction. After the cavity was flooded, the tanks served to condense the steam and, based on the measured condensation rate, provided data on the corium cooling rate. In both cases, the helium covergas and non-condensables (CO, CO_2, and H_2) passed through the tanks and were vented through an off gas system that included a demister and filters. The gases were eventually exhausted through the containment ventilation system and a series of high efficiency filters before finally being released from the building stack.

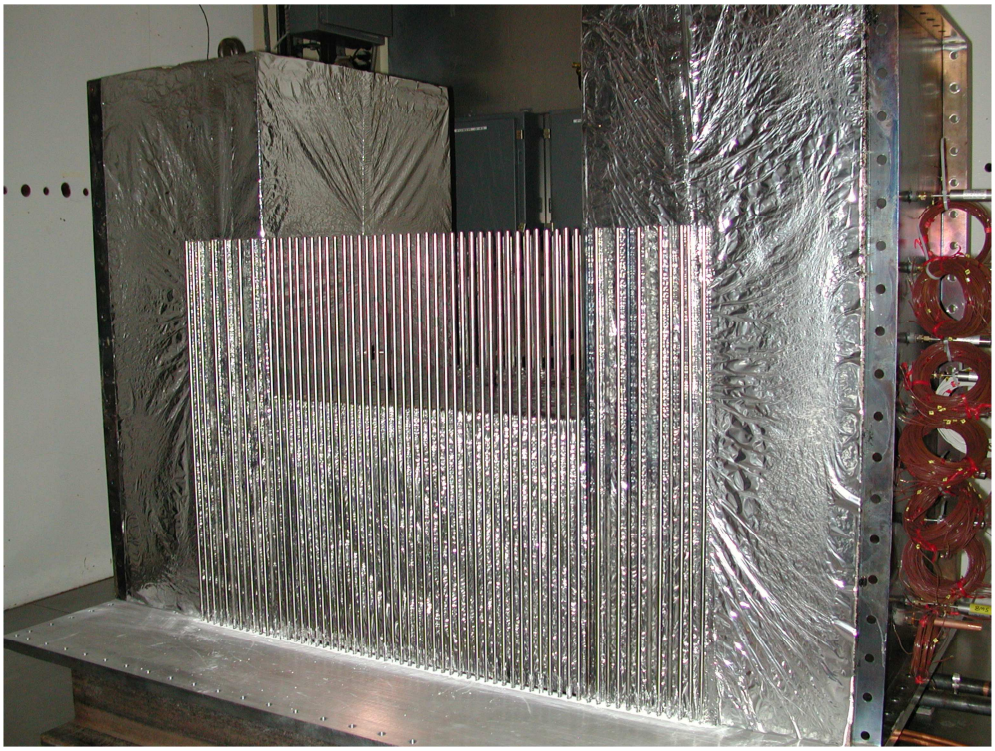

Figure 2-7. Photograph Showing Electrode Installation (concrete basemat and sidewalls covered with aluminized Saran to prevent moisture infiltration into thermite).

After a specified period of dry core-concrete interaction, water was introduced into the test section through weirs located in the upper sidewall section just beneath the lid of the apparatus. The layout for the weirs is shown in Figure 2-8. A total of nine penetrations were cast into the upper lid of the test section. Of these penetrations, seven were utilized for CCI-6: one lid video camera view port, a port for an insertable water level probe, a port for the crust lance, a 15 cm steam line to the quench system, two light ports, and a port for an optical pyrometer to view the melt upper surface.

The test section components were bolted together on the stationary half of the existing ZPR-9 reactor bed. Zirconia felt and silicon gasket material were used to seal the flanges. An illustration is provided in Figure 2-9. Installation and torquing of test section flange bolts was performed according to an approved procedure to ensure uniform preload on the flange surfaces. Additional reinforcement of each test section component was provided by clamping bars installed in both the North-South and East-West directions.

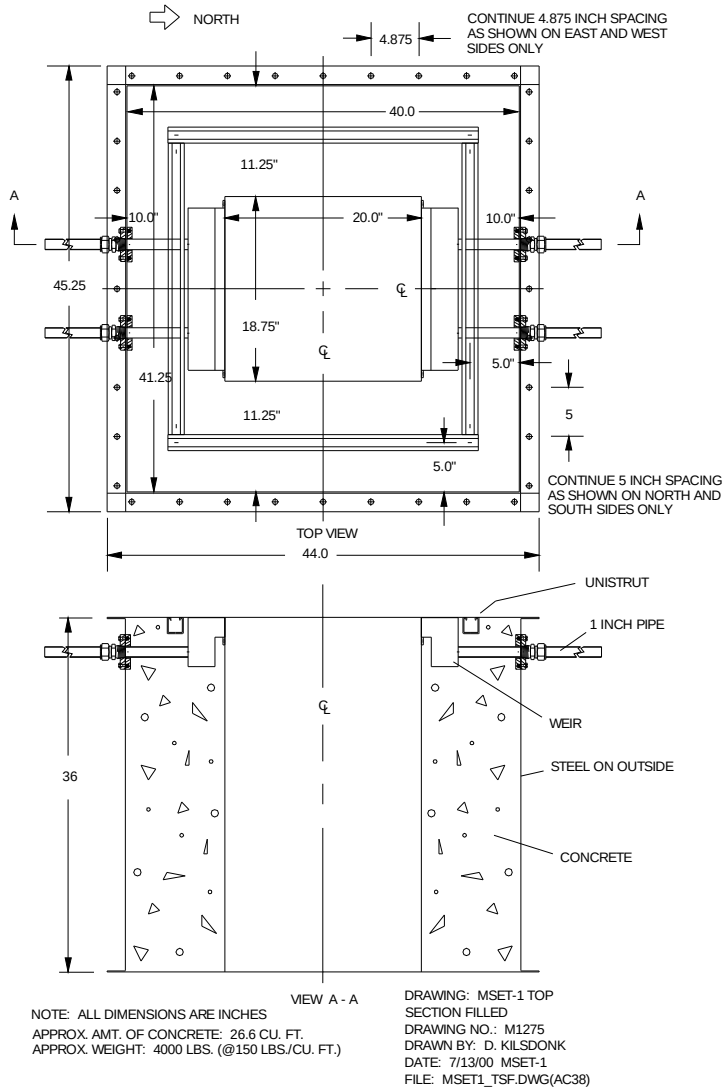

Figure 2-8. Details of the Top Test Section Showing Water Weirs.

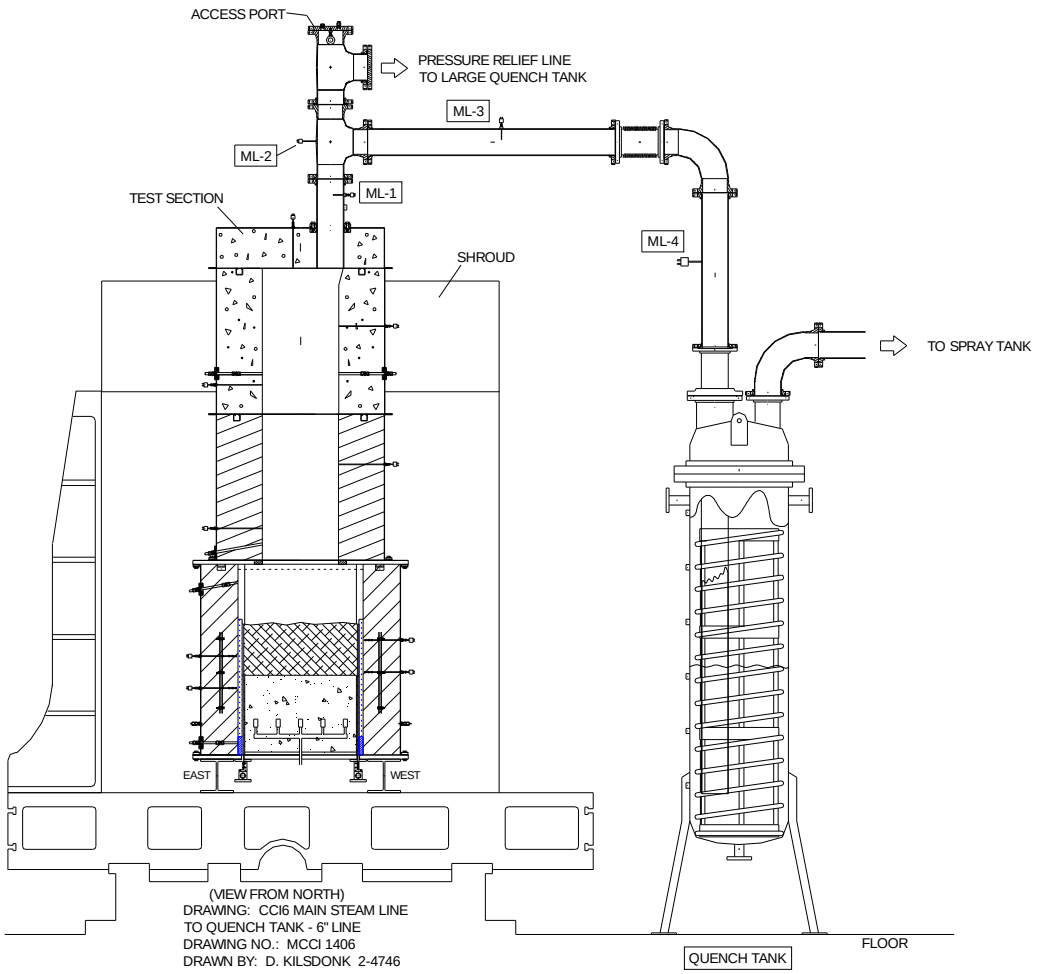

Figure 2-9. Illustration of CCI-6 Test Section Mounted on ZPR-9 Reactor Bed.

After a specified time with water present in the cavity, the option was provided to break the crust formed at the melt-water interface with an insertable crust lance to obtain data on the crust breach cooling mechanism. An illustration of the lance installed in the test section is shown in Figure 2-10. The lance was made from 2.54 cm diameter, 304 stainless steel rod with a pointed tip. The lance contained an electrical isolation hub so that there was no need to terminate power input to the melt during the crust loading procedure. As shown in Figure 2-10, the driving force for the lance was simply a 450 kg dead weight that was remotely lowered with the crane during the test. Applied load was monitored with a load cell and travel distance was monitored with a displacement transducer.

2.2 Basemat Water Supply System

A schematic illustration of the basemat water nozzle supply system is shown in Figure 2-11. The instrumentation locations for this system are also shown in the figure. As concrete erosion proceeded, the point would eventually be reached at which the porous concrete nozzles in the basemat would open by ablation. When the axial ablation depth reached a predefined level, the isolation valves that separated the nozzle header tank from the nozzles would be opened (i.e.,

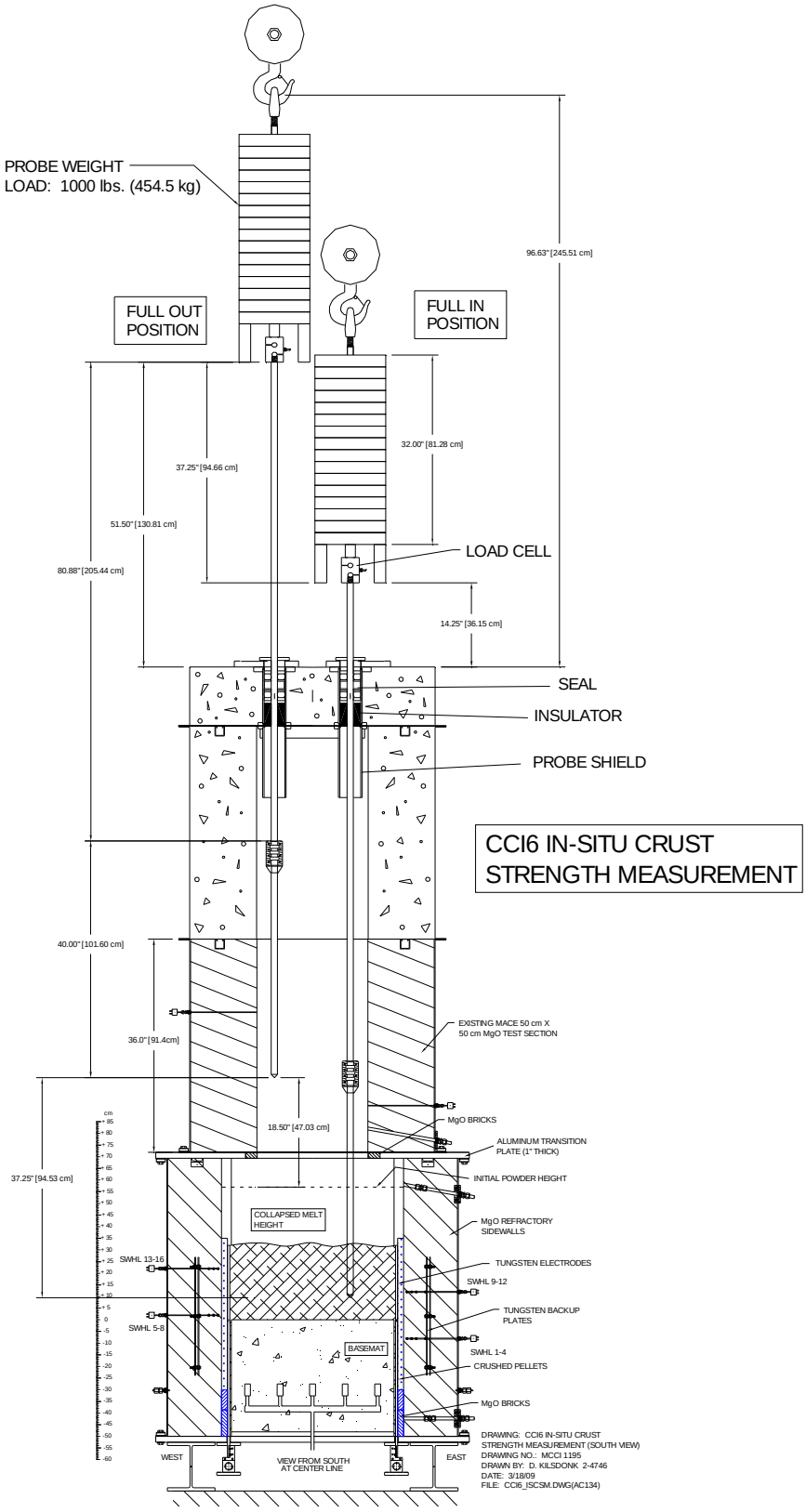

Figure 2-10. Illustration of CCI-6 Crust Lance Assembly Mounted in Test Section.

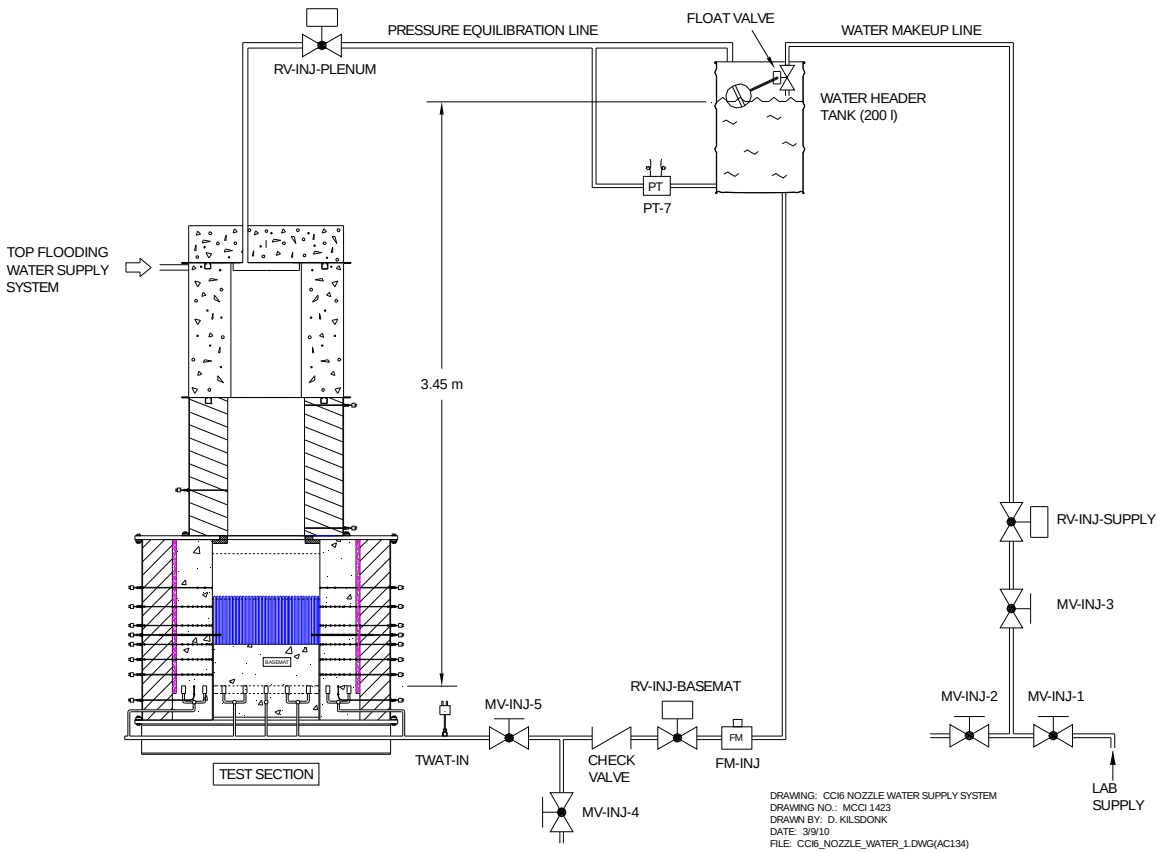

Figure 2-11. Basemat Water Nozzle Water Supply System.

valve RV-INJ-BASEMAT and RV-INJ-PLENUM in Figure 2-11) in preparation for water injection from below. The total head included that required to offset the melt hydrostatic head, which was estimated as ~ 23.6 kPa[2]. Thus, the header tank was configured in the test cell to provide a static water height of 3.45 m to the nozzles. The plenum of the header tank was attached by a 1.3 cm ID pressure equilibration line to the test section plenum to ensure that the proper head was maintained as the test section plenum pressure fluctuated. As the quench process progressed, makeup water to the header tank would be provided automatically by a water supply line that included a float switch so that the net head would be maintained in the range of 10±0.1 kPad. The water supply line to the nozzles was instrumented with a flowmeter to measure the total water injection flowrate. The injection flowrate would achieve a peak value of 170 g/sec (10 lpm) if all 45 nozzles completely opened during the test and there was effectively no hydraulic resistance offered by the debris downstream of the nozzle exits. After bottom water injection was initiated, additional water would only be added from the top if the test section plenum temperature started to rise significantly above saturation, indicating that the top coolant layer had been evaporated. This step would be taken to prevent damage to the upper internals

[2]The total melt hydrostatic head at the time of nozzle opening was estimated to be 23.6 kPa, which included the 18.3 kPa head due to the initial 28 cm collapsed melt depth (melt density taken equal to 6640 kg/m^3), plus an additional 5.6 kPa of head due to the erosion of 27.5 cm of concrete (concrete density taken equal to 2270 kg/m^3, and 13.74 wt% of the concrete mass was assumed to be lost due to liberation of the decomposition gases CO_2 and H_2O from the concrete. See Table 2-4 for concrete composition).

from highly superheated steam that is produced by bottom flooding in the early stages of the transient before the bulk melt temperature has declined significantly.

2.3 Test Section Top Flooding Water Supply System

The top flooding water supply system consisted of a 1900 l capacity tank connected to the flooding weirs in the north and south sidewalls of the top test section through a valve-controlled supply line that provided water to the test section at a specified flow rate. A schematic illustration of the supply system is provided in Figure 2-12; details of the flooding weirs are shown in Figure 2-8. The supply system flowmeter, pressure transducer, level sensor, and thermocouple instrumentation locations are also shown in Figure 2-12. Water flow through the system was driven by a ~ 1 Bar differential pressure in the supply tank at a nominal flow rate of 120 lpm (2 l/s). The inlet water flow rate of 120 lpm corresponds to a melt/water heat flux in excess of 10 MW/m^2 based on a specific enthalpy of 2.6 MJ/kg for saturated steam at atmospheric pressure, assuming heat transfer occurs through boiling of the overlying coolant. The inlet water flow rate to the test section was monitored with a paddlewheel flowmeter. Both the initial water inventory (125 l) and makeup were provided through pneumatic ball valve RV-1, which was opened as needed at the control console to maintain the water volume inside the test section constant at 125 ± 25 l (25 ± 5 cm head). A redundant supply line, activated by pneumatic ball valve RV-2, was provided in case RV-1 failed to open during the test. A third pneumatic valve, RV-3, was provided in case RV-1 or RV-2 failed in the open position. The test was initiated with valve RV-3 in the open position.

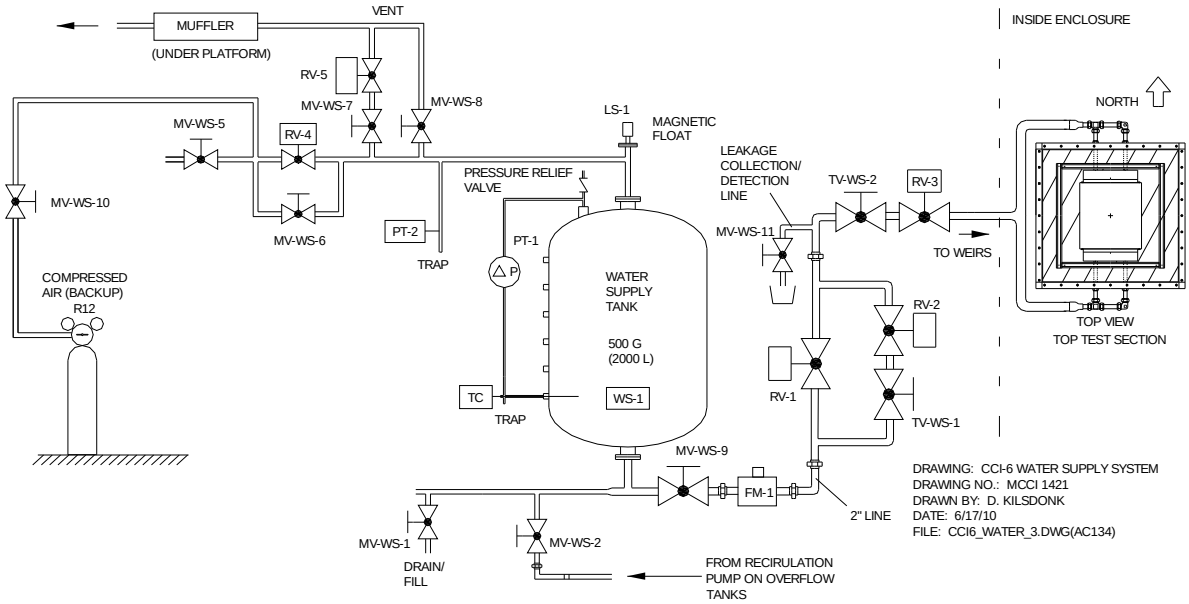

Figure 2-12. CCI-6 Test Section Top Flooding Water Supply System.

Note from Figure 2-12 that the supply line to the test section contained a manual bypass valve downstream of water injection valves RV-1 and RV-2. This valve was vented to a catch pan equipped with an alarmed water detector. During pretest procedures, this valve was left in the open position to divert any water leakage away from the test section. The alarm was

intended to notify personnel that a leak was present so that corrective action could be taken. This valve was closed as one of the final steps of pretest operations prior to evacuation of the cell.

2.4 Quench System

The quench system, shown in Figures 2-13 and 2-14, consisted of a primary quench tank, a secondary spray tank, and two condensate overflow tanks. The quench system flowmeter, pressure transducer, level sensor, and thermocouple instrumentation locations are also shown in these two figures. Steam and concrete decomposition gases passed from the test section through a 15 cm stainless steel pipe into the 680 l capacity, 60 cm ID primary quench tank. This tank contained an initial water inventory of ~ 250 l. With this amount of water, a pool void fraction of ~ 60% could be accommodated before the voided water height reached the top of the tank. The quench tank was equipped with a 1.9 cm diameter cooling coil to remove heat from steam condensation, thereby maintaining a subcooled state.

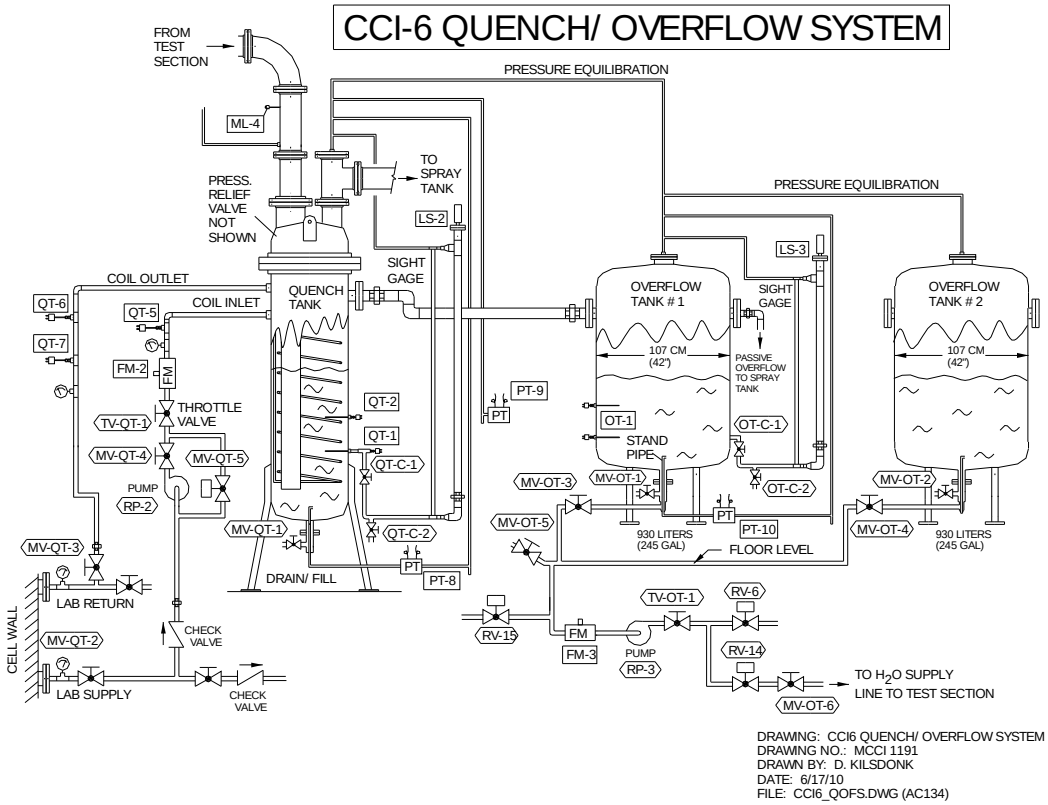

Figure 2-13. CCI-6 Quench and Overflow Tanks.

Once the water level in the quench tank rose to 560 l, spillover into two adjacent 960 l capacity overflow tanks would begin. Water head in these two tanks was kept the same by a 2.54 cm diameter balancing line that connected the two tanks at the bottom. Water inventory requirements were greater for this increased scale test. As a result, a recirculation line was provided so that water could be transferred from the overflow tanks to the top flooding water supply tank at the operator's discretion. This was accomplished by first closing RV-4 and opening RV-5 on the supply system (Figure 2-12) to depressurize the supply tank. Once the

differential pressure in the supply tank fell below ~ 0.5 bar, the transfer operation was initiated by opening RV-14 and starting pump RP-3 on the transfer line between the overflow tanks and the supply tank (see Figure 2-13). After the target amount of water had been transferred, the pump was turned off and the transfer line isolated by closing RV-14. The supply tank was then repressurized by closing RV-5 and opening RV-4 so that additional makeup water could be added to the test section as needed.

The secondary 1230 l capacity spray tank was connected to the quench tank by a 15 cm stainless steel pipe. In the event that the steam generation rate overwhelmed the primary quench tank, the secondary spray tank served to condense the remaining steam. This tank contained an initial water inventory of 375 l. With this amount of water, a pool void fraction in excess of 70% could be accommodated before the voided water height reached the top of the tank. The spray tank and interconnecting piping between the spray and quench tanks was also insulated to minimize heat losses.

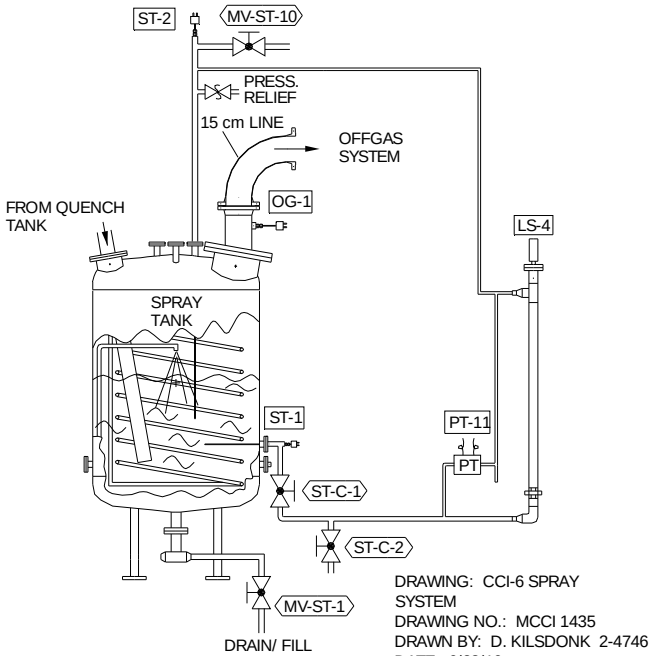

Figure 2-14. CCI-6 Spray Tank System.

2.5 Test Section Pressure Relief System

A pressure relief system was provided to prevent over-pressurization and possible failure of the test section. A schematic illustration of the system is shown in Figure 2-15. The system consisted of a 15 cm vent line from the test section to an auxiliary tank containing a nominal initial water inventory of 400 l. The auxiliary tank had an inside diameter of 1.22 m and a capacity of 4100 l. The tank exit line was open to the cell atmosphere. The pressure relief line to the tank was equipped with a passive, counter-weighted check valve set to open at a differential pressure of nominally 68 kPa. A rupture diaphragm (68 ± 13.4 kPa differential failure pressure) upstream from the check valve prevented any flow through the line unless the pressure in the test section exceeded the design value of 68 kPa differential. As shown in Figure

2-15, the relief line was also equipped with a 7.5 cm vacuum breaker valve. This valve was provided to prevent water hammer from occurring due to stream condensation should the pressure relief valve open and then reseat after water had been introduced into the test section.

The initial 400 1water inventory in the auxiliary tank was provided to cool gases from the test section and to remove aerosols before any noncondensables present in the gas stream passed into the cell atmosphere. The tank was instrumented with a Type K thermocouple to measure water temperature and a differential pressure transducer to measure water depth. The instrumentation locations are shown in Figure 2-15. Water depth and temperature instruments were provided so that the steam condensation rate could be determined should the pressure relief valve open during the test. In this manner, there would be no loss of data should the pressure relief system activate.

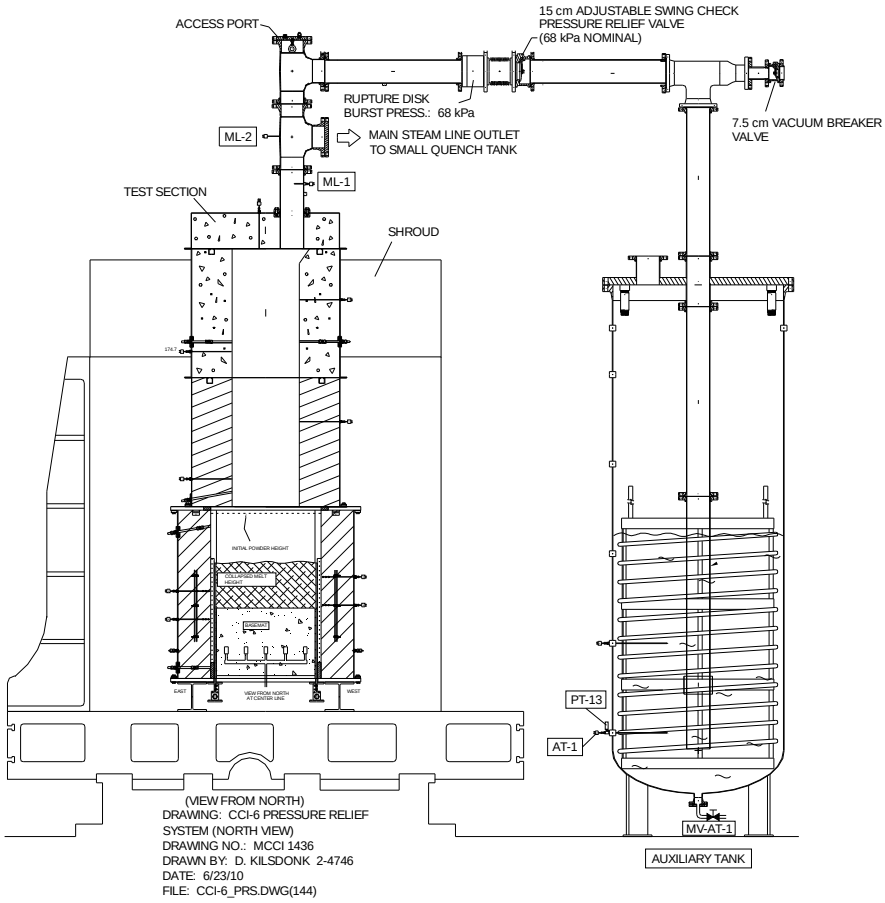

Figure 2-15. CCI-6 Test Section Pressure Relief System.

2.6 Off Gas System

An illustration of the off gas system is provided in Figure 2-16. This system filtered and vented the noncondensable concrete decomposition gases to the cell exhaust. The gases (H_2, CO, CO_2 and the cover gas) exited the spray tank and passed through a flow separator. The cleanup efficiency of the separator was 99% of all entrained solid and liquid when the particle size exceeded 10 microns. After passing through the flow separator, the flow could potentially

split into two parallel off gas system lines. One line was constructed from 7.5 cm piping, while the second was made from 10.0 cm piping. The system was designed with the capacity to accommodate large-scale (up to 120 cm x 120 cm) tests. Since CCI-6 used a reduced scale 70 cm x 70 cm test section, the 7.5 cm side of the parallel off gas system was taken out of service using a blank-off plate at the branch point in the system (see Figure 2-16). As a result, all gas flow was diverted through the 10 cm side of the off gas system. The final filters in the system (4 individual filters per filter housing, yielding a total of 8 filters for each side of the system) removed any remaining particulate before venting the off gases through the flowmeter to the cell atmosphere. The filters (10 cm) were equipped with a passive counter-weighted check valve set to open at a nominal differential pressure of 7 kPa. The bypass was provided in the event that the filters plugged during the experiment.

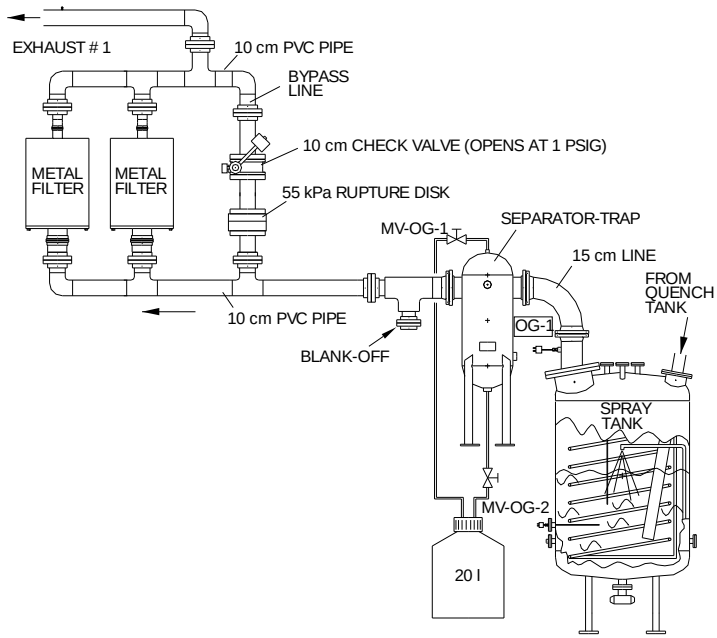

Figure 2-16. CCI-6 Off Gas System.

2.7 Cover Gas System

During the test a uniform flow rate of helium was fed into the test section to suppress burning of combustible concrete decomposition gases (H_2 and CO) and protect test section internals. An illustration of the cover gas system is shown in Figure 2-17. Cover gas flow was modulated by a total of three Hastings Flow Controllers (FC's). One 0-200 slpm FC provided cover gas to the lid camera and light port penetrations, while a second 0-350 slpm FC provided dedicated cover gas flow to the lid camera and optical pyrometer to prevent aerosol deposition on the camera and pyrometer quartz windows through which the melt surface was viewed. A third 0-100 slpm FC was used to inert the apparatus on the evening before the test.

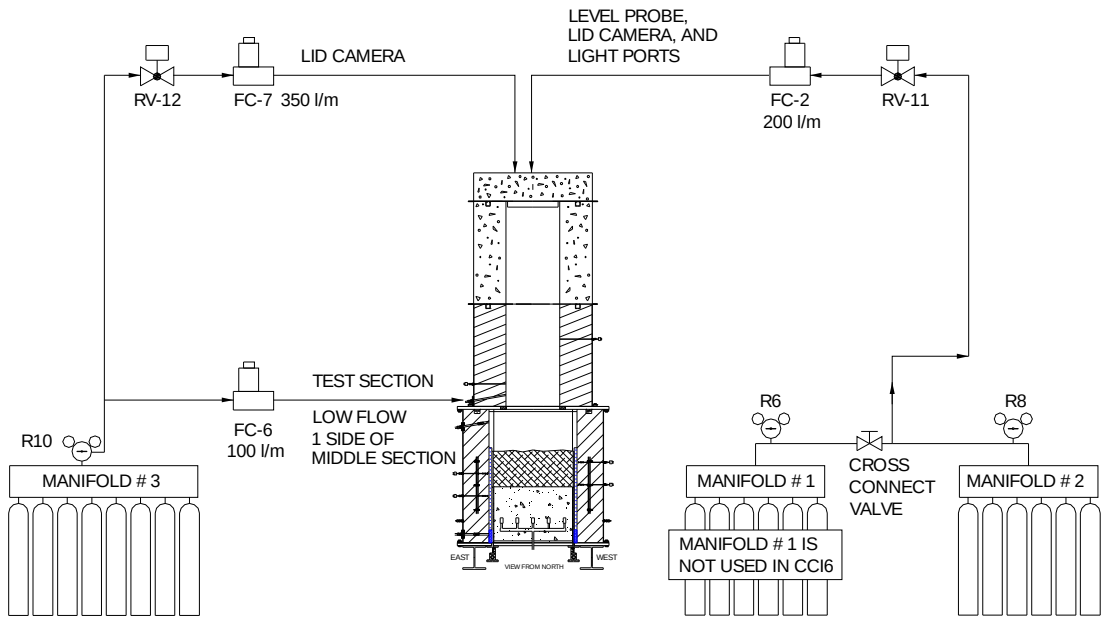

Figure 2-17. CCI-6 Cover Gas System.

2.8 Power Supply

The power for Direct Electrical Heating (DEH) of the corium was provided by a 0.56 MW single phase AC power supply made by NWL Transformers. Output of the power supply was voltage or current controlled. The supply had four voltage/current ranges: 56.4 V/10 kA, 113 V/5 kA, 169 V/3.3 kA, and 226 V/2.5 kA. The power supply was connected to the two arrays of tungsten electrodes in the test section through water cooled copper pipes that passed through a wall of the former reactor fuel loading compartment. The calculated total voltage drop through the water cooled copper pipes and tungsten electrodes at operational temperature and maximum current was less than 0.5 V. The leakage current through the overlying water pool during test operation has been estimated to be less than 1% of the total current.

2.9 Corium Composition

As shown in Table 1-1, the corium oxide phase composition for CCI-6 was specified to contain 6 wt % calcined siliceous concrete as an initial constituent. As part of the developmental work for this test, a specific thermite was developed to produce this particular melt composition. The thermite reaction is of the form:

$$1.22U_3O_8 + 3.3Zr + 0.649Si + 0.531SiO_2 + 0.017Mg + 0.25CaO + 0.084Al + 1.866CrO_3 \rightarrow$$

$$3.66UO_2 + 3.3ZrO_2 + 1.18SiO_2 + 0.017MgO + 0.25CaO + 0.042Al_2O_3 + 1.866Cr;$$

$$Q = -269.08 \text{ kJ/mole } (1.756 \text{ MJ/kg});$$

$$T_{adiabatic} = 2692\ °C;\ T_{actual} \sim 2310\ °C$$

The composition of the melt produced from this reaction is summarized in Table 2-2, while the detailed pre- and post-reaction compositions are provided in Table 2-3. The actual reaction temperature shown under the above chemical reaction was determined by igniting a 1 kg sample in a crucible and measuring the peak temperature with a Type C thermocouple; the raw data are provided in Figure 2-18. As is evident, the temperature plateau occurs at ~ 2310 C.

Note that the pre- and post-reaction compositions shown in Tables 2-2 and 2-3 do not include the additional mass of crushed UO_2 pellets and U_3O_8 powder that were used to line the test section MgO sidewalls. Experience has shown that this material does not participate in the initial exothermic chemical reaction, and remains essentially intact as a protective layer during the ensuing core-concrete interaction. Thus, this material is not included in the initial melt mass estimate for the test.

The thermite powders were packed into the test section in a large, 1.7 mil aluminized Saran bag that was pre-installed over the basemat to prevent water absorption by CrO_3 and concrete oxides (principally CaO and SiO_2), since these constituents are hygroscopic. As an additional measure to prevent moisture infiltration into the thermite from the concrete, the basemat and sidewalls were completely covered with continuous sheets of Saran film before thermite loading. (see Figure 2-7).

Table 2-1. Post-Reaction Bulk Composition for CCI-6 Thermite.

Constituent	Wt%
UO_2	62.51
ZrO_2	25.67
Calcined Concrete	5.68[a]
Cr	6.14

[a]Calcined siliceous concrete, consisting of 79.0/0.9/15.6/4.5 wt% SiO_2/MgO/CaO/Al_2O_3

Table 2-2. Detailed Pre- and Post-Reaction Compositions for CCI-6 Thermite.

Constituent	Reactant		Product	
	Wt %	Mass, kg	Wt %	Mass, kg
U_3O_8	64.99	584.91	-	-
UO_2	-	-	62.50	562.50
Zr	18.99	170.91	-	-
ZrO_2	-	-	25.67	231.03
Si	1.15	10.35	-	-
SiO_2	2.02	18.18	4.49	40.41
Mg	0.01	0.09	-	-
MgO	-	-	0.04	0.36
Al	0.14	1.26	-	-
Al_2O_3	-	-	0.27	2.43
CaO	0.89	8.01	0.89	8.01
CrO_3	11.81	106.29	-	-
Cr	-	-	6.14	55.26
Total	100.00	900.00	100.00	900.00

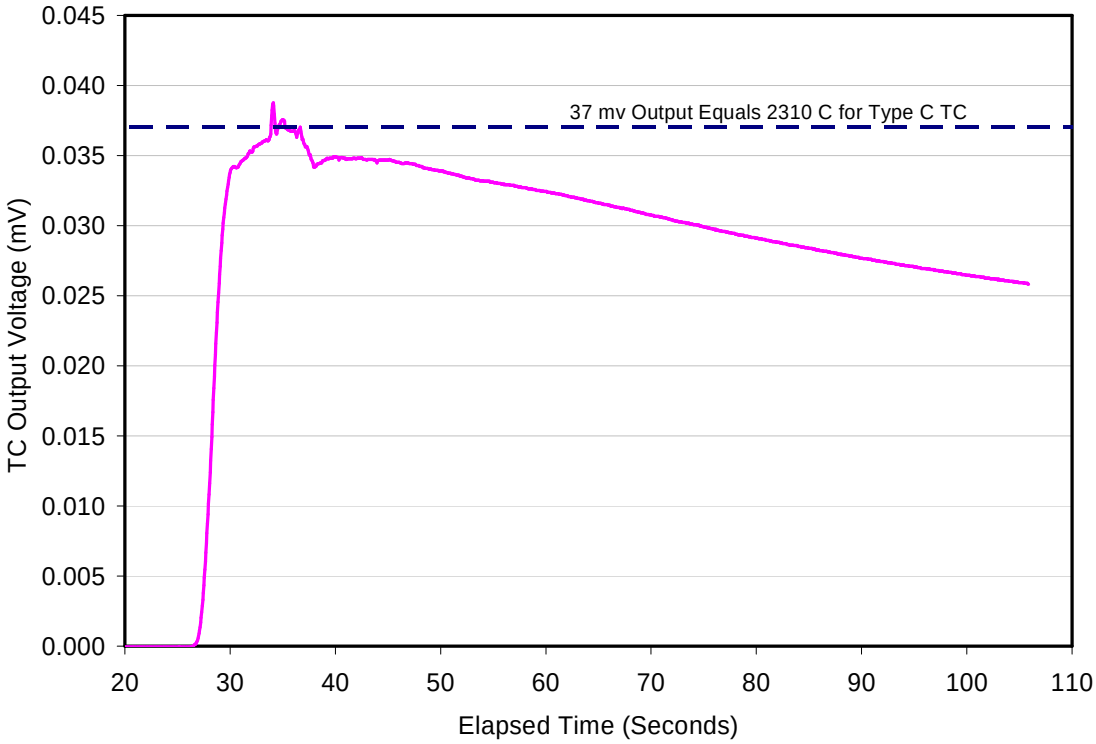

Figure 2-18. Thermite Reaction Temperature Measured by Ignition of a 1 kg Sample.

2.10 Concrete Composition

As shown in Table 1-1, the composition of the CCI-6 concrete basemat and sidewalls was specified to be of the siliceous type. The engineering composition for this particular concrete is shown in Table 2-3. The sand and aggregate for the mix were supplied by CEA as an in-kind contribution to the program. The chemical composition of this concrete is shown in Table 2-4. The composition was determined[3] based on chemical analysis of the archive sample that was produced when the components for this test were poured.

To prevent downward migration and possible escape of concrete decomposition gases during the course of the experiment, the electrode penetrations through the bottom support plate were sealed using O-rings. As described in the next section, the test section was leak checked at 83 kPa differential pressure as part of pretest operations to verify a low leak rate. On this basis, essentially all concrete decomposition gases migrated upwards through the melt pool during the experiment, as opposed to partial loss through the bottom support plate of the apparatus. Reinforcing rod was eliminated so that it did not mask or delay attainment of a fully oxidized melt. The density of the siliceous concrete for this test was ~ 2341 kg/m^3, which was calculated based on the measured mass and volume of the CCI-6 concrete archive sample.

[3]Chemical analysis carried out by the Construction Technologies Laboratories (CTL Group) in Skokie, Illinois.

Table 2-3. Engineering Composition of CCI-6 Siliceous Concrete.

Constituent	wt %	Size Distribution
Aggregate	47.4	5-8 mm: 16.6 wt % 8-11 mm: 20.4 wt% 11-16 mm: 10.4 wt%
Sand	30.6	0-2 mm: 12.2 wt % 2-4 mm: 18.4 wt %
Type 1 Cement	15.3	N/A
Tap Water	6.7	N/A

Table 2-4. Chemical Composition of Siliceous Concrete.

Oxide	*Wt%*
SiO_2	*53.65*
Al_2O_3	*4.03*
Fe_2O_3	*1.30*
CaO	*22.42*
MgO	*0.90*
SO_3	*0.77*
Na_2O	*0.67*
K_20	*0.97*
TiO_2	*0.15*
P_2O_5	*0.07*
Mn_2O_3	*0.07*
SrO	*0.04*
CO_2	*8.74*
H_2O, Free	*2.87*
H_2O, Bound	*3.61*
Total	*100.26*

2.11 Instrumentation and Data Acquisition

The CCI-6 facility was instrumented to monitor and guide experiment operation and to log data for subsequent evaluation. Principal parameters that were monitored during the course of the test included the power supply voltage, current, and gross input power to the melt; melt temperature and temperatures within the concrete basemat and sidewalls; crust lance position and applied load; supply water flow rate to the test section weirs as well as to the concrete nozzles; water volume and temperature within the test apparatus, and water volume and temperature within the quench system tanks. Other key data recorded by the DAS included temperatures within test section structural sidewalls, off gas temperature and flow rate, and pressures at various locations within the system.

All data acquisition and process control tasks were managed by a PC executing LabVIEW 8.2 under Windows XP. Sensor output terminals were connected inside the test cell to model HP E1345A 16-channel multiplexers that were integrated into a mainframe chassis in groups of eight. An illustration of the DAS setup is provided in Figure 2-19. The multiplexers directed signals to an HP E1326B 5 ½ digit multimeter incorporated into each chassis. Three

independent 128 channel systems were used for CCI-6. The detailed channel assignment lists for each of these systems are provided in Appendix A.

Signal noise was reduced by the digitizer through integration over a single power line cycle (16.7 ms). The digitized sensor readings were routed from the test cell to the PC in the control room via two HP-IB extenders. The extenders allowed the ASCII data from the HP to be sent through the cell wall over a BNC cable. The extender within the control room then communicated with a GPIB card within the PC. This configuration also permitted remote control of the multimeter through LabVIEW.

Integration of the signals over the period of a power line cycle limited the speed with which the multiplexer could scan the channel list. The minimum time for the digitizer to scan the list was ~1.7 s (16.7 ms • 100 channels/chassis for this test). Though the three systems operate independently, implying the ability to update all 300 channels in roughly two seconds, the actual time required for the update was about 5 seconds.

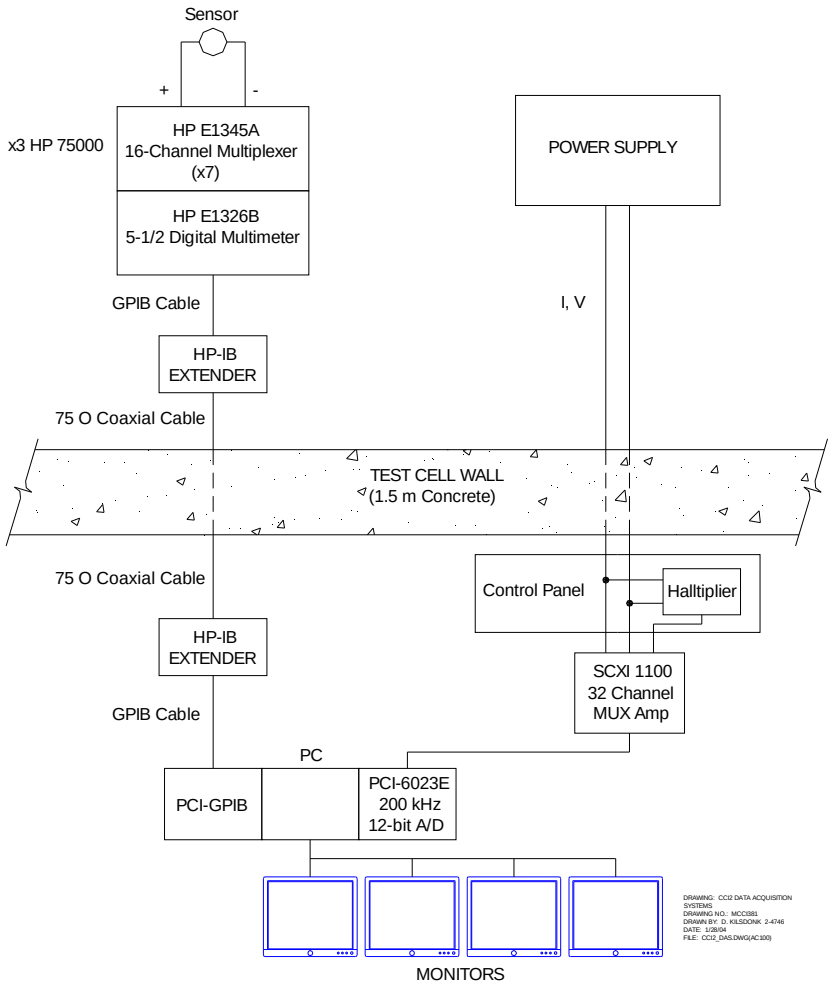

Figure 2-19. Data Acquisition System Setup for CCI-6.

The concrete basemat and sidewalls for CCI-6 were instrumented to monitor melt temperature during both the top flooding and bottom water injection phases of the test using multi-junction Type C thermocouples in tungsten thermowells. In addition, a two-color optical pyrometer was used to measure the debris upper surface temperature before water addition and during periods when aerosol production did not optically occlude the view of the surface. Multi-junction Type K thermocouples cast directly into the basemat and sidewalls were also used to track the progression of the concrete ablation front. Plan and elevation views of the basemat thermocouple layout are provided in Figures 2-20 and 2-21, while the sidewall thermocouple layout is shown in Figure 2-3. Note that the thermocouple junction locations were spread out to provide melt temperature and ablation front location data over the full range of possible concrete ablation depths. As shown in Figure 2-3, for CCI-6 the first junctions of the laterally mounted Type C thermocouples in the concrete sidewalls were extended out 5.0 cm from the concrete surface to provide data on melt temperature adjacent to the walls early in the experiment.

A further instrumentation requirement[4] was to provide sufficient thermocouple planar density to detect concrete ablation to a depth of 2.5 cm into the concrete basemat and/or sidewalls, since the cavity was to be flooded when any combination of two thermocouples at this depth indicated arrival of the ablation front (see Table 1-1). The positions of the various thermocouples that were installed to achieve this detection capability are shown in Table 2-5.

Table 2-5. Type K Thermocouple Locations Used to Determine the Timing of Water Addition to the Test Section.

Instrument Name	Test Section Concrete Component	Planar Position	Depth Below Concrete Surface
A-2	Basemat	Centerline	2.5 cm
B-2	Basemat	Northwest quadrant	2.5 cm
C-2	Basemat	Northeast quadrant	2.5 cm
D-2	Basemat	Southeast quadrant	2.5 cm
E-2	Basemat	Southwest quadrant	2.5 cm
SWG-2	North wall	Lateral centerline, 0.0 cm above basemat	2.5 cm
SWI-2	North wall	Lateral centerline, +12.5 cm above basemat	2.5 cm
SWK-2	North wall	Lateral centerline, +25.0 cm above basemat	2.5 cm
SWH-2	South wall	Lateral centerline, 0.0 cm above basemat	2.5 cm
SWJ-2	South wall	Lateral centerline, +12.5 cm above basemat	2.5 cm
SWL-2	South wall	Lateral centerline, +25.0 cm above basemat	2.5 cm

The test section sidewalls were also instrumented with a total of 12 Type K and Type C thermocouples to measure the sidewall heat up prior to water addition, and also to measure the sidewall cooling rate above the melt surface after water was added. Illustrations of the remaining functional thermocouple locations in the test section sidewalls are provided in Figures 2-22 and 2-23. When these sidewall components were originally built, there were significantly more thermocouples cast in the walls, but many failed over the course of the 6 large scale tests conducted as part of the MCCI-1 and MCCI-2 programs. Thus, for CCI-6, only 12 functioning junctions remained to record sidewall thermal response during the test.

[4] See Action 6.3 from the Minutes of the 6th OECD/MCCI-2 PRG meeting held at Argonne 20-21 April, 2009.

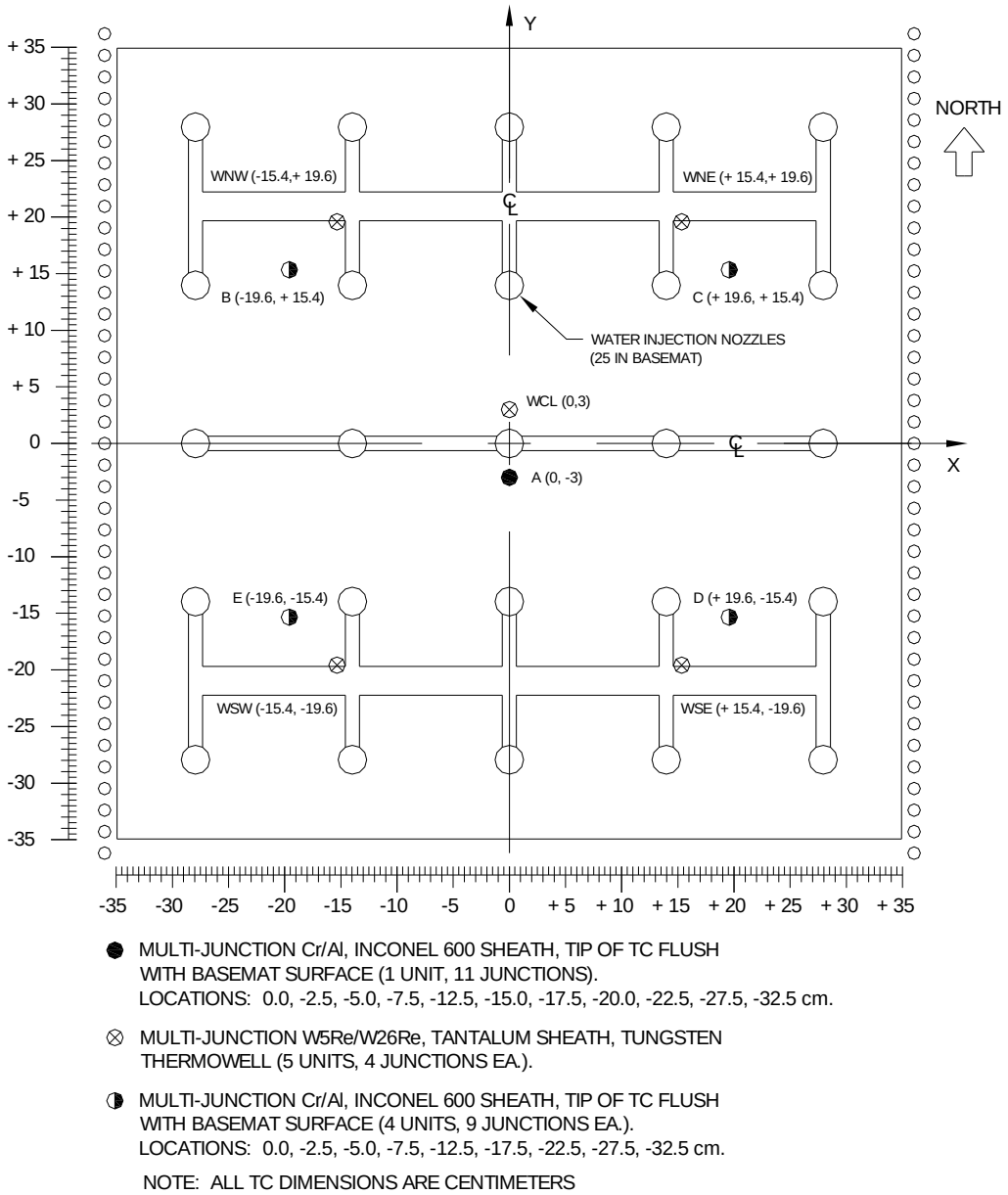

Figure 2-20. Plan View of Basemat Instrumentation Layout (dimensions are in cm).

One method for monitoring water level in the test section was provided by a differential level probe which was inserted through a sealed penetration in the lid. The probe was maintained in a retracted position during the dry ablation phase until water was added to the test section. After water addition, the probe was intended to be inserted to a distance of 48 cm from the initial basemat surface (20 cm from the initial collapsed melt surface). The probe tip was instrumented with two 1.6 mm diameter ungrounded junction Type K TC's which monitored plenum gas temperature prior to water addition; thereafter, the TC's monitored the water temperature over the melt surface. The probe tip locations after insertion are shown in Figure 2-24.

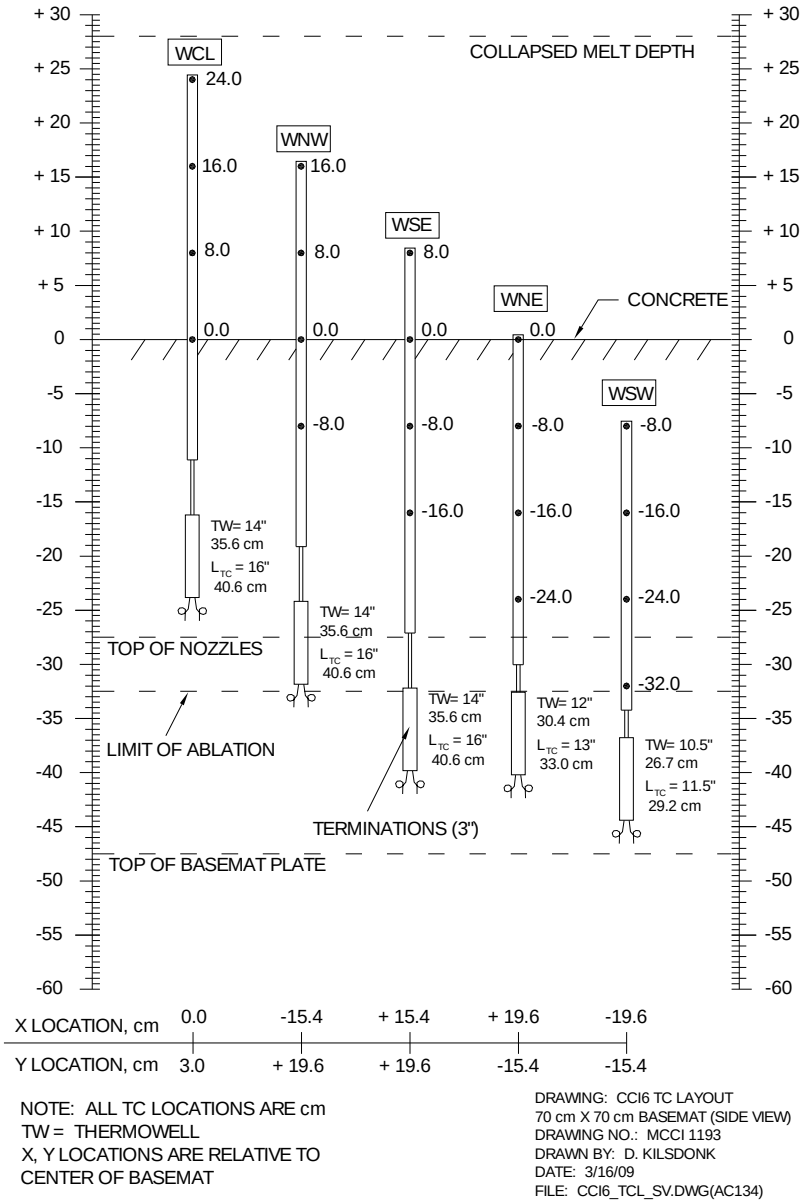

Figure 2-21. Elevation View of Basemat Type C Thermocouple Locations.

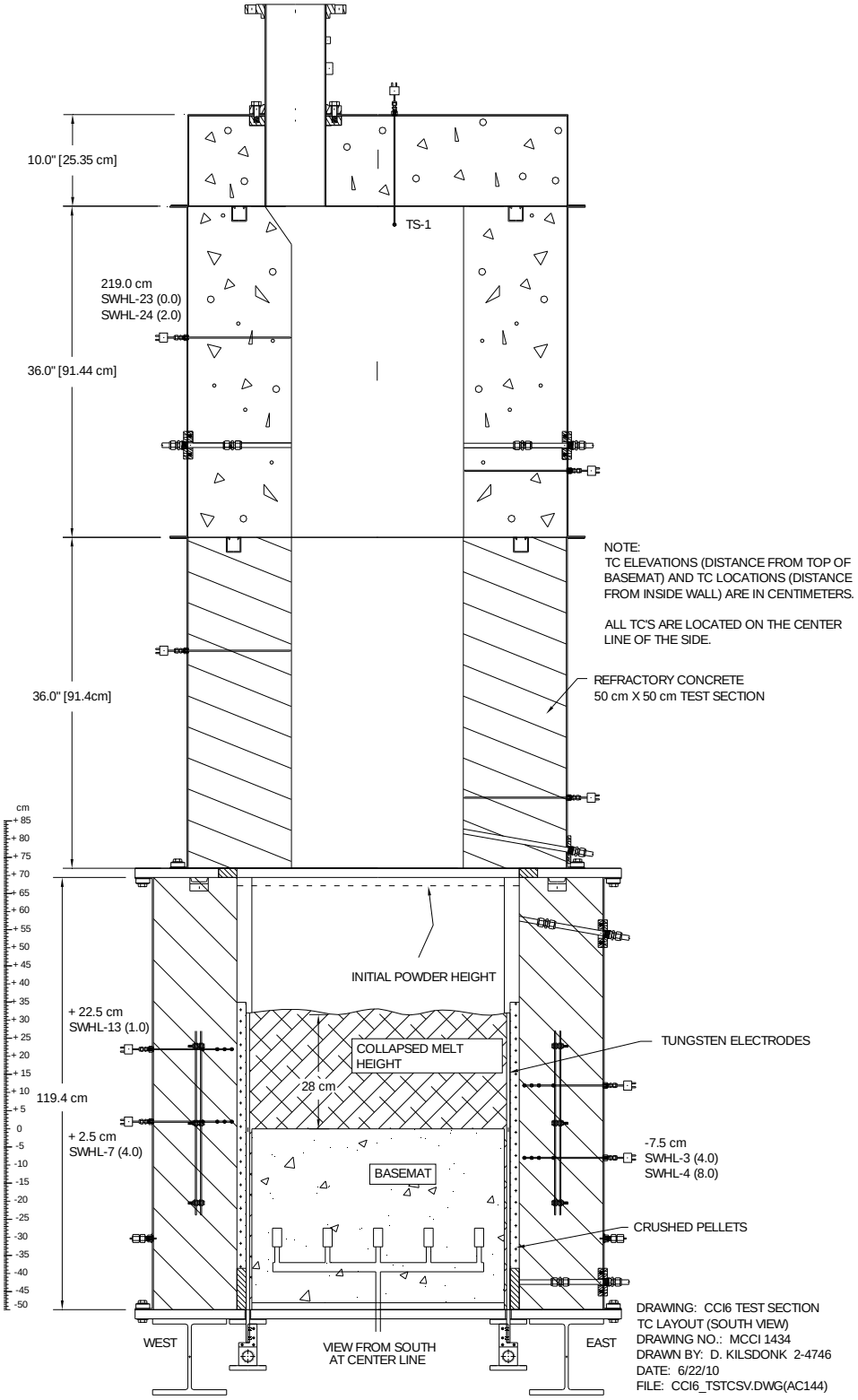

Figure 2-22. CCI-6 Test Section Sidewall Instrumentation (view from west).

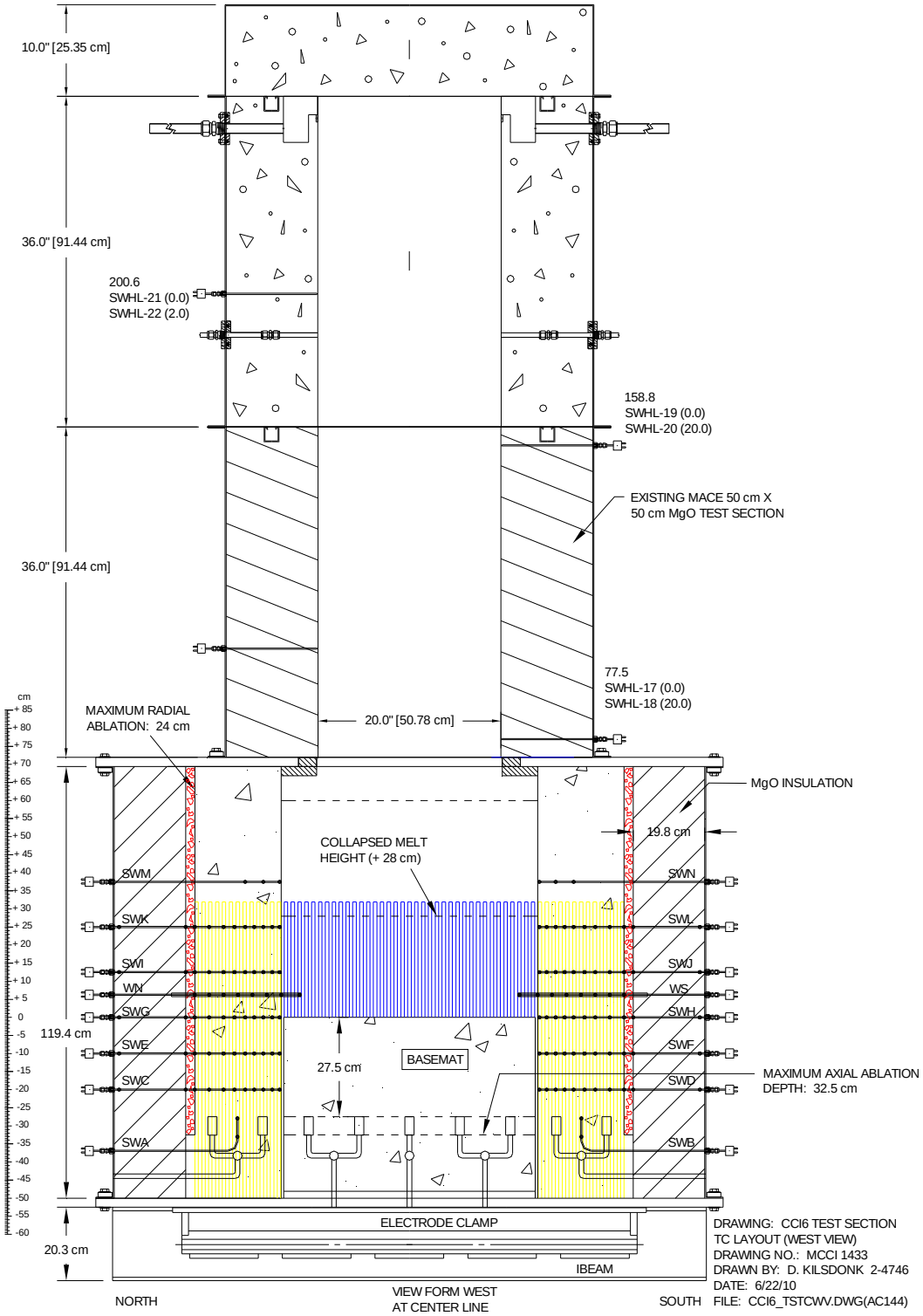

Figure 2-23. CCI-6 Test Section Sidewall Instrumentation (view from south).

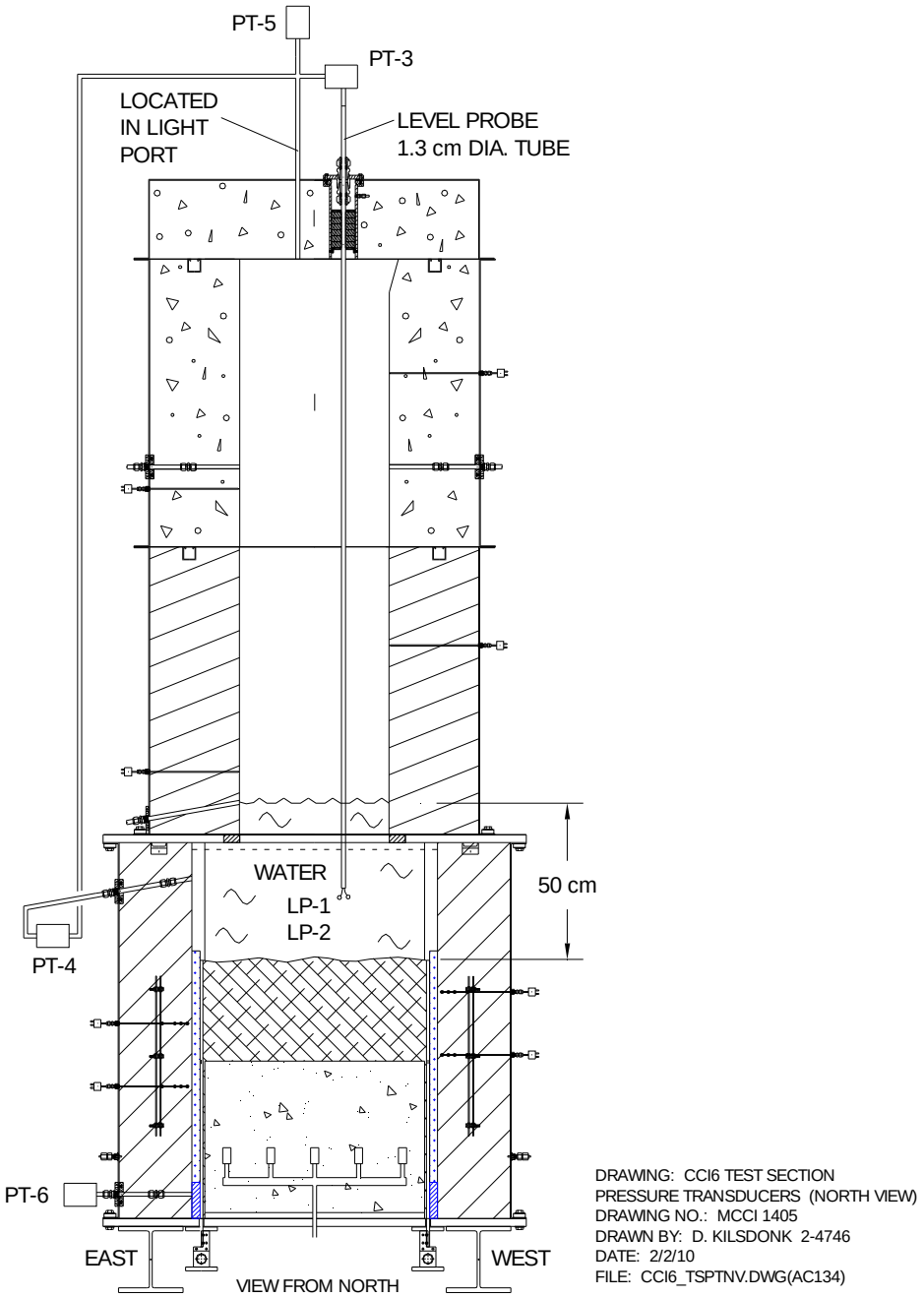

Figure 2-24. CCI-6 Test Section Pressure Transducer Layout.

Aside from the insertable water level probe, two additional methods were provided to monitor the water volume in the test section. The first was a static water level port located in the North sidewall 57.5 cm from the initial basemat surface (~30 cm from the initial collapsed melt surface). The port location is shown in Figure 2-24. The second method was provided by an on-line calculation of the water volume in the test section based on conservation of mass; i.e., the water volume in the test section at any time was equal to the initial volume in the supply/quench system tanks minus the volume in the same tanks at the current time.

The top flooding water supply tank was equipped with a magnetic float to measure the time-dependent water level. As a redundant level measurement technique, the tank was also equipped with a differential PT. Water flow rate to the test section was monitored by a paddlewheel flowmeter. The location of the supply system instrumentation is shown in Figure 2-12. The basemat water nozzle header tank was equipped with a differential PT to measure water head, and the supply line to the nozzles was equipped with an ultrasonic flowmeter. Instrument locations for this system are shown in Figure 2-11.

The quench, overflow, and spray tanks were instrumented to measure the transient energy deposition due to steam generation from corium quenching in the test section. The quench and overflow tank instruments are shown in Figure 2-13, while the spray tank instrumentation is shown in Figure 2-14. Each tank was equipped with a magnetic float and (redundant) differential PT to measure the accumulating water volume due to steam condensation. Transient water temperatures in all tanks were monitored using Type K TC's (two in the quench and spray tanks and one in each overflow tank). Water flow rate and temperature differential across the quench tank cooling coil were monitored with a paddlewheel flowmeter and Type K TC's, respectively, thus providing a measurement of the time-dependent energy extraction rate from the water mass in the tank. The main steamline between the test section and quench tank was instrumented with Type K TC's to measure the local gas and pipe structure temperatures. The steamline thermocouple locations are shown in Figure 2-9.

Key system pressures were monitored with strain-gauge type pressure transducers manufactured by Sensym, Inc. As shown in Figures 2-12 through 2-14 and 2-24, the pressure in all system tanks was monitored, as well as the test section plenum pressure. An additional PT was located in the lower test section to monitor the pressure beneath the melt upper surface. This transducer was mounted on the east sidewall of the test section at an elevation of 43 cm beneath the initial concrete surface (see Figure 2-24). The gap between the MgO sidewalls and the electrodes was packed with crushed UO_2 pellets and U_3O_8 powder during corium loading. Thus, this PT could sense the pressure beneath the melt surface as long as the gap did not plug during the test.

In terms of the power supply operating parameters, voltage drop across the tungsten electrode bank was monitored with the DAS voltmeter, while current input was monitored with two parallel 5000:1 current transformers. Power input to the melt was monitored with two Hall Effect meters.

In addition to the above instrumentation, visual information regarding the core-concrete interaction and melt quenching behavior was provided by a video camera mounted on the upper lid of the apparatus. Five area video monitors were also used in the cell to monitor for leaks, and to record any disruptive events (e.g., steam explosion) should one occur.

3.0 TEST PROCEDURES

3.1 Pretest Preparations

Assembly of the apparatus began through the installation of the 126 tungsten electrodes into machined copper electrode clamps. The electrode clamps were then attached to the bottom of the 2.54 cm thick aluminum support plate, which served as the foundation for the entire apparatus. With the electrode clamps installed, the instrumented basemat, two concrete sidewalls, and finally the two inert MgO walls were set in place on the support plate. The lower section flange bolts and clamping bars were then installed and tightened. Following this step, the water nozzle assemblies in the basemat and two walls were leak checked to verify that they had not been damaged during the fabrication, transport, and installation stages of the test preparations. Following verification that the nozzles were still leak tight, the basemat and sidewall instruments were then connected to terminal boxes that were prewired to the data acquisition system.

In parallel with test section assembly, the thermite powders were mixed in preparation for corium loading. As a precursor for initiating mixing, a gas sample test[a] was conducted to verify that the initial level of volatile impurities in a sample prepared from the CCI-6 thermite constituents was sufficiently low to preclude excessive gas release during the burn. The results of this test indicated that the moisture content was within acceptable limits. On this basis, mixing was initiated.

Once the lower section was assembled, preparations for loading of the corium charge were initiated. A single large 1.7 mil aluminized Saran bag was preinstalled over the basemat. During loading, the 900 kg thermite charge was placed within this bag in order to reduce the amount of bagging material present in the thermite. As the powders were placed in the test section, the basemat melt temperature thermocouples were monitored to detect any localized heating in the corium powders. If heating was observed, the cell was to be evacuated immediately. Prior to loading of the thermite, the gaps between the tungsten electrodes and MgO sidewalls, as well as the gap between the concrete and backup MgO on the concrete sidewalls, was filled with crushed UO_2 pellets and U_3O_8 powder. The crushed pellets and powder served as a protective layer against excessive chemical/thermal attack by the corium during the test. Once loading was completed, two sparkler igniters were placed a few centimeters below the top of the powders near the center of the test section, and then the bag was folded and sealed.

Once loading was completed, a removable train containing a 1.0 kg bagged sample of thermite was installed over the powder bed; an illustration is provided in Figure 3-1. The sample train was removed weekly and the sample weighed to monitor the moisture pickup by the thermite during the period between loading and test initiation. Note from Figure 3-1 that the top portion of the train also contained a 4.5 kg canister of desiccant. The desiccant was provided to maintain the plenum gas as dry as possible during pretest operations. As an additional measure

[a]The gas sample test procedure consisted of igniting a representative sample of the thermite in a closed vessel. The amount of noncondensable gas produced was determined from the ideal gas law; the composition of the evolved gases was assumed to consist of hydrogen evolved from moisture present in the thermite.

to prevent moisture accumulation in the powder bed, the lower test section was continuously purged with argon (2 slpm) from the time loading was completed until the test was initiated.

Following loading, the remainder of the test apparatus was assembled. This included installation of the two upper sections and the enclosure lid. Peripheral instruments were then installed and connected to terminal boxes. The main gas line from the test section to the quench tank was installed, as well as the pressure relief line from the test section to the auxiliary tank. (The main steamline was closed off from the test section using an insertable blank-off plate throughout pretest operations to preclude moisture migration from the quench tank back into the test section).

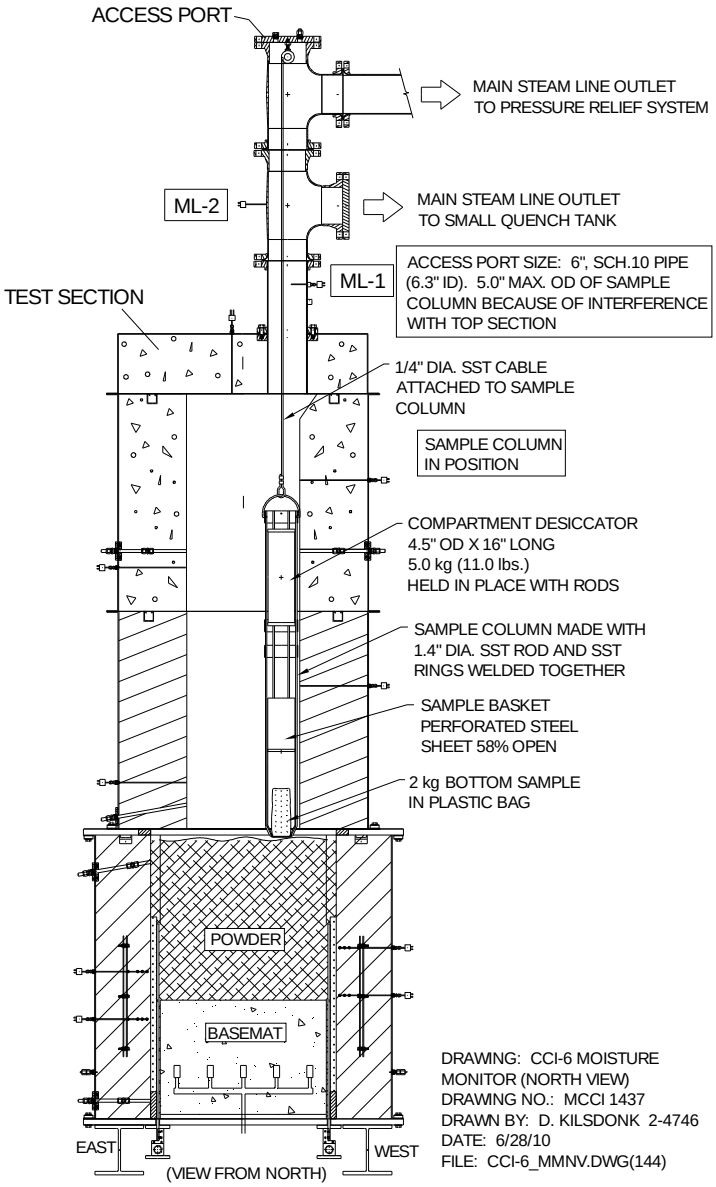

Figure 3-1. Illustration of Thermite Sample Train Installed in Test Section.

After assembly was completed, extensive system checkout procedures were performed to ensure that the facility was in proper working order. This included a proof test of the test section at 83 kPad, which is 20 % in excess of the pressure relief system activation pressure of 69 kPad. The pressurization gas for this test was argon. An insertable blind flange was installed upstream of the rupture disk in the pressure relief line to isolate this system. During the test, the apparatus was gradually pressurized to the proof pressure. After a 1 minute hold at this pressure, the system was isolated to determine the leak rate. The leak rate of the CCI-6 test section was found to be 4.1 kPa/min (26.3 slpm) at a nominal pressure of 55 kPad, which was significantly below the acceptable leak rate of the fully assembled test section (i.e., < 2 % of the expected peak gas/vapor generation rate during the test).

Pretest preparations for CCI-6 culminated with a final full system checkout that involved remotely running all equipment with the power supply in operation across a water cooled dummy load. Once the full system check was completed, final system preparations were carried out. These efforts included: (i) hookup of the power supply to the tungsten electrodes through water cooled buss bars, (ii) installation of the final piping connections between the top flooding and bottom water injection water supply systems to the test section, and (iii) removal of the sample train from within the test section. Following connection of the power supply to the electrode clamps, the key for the power supply lockout located in the cell, as well as the key for the interlock located on the control room console, were assigned to a custodian who kept the keys in their possession until the test was initiated. This step was taken to preclude inadvertent activation of the power supply.

Over the six week time interval spanning pretest operations that included onset of thermite mixing through test execution, the moisture content of the removable sample of bagged thermite increased gradually from 0.043 wt % to 0.07 wt %. The final moisture content was within the maximum permissible level of 0.3 wt %. On this basis, final approval was granted to proceed with the execution of Test CCI-6.

3.2 Test Operations

The planned test operating procedure is described first, followed by a summary of the actual operating procedure.

Prior to initiating the thermite reaction, a helium gas flow rate would be established through the lid of the test section. The thermite would then be ignited using sparklers located at the top of the powder charge. Once the reaction was complete (~ 30 seconds), the power supply would be ramped at a rate of ~ 3000 Amps/minute up to the initial target power level which was specified to be 210 kW (see Table 1-1).

Unlike previous CCI tests, the operating procedure for CCI-6 called for early cavity flooding after ablation had been established. The specific criterion for initiation of flooding was that any combination of two different thermocouples located 2.5 cm within the concrete indicated arrival of the ablation front (see Table 1-1). The specific instruments that would be used to make this determination are shown in Table 2-5. At this point, the cavity would be flooded. Following completion of bulk cooling, the power supply operating mode would be

switched from constant power at the initial level of 210 kW (see Table 1-1), to constant voltage. Thus, if significant debris quenching occurred, power supply operation in this mode would approximately maintain *the specific power density in the remaining melt constant at the level established prior to cavity flooding* (recall that the direct electrical heating method does not significantly heat solidified debris; see Appendix B for the underlying technical basis for this statement).

The test would operate in this manner until the axial ablation depth reached 22.5 cm. During this phase, water depth over the melt would be kept in the range of 25±5 cm. If the lateral ablation reached 24 cm, then the backup UO_2 pellet and U_3O_8 powder liner and MgO sidewalls would terminate sidewall ablation and allow axial ablation to progress further. The crust lance would be used to break the crust at the melt water interface during this phase to provide data on *in-situ* crust strength, as well as information on the nature and extent of cooling after the crust is breached.

If the melt quenched and stabilized during the early flooding stage, then the test would be terminated. However, if the 22.5 cm ablation depth was reached, the water injection system would be reconfigured to inject water from below under a static water head of ~ 10 kPa as the nozzles gradually opened. When the axial ablation depth reached the 22.5 cm depth, the isolation valve that separates the nozzle header supply tank from the nozzles would be opened (i.e., valves RV-INJ-BASEMAT and RV-INJ-PLENUM in Figure 2-17) in preparation for water injection from below as the nozzles opened by ablation. As water was injected, makeup to the header tank would be provided automatically by a supply line with a float switch that maintained the head in the range of 10±0.1 kPad. Additional water would only be added from the top at this stage if the test section plenum temperature started to rise above saturation, indicating that the top coolant layer had been evaporated. Past this point, the melt would either quench, or axial ablation would proceed to 32.5 cm. In either case, the experiment would be terminated by turning off the power supply that provides DEH to the melt.

CCI-6 was performed on 18 March 2010. On the evening prior to the experiment, the apparatus was inerted with a slow bleed of helium into the test section. On the day of the experiment, the apparatus was brought up to operating conditions, a final walk through inspection was performed by operating personnel, the thermite igniter was hooked up, and finally the power supply was energized before the containment was evacuated and sealed. Per the normal test procedures, the Argonne Fire Department was called and notified of the intended test startup, and a communications link between the department and MCCI control room was established. Data acquisition was initiated at 17:22. Coolant and cover gas flows were brought up to design conditions, and the cell ventilation system was closed and sealed per test procedures.

An event sequence for CCI-6 is provided in Table 3-1. In the discussion that follows, time t = 0 corresponds to melt contact with the concrete basemat. The criterion used to define the onset of concrete ablation at a given location was that the local temperature reached the siliceous concrete liquidus of 1250 °C. [6]

Table 3-1. CCI-6 Event Sequence.

Time (Min)	Event
-6.64	Data acquisition initiated.
-0.8	Power applied to thermite igniter wire.
-0.6	Thermite burn initiated
0.0	Thermite burn completed (burn time ~ 40 seconds); melt temperature ~2100 °C.
0.17	Main steamline fails at test section Tee leading to high temperature gas jet into cell. Gas discharged into the cell over the balance of the test.
0.66	No. 4 filter inserted; view reveals that plenum is dense with aerosols; churning melt conditions are evident.
0.71	Cavity flooded (to reduce temperature of gas jet into cell). Initially, the heat transfer rate to water is so intense that the water is boiled off as soon as it is added. Peak melt-water heat flux reaches 5 MW/m^2 and then steadily declines.
1.45	Continued water addition finally clears aerosols from plenum. View shows melt surface partially covered by crust that is floating on top of melt. Multiple eruptions occur through crust material. Water rapidly boiled away.
2.04-2.31	Surface dries out, revealing floating crust. Additional water was added, followed by eruptions at various locations on surface. Eruptions move around almost continuously on surface; site density is ~ 20 $holes/m^2$.
2.3	DEH input power reaches 210 kW but not held; conditions are unstable.
3.1	Melt surface eventually goes dark, indicating stable crust formation. Intense boiling off the surface of the crust. Occasional small eruptions lasting a second or two occur randomly around the surface of the crust.
4.14-7.29	Large scale eruptions begin in northwest corner of test section and these occur almost continuously until they stop at 7.29 minutes.
7.29-21.1	No sustained eruptions occur, and the debris-water heat flux steadily declines from ~ 500 kW/m^2 to ~350 kW/m^2 over the interval.
5.8-20.8	Power brought back to 210 kW, but current limit of 9000 Amps is also reached. During the period operations were maintained at the 9000 Amp limit, while power gradually drifted down to 190 kW.
9.57-39.4	Onset of axial basemat ablation at centerline and in all four quadrants; ablation rate remains slow during the balance of the test at ~ 2 cm/hour.
20.9-26.0	Onset of rapid ablation transient in south wall as the 2.5 cm erosion depth is reached at the +12.5 cm elevation at 20.9 minutes. Ablation rate averages 2.7 cm/min over this time interval as the ablation depth proceeds to 16 cm and then slows dramatically. North wall ablation is minimal.
22.9	2.5 cm erosion depth reached at the 0.0 cm elevation in the south wall.
21.1-25.9	Large melt eruptive events occur over the interval that result in a significant increase in upwards heat transfer rate. Eruptions start near the center of the south concrete wall at 21.1 minutes. The eruptions proceed at this location almost continuously until 23.2 minutes. Then the crust surface remains dark until 24.5 minutes. At this time, a large eruption event is initiated in the northeast corner of the test section, and proceeds almost continuously until ending at 25.9 minutes; the heat flux peaks at 3 MW/m^2 at 25.3 minutes. The crust surface goes dark again and remains that way for the rest of the test.
22.2	Operator is able to increase power back to target level of 210 kW due to increase in melt resistance; constant voltage operation begins at 27 volts.
24.6	Power supply operations switched from current to voltage control mode.
22.2-26.5	Input power falls steadily at constant voltage from 210 to 65 kW; at the end of the period the rate of power decrease slowed dramatically.
27.2	Ablation depth reaches 13 cm in south wall at 0.0 cm elevation before stabilizing
60.3-66.7	Crust lance inserted; modest load encountered until ~ 1.3 cm elevation is reached. Cooling transient observed on video *after* the lance is withdrawn.
26.5-150.9	Power gradually falls from 65 kW to zero at constant voltage. Power supply operations terminated at 150.9 minutes.
170.8	Data logging terminated.

As shown in Table 3-1, data acquisition began at -6.64 minutes relative to initial melt contact with the basemat. As shown in Figure 3-2, power was applied to the nichrome wire/sparkler located at the top of the powder charge at -0.8 minutes. Based on video camera data from the test section and plenum gas temperature readings (Figure 3-3), thermite ignition was announced and logged in the control room at -0.6 minutes. Based on readings from the Type K thermocouples cast flush with the concrete basemat surface (Figures 2-20 and 3-4), the burn front reached the bottom of the powder bed and contacted the concrete in ~ 40 seconds (i.e., at 0.0 minutes), which was within the planning basis for the experiment. The readings from selected melt temperature thermocouples are shown in Figure 3-5 over the first few minutes of the interaction. As is evident from this collection of data, peak melt temperatures near the center of the melt over the first minute of the test reached 2100 °C.

Soon after the burn was completed (i.e. at 0.17 minutes), a hole was melted through the main steamline at the piping Tee directly on top of the test section, leading to a high temperature gas jet discharging into the cell. A substantial fraction of the gas products generated from the test leaked through this hole directly into the cell atmosphere over the balance of the test. Posttest examinations would reveal that this occurred due to the fact that high temperature melt was entrained into the steam line, and the subsequent melt impingement heat transfer at the Tee caused local melt through of the pipe.

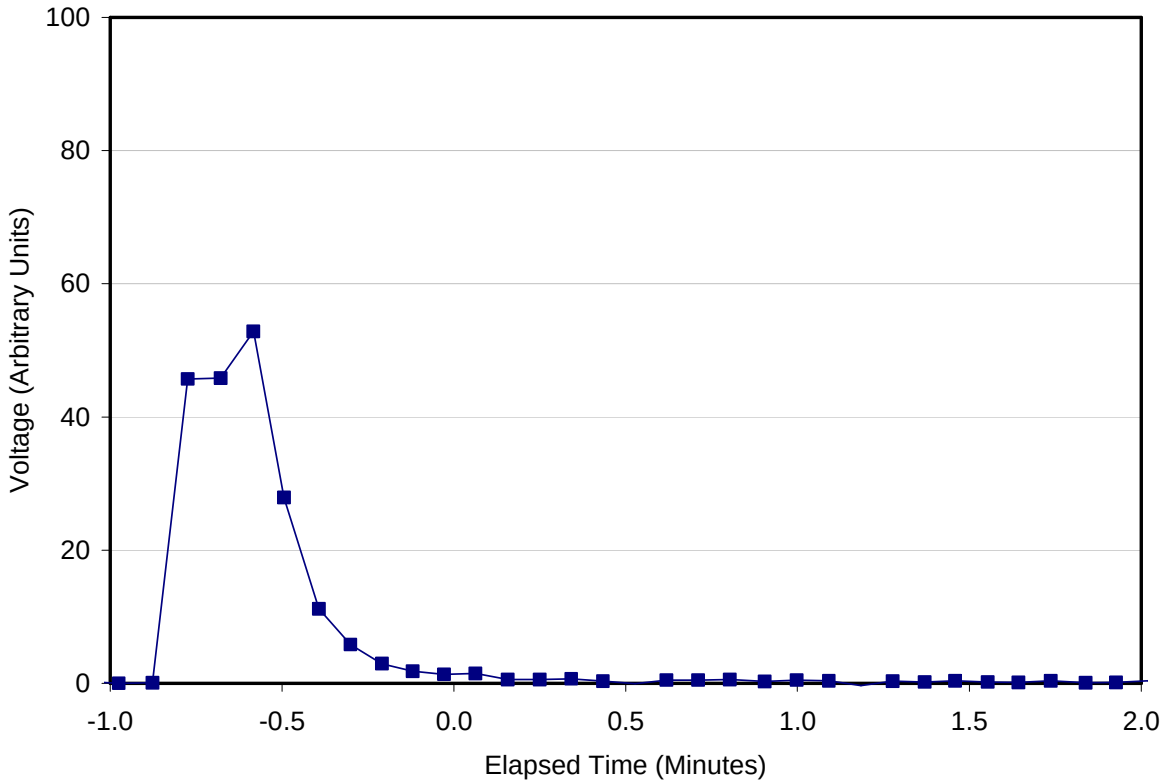

Figure 3-2. Voltage Across Thermite Igniter Shunt.

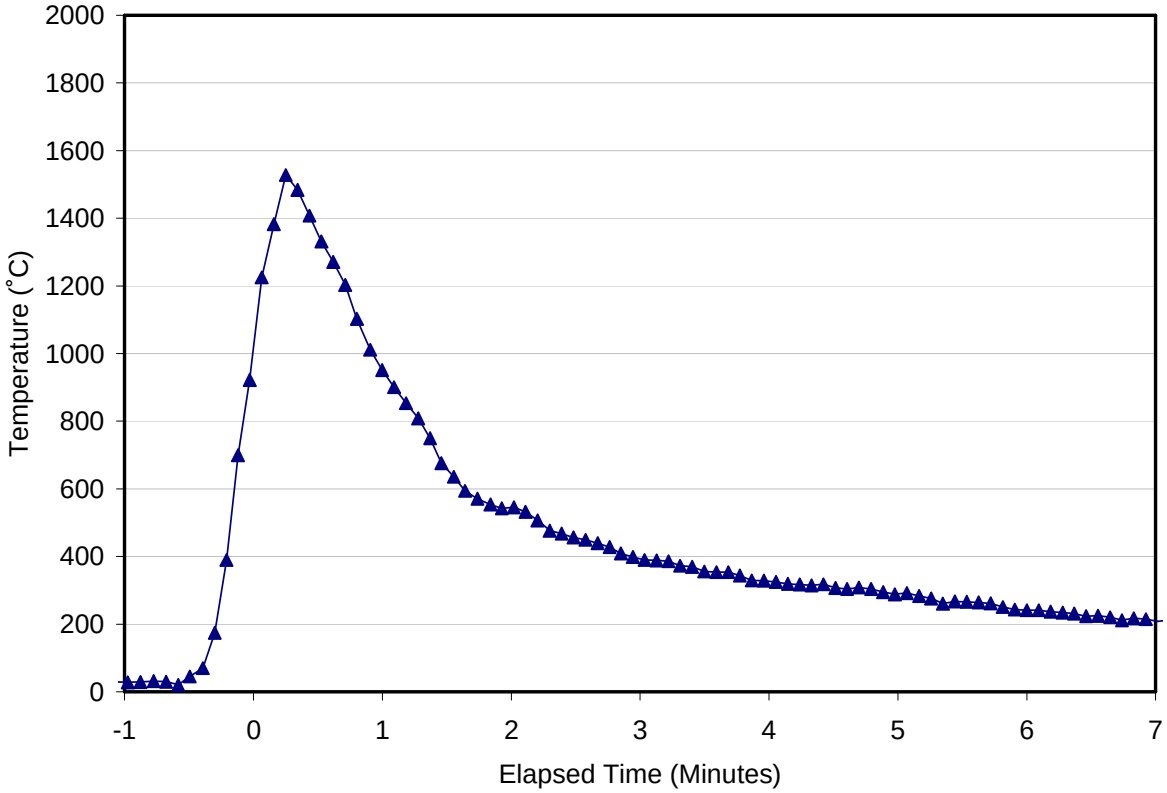

Figure 3-3. Test Section Upper Plenum Gas Temperature during the Initial Interaction.

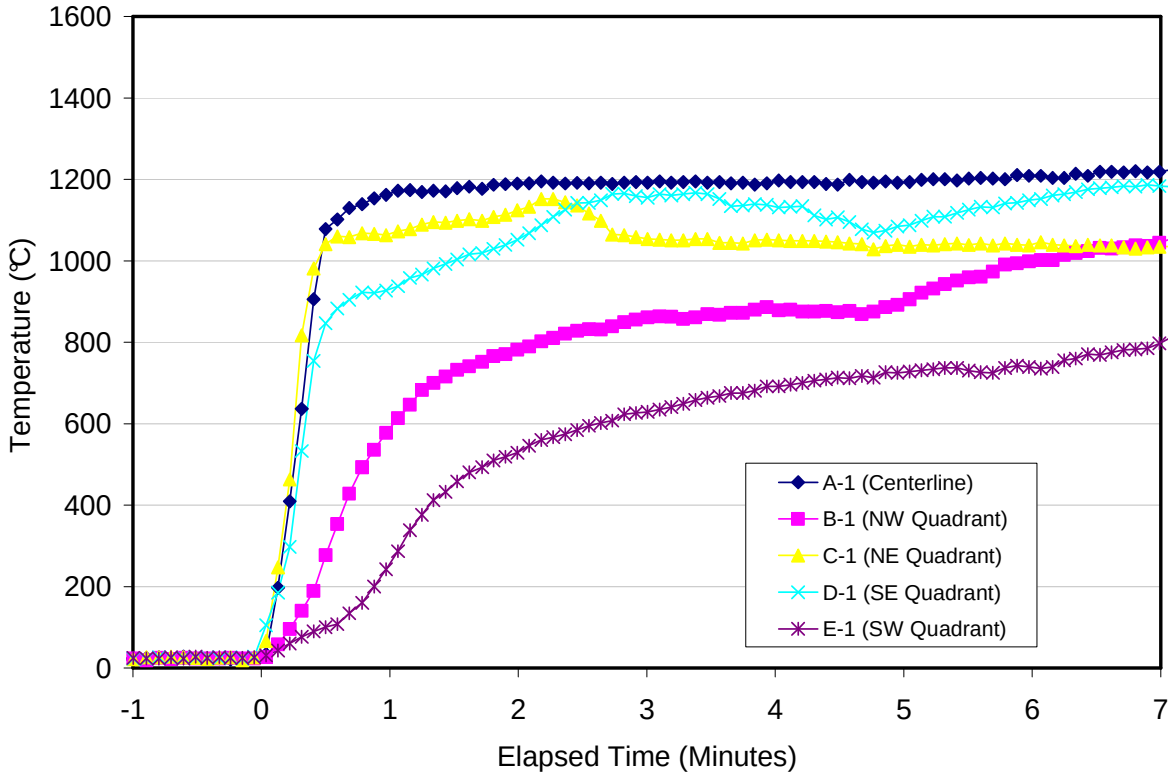

Figure 3-4. Concrete Surface Temperatures over the First 10 Minutes of the Interaction.

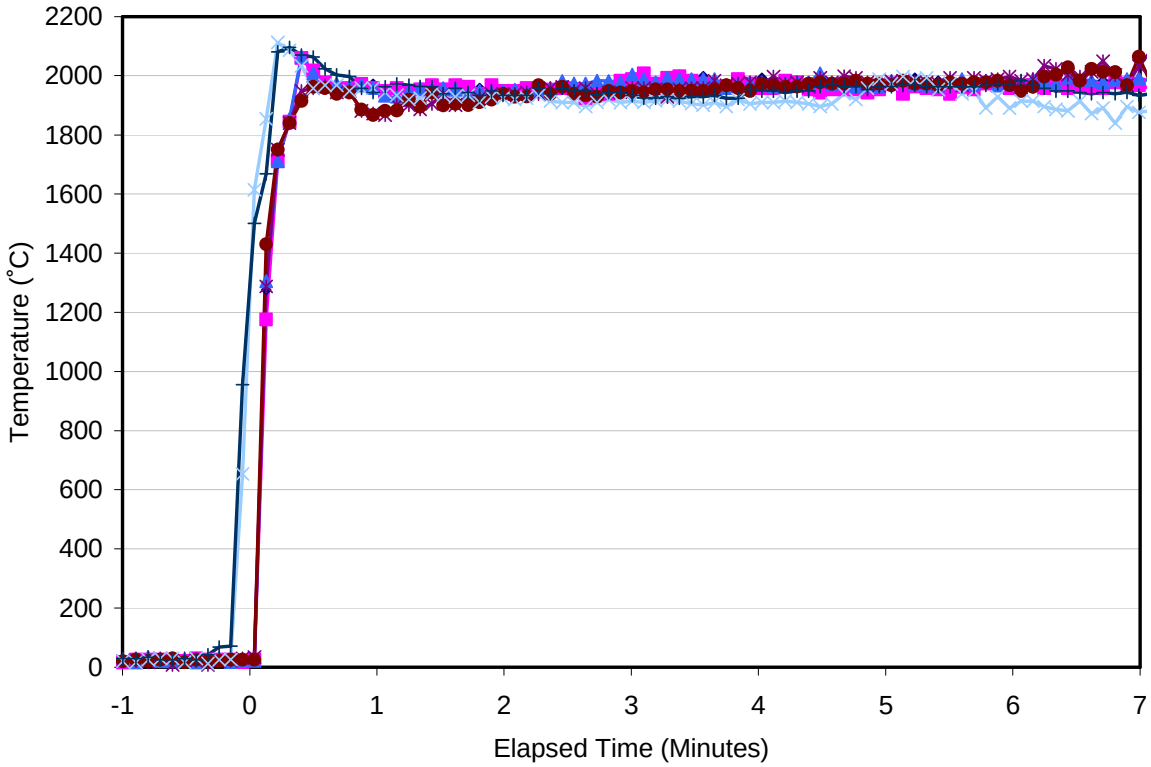

Figure 3-5. Bulk Melt Temperature Data over the First 7 Minutes of the Interaction.

Although the fire alarms in the cell had been silenced before the experiment, one of the alarms nonetheless sounded (time not recorded, but estimated as ~ 2 minutes in the experiment sequence). The Fire Marshall called the control room within 30 seconds to enquire about the state of test operations and to ask whether or not the department should respond. The lead experimenter informed the Marshall that the experiment would proceed as planned since the planning basis was that any event within the cell would be maintained within containment boundary, which it was. However, the Fire Marshall and two deputies came to the control room to observe the situation as an added precaution. They remained for approximately the next hour of the test to monitor the situation.

Aside from the perturbation in test operations related to the sounding of the fire alarm, the experiment moved forward. At 0.66 minutes, a No. 4 filter was inserted on the lid video camera which revealed that a fairly robust core-concrete interaction was underway. The high temperature gas jet was focused upwards and appeared to be impinging upon the crane trolley that was positioned over the test section for later use when the crust lance would be lowered to breach the crust (see Section 2.1 and Figure 2-10). On this basis, the operators flooded the cavity at 0.71 minutes to reduce the temperature of the gas jet issuing into the cell, as opposed to waiting for onset of ablation at the 2.5 cm depth at two concrete locations as the planned operating procedure dictated. The water system operator periodically added water to the test section for the balance of the experiment.

The initial heat transfer rate to water was so intense that the water is boiled off about as rapidly as it was added. The peak melt-water heat flux reached 5 MW/m^2 and then steadily

declined. By 1.45 minutes, continued water addition finally cleared the aerosols in the plenum to the point that the debris surface could be clearly seen. The view indicated that the melt surface was partially covered by crust that was floating on top of melt. Multiple eruptions occurred through crust material. Water continued to boil aggressively, and the surface dried out from 2.04 to 2.31 minutes. This enhanced view showed that the crust segments were not bonded; rather, the structure fluctuated with the melt turbulence. More water was added during this interval; eruptions occurred following addition. Eruption sites seemed to move continuously on surface; site densities were ~ 20 holes/m^2.

By 2.3 minutes, the operator was able to raise the DEH input power to the target level of 210 kW but that level could not be held as the conditions were unstable. By 3.1 minutes, the surface of the crust eventually went dark, indicating stable crust formation. Intense boiling off the surface was observed. Occasional small eruptions lasting a second or two occurred randomly around the surface of the crust. At 4.14 minutes, large scale eruptions began in the northwest corner of the test section and these occurred almost continuously until finely stopping at 7.29 minutes. From 7.29 to 21.1 minutes, no sustained eruptions occurred, and the debris-water heat flux steadily declined from ~ 500 kW/m^2 to ~350 kW/m^2 over the interval.

Over the time interval from 5.8 to 20.8 minutes, the input power was initially brought back to the 210 kW level, but the current limit of 9000 Amps was also reached. As a result, the operator held the current at the 9000 Amp limit, while power gradually drifted down to 190 kW. From 9.57 to 39.4 minutes, onset of axial ablation was detected at the basemat centerline and in all four quadrants. Axial ablation rate remained slow but steady during the balance of the test.

At 20.9 minutes, a rapid ablation transient was initiated in the south wall of the test section when the 2.5 cm erosion depth was reached at the +12.5 cm elevation. Over the next five minutes, the south wall ablation rate averaged 2.7 cm/min as the ablation progressed to 16 cm before slowing dramatically. Ablation of the north wall was minimal during this time. Concurrent with the sidewall ablation burst, large melt eruptive events were observed that resulted in a significant increase in the upwards heat transfer rate. The eruptions started near the center of the south concrete wall at 21.1 minutes and proceeded virtually unabated until 23.2 minutes. The crust surface then went dark until 24.5 minutes. At this time, a large eruption event was initiated in the northeast corner of the test section that proceeded almost continuously until 25.9 minutes; the heat flux peaked at 3 MW/m^2 during this period (at 25.3 minutes). The crust surface went dark again at this time and remained that way for the rest of the test.

The loss of electrical conductor from the melt zone due to the eruptions caused the effective resistance of the melt to increase. As a result, the electrical current requirement dropped and at 22.2 minutes the power supply operator was able to raise the power back to 210 kW. Constant voltage operation began at this time at 27 volts. At 24.6 minutes, power supply operations were switched from current to voltage control mode to make this procedure simpler. Once constant voltage operation was initiated, input power fell steadily from 210 to 65 kW at 26.5 minutes; at the end of this period the rate of power decrease slowed dramatically.

Past this point, power supply operation continued at constant voltage, and the input power declined slowly. From 60.3 to 66.7 minutes, the crust lance was slowly inserted to gain additional information about the debris profile and crust failure strength. Only a modest load

was encountered until the probe tip reached ~ 1.3 cm elevation above the initial concrete surface elevation. A significant cooling transient occurred, but only after the lance was withdrawn. The video data seemed to indicate that water was flooding into a hole made in the debris by the lance after withdrawal. From 26.5 to 150.9 minutes, the power gradually fell from 65 kW to zero at constant voltage. Power supply operations were terminated at 150.9 minutes. Data logging was subsequently terminated at 170.8 minutes. At this point, the system was shutdown following normal termination procedures. The DAS was restarted to record the long-term cool down data. The experiment was left unattended to cool down overnight.

4.0 RESULTS

A summary of the principal thermalhydraulic results from CCI-6 is provided in this section. A complete list of instruments used in the test is provided in Appendix A, while plots of all data logged from these instruments are provided in Appendix C. The presence of the steam in the cell due to the breached main steamline did not seem to influence instrument performance for most of the instruments used in the experiment. Exceptions to that observation are the instruments logged on the Basemat DAS system. Steam infiltration into the hardware appeared to cause some mild current shunting that resulted in a reduction in signal responses from thermocouples wired to this system. An assessment of the impact of this occurrence on the quality of the data logged on the Basemat DAS is provided in Appendix C.

4.1 Electric Power

Power supply voltage, current, and total electric power over the course of the experiment are shown in Figures 4-1 through 4-3, respectively, while a plot showing voltage and current over an expanded timescale near the start of the test is provided in Figure 4-4.

By 2.3 minutes, the operator was able to raise the DEH input power to the target level of 210 kW but that level could not be held as the conditions were unstable. Over the time interval from 5.8 to 20.8 minutes, the input power was initially brought back to the 210 kW level, but the current limit of 9000 Amps was also reached. As a result, the operator held the current at the 9000 Amp limit, while power gradually drifted down to 190 kW. The loss of electrical conductor from the melt zone due to the onset of eruptions at 21.1 minutes caused the effective resistance of the melt to increase. As a result, the electrical current requirement dropped and at 22.2 minutes the power supply operator was able to raise the power back to 210 kW. Constant voltage operation began at this time at 27 volts. Due to the current limit, the average input power to the melt from time t = 0 until constant voltage operation was initiated at 22.2 minutes was 178 kW, which was ~ 15 % below target power of 210 kW.

At 24.6 minutes, power supply operations were switched from current to voltage control mode to make operation at constant voltage simpler. Once constant voltage operation was initiated, input power fell steadily from 210 to 65 kW at 26.5 minutes; at the end of this period the rate of power decrease slowed dramatically. In particular, from 26.5 to 150.9 minutes, the power gradually fell to zero. Power supply operations were terminated at that point.

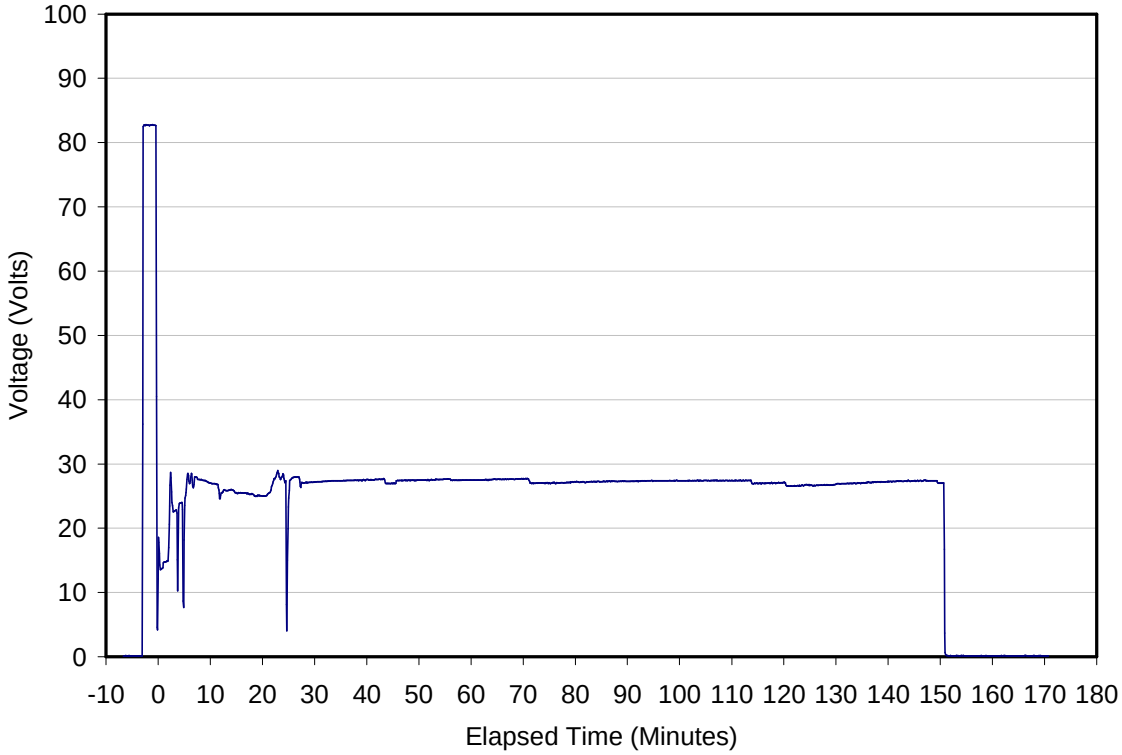

Figure 4-1. Power Supply Voltage.

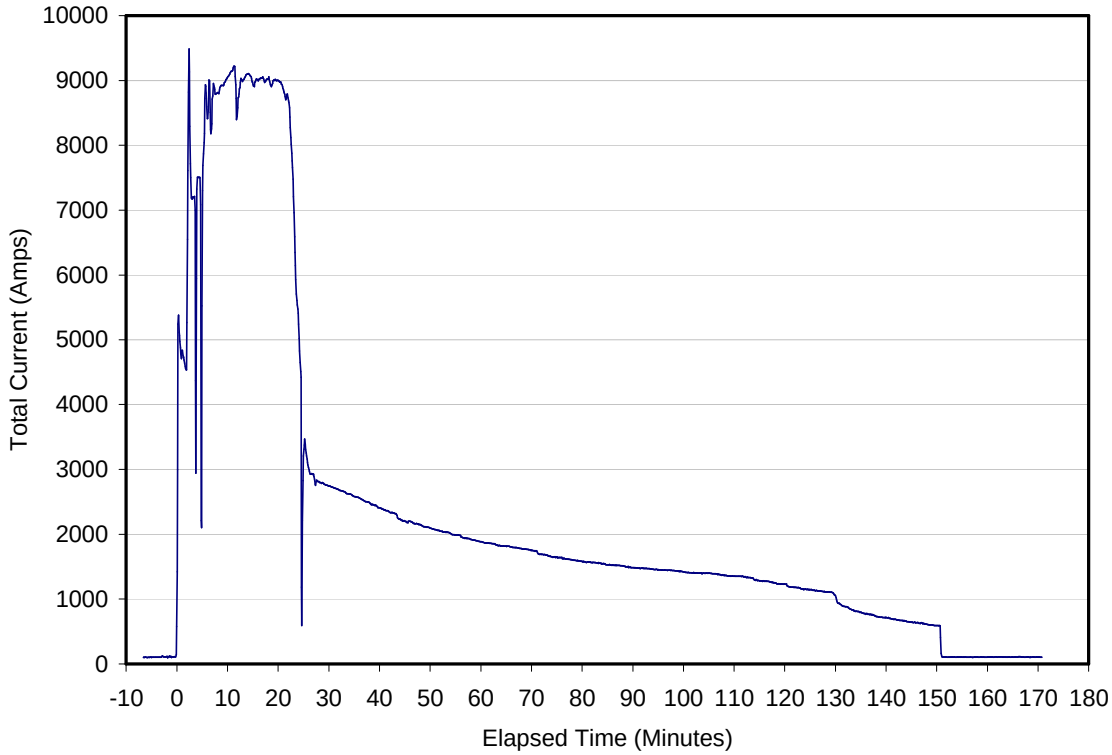

Figure 4-2. Power Supply Current.

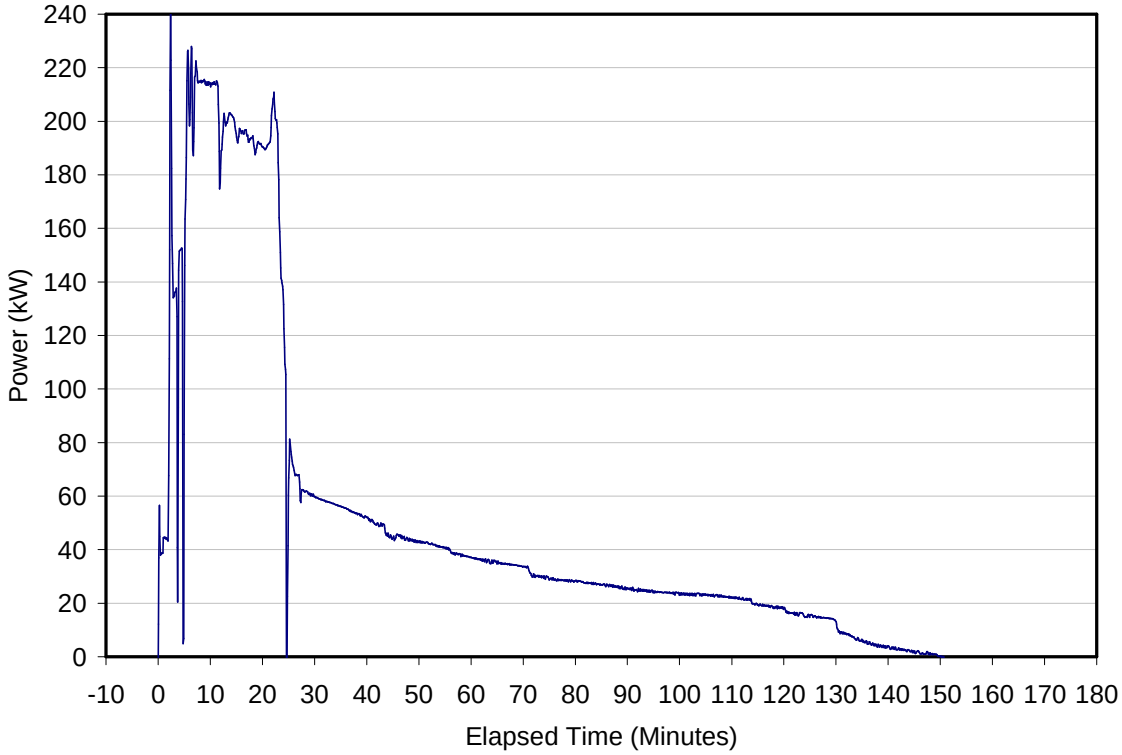

Figure 4-3. Total DEH Input Power.

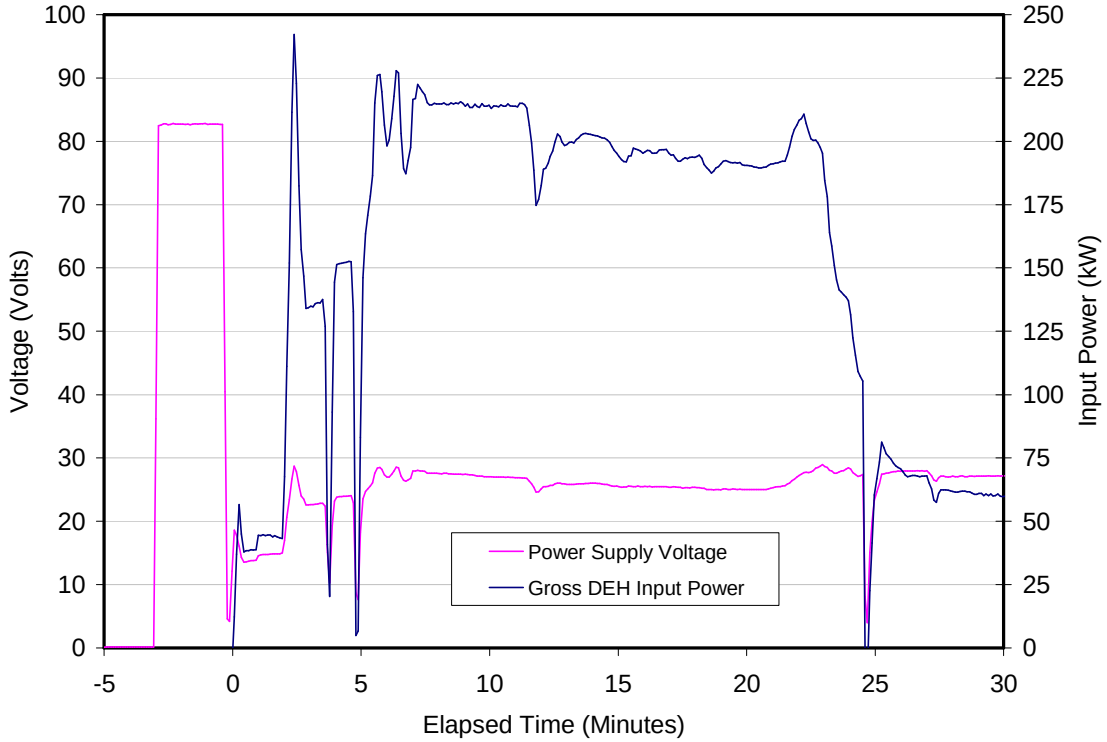

Figure 4-4. Power Supply Voltage and Power: Expanded Timescale.

4.2 Melt Temperatures

A total of thirty two W5%Re/W26%Re (Type C) thermocouple junctions were used to monitor melt temperatures at various axial and radial locations in CCI-6. In addition, a two-color optical pyrometer mounted in the lid of the apparatus was provided to measure melt upper surface temperature prior to water addition. However, this instrument provided no useful data as the cavity was flooded ~ 42 seconds after melt pool production, and aerosols had not cleared sufficiently from the test section plenum to obtain any data by that time.

The basemat thermocouples were configured within five four-junction arrays that were mounted vertically in the concrete. The locations of the junctions for these units are shown in Figures 2-20 and 2-21. Each of these arrays was protected by a 0.95 cm diameter long-body tungsten thermowell. Conversely, each concrete sidewall was instrumented with a six-junction Type C array that was mounted horizontally at an elevation of 5.0 cm above the initial concrete surface. Each unit was protected by a 12.7 mm diameter long-body tungsten thermowell.

Data from the arrays located in the concrete basemat that saw melt conditions during the test are provided in Figures 4-5 through 4-7, while data from the two sidewall arrays are provided in Figures 4-8 and 4-9. To provide an indication of the overall melt temperature behavior during the test, a graph showing data from all thermocouples is provided in Figure 4-10. To improve readability, two steps were taken: i) the data have been averaged over ~30 second (i.e., 6 point) intervals, and ii) only data preceding the first off-scale reading by the units are shown. Past the first off-scale reading, the thermocouple junctions are assumed to have failed, and thus the data are not deemed to be reliable.

Examination of this collection of data indicates that the peak melt temperature following the thermite reaction was ~ 2100˚C. From the start of the experiment until onset of the rapid ablation burst in the south wall at ~ 21 minutes, melt temperatures declined steadily to an average of ~ 1900˚C. The solidus temperature for the initial CCI-6 corium composition was estimated as ~ 1880˚C using the property subroutines in CORQUENCH [7]. Thus, the temperature response data shown in Figures 4-8 and 4-11 seems to indicate the sustained presence of solid crust material near the north and south walls up to 21 minutes. However, shortly after 21 minutes the temperatures near the south wall rapidly increased to ~ 2100˚C, which is coincident with the onset of rapid ablation in this wall. The temperature escalation is thus consistent with the sudden loss or failure of a crust that was protecting this wall. Over the next six minutes, the temperatures near the south wall drop steadily until they plateau at ~ 27 minutes at a level of 1800˚C. This plateau occurs at about the same time as the ablation transient in the south wall terminates (see Table 3-1). The data in Figure 4-10 suggest that the melt temperature decline provided the sensible energy for ablation during the transient was fairly localized near the south wall. This observation can be checked using data from the posttest examinations, which revealed that the ablation in the south wall totaled about 13 l in volume, or ~ 31 kg given the concrete density of ~ 2370 kg/m^3 (see Section 2.10). Assuming a decomposition enthalpy of ~ 2 MJ/kg for siliceous concrete, then the energy required to ablate the 31 kg of concrete would be 62 MJ. Assuming a corium specific heat of 600 J/kg-K and given the fact that the local melt temperature drop during the ablation transient was ~ 300˚C, then a

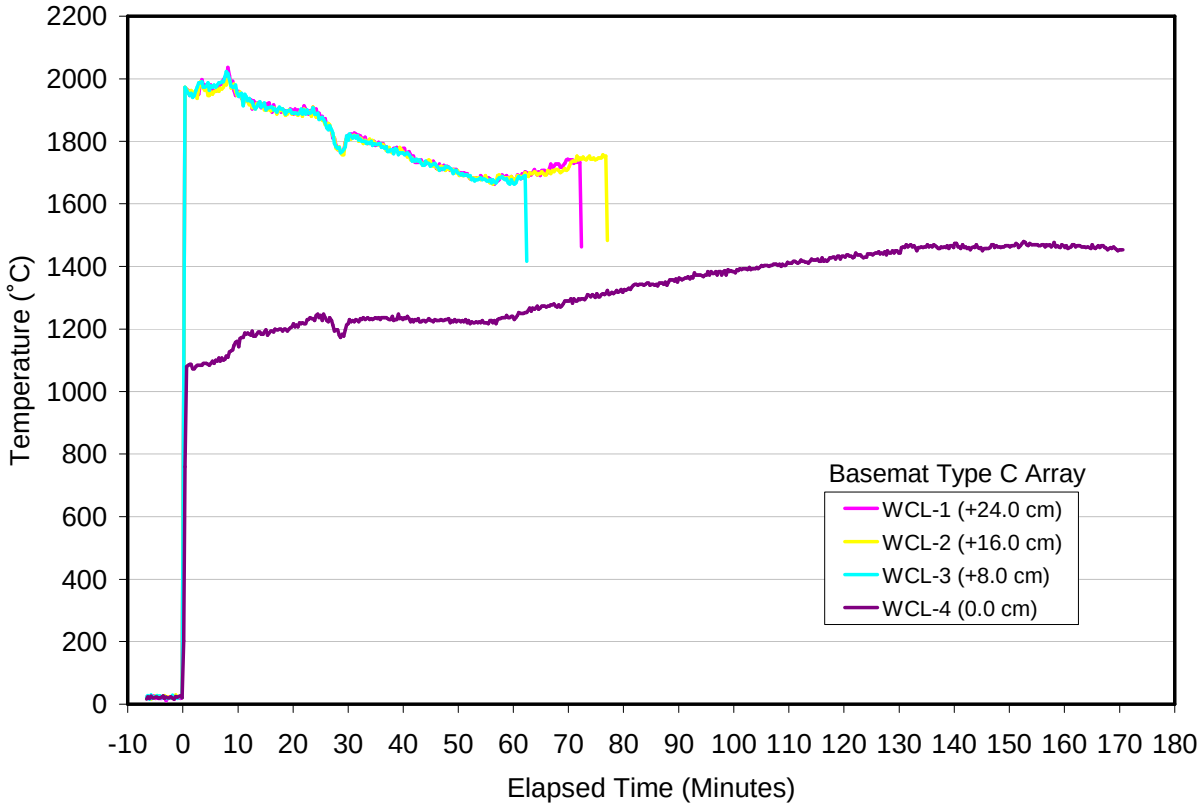

Figure 4-5. Melt Temperature Data from Basemat Type C "WCL" Array.

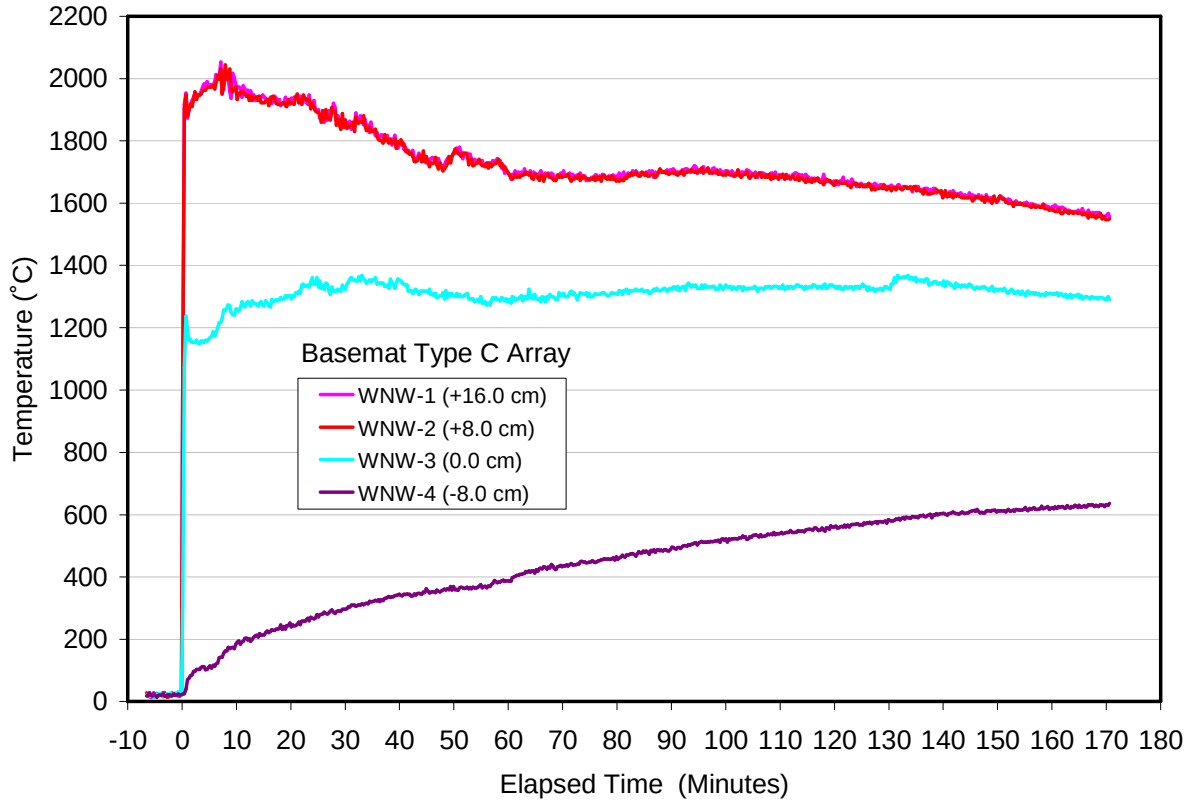

Figure 4-6. Melt Temperature Data from Basemat Type C "WNW" Array.

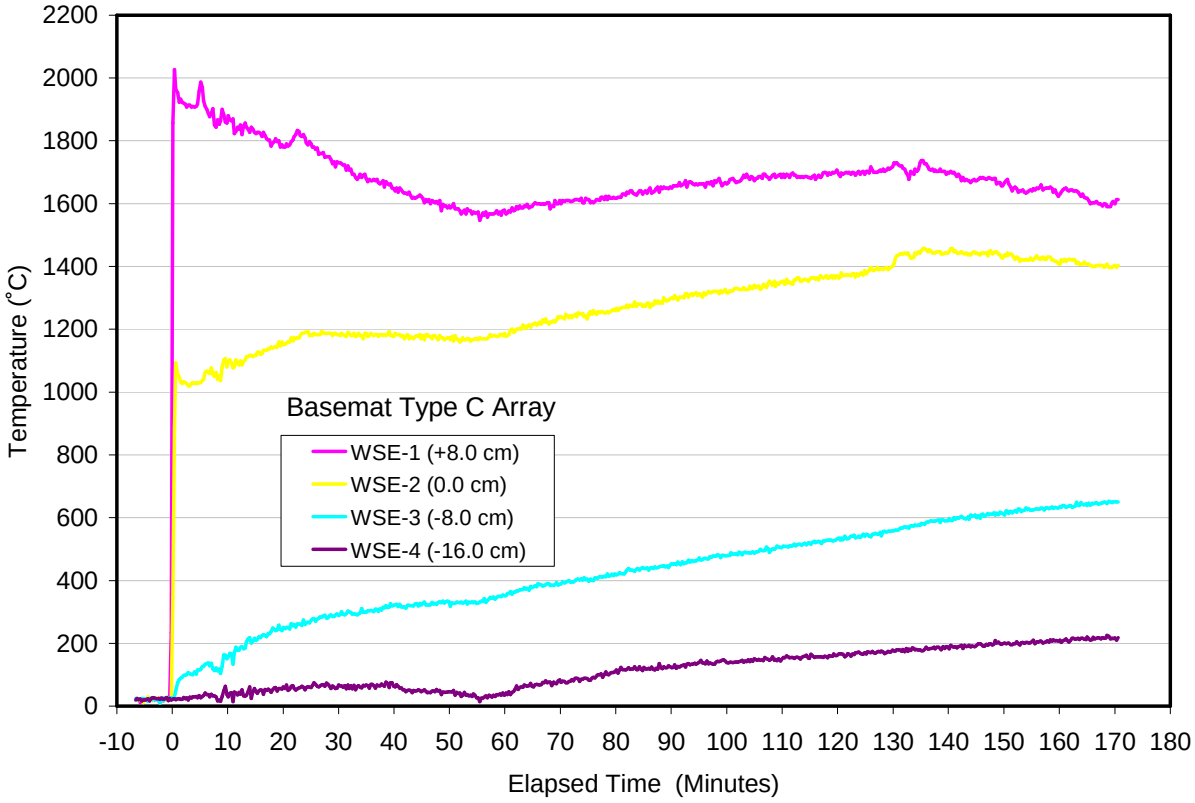

Figure 4-7. Melt Temperature Data from Basemat Type C "WSE" Array.

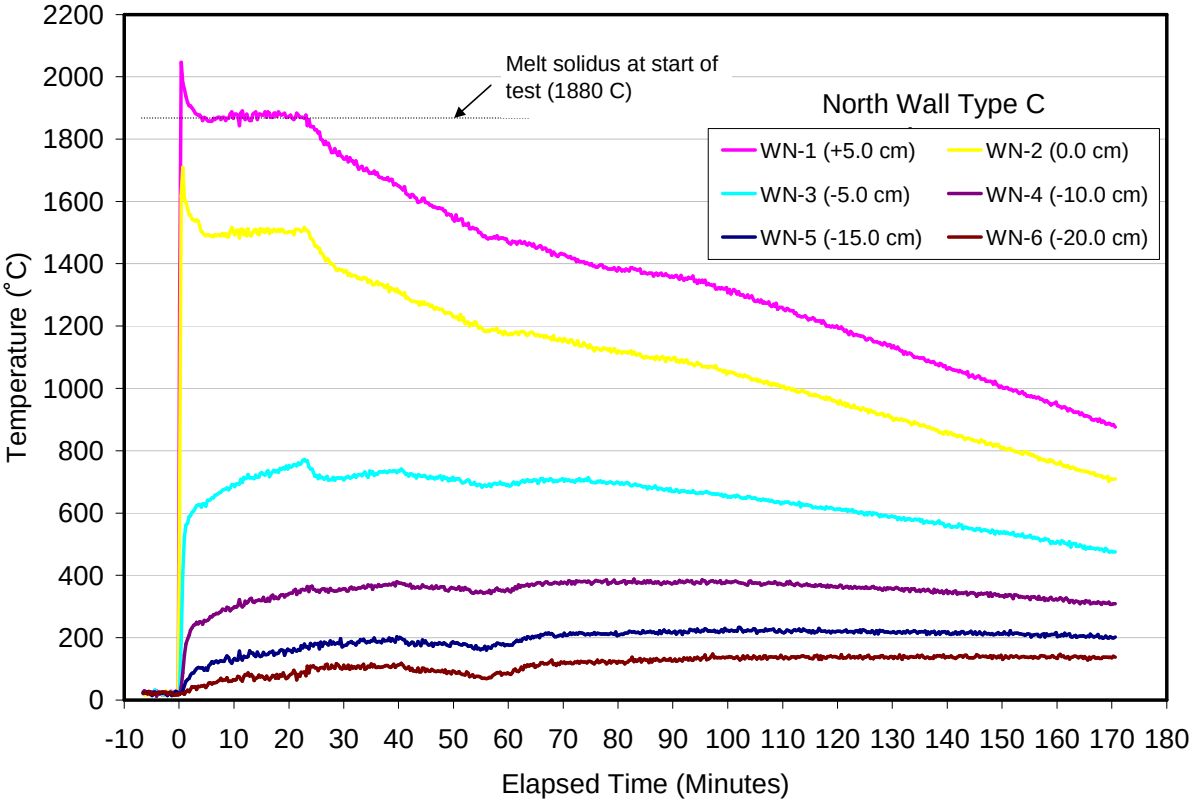

Figure 4-8. Melt Temperature Data from North Side Wall Type C "WN" Array.

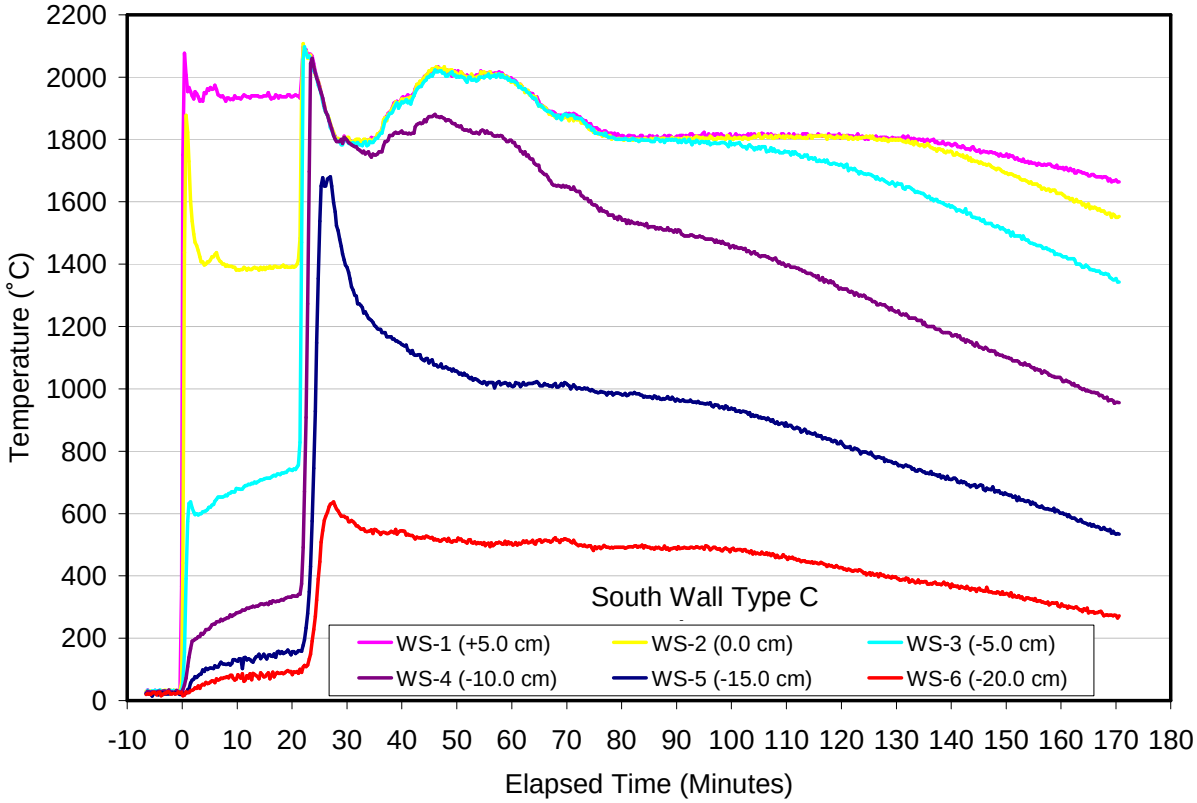

Figure 4-9. Melt Temperature Data from South Side Wall Type C "WS" Array.

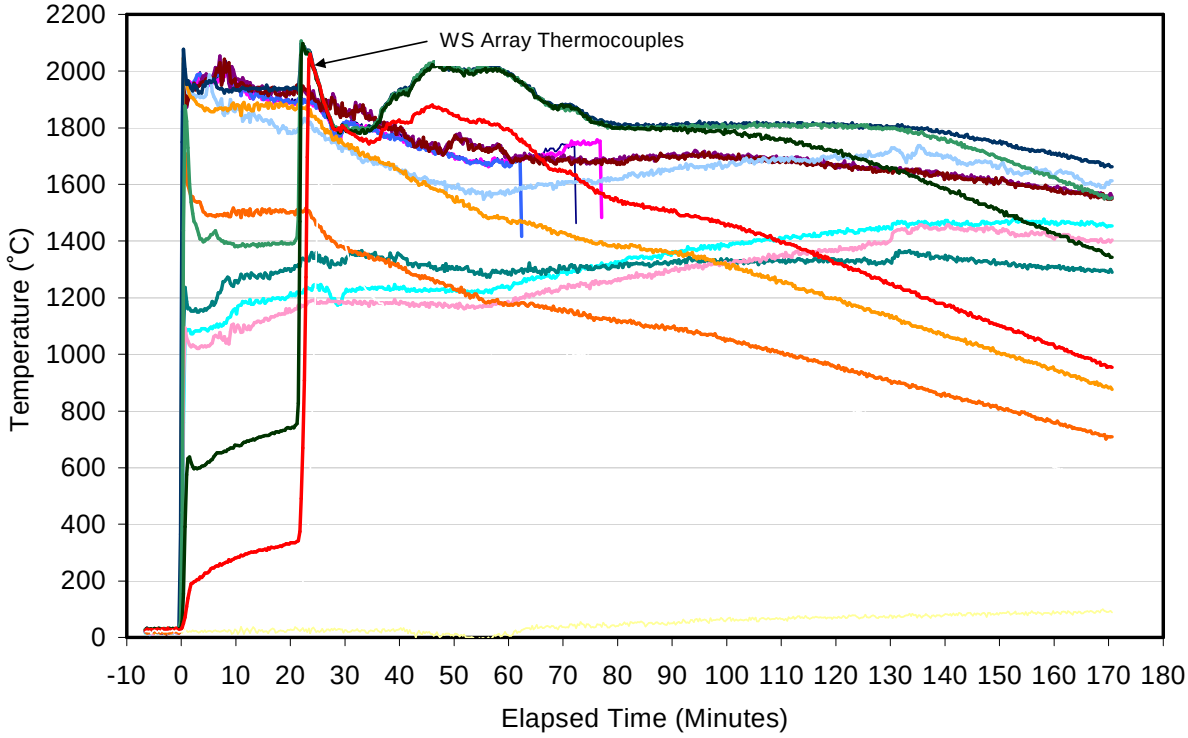

Figure 4-10. Data from all Melt Temperature Thermocouples.

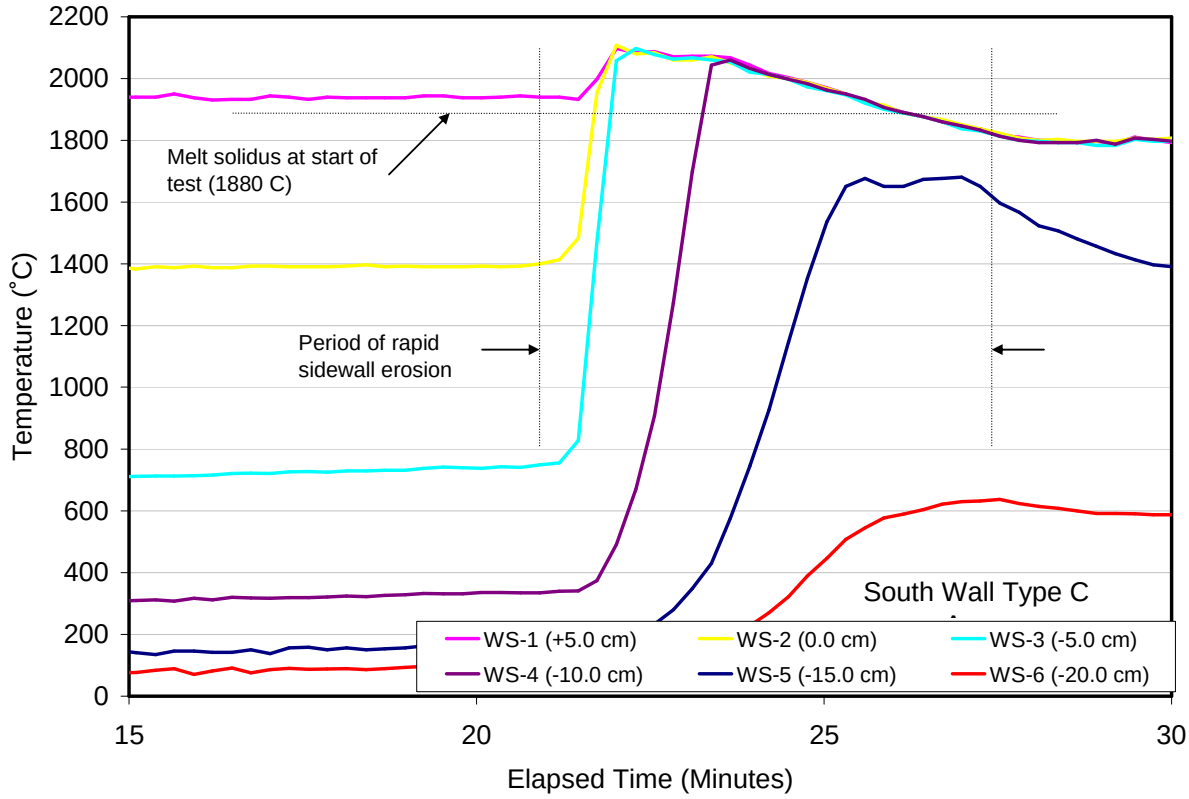

Figure 4-11. Melt Temperature Data from "WS" Array: Expanded Scale.

simple energy balance reveals that the melt mass that participated in the transient was ~ 340 kg. This amounts to ~ 1/3 the initial melt mass used in the experiment. Thus, the concept that the ablation transient was localized and involved only a fraction of the overall melt pool seems plausible

Another possible explanation[5] for the temperature transient near the wall is based on a cement paste liquefaction concept wherein the siliceous aggregate was only partially melted when the crust disappeared. This relatively cold material was then introduced into the melt pool once the crust failed, causing the temperature decrease. After the aggregate melted, the pool temperature was then able to rise again.

Following the ablation transient, the data from the Type K arrays cast in the concrete (see Section 4.3) suggest that concrete ablation was minimal. Thus, gas sparging from concrete decomposition would have been quite small also. As is evident from Figure 4-10, the lack of bubble-induced convection within the melt resulted in large temperature gradients across the extent of the test section that ranged up to 500˚C or more. The disparity is enhanced by the fact that this test contained the lowest initial concrete content of any tested in the program (i.e., 6 wt %), and ablation was minimal so that substantial concrete was not added to the melt which would have acted to lower the freezing point. Thus, the melt would have been quite stiff and conduction within the debris would not have been negligible. Under these conditions, large temperature gradients can develop. By the end of the experiment, the temperatures varied from 700 to 1680˚C.

[5] M. Cranga and J.-M. Bonnet, IRSN, personal communication (e-mail) to M. T. Farmer, ANL, 28 September 2010.

4.3 Concrete Basemat and Sidewall Ablation Rates

The basemat was instrumented with five multi-junction Type K thermocouple arrays to monitor the axial progression of the ablation front, while each concrete sidewall was instrumented with six arrays (mounted along the wall axial centerline) to monitor the radial ablation front progression at six different elevations. The location and identification of these thermocouple assemblies are shown in Figures 2-3 and 2-20. The first junction of each array was mounted flush with the concrete surface. When a thermocouple reached the siliceous concrete liquidus temperature of 1250 ºC [6], the melt was considered to be in contact with the thermocouple at the junction location.

The sequential rise in signals from the basemat centerline array as the test progressed is shown in Figure 4-12. As noted earlier, only data preceding the first off-scale reading by the thermocouples are shown. The analogous plots showing the thermal response in the North and South concrete sidewalls at the +12.5 cm elevation are provided in Figures 4-13 and 4-14, respectively. Plots of the thermal response at all basemat and sidewall array locations are provided in Appendix C.

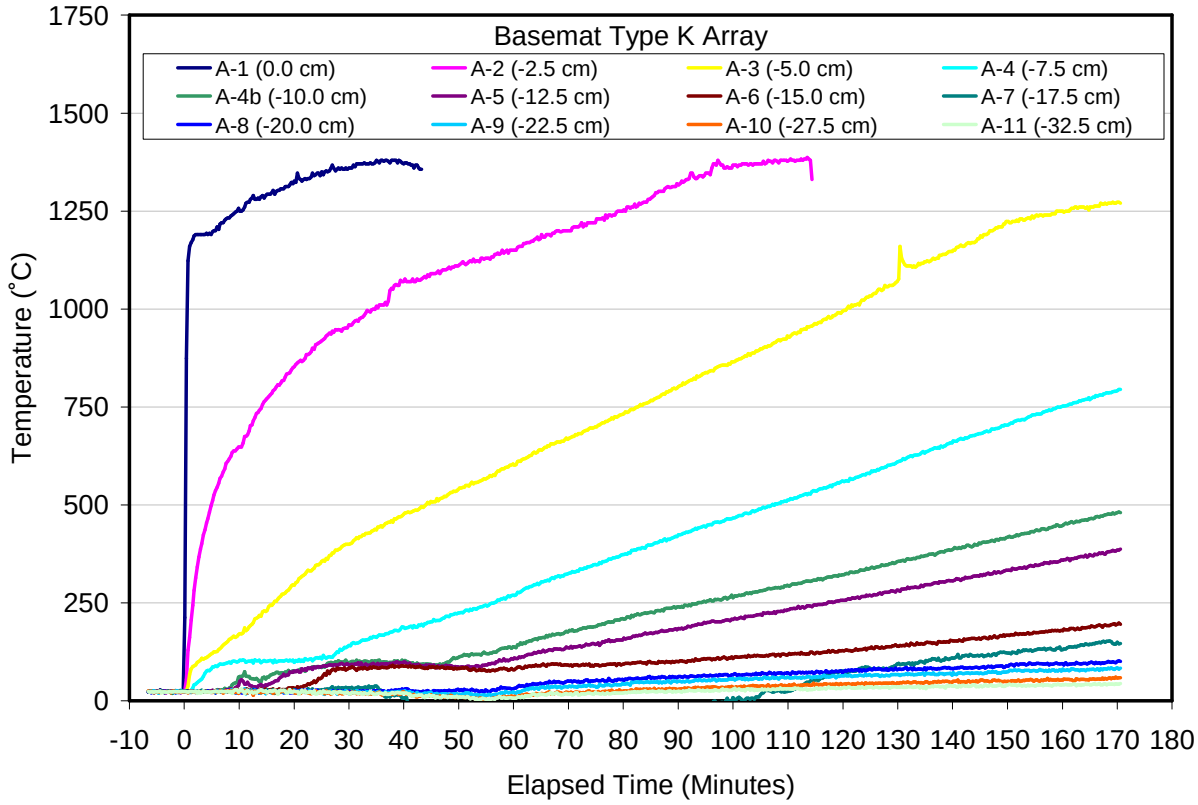

Figure 4-12. Thermal Response of the Concrete Basemat at the Centerline ("A" Array).

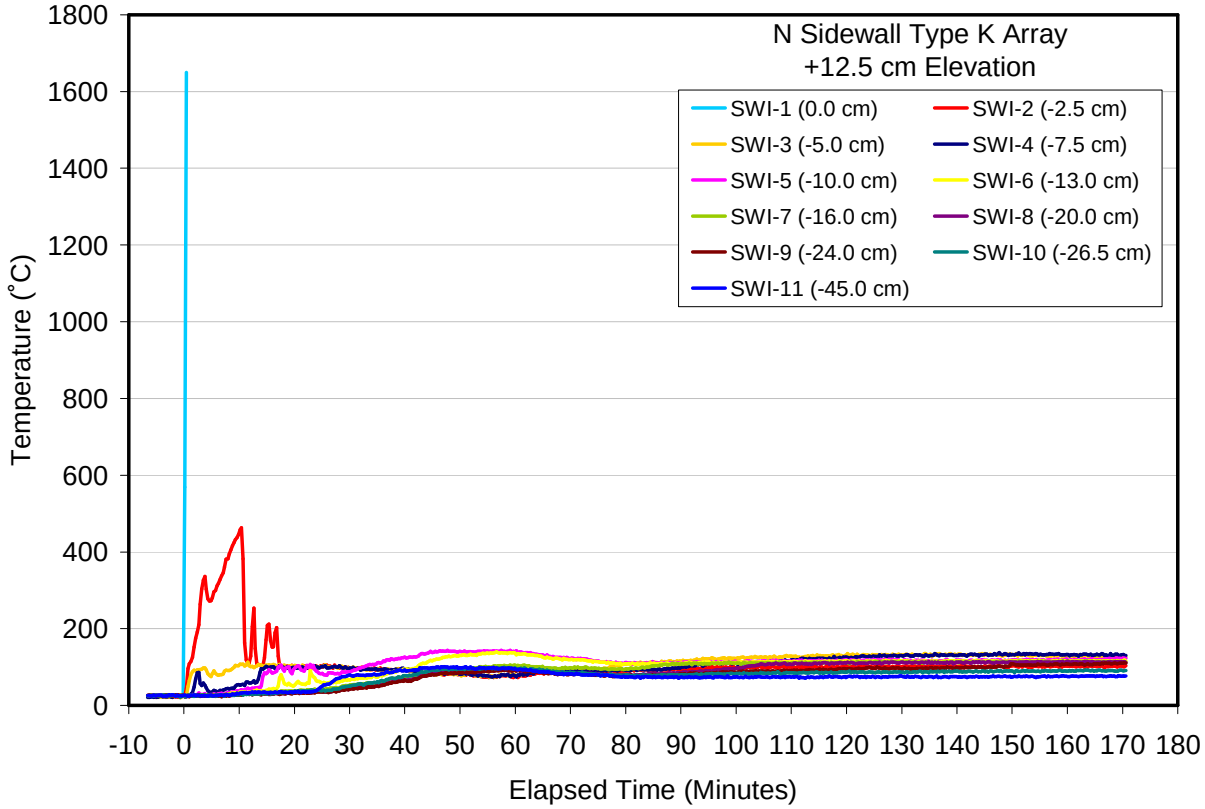

Figure 4-13. North Concrete Sidewall Thermal Response at +12.5 cm ("SWI" Array).

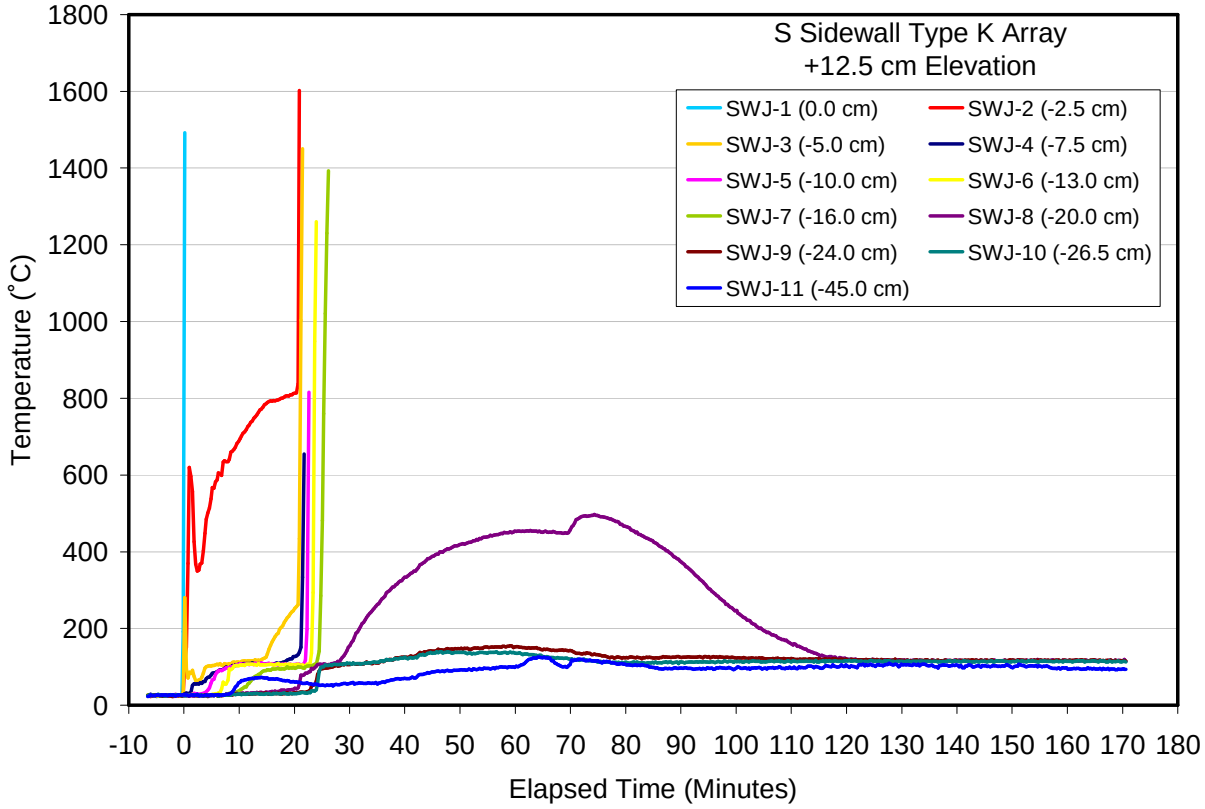

Figure 4-14. South Concrete Sidewall Thermal Response at +12.5 cm ("SWJ" Array).

Figure 4-15 provides the axial ablation depth versus time based on the signal responses from the Type K basemat arrays, while Figure 4-16 provides the analogous plot of the radial ablation depth in the South sidewall. As can be inferred from Figure 4-13, ablation in the North wall was minimal for this test. Finally, Figure 4-17 provides a comparison of the ablation depths versus time recorded on all three concrete surfaces during the test. Examination of these figures indicates that axial ablation proceeded relatively slowly but steadily at a rate of ~ 2 cm/hour over the course of the experiment. Conversely, the only significant sidewall ablation occurred in the south wall over the time interval from ~ 21 to ~ 27 minutes. During this interval, the ablation depth progressed to a depth of 16 cm, yielding an average ablation rate of ~ 2.7 cm/min. As is evident from Figure 4-14, water eventually infiltrated down in the corium adjacent to the wall at this location (as well as the north wall; see Figure 4-13), thereby terminating sidewall heatup and ablation. Assuming a siliceous concrete decomposition enthalpy of 2 MJ/kg, then the local ablation rate of 2.7 cm/min observed on the south wall would require a convective heat transfer rate from the melt of ~ 2.1 MW/m^2. This intense heating rate is consistent with the rapid melt temperature drop observed near this wall when the transient occurred; see Section 4.2.

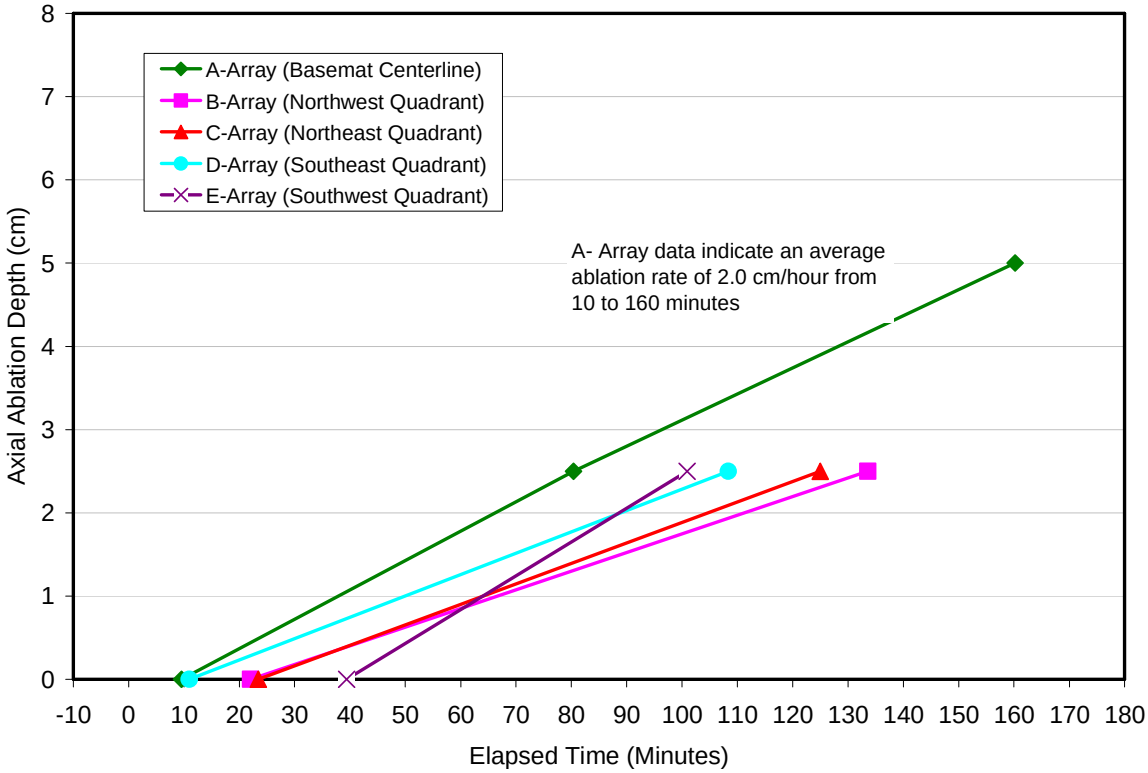

Figure 4-15. Basemat Axial Ablation Front Location.

4.4 Crust Lance Data

Two objectives for CCI-6 were to: i) obtain in-situ crust strength data to supplement the room temperature strength database being assembled as part of the SSWICS program, and ii) provide information on the nature and the extent of the debris cooling that occurs after the crust fails. This subsection provides the results of the crust strength measurement, while the debris cooling data is provided in the next subsection.

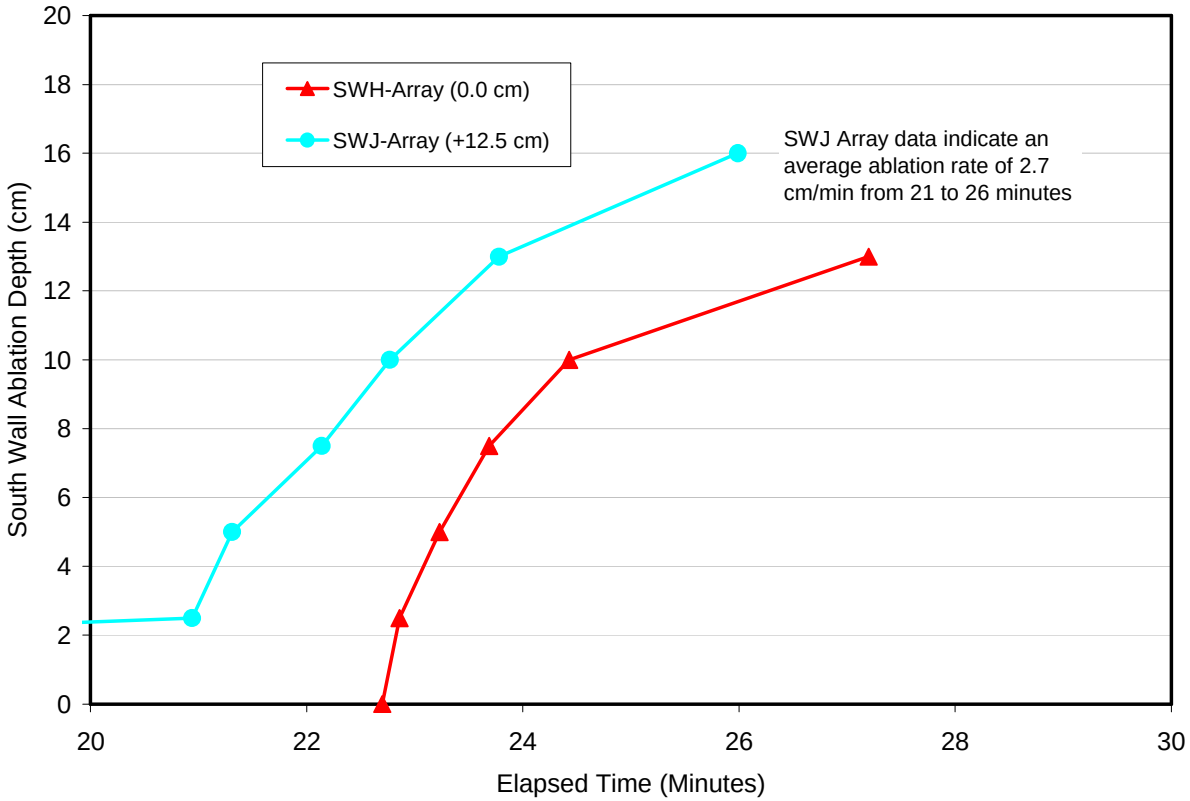

Figure 4-16. South Sidewall Radial Ablation Front Location.

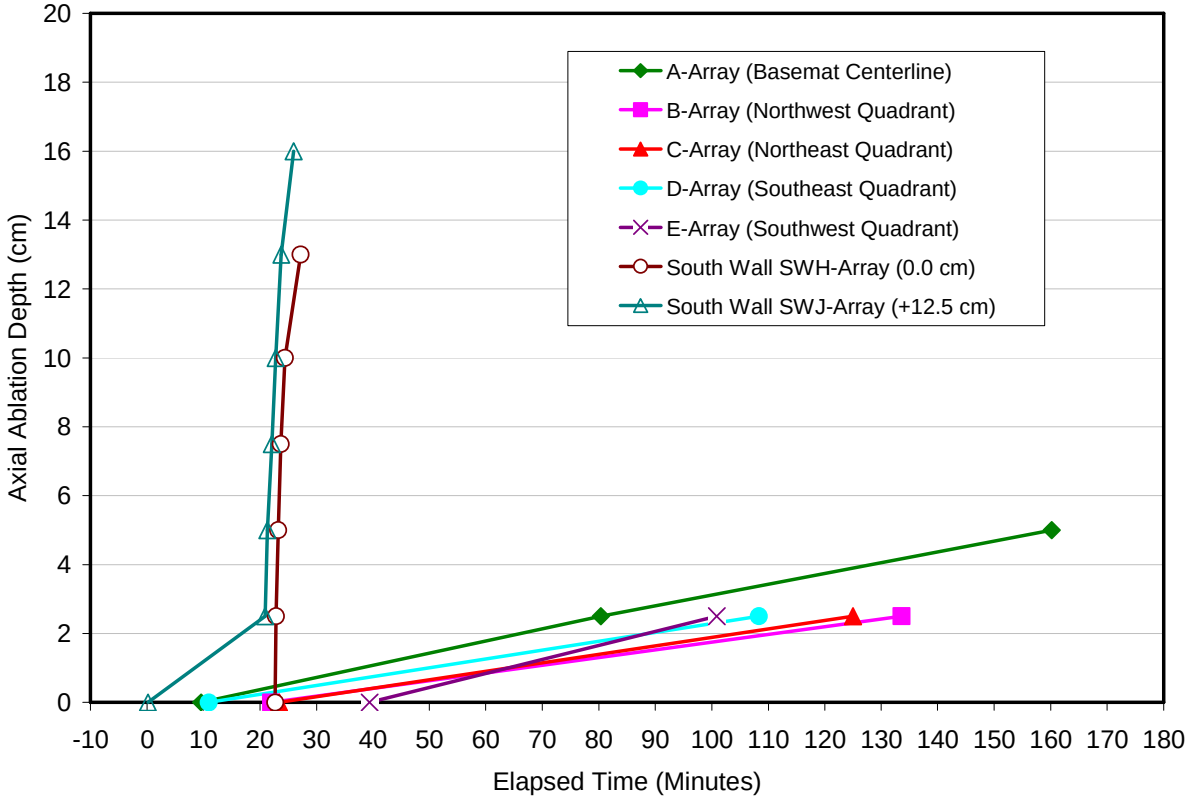

Figure 4-17. Comparison of Axial and Radial Ablation Depth Data versus Time.

As shown in Table 3-1, the lance was inserted to obtain crust strength data after the cavity was flooded. The outputs from the lance force and displacement transducers are shown in Figure 4-18. Also shown on the figure are the approximate elevations of key debris interfaces that were determined on the basis of the posttest examinations (see Section 4.6) as well as other test data. These interfaces included the top of a particle bed produced by melt eruptions; the interface between the bed and an underlying fractured crust; the top surface of the solidified melt pool; and finally the location of the concrete basemat surface at the time the lance was inserted (inferred from Figure 4-15).

Lance insertion was initiated at 57.5 minutes, but no detectable load was measured until the lance tip had reached the 22 cm elevation over the initial concrete surface at 60.3 minutes. At this elevation, the tip was already 6 cm below the collapsed pool depth of 28 cm at the start of the test. The data further indicate that the lance had already penetrated through the ~ 18 cm deep particle bed by this time. The lack of a significant load indicates that the bed was quite loosely packed. The first load detection at the 22 cm elevation was most likely the top of the fractured crust, but the load was quite small (< 7 kg). On this basis, the lance was inserted further. The load continued to increase, but not in a step-function fashion as would be expected for a rigid structure. Rather, the load increased gradually, and load increases were followed by gradual relaxation periods as opposed to a rapid release of strength that again would be associated with the failure of a rigid structure. Posttest examinations indicated that in this range, the probe tip was passing through fractured crust material that could be removed by hand, and this explains the

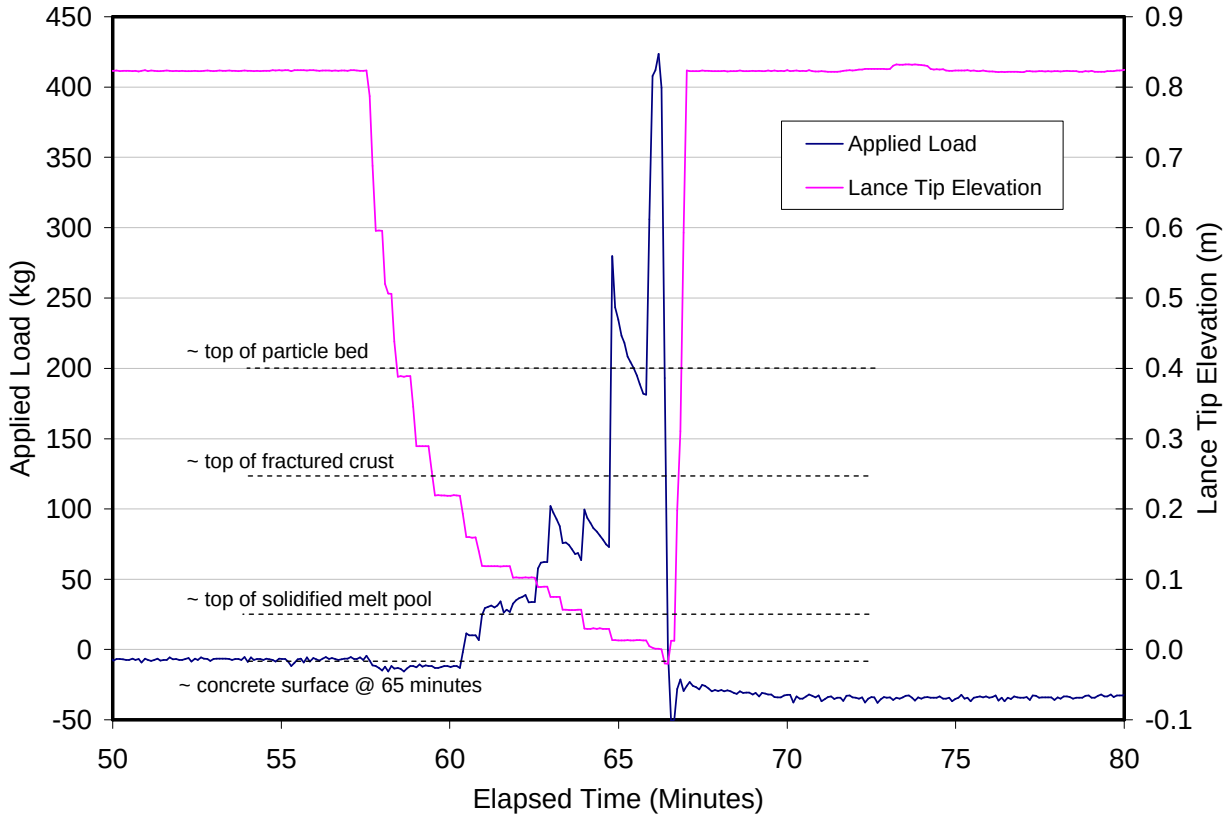

Figure 4-18. Load Force Exerted on Crust vs. Time.

relatively low force required to penetrate the material. Finally, at 65.8 minutes when the probe tip was at the 1.3 cm elevation, the lance load increased to near capacity (i.e., 424 kg vs. the deadweight mass of 450 kg), and a brittle-type failure occurred. At this time in the experiment, the axial ablation depth was in the range of 1-2 cm (see Figure 4-15). Thus, the presence of the hard material at the 1.3 cm elevation would be consistent with a 2-3 cm thick crust over the concrete surface at this time, and the measured load would be indicative of the failure of this crust as opposed to one formed at the melt-water interface.

During the insertion period, there was no detectable increase in the debris cooling rate (see Section 4.5). However, when the lance was removed the quench rate increased, and the lid video camera showed a weak image of a hole present in the crust with water apparently flooding beneath. Thus, removal of the lance apparently made a hole for the water to infiltrate down into the rubble bed and further increase the debris cooling rate.

4.5 Corium Quench Rate

Other key test objectives were to: i) obtain data on the nature and extent of the corium quench process under early corium top flooding cavity conditions, and ii) obtain data on the extent of corium cooling under the condition of bottom water injection through porous concrete nozzles cast in the basemat. However, the latter objective could only be satisfied if the axial ablation depth proceeded to 27.5 cm. For this test, axial ablation was limited to ~ 5 cm and so data on the second (bottom water injection) cooling mechanism was not obtained as a part of this experiment.

Normally, all steam from the test section is condensed within instrumented quench system tanks. The debris-water heat flux can then be readily deduced from the steam condensation rate in the quench tanks. However, meltthrough of the main steamline meant that part of the steam was vented directly into the cell atmosphere, and other methods (instruments) had to be used to evaluate the overall steaming rate over the test. This method is straightforward but rather tedious; full details of the analysis are provided in Appendix D.

The resultant steam formation rate from the corium-water interaction is reproduced from Appendix D in Figure 4-19. With this result, the debris-water heat flux could then be calculated directly assuming a saturated coolant latent heat of vaporization at atmospheric pressure of 2.256 MJ/kg, as well as a planar corium surface area of 0.7 m x 0.7 m = 0.49 m^2. The result is shown in Figure 4-20. The DEH input power, normalized with the test section planar area, is also shown in the figure along with the times of key events such as melt eruptions and the lance insertion sequence (see Table 3-1).

The peak melt-water heat flux reached 5 MW/m^2 soon after initial cavity flooding and then steadily declined. During the initial interaction, the high initial value of the heat flux was partially attributable to melt eruptions that were observed over the first few minutes of the experiment. From 7.29 to 21.1 minutes, no sustained eruptions occurred, and during this phase the debris-water heat flux declined further from ~ 500 kW/m^2 to ~350 kW/m^2.

Over the time interval from 21 to 27 minutes, multiple melt eruptions were observed that caused a transient increase in the heat flux up to a level of 3 MW/m^2. Following this event, the heat flux steadily declined from ~ 500 kW/m^2 to ~ 120 kW/m^2 at the time the crust lance was inserted at 60 minutes. Upon removal of the lance, another transient increase in the flux occurred up to a level of ~ 1 MW/m^2. The video data seemed to indicate that water was flooding into a hole made within the debris after the lance was withdrawn, and this water inflow resulted in the increase in the cooling rate. After the lance was removed, the heat flux declined and stabilized at an average value of ~ 100 kW/m^2 where it remained for the balance of the test.

The integrated energy removal upwards to overlying water is compared to the integrated heat input from DEH in Figure 4-21. This data, as well as that shown in Figure 4-20, indicates that the debris-water cooling rate far exceeded heat input over the course of this test. This finding is consistent with the limited cavity erosion that was observed during the test, and is further rationalized by the posttest debris morphology that indicated a large debris fraction that appeared to be quenched in a coolable debris configuration.

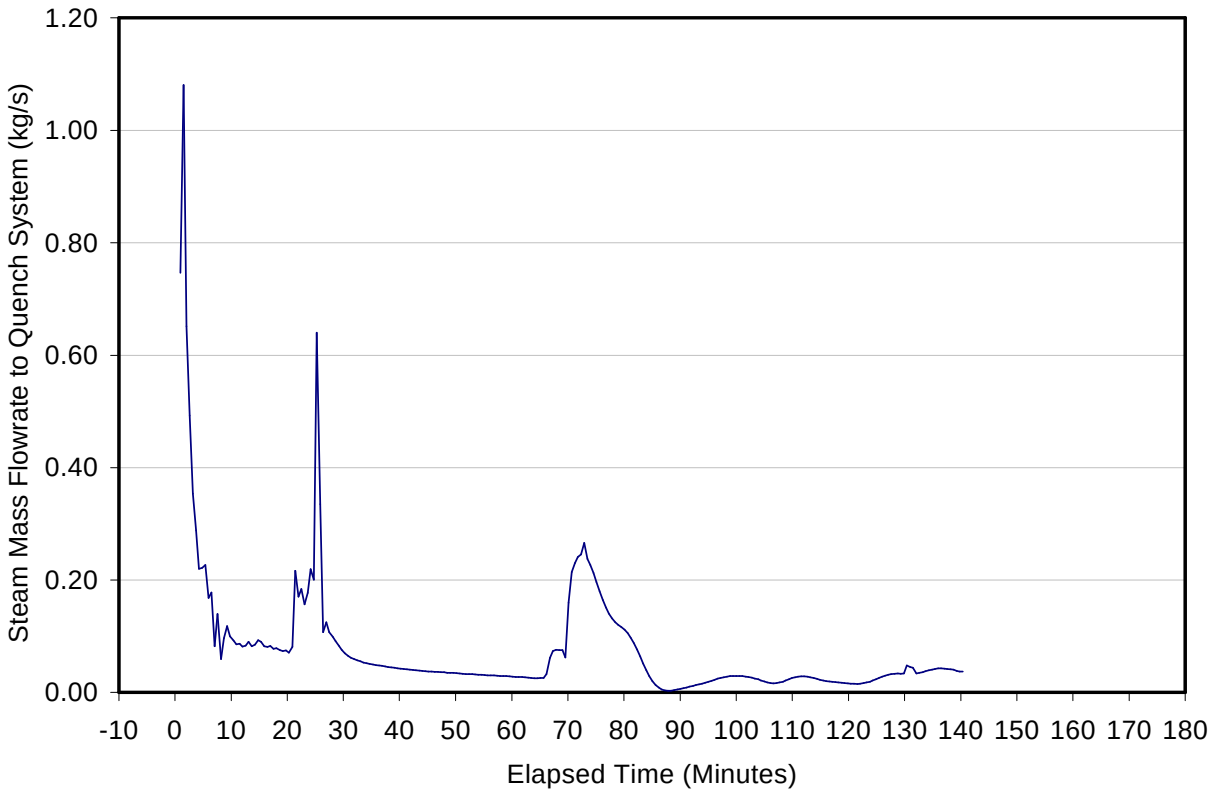

Figure 4-19. Cumulative Steam Flowrate from Debris-Water Interaction.

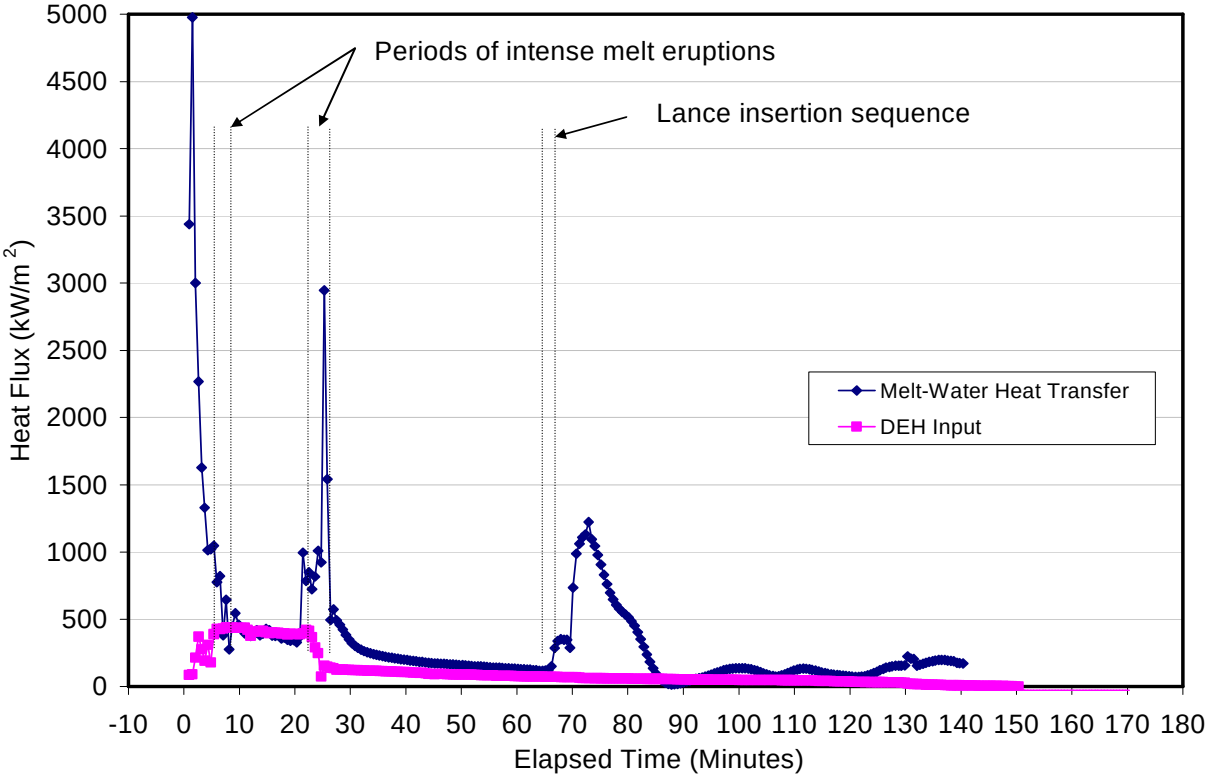

Figure 4-20. CCI-6 Debris-Water Heat Flux (Top Flooding).

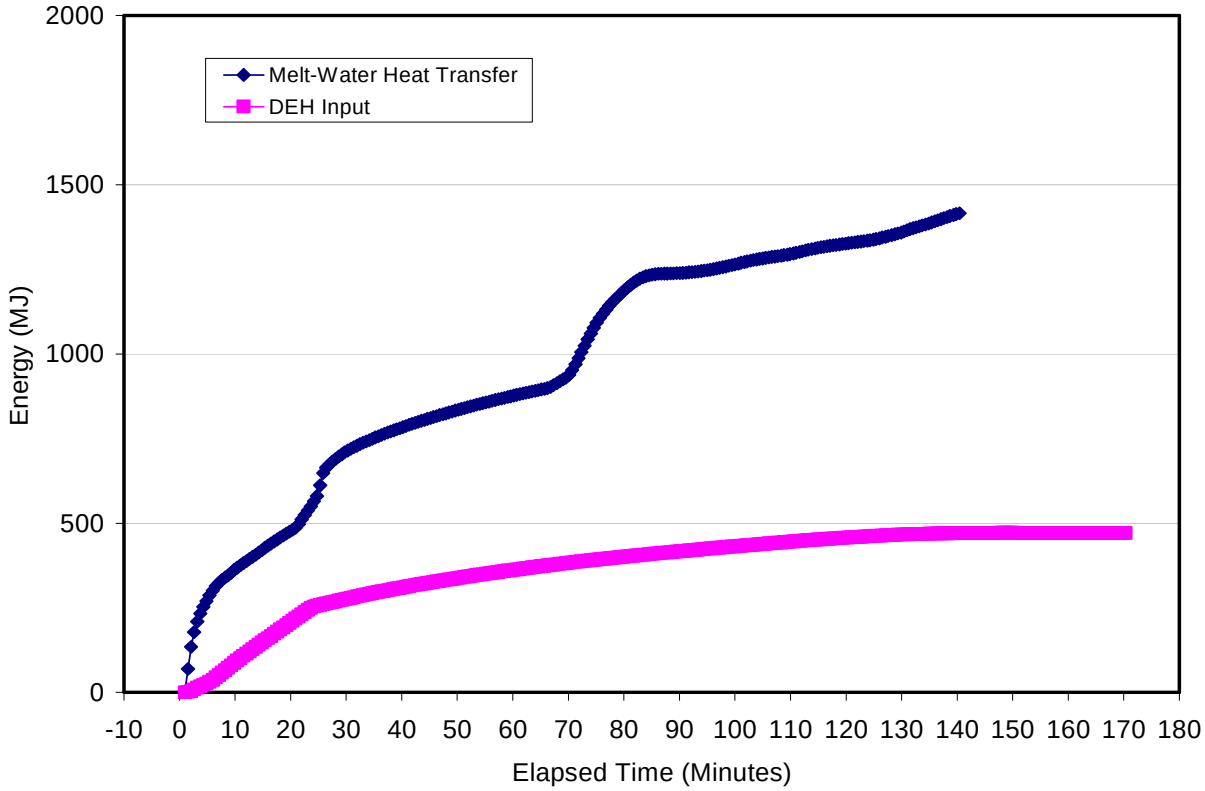

Figure 4-21. Integrated Heat Removal to Water and Heat Input to Melt from DEH.

4.6 Posttest Examinations

Following the experiment, the apparatus was carefully disassembled to document the posttest debris configuration. Upon initial reentry of the cell following the test, the area needed to be decontaminated as a result of the melt through of the main steamline that occurred soon after the thermite burn was completed (see Table 3-1). During this exercise, the steamline was examined to characterize the leak sites. Two were found; the first was located in the Tee that sat on top of the test section, while the second was in the bellows located downstream of the Tee (see Figure 2-9). Photographs are provided in Figure 4-22. The area of the hole in the Tee was ~ 6 cm^2, while the hole in the bellows was significantly smaller (~0.2 cm^2).

After the area was cleaned, disassembly of the test section began. The first step was to remove the main steamline and pressure relief piping runs from the top of the test section. The interior of the Tee was examined upon removal; this revealed the presence of a thin layer of corium coating the interior of the pipe surface (see Figure 4-23). This entrained material probably lead to excessive heatup and eventual meltthrough of the pipe.

The lid of the test section was then removed, which provided the first view of the posttest debris configuration. A photograph looking down into the test section is provided in Figure 4-24. Initial height measurements taken at this point indicated that the upper surface of the debris was at an elevation of 35 to 40 cm over the initial concrete surface, which was slightly above the initial collapsed melt depth of 28 cm.

After these initial measurements, the top and middle sidewall sections were removed and cleaned; corium splattered on these components (as well as the lid) was collected for weighing. These efforts revealed the top surface of the debris (Figure 4-25). The upper surface of the material appeared to be composed of a loose particle bed. Probing indicated that this indeed was the case. The particle bed material was removed by hand and segregated for a separate weight measurement. A photograph of this material is provided in Figure 4-26. These efforts revealed the top of a crust layer that was quite fragile and could also be removed by hand. These steps also revealed the presence of two volcanic mounds. The first was located adjacent to the south wall, while the second was centered just north of the centerline of the debris. Photographs are provided in Figure 4-27. During removal of these mounds, an effort was made to try to characterize the 'vent holes' through this material, but this proved to be difficult. First, the material was quite porous and was filled with pores and holes that ranged from a few millimeters to a centimeter. Second, when one attempted to remove this material, it crumbled quite easily which made it even more difficult to trace any continuous pathway through the material. However, the volcano near the test section centerline had a large fold or crease that could have formed a pathway for melt eruptions (see Figure 4-27b). This opening was approximately 3 cm in width.

Once the crust surface characteristics and elevation profile were documented, disassembly moved forward by first removing the two inert MgO sidewalls and then the two concrete walls to reveal the corium remaining over the basemat. Face-on views of the two sidewalls after removal are shown in Figure 4-28, while photographs of the corium remaining over the basemat are provided in Figure 4-29. Further examinations confirmed the data recorded

during the test; i.e., ablation of the north wall was minimal, while the peak ablation depth into the south wall was ~ 16 cm. Moreover, the crust material remaining over the basemat was also found to be quite fragile and porous, and this material could also be removed by hand. Thus, this fractured crust material was also recovered and segregated for weight determination; a photograph illustrating the nature of this material is provided in Figure 4-30. Although there were several large pockets of porosity found in this material (see Figure 4-29), this stage of disassembly did not reveal any large continuous caverns that separated the crust from the underlying melt pool, as occurred in the MACE tests [8]. On this basis, the test configuration appeared to achieve a floating, or at least non-separated, boundary condition that may well explain the exceptional cooling behavior that was observed.

(a) **(b)**

Figure 4-22. Photographs of Holes in the Main Steamline at (a) the Test Section Tee, and (b) the Bellows Downstream of the Tee.

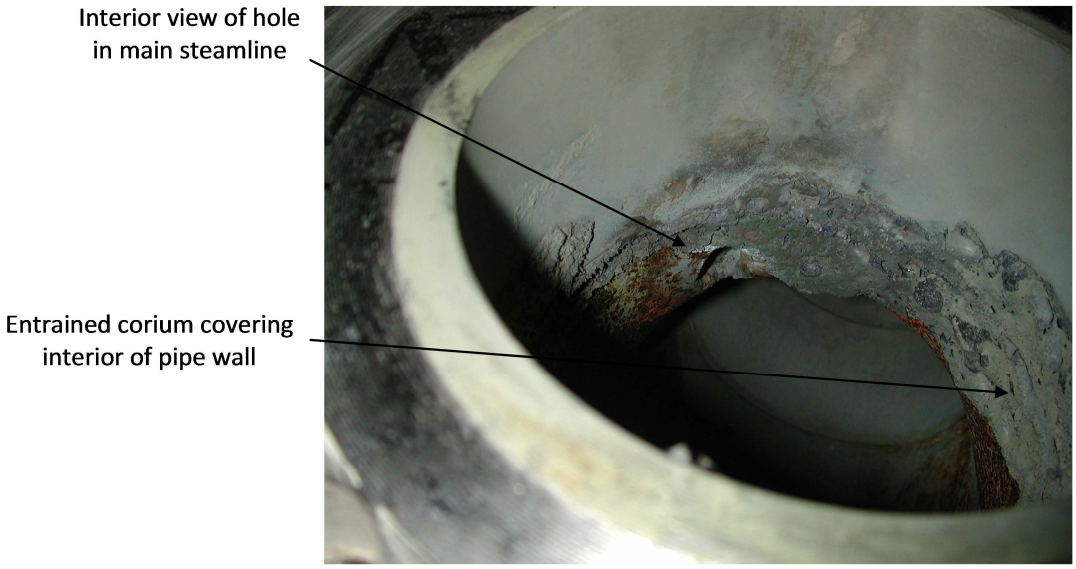

Figure 4-23. Photograph of the Interior of the Steamline Tee Showing Entrained Corium Solidified on the Pipe Interior Surface.

Figure 4-24. Top View of Posttest Debris after Removal of Test Section Lid.

Figure 4-25. Top View of Particle Bed After Removal of Upper Sidewall Sections.

Figure 4-26. Closeup Photograph of Material Removed fro m Particle Bed Over Fractured Crust.

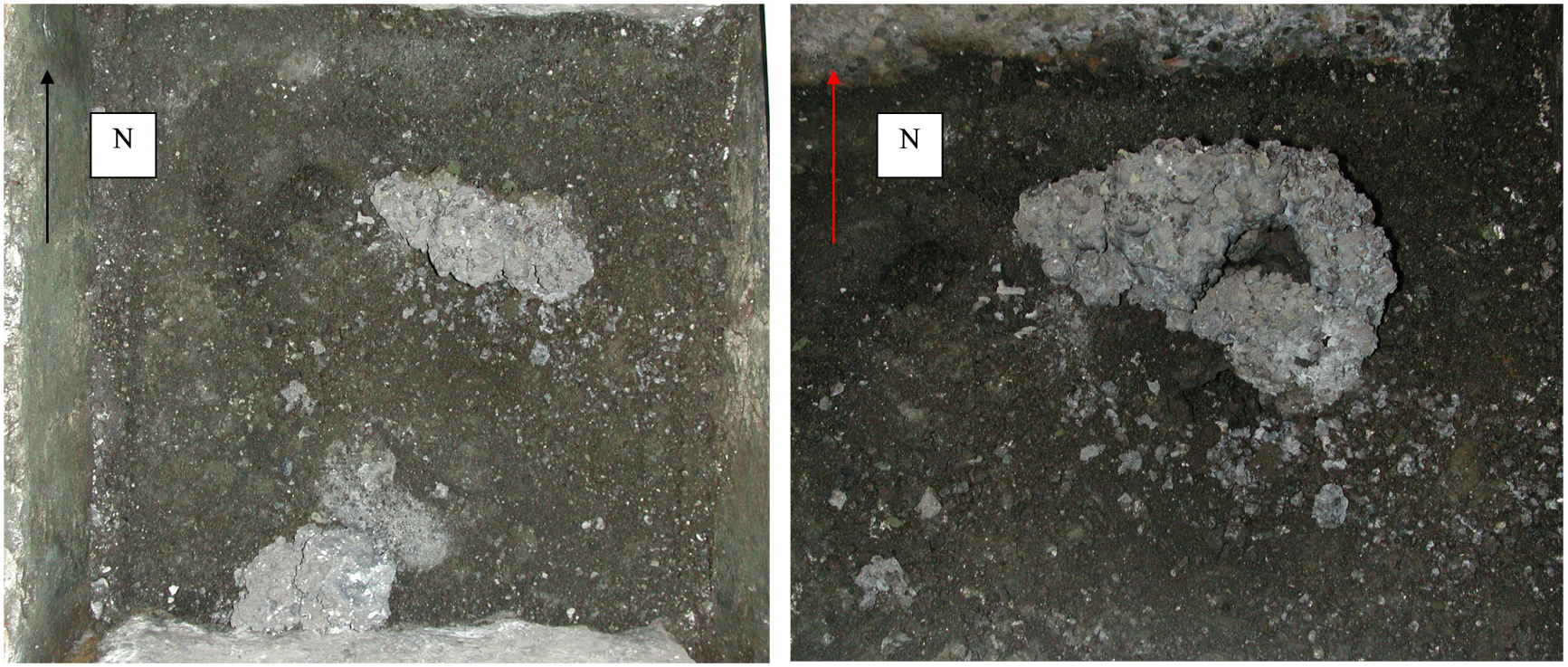

(a) **(b)**

Figure 4-27. Views of the Debris After Particle Bed Removal (a) from the Top and (b) Closeup of the Volcanic Mound in the North-Central Region of the Debris as Viewed from the South.

(a) **(b)**

Figure 4-28. Face-on Views of (a) North and (b) South Concrete Sidewalls After Removal.

(a) **(b)**

Figure 4-29. Views of Corium Debris Remaining Over the Basemat as Viewed from (a) North and (b) South.

Figure 4-30. Closeup Photograph of Fractured Crust Material after Removal from Test Section.

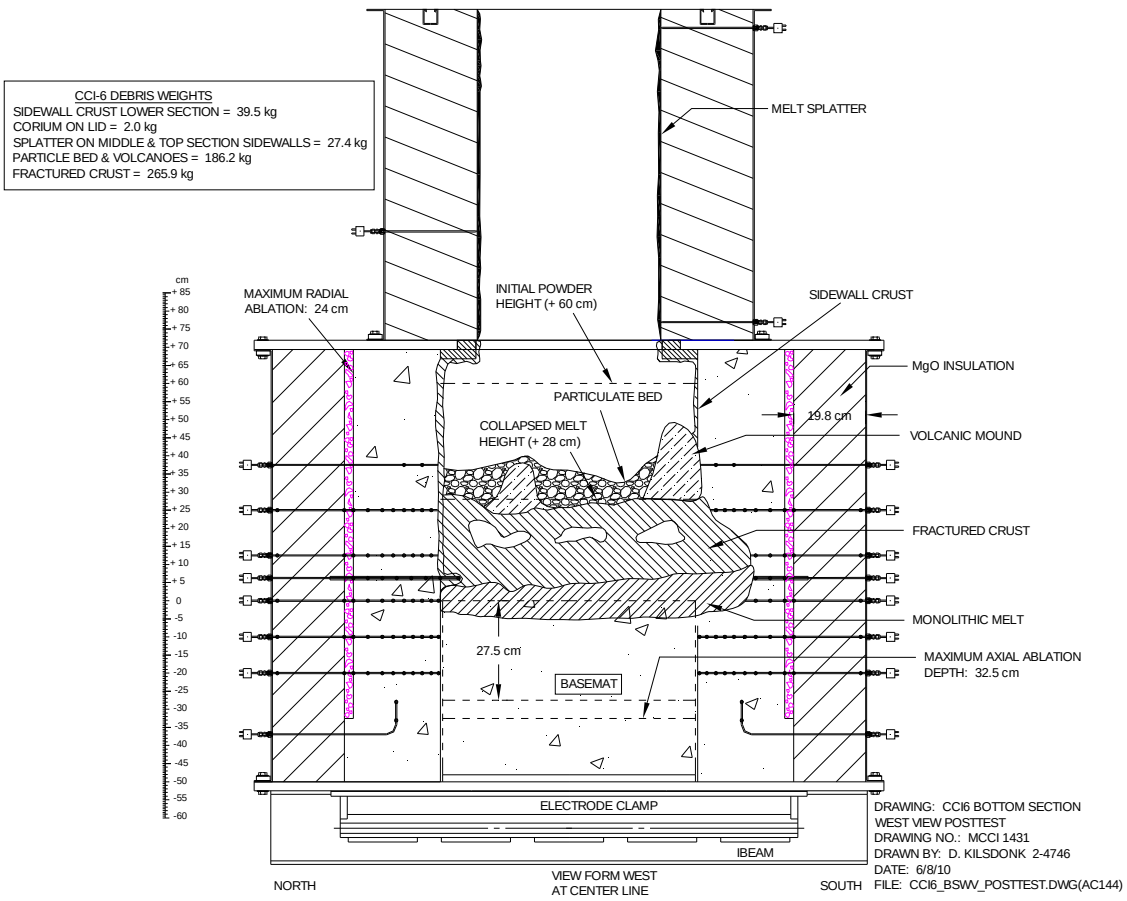

Figure 4-31. Rendering of Posttest Debris Configuration.

During disassembly, the various debris regions were carefully segregated and weighed to better document the debris distribution. A drawing showing key features is provided in Figure 4-31. These measurements indicated that 186 kg of core melt was rendered in the form of a porous debris bed due to melt eruptions, which amounts to ~ 21 % of the initial melt mass. The mass of porous, fractured crust material that could also be easily removed by hand amounted to 266 kg, which amounts to ~ 30 % of the initial mass. Thus, over ½ of the initial core melt inventory appears to have been quenched and rendered into a coolable debris configuration. The data also indicated that this most likely occurred over the first 30 minutes of the core-concrete interaction.

Further analysis of the posttest debris configuration indicates that ~ 87 kg of concrete was eroded during the test. Given the H_2O and CO_2 contents of the concrete (see Table 2-4), then this amount of material would liberate ~ 379 moles of gas upon decomposition, which is equivalent to a gas volume of ~ 9.3 m^3 at standard conditions, or ~ 71 m^3 at an assumed melt temperature of 2000˚C. Conversely, the 186 kg of erupted core melt corresponds to a liquid volume of ~ 28 liters (calculated density for CCI-6 initial melt composition is ~ 6560 kg/m^3). Thus, the melt entrainment coefficient (defined as erupted melt volume divided by total gas volume produced by core-concrete interaction at melt conditions) is calculated to be 0.04 % for CCI-6. As shown by Bonnet et al. [9], this entrainment coefficient is within the range of that which can achieve debris coolability on the basis of melt eruption cooling behavior alone during a prototypic ex-vessel core melt accident.

5.0 REFERENCES

1. M. T. Farmer, D. J. Kilsdonk, S. Lomperski, and R. W. Aeschlimann, "Category 4 Integral Test to Validate Severe Accident Codes: Core-Concrete Interaction Test Six (CCI-6) Test Plan," OECD/MCCI-2009-TR02, March 2009.

2. M. T. Farmer, S. Lomperski, D. J. Kilsdonk, and R. W. Aeschlimann, "OECD MCCI Project 2-D Core Concrete Interaction (CCI) Tests: Final Report," OECD/MCCI-2005-TR05, January 2, 2006.

3. M. T. Farmer, R. W. Aeschlimann, D. J. Kilsdonk, and, S. Lomperski, "2-D Core Concrete Interaction (CCI) Tests:CCI-4 Final Report," Rev.0, OECD/MCCI-2007-TR06, November, 2007.

4. M. T. Farmer, D. J. Kilsdonk, S. Lomperski, and R. W. Aeschlimann, "CCI-5 Quick Look Data Report," OECD/MCCI-2008-TR07, November, 2008.

5. S. Lomperski, M. T. Farmer, D. Kilsdonk, and R. W. Aeschlimann, "Small-Scale Water Ingression and Crust Strength Tests (SSWICS) SSWICS-12 Design," OECD/MCCI-2008-TR06, October, 2008.

6. D. H. Thompson, M. T. Farmer, J. K. Fink, D. R. Armstrong, and B. W. Spencer, "ACE Phase C Final Report: Volume I-MCCI Thermalhydraulic Results," EPRI/ACE-TR-C42, September, 1997.

7. M. T. Farmer, "The CORQUENCH Code for Modeling of Ex-Vessel Corium Coolability under Top Flooding Conditions, Code Manual – Version3.03," OECD/MCCI-2010-TR03, March 2010.

8. M. T. Farmer, D. J. Kilsdonk, and R. W. Aeschlimann, "Corium Coolability under Ex-Vessel Accident Conditions for LWRs," Nuclear Eng. Technology, Vol. 41, pp. 575-602, June 2009.

9. J. M. Bonnet and J. M. Seiler, "Coolability of Corium Spread Onto Concrete Under Water, the PERCOLA Model," *2nd CSNI Specialist Meeting on Core Debris-Concrete Interactions*," Karlsruhe, Germany, April 1-3, 1992

APPENDIX A
Data Acquisition System Channel Assignments

This Appendix provides the channel assignments for the three independent DAS systems that were used to guide operations and record test data for CCI-6. For convenience, these three 128 channel systems were referred to the "Basemat," "Power," and "Quench" systems by operating personnel. The channel assignment lists for these three systems are provided in Tables A-1 through A-3, respectively. The data recorded on each of channel is provided in Appendix C.

Table A-1. "Basemat" DAS Channel Assignments for CCI-6.

Channel	Variable	Sensor	Location	Level	Range/Limit	Accuracy
00	T	Diode Sensor	TC compensation Chs. B01-B49		130 C	±0.5ºC
01	T	TC Type C	Basemat 0.0 cm, +3.0 cm WCL-1	+24.0 cm	2320 C	+30 ºC/- 1%
02	T	TC Type C	Basemat 0.0 cm, +3.0 cm WCL-2	+16.0 cm	2320 C	+30 ºC/- 1%
03	T	TC Type C	Basemat 0.0 cm, +3.0 cm WCL-3	+8.0 cm	2320 C	+30 ºC/- 1%
04	T	TC Type C	Basemat 0.0 cm, +3.0 cm WCL-4	0.0 cm	2320 C	+30 ºC/- 1%
05	T	TC Type C	Basemat -15.4 cm, +19.6 cm WNW-1	+16.0 cm	2320 C	+30 ºC/- 1%
06	T	TC Type C	Basemat -15.4 cm, +19.6 cm WNW-2	+8.0 cm	2320 C	+30 ºC/- 1%
07	T	TC Type C	Basemat -15.4 cm, +19.6 cm WNW-3	0.0 cm	2320 C	+30 ºC/- 1%
08	T	TC Type C	Basemat -15.4 cm, +19.6 cm WNW-4	-8.0 cm	2320 C	+30 ºC/- 1%
09	T	TC Type C	Basemat +19.6 cm, +15.4 cm WNE-1	0.0 cm	2320 C	+30 ºC/- 1%
10	T	TC Type C	Basemat +19.6 cm, +15.4 cm WNE-2	-8.0 cm	2320 C	+30 ºC/- 1%
11	T	TC Type C	Basemat +19.6 cm, +15.4 cm WNE-3	-16.0 cm	2320 C	+30 ºC/- 1%
12	T	TC Type C	Basemat +19.6 cm, +15.4 cm WNE-4	-24.0 cm	2320 C	+30 ºC/- 1%
13	T	TC Type C	Basemat +15.4 cm, -19.6 cm WSE-1	+8.0 cm	2320 C	+30 ºC/- 1%
14	T	TC Type C	Basemat +15.4 cm, -19.6 cm WSE-2	0.0 cm	2320 C	+30 ºC/- 1%
15	T	TC Type C	Basemat +15.4 cm, -19.6 cm WSE-3	-8.0 cm	2320 C	+30 ºC/- 1%
16	T	TC Type C	Basemat +15.4 cm, -19.6 cm WSE-4	-16.0 cm	2320 C	+30 ºC/- 1%
17	T	TC Type C	Basemat -19.6 cm, -15.4 cm WSW-1	-8.0 cm	2320 C	+30 ºC/- 1%
18	T	TC Type C	Basemat -19.6 cm, -15.4 cm WSW-2	-16.0 cm	2320 C	+30 ºC/- 1%
19	T	TC Type C	Basemat -19.6 cm, -15.4 cm WSW-3	-24.0 cm	2320 C	+30 ºC/- 1%
20	T	TC Type C	Basemat -19.6 cm, -15.4 cm WSW-4	-32.0 cm	2320 C	+30 ºC/- 1%
21	T	TC Type C	N Sidewall, +5.0 cm from wall, WN-1	+5.0 cm	2320 C	+30 ºC/- 1%
22	T	TC Type C	N Sidewall, 0.0 cm deep, WN-2	0.0 cm	2320 C	+30 ºC/- 1%
23	T	TC Type C	N Sidewall, 5.0 cm deep, WN-3	-5.0 cm	2320 C	+30 ºC/- 1%
24	T	TC Type C	N Sidewall, 10.0 cm deep, WN-4	-10.0 cm	2320 C	+30 ºC/- 1%
25	T	TC Type K	N Sidewall 0.0 cm deep SWI-1	+12.5 cm	1400 C	+30 ºC/- 0.75%
26	T	TC Type K	N Sidewall 2.5 cm deep SWI-2	+12.5 cm	1400 C	+30 ºC/- 0.75%

27	T	TC Type K	N Sidewall 5.0 cm deep SWI-3	+12.5 cm	1400 C	+30 ºC/- 0.75%
28	T	TC Type K	N Sidewall 7.5 cm deep SWI-4	+12.5 cm	1400 C	+30 ºC/- 0.75%
29	T	TC Type K	Basemat 0.0 cm, -3.0 cm A-1	0.0 cm	1400 C	+30 ºC/- 0.75%
30	T	TC Type K	Basemat 0.0 cm, -3.0 cm A-2	-2.5 cm	1400 C	+30 ºC/- 0.75%
31	T	TC Type K	Basemat 0.0 cm, -3.0 cm A-3	-5.0 cm	1400 C	+30 ºC/- 0.75%
32	T	TC Type K	Basemat 0.0 cm, -3.0 cm A-4	-7.5 cm	1400 C	+30 ºC/- 0.75%
33	T	TC Type K	Basemat 0.0 cm, -3.0 cm A-5	-12.5 cm	1400 C	+30 ºC/- 0.75%
34	T	TC Type K	Basemat 0.0 cm, -3.0 cm A-6	-15.0 cm	1400 C	+30 ºC/- 0.75%
35	T	TC Type K	Basemat 0.0 cm, -3.0 cm A-7	-17.5 cm	1400 C	+30 ºC/- 0.75%
36	T	TC Type K	Basemat 0.0 cm, -3.0 cm A-8	-20.0 cm	1400 C	+30 ºC/- 0.75%
37	T	TC Type K	Basemat 0.0 cm, -3.0 cm A-9	-22.5 cm	1400 C	+30 ºC/- 0.75%
38	T	TC Type K	Basemat 0.0 cm, -3.0 cm A-10	-27.5 cm	1400 C	+30 ºC/- 0.75%
39	T	TC Type K	Basemat 0.0 cm, -3.0 cm A-11	-32.5 cm	1400 C	+30 ºC/- 0.75%
40	T	TC Type K	Basemat –19.6 cm, +15.4 cm B-1	0.0 cm	1400 C	+30 ºC/- 0.75%
41	T	TC Type K	Basemat –19.6 cm, +15.4 cm B-2	-2.5 cm	1400 C	+30 ºC/- 0.75%
42	T	TC Type K	Basemat –19.6 cm, +15.4 cm B-3	-5.0 cm	1400 C	+30 ºC/- 0.75%
43	T	TC Type K	Basemat –19.6 cm, +15.4 cm B-4	-7.5 cm	1400 C	+30 ºC/- 0.75%
44	T	TC Type K	Basemat –19.6 cm, +15.4 cm B-5	-12.5 cm	1400 C	+30 ºC/- 0.75%
45	T	TC Type K	Basemat –19.6 cm, +15.4 cm B-6	-17.5 cm	1400 C	+30 ºC/- 0.75%
46	T	TC Type K	Basemat –19.6 cm, +15.4 cm B-7	-22.5 cm	1400 C	+30 ºC/- 0.75%
47	T	TC Type K	Basemat –19.6 cm, +15.4 cm B-8	-27.5 cm	1400 C	+30 ºC/- 0.75%
48	T	TC Type K	Basemat –19.6 cm, +15.4 cm B-9	-32.5 cm	1400 C	+30 ºC/- 0.75%
49	T	TC Type C	N Sidewall, 15.0 cm deep, WN-5	-15.0 cm	2320 C	+30 ºC/- 1%
50	T	Diode Sensor	TC compensation Chs. B51-B99		130 C	±0.5ºC
51	T	TC Type K	Basemat +19.6 cm, +15.4 cm C-1	0.0 cm	1400 C	+30 ºC/- 0.75%
52	T	TC Type K	Basemat +19.6 cm, +15.4 cm C-2	-2.5 cm	1400 C	+30 ºC/- 0.75%
53	T	TC Type K	Basemat +19.6 cm, +15.4 cm C-3	-5.0 cm	1400 C	+30 ºC/- 0.75%
54	T	TC Type K	Basemat +19.6 cm, +15.4 cm C-4	-7.5 cm	1400 C	+30 ºC/- 0.75%

55	T	TC Type K	Basemat +19.6 cm, +15.4 cm C-5	-12.5 cm	1400 C	+30 ºC/- 0.75%
56	T	TC Type K	Basemat +19.6 cm, +15.4 cm C-6	-17.5 cm	1400 C	+30 ºC/- 0.75%
57	T	TC Type K	Basemat +19.6 cm, +15.4 cm C-7	-22.5 cm	1400 C	+30 ºC/- 0.75%
58	T	TC Type K	Basemat +19.6 cm, +15.4 cm C-8	-27.5 cm	1400 C	+30 ºC/- 0.75%
59	T	TC Type K	Basemat +19.6 cm, +15.4 cm C-9	-32.5 cm	1400 C	+30 ºC/- 0.75%
60	T	TC Type C	N Sidewall, 20.0 cm deep, WN-6	-20.0 cm	2320 C	+30 ºC/- 0.75%
61	T	TC Type K	Basemat +19.6 cm, -15.4 cm D-1	0.0 cm	1400 C	+30 ºC/- 0.75%
62	T	TC Type K	Basemat +19.6 cm, -15.4 cm D-2	-2.5 cm	1400 C	+30 ºC/- 0.75%
63	T	TC Type K	Basemat +19.6 cm, -15.4 cm D-3	-5.0 cm	1400 C	+30 ºC/- 0.75%
64	T	TC Type K	Basemat +19.6 cm, -15.4 cm D-4	-7.5 cm	1400 C	+30 ºC/- 0.75%
65	T	TC Type K	Basemat +19.6 cm, -15.4 cm D-5	-12.5 cm	1400 C	+30 ºC/- 0.75%
66	T	TC Type K	Basemat +19.6 cm, -15.4 cm D-6	-17.5 cm	1400 C	+30 ºC/- 0.75%
67	T	TC Type K	Basemat +19.6 cm, -15.4 cm D-7	-22.5 cm	1400 C	+30 ºC/- 0.75%
68	T	TC Type K	Basemat +19.6 cm, -15.4 cm D-8	-27.5 cm	1400 C	+30 ºC/- 0.75%
69	T	TC Type K	Basemat +19.6 cm, -15.4 cm D-9	-32.5 cm	1400 C	+30 ºC/- 0.75%
70	T	TC Type C	S Sidewall, 15.0 cm deep, WS-5	-15.0 cm	2320 C	+30 ºC/- 0.75%
71	T	TC Type K	Basemat -19.6 cm, -15.4 cm E-1	0.0 cm	1400 C	+30 ºC/- 0.75%
72	T	TC Type K	Basemat -19.6 cm, -15.4 cm E-2	-2.5 cm	1400 C	+30 ºC/- 0.75%
73	T	TC Type K	Basemat -19.6 cm, -15.4 cm E-3	-5.0 cm	1400 C	+30 ºC/- 0.75%
74	T	TC Type K	Basemat -19.6 cm, -15.4 cm E-4	-7.5 cm	1400 C	+30 ºC/- 0.75%
75	T	TC Type K	Basemat -19.6 cm, -15.4 cm E-5	-12.5 cm	1400 C	+30 ºC/- 0.75%
76	T	TC Type K	Basemat -19.6 cm, -15.4 cm E-6	-17.5 cm	1400 C	+30 ºC/- 0.75%
77	T	TC Type K	Basemat -19.6 cm, -15.4 cm E-7	-22.5 cm	1400 C	+30 ºC/- 0.75%
78	T	TC Type K	Basemat -19.6 cm, -15.4 cm E-8	-27.5 cm	1400 C	+30 ºC/- 0.75%
79	T	TC Type K	Basemat -19.6 cm, -15.4 cm E-9	-32.5 cm	1400 C	+30 ºC/- 0.75%
80	T	TC Type C	S Sidewall, 20.0 cm deep, WS-6	-20.0 cm	2320 C	+30 ºC/- 1%
81	T	TC Type K	N Sidewall -12.5 cm deep SWA-1	-27.5 cm	1400 C	+30 ºC/- 0.75%
82	T	TC Type K	N Sidewall -12.5 cm deep SWA-2	-32.5 cm	1400 C	+30 ºC/- 0.75%

83	T	TC Type K	S Sidewall -12.5 cm deep SWB-1	-27.5 cm	1400 C	+30 ºC/- 0.75%
84	T	TC Type K	S Sidewall -12.5 cm deep SWB-2	-32.5 cm	1400 C	+30 ºC/- 0.75%
85	T	TC Type K	N Sidewall 24.0 cm deep SWK-9	+25.0 cm	1400 C	+30 ºC/- 0.75%
86	T	TC Type K	N Sidewall 26.5 cm deep SWK-10	+25.0 cm	1400 C	+30 ºC/- 0.75%
87	T	TC Type K	N Sidewall 45.0 cm deep SWK-11	+25.0 cm	1400 C	+30 ºC/- 0.75%
88	T	TC Type K	S Sidewall 13.0 cm deep SWL-6	+25.0 cm	1400 C	+30 ºC/- 0.75%
89	T	TC Type K	S Sidewall 16.0 cm deep SWL-7	+25.0 cm	1400 C	+30 ºC/- 0.75%
90	T	TC Type K	S Sidewall 20.0 cm deep SWL-8	+25.0 cm	1400 C	+30 ºC/- 0.75%
91	T	TC Type K	S Sidewall 24.0 cm deep SWL-9	+25.0 cm	1400 C	+30 ºC/- 0.75%
92	T	TC Type K	S Sidewall 26.5 cm deep SWL-10	+25.0 cm	1400 C	+30 ºC/- 0.75%
93	T	TC Type K	S Sidewall 45.0 cm deep SWL-11	+25.0 cm	1400 C	+30 ºC/- 0.75%
94	T	TC Type K	N Sidewall 0.0 cm deep SWC-1	-20.0 cm	1400 C	+30 ºC/- 0.75%
95	T	TC Type K	N Sidewall 2.5 cm deep SWC-2	-20.0 cm	1400 C	+30 ºC/- 0.75%
96	T	TC Type K	N Sidewall 5.0 cm deep SWC-3	-20.0 cm	1400 C	+30 ºC/- 0.75%
97	T	TC Type K	Basemat 0.0 cm, -3.0 cm A-4b	-10.0 cm	1400 C	+30 ºC/- 0.75%
98	Reserve					
99	F	Ultrasonic	Basemat Water Injection Flowrate FM-Inj	R=49.94 Ω	38 lpm	± 0.3 lpm

Explanation of Variable Notations
T = temperature; F = flowrate

Table A-2. "Power" DAS Channel Assignments for CCI-6.

Channel	Variable	Sensor	Location	Level	Range/Limit	Accuracy
00	Reserve					
01	T	TC Type K	N Sidewall 7.5 cm deep SWC-4	-20.0 cm	1400 C	± 0.75%
02	T	TC Type K	N Sidewall 10.0 cm deep SWC-5	-20.0 cm	1400 C	± 0.75%
03	T	TC Type K	N Sidewall 13.0 cm deep SWC-6	-20.0 cm	1400 C	± 0.75%
04	T	TC Type K	N Sidewall 16.0 cm deep SWC-7	-20.0 cm	1400 C	± 0.75%
05	T	TC Type K	N Sidewall 20.0 cm deep SWC-8	-20.0 cm	1400 C	± 0.75%
06	T	TC Type K	N Sidewall 24.0 cm deep SWC-9	-20.0 cm	1400 C	± 0.75%
07	T	TC Type K	N Sidewall 26.5 cm deep SWC-10	-20.0 cm	1400 C	± 0.75%
08	T	TC Type K	N Sidewall 45.0 cm deep SWC-11	-20.0 cm	1400 C	± 0.75%
09	T	TC Type K	S Sidewall 0.0 cm deep SWD-1	-20.0 cm	1400 C	± 0.75%
10	T	TC Type K	S Sidewall 2.5 cm deep SWD-2	-20.0 cm	1400 C	± 0.75%
11	T	TC Type K	S Sidewall 5.0 cm deep SWD-3	-20.0 cm	1400 C	± 0.75%
12	T	TC Type K	S Sidewall 7.5 cm deep SWD-4	-20.0 cm	1400 C	± 0.75%
13	T	TC Type K	S Sidewall 10.0 cm deep SWD-5	-20.0 cm	1400 C	± 0.75%
14	T	TC Type K	S Sidewall 13.0 cm deep SWD-6	-20.0 cm	1400 C	± 0.75%
15	T	TC Type K	S Sidewall 16.0 cm deep SWD-7	-20.0 cm	1400 C	± 0.75%
16	T	TC Type K	S Sidewall 20.0 cm deep SWD-8	-20.0 cm	1400 C	± 0.75%
17	T	TC Type K	S Sidewall 24.0 cm deep SWD-9	-20.0 cm	1400 C	± 0.75%
18	T	TC Type K	S Sidewall 26.5 cm deep SWD-10	-20.0 cm	1400 C	± 0.75%
19	T	TC Type K	S Sidewall 45.0 cm deep SWD-11	-20.0 cm	1400 C	± 0.75%
20	T	TC Type K	N Sidewall 0.0 cm deep SWE-1	-10.0 cm	1400 C	± 0.75%
21	T	TC Type K	N Sidewall 2.5 cm deep SWE-2	-10.0 cm	1400 C	± 0.75%
22	T	TC Type K	N Sidewall 5.0 cm deep SWE-3	-10.0 cm	1400 C	± 0.75%
23	T	TC Type K	N Sidewall 7.5 cm deep SWE-4	-10.0 cm	1400 C	± 0.75%
24	T	TC Type K	N Sidewall 10.0 cm deep SWE-5	-10.0 cm	1400 C	± 0.75%
25	T	TC Type K	N Sidewall 13.0 cm deep SWE-6	-10.0 cm	1400 C	± 0.75%

26	T	TC Type K	N Sidewall 16.0 cm deep SWE-7	-10.0 cm	1400 C	± 0.75%
27	T	TC Type K	N Sidewall 20.0 cm deep SWE-8	-10.0 cm	1400 C	± 0.75%
28	T	TC Type K	N Sidewall 24.0 cm deep SWE-9	-10.0 cm	1400 C	± 0.75%
29	T	TC Type K	N Sidewall 26.5 cm deep SWE-10	-10.0 cm	1400 C	± 0.75%
30	T	TC Type K	N Sidewall 45.0 cm deep SWE-11	-10.0 cm	1400 C	± 0.75%
31	T	TC Type K	S Sidewall 0.0 cm deep SWF-1	-10.0 cm	1400 C	± 0.75%
32	T	TC Type K	S Sidewall 2.5 cm deep SWF-2	-10.0 cm	1400 C	± 0.75%
33	T	TC Type K	S Sidewall 5.0 cm deep SWF-3	-10.0 cm	1400 C	± 0.75%
34	T	TC Type K	S Sidewall 7.5 cm deep SWF-4	-10.0 cm	1400 C	± 0.75%
35	T	TC Type K	S Sidewall 10.0 cm deep SWF-5	-10.0 cm	1400 C	± 0.75%
36	T	TC Type K	S Sidewall 13.0 cm deep SWF-6	-10.0 cm	1400 C	± 0.75%
37	T	TC Type K	S Sidewall 16.0 cm deep SWF-7	-10.0 cm	1400 C	± 0.75%
38	T	TC Type K	S Sidewall 20.0 cm deep SWF-8	-10.0 cm	1400 C	± 0.75%
39	T	TC Type K	S Sidewall 24.0 cm deep SWF-9	-10.0 cm	1400 C	± 0.75%
40	T	TC Type K	S Sidewall 26.5 cm deep SWF-10	-10.0 cm	1400 C	± 0.75%
41	T	TC Type K	S Sidewall 45.0 cm deep SWF-11	-10.0 cm	1400 C	± 0.75%
42	T	TC Type K	N Sidewall 0.0 cm deep SWG-1	0.0 cm	1400 C	± 0.75%
43	T	TC Type K	N Sidewall 2.5 cm deep SWG-2	0.0 cm	1400 C	± 0.75%
44	T	TC Type K	N Sidewall 5.0 cm deep SWG-3	0.0 cm	1400 C	± 0.75%
45	T	TC Type K	N Sidewall 7.5 cm deep SWG-4	0.0 cm	1400 C	± 0.75%
46	T	TC Type K	N Sidewall 10.0 cm deep SWG-5	0.0 cm	1400 C	± 0.75%
47	T	TC Type K	N Sidewall 13.0 cm deep SWG-6	0.0 cm	1400 C	± 0.75%
48	T	TC Type K	N Sidewall 16.0 cm deep SWG-7	0.0 cm	1400 C	± 0.75%
49	T	TC Type K	N Sidewall 20.0 cm deep SWG-8	0.0 cm	1400 C	± 0.75%
50	T	TC Type K	N Sidewall 24.0 cm deep SWG-9	0.0 cm	1400 C	± 0.75%
51	T	TC Type K	N Sidewall 26.5 cm deep SWG-10	0.0 cm	1400 C	± 0.75%
52	T	TC Type K	N Sidewall 45.0 cm deep SWG-11	0.0 cm	1400 C	± 0.75%
53	Reserve					

54	T	TC Type K	S Sidewall 0.0 cm deep SWH-1	0.0 cm	1400 C	± 0.75%
55	T	TC Type K	S Sidewall 2.5 cm deep SWH-2	0.0 cm	1400 C	± 0.75%
56	T	TC Type K	S Sidewall 5.0 cm deep SWH-3	0.0 cm	1400 C	± 0.75%
57	T	TC Type K	S Sidewall 7.5 cm deep SWH-4	0.0 cm	1400 C	± 0.75%
58	T	TC Type K	S Sidewall 10.0 cm deep SWH-5	0.0 cm	1400 C	± 0.75%
59	T	TC Type K	S Sidewall 13.0 cm deep SWH-6	0.0 cm	1400 C	± 0.75%
60	T	TC Type K	S Sidewall 16.0 cm deep SWH-7	0.0 cm	1400 C	± 0.75%
61	T	TC Type K	S Sidewall 20.0 cm deep SWH-8	0.0 cm	1400 C	± 0.75%
62	T	TC Type K	S Sidewall 24.0 cm deep SWH-9	0.0 cm	1400 C	± 0.75%
63	T	TC Type K	S Sidewall 26.5 cm deep SWH-10	0.0 cm	1400 C	± 0.75%
64	T	TC Type K	S Sidewall 45.0 cm deep SWH-11	0.0 cm	1400 C	± 0.75%
65	T	TC Type C	S Sidewall, +5.0 cm from wall, WS-1	+5.0 cm	2320 C	± 1%
66	T	TC Type C	S Sidewall, 0.0 cm deep, WS-2	0.0 cm	2320 C	± 1%
67	T	TC Type C	S Sidewall, 5.0 cm deep, WS-3	-5.0 cm	2320 C	± 1%
68	T	TC Type C	S Sidewall, 10.0 cm deep, WS-4	-10.0 cm	2320 C	± 1%
69	T	TC Type K	N Sidewall 10.0 cm deep SWI-5	+12.5 cm	1400 C	± 0.75%
70	T	TC Type K	N Sidewall 13.0 cm deep SWI-6	+12.5 cm	1400 C	± 0.75%
71	T	TC Type K	N Sidewall 16.0 cm deep SWI-7	+12.5 cm	1400 C	± 0.75%
72	T	TC Type K	N Sidewall 20.0 cm deep SWI-8	+12.5 cm	1400 C	± 0.75%
73	T	TC Type K	N Sidewall 24.0 cm deep SWI-9	+12.5 cm	1400 C	± 0.75%
74	T	TC Type K	N Sidewall 26.5 cm deep SWI-10	+12.5 cm	1400 C	± 0.75%
75	T	TC Type K	N Sidewall 45.0 cm deep SWI-11	+12.5 cm	1400 C	± 0.75%
76	T	TC Type K	S Sidewall 0.0 cm deep SWJ-1	+12.5 cm	1400 C	± 0.75%
77	T	TC Type K	S Sidewall 2.5 cm deep SWJ-2	+12.5 cm	1400 C	± 0.75%
78	T	TC Type K	S Sidewall 5.0 cm deep SWJ-3	+12.5 cm	1400 C	± 0.75%
79	T	TC Type K	S Sidewall 7.5 cm deep SWJ-4	+12.5 cm	1400 C	± 0.75%
80	T	TC Type K	S Sidewall 10.0 cm deep SWJ-5	+12.5 cm	1400 C	± 0.75%
81	T	TC Type K	S Sidewall 13.0 cm deep SWJ-6	+12.5 cm	1400 C	± 0.75%

82	T	TC Type K	S Sidewall 16.0 cm deep SWJ-7	+12.5 cm	1400 C	± 0.75%
83	T	TC Type K	S Sidewall 20.0 cm deep SWJ-8	+12.5 cm	1400 C	± 0.75%
84	T	TC Type K	S Sidewall 24.0 cm deep SWJ-9	+12.5 cm	1400 C	± 0.75%
85	T	TC Type K	S Sidewall 26.5 cm deep SWJ-10	+12.5 cm	1400 C	± 0.75%
86	T	TC Type K	S Sidewall 45.0 cm deep SWJ-11	+12.5 cm	1400 C	± 0.75%
87	T	TC Type K	N Sidewall 0.0 cm deep SWK-1	+25.0 cm	1400 C	± 0.75%
88	T	TC Type K	N Sidewall 2.5 cm deep SWK-2	+25.0 cm	1400 C	± 0.75%
89	T	TC Type K	N Sidewall 5.0 cm deep SWK-3	+25.0 cm	1400 C	± 0.75%
90	T	TC Type K	N Sidewall 7.5 cm deep SWK-4	+25.0 cm	1400 C	± 0.75%
91	T	TC Type K	N Sidewall 10.0 cm deep SWK-5	+25.0 cm	1400 C	± 0.75%
92	T	TC Type K	N Sidewall 13.0 cm deep SWK-6	+25.0 cm	1400 C	± 0.75%
93	T	TC Type K	N Sidewall 16.0 cm deep SWK-7	+25.0 cm	1400 C	± 0.75%
94	T	TC Type K	N Sidewall 20.0 cm deep SWK-8	+25.0 cm	1400 C	± 0.75%
95	T	TC Type K	S Sidewall 0.0 cm deep SWL-1	+25.0 cm	1400 C	± 0.75%
96	T	TC Type K	S Sidewall 2.5 cm deep SWL-2	+25.0 cm	1400 C	± 0.75%
97	T	TC Type K	S Sidewall 5.0 cm deep SWL-3	+25.0 cm	1400 C	± 0.75%
98	T	TC Type K	S Sidewall 7.5 cm deep SWL-4	+25.0 cm	1400 C	± 0.75%
99	T	TC Type K	S Sidewall 10.0 cm deep SWL-5	+25.0 cm	1400 C	± 0.75%

Explanation of Variable Notations
T = temperature

Table A-3. "Quench" DAS Channel Assignments for CCI-6.

Channel	Variable	Sensor	Location	Level	Range/Limit	Accuracy	Notes
00	T	Diode Sensor	TC Compensation CH Q00-Q49		130 C	± 0.5 C	
01	Reserve						
02	Reserve						
03	Reserve						
04	Reserve						
05	Reserve						
06	T	TC Type C	E Sidewall 4.0 cm deep SWHL-3	-7.5 cm	2320 C	± 1.0%	
07	T	TC Type C	E Sidewall 8.0 cm deep SWHL-4	-7.5 cm	2320 C	± 1.0%	
08	Reserve						
09	Reserve						
10	T	TC Type C	W Sidewall 4.0 cm deep SWHL-7	+2.5 cm	2320 C	± 1.0%	
11	Reserve						
12	Reserve						
13	Reserve						
14	Reserve						
15	Reserve						
16	Reserve						
17	Reserve						
18	Reserve						
19	T	TC Type C	W Sidewall 1.0 cm deep SWHL-13	+22.5 cm	2320 C	± 1.0%	
20	L	Potentiometer	Lance Position Indicator		0-125 cm	± 10 mm	
21	T	TC Type K	Steamline internal vertical run from vessel ML-1		1400 C	± 0.75%	
22	T	TC Type K	Steamline external vertical run from vessel ML-2		1400 C	± 0.75%	
23	T	TC Type K	Steamline external lateral run from vessel ML-3		1400 C	± 0.75%	
24	T	TC Type K	Steamline external vertical run to quench tank ML-4		1400 C	± 0.75%	
25	T	TC Type K	S Middle Section Sidewall, 0.0 cm deep SWHL-17	+77.5 cm	1400 C	± 0.75%	
26	T	TC Type K	S Middle Section Sidewall, 20.0 cm deep SWHL-18	+77.5 cm	1400 C	± 0.75%	
27	Reserve						

28	FOR	Strain	Crust Force Load		0-44.6 kN		
29	T	TC Type K	Quench tank internal QT-1	21 cm	1400 C	± 0.75%	
30	T	TC Type K	Quench tank internal QT-2	55 cm	1400 C	± 0.75%	
31	T	TC Type K	N Sidewall 0.0 cm deep SWM-1	+37.5 cm	1400 C	± 0.75%	
32	T	TC Type K	N Sidewall 5.0 cm deep SWM-2	+37.5 cm	1400 C	± 0.75%	
33	T	TC Type K	N Sidewall 10.0 cm deep SWM-3	+37.5 cm	1400 C	± 0.75%	
34	T	TC Type K	Overflow tank No. 2 internal OT-2	16 cm	1400 C	± 0.75%	
35	T	TC Type K	Quench tank coil inlet QT-5		1400 C	± 0.75%	
36	T	TC Type K	Quench tank coil outlet QT-6		1400 C	± 0.75%	
37	T	TC Type K	Quench tank coil outlet QT-7		1400 C	± 0.75%	
38	T	TC Type K	Overflow tank No. 1 internal OT-1	16 cm	1400 C	± 0.75%	
39	T	Voltage	Igniter Current		100 mV		
40	T	TC Type K	Spray tank internal ST-1	10 cm	1400 C	± 0.75%	
41	Reserve						
42	T	TC Type K	S Middle Section Sidewall 0.0 cm deep SWHL-19	+158.8 cm	1400 C	± 0.75%	
43	T	TC Type K	S Middle Section Sidewall 2.0 cm deep SWHL-20	"	1400 C	± 0.75%	
44	T	TC Type K	N Top Section Sidewall, 0.0 cm deep SWHL -21	+200.6 cm	1400 C	± 0.75%	
45	T	TC Type K	N Top Section Sidewall, 2.0 cm deep SWHL-22	"	1400 C	± 0.75%	
46	T	TC Type K	W Top Section Sidewall 0.0 cm deep SWHL-23	+219.0 cm	1400 C	± 0.75%	
47	T	TC Type K	W Top Section Sidewall 2.0 cm deep SWHL-24	"	1400 C	± 0.75%	
48	Reserve						
49	T	TC Type K	Twat-in (nozzle water injection manifold)		1400 C	± 0.75%	
50	T	Diode Sensor	TC Compensation CH Q50-Q99		130 C	± 0.5 C	
51	T	TC Type K	S Sidewall 0.0 cm deep SWN-1	+37.5 cm	1400 C	± 0.75%	
52	T	TC Type K	S Sidewall 5.0 cm deep SWN-2	+37.5 cm	1400 C	± 0.75%	
53	T	TC Type K	S Sidewall 10.0 cm deep SWN-3	+37.5 cm	1400 C	± 0.75%	
54	T	TC Type K	Internal, exhaust line OG-1		1400 C	± 0.75%	
55	T	TC Type K	Water supply tank internal WS-1	45 cm	1400 C	± 0.75%	

56	Reserve						
57	T	TC Type K	Water level probe LP-1	167/48 cm	1400 C	± 0.75%	
58	T	TC Type K	Water level probe LP-2	167/48 cm	1400 C	± 0.75%	
59	T	TC Type K	Test vessel plenum gas TS-1		1400 C	± 0.75%	
60	L	Strain	Supply tank head PT-1		0-35 kPad	± 0.4 kPa	D-6
61	P	Strain	Supply tank pressure PT-2		0-408 kPa	± 2.0 kPa	PT-2
62	L	Strain	Test vessel head, insertion probe PT-3		0-35 kPad	± 0.4 kPa	D-3
63	L	Strain	Test vessel head, static probe PT-4		0-35 kPad	± 0.4 kPa	D-1
64	P	Strain	Test vessel plenum pressure PT-5		0-204 kPa	± 2.0 kPa	A-1
65	P	Strain	Basemat side pressure PT-6		0-204 kPa	± 2.0 kPa	A-3
66	L	Strain	Nozzle Header Tank Water Level PT-7		0-35 kPad	± 0.4 kPa	D-2
67	L	Strain	Quench tank head PT-8		0-35 kPad	± 0.4 kPa	D-4
68	P	Strain	Quench/overflow tank pressure PT-9		0-204 kPa	± 2.0 kPa	A-17
69	L	Strain	Overflow tank head PT-10		0-35 kPad	± 0.4 kPa	D-8
70	L	Strain	Spray tank head PT-11		0-35 kPad	± 0.4 kPa	D-5
71	Reserve						
72	L	Magnetic Float	Supply tank volume LS-1		350-2000 l	± 5 l	
73	L	Magnetic Float	Quench tank volume LS-2		80-590 l	± 2 l	
74	L	Magnetic Float	Overflow tank volume LS-3		400-1800 l	± 5 l	
75	L	Magnetic Float	Spray tank volume LS-4		240-1290 l	± 5 l	
76	F	Paddlewheel	Water supply flowrate FM-1		680 lpm	± 4 %	
77	F	Paddlewheel	Quench tank coil flowrate FM-2		190 lpm	± 4 %	
78	Reserve						
79	Reserve						
80	Reserve	Pyrometer	Melt Surface temperature pyrometer		600-1800 C	± 4.0 C	
81	Reserve						
82	Reserve						
83	FC	Flowcontroller	Lid lights & camera covergas flowrate FC-2		0-200 lpm	± 1.0 %	

84	Reserve						
85		-	Calculated Total Current (Q92+Q93)		0 -10,000 A		
86		-	Calculated Total Power (Q94+Q95)		0-500 kW	± 0.3 %	
87	FC	Flowcontroller	Test vessel covergas flowrate FC-6		0-100 lpm	± 1.0 %	
88	FC	Flowcontroller	Lid camera covergas flowrate FC-7		0-350 lpm	± 1.0 %	
89	V		Pressure transducer power supply #1 voltage		0-30 V	0.008 %	
90	V		Pressure transducer power supply #2 voltage		0-30 V	± 0.008 %	
91	V	Voltmeter	Power supply voltage		0-200 V	± 0.008 %	
92	A	Transformer	Power supply current #2		5000 A		
93	A	Transformer	Power supply current #1		5000 A		
94	W	Hall Meter	Power supply power #2		1100 kW	± 0.2 %	
95	W	Hall Meter	Power supply power #1		1100 kW	± 0.2 %	
96	L	Strain	Auxiliary Tank Head PT-13		0-35 kPad	± 0.4 kPa	D-10
97	T	TC Type K	Auxiliary Tank Internal AT-1	43 cm	1400 C	± 0.75%	
98	Reserve						
99	Reserve						

Explanation of variable notations
T = temperature P = Pressure FOR=Force L = Level V = Voltage F = Flowrate A = Current W = Power FC = Flow Controller

Appendix B
Power Supply Constant Voltage Operating Method

The purpose of this appendix is to provide the theory underlying the concept of operating the DEH power supply in a constant voltage mode after water addition as a means of preserving specific power density in the melt.

Based on Ohms law, the relationship between voltage drop E across a conductor of resistance R and the power input is of the form:

$$P = \frac{E^2}{R}$$

Assuming the melt that is electrically heated with the power supply can be modeled using an idealized rectilinear geometry in which the length between the electrodes is L, the uniform melt depth is h, and the cavity width is W, then the relationship between the melt resistivity ξ and conductor area $A = Wh$ is of the form:

$$R = \frac{\xi L}{A} = \frac{\xi L}{Wh}$$

Thus, the input power expressed in terms of melt resistivity is simply:

$$P = \frac{E^2}{R} = \frac{WhE^2}{\xi L}$$

Making note of the fact that the volume of the melt is given by $V = WhL$, then the power per unit volume is given as:

$$\frac{P}{V} = \frac{WhE^2}{\xi LV} = \frac{E^2}{\xi L^2}$$

For the tests, L is a constant. Furthermore, the DEH method does not appreciable heat material that has been quenched. Thus, from this expression one can see that operation in a constant voltage mode preserves the specific volumetric heating rate in the remaining melt if one operates in constant voltage. Furthermore, one should see a power decrease as the melt quenches, and the reduction in power should be directly proportional to the amount of material quenched. This assumes that the melt specific resistivity is constant, but in fact the resistivity increases as more concrete is brought into the melt, and as the melt temperature decreases. However, making online corrections for these two effects during the test is quite difficult, and so resistivity variations are neglected during the tests.

However, if we neglect the fact that decay heat in fuel debris dissipates with time, then the parameter that is actually preserved during core-concrete interaction is not the specific power

per unit volume but the specific power per unit mass of fuel. In particular, as concrete is brought into the melt, *P/V* actually decreases but *V* increases, and so *PV* equals a constant that is determined from the reactor power rating and the amount of fuel that has relocated to the reactor cavity. The actual fuel content in the core-concrete mixture is $m_f = \rho\chi_f V$, where ρ is the melt density and χ_f is the mass fraction of fuel in the melt. Thus, the specific power density expressed in terms of the fuel power density can be written as:

$$\frac{P}{m_f} = \frac{E^2}{\rho\chi_f \xi L^2}$$

As the core-concrete interaction proceeds, melt density and the weight fraction of fuel in the melt actually decrease, and so these two trends offset to some extent the increase in melt resistance with increasing concrete content. However, the extent that these two trends offset each other has not been quantified at this time.

APPENDIX C
Test Data

This Appendix provides plots of all data recorded during Test CCI-6. The complete channel assignment list is provided in Appendix A. Time t = 0 in all plots is referenced to the time at which melt made initial contact with the concrete basemat. This corresponds to 6.64 minutes after onset of data acquisition; see Table 3-1. All data was logged at ~ 5.5 second time intervals during the test. Selected channels have been averaged to improve readability.

Preliminary data analysis revealed anomalous signal behavior from the thermocouples and cold junction compensation sensors associated with the Basemat measurement hardware. The problem is illustrated in Figure C-1, which shows the measurements from the cold junction compensators (diodes sensors) in the 'Basemat' and 'Quench' system Hoffman boxes to which thermocouples were wired. Due to steam discharge into the cell, the temperatures in these boxes should have increased over the course of the test, and this was indeed the trend exhibited by the compensators that were in the Quench system boxes. However, in the Basemat boxes the compensators exhibited temperature dips from 14 to 118 minutes during the experiment. No anomalous behavior was observed for instruments wired to the 'Quench' and 'Power' systems.

Post test examination of the Basemat junction box showed that it had remained dry. A closer examination of the data revealed that the thermocouple signals dropped along with the cold junction sensors, though the drop is less pronounced. The evidence points to a likely steam intrusion into the A/D converter, the associated relay bank, or the connector. None of these components are as well protected as the junction boxes because continuous air flow is required for cooling of the A/D converter. It appears that the steam intrusion allowed a small amount of current shunting, which depressed instrument signals. Recovery of the signals later in the test suggests that the steam eventually evaporated to allow the measurement system to return to normal operation.

To partially remedy the situation, the raw signals from these thermocouples were compensated for ambient temperature by using the Quench system cold junction compensators; see Figure C-1. This approach is motivated by the logic that although there is a problem with the measurement of raw thermocouple voltages, this does not oblige us to compound the error by adding on a faulty cold junction reading. Through additional examination of the data, the apparent temperature dip in the readings for units in which this behavior was observed was at most 30ºC. Thus, the maximum positive error limit was set at + 30ºC for both Type C and Type K junctions that were wired into the Basemat boxes, which can be compared with the usual limits of +1.0 % and +0.75 %, respectively, for these two thermocouple types. The lower error limits were kept at the usual limits (i.e., -1.0 % and -0.75 % for Type C and Type K thermocouples, respectively), since the effect of the shunting was to bias the thermocouple readings in the direction of an apparent temperature reduction.

In any event, all thermocouples in the Basemat wiring boxes were located in the concrete that underwent core-concrete interaction during the test. As a result, the temperature range of interest is at or above 1000ºC for these units, and in this temperature range a bias of 30ºC has little if any bearing on the interpretation of the test results.

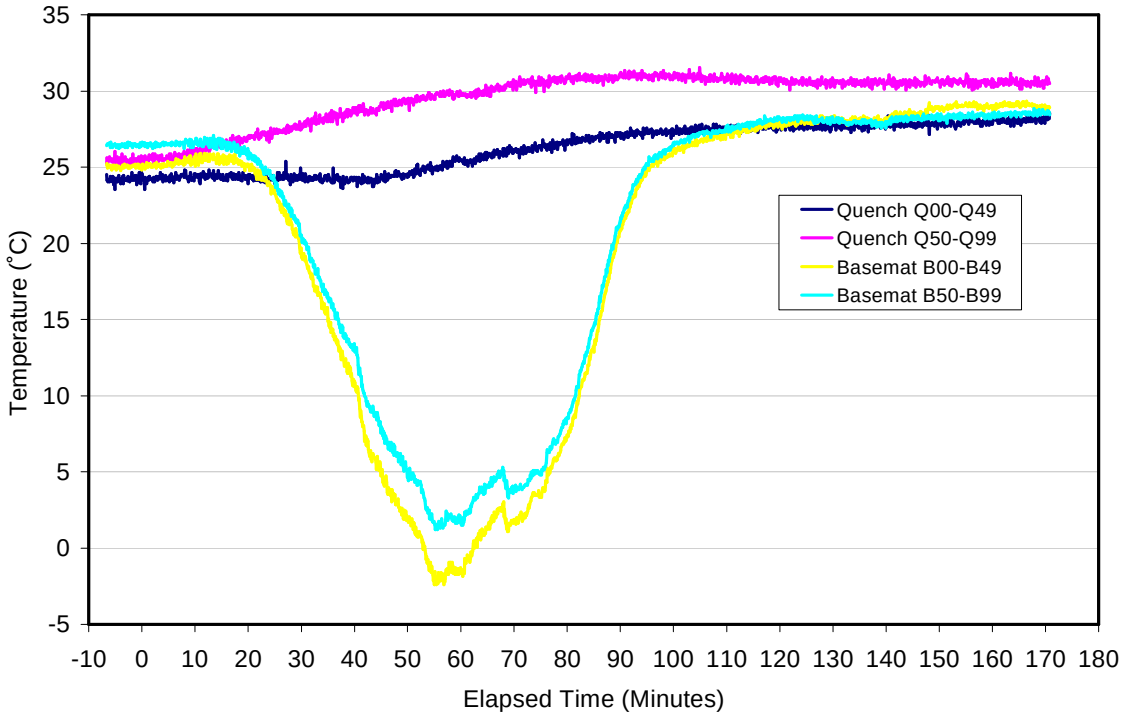

Figure C-1. Cold Junction Compensators for Basemat and Quench System Wiring.

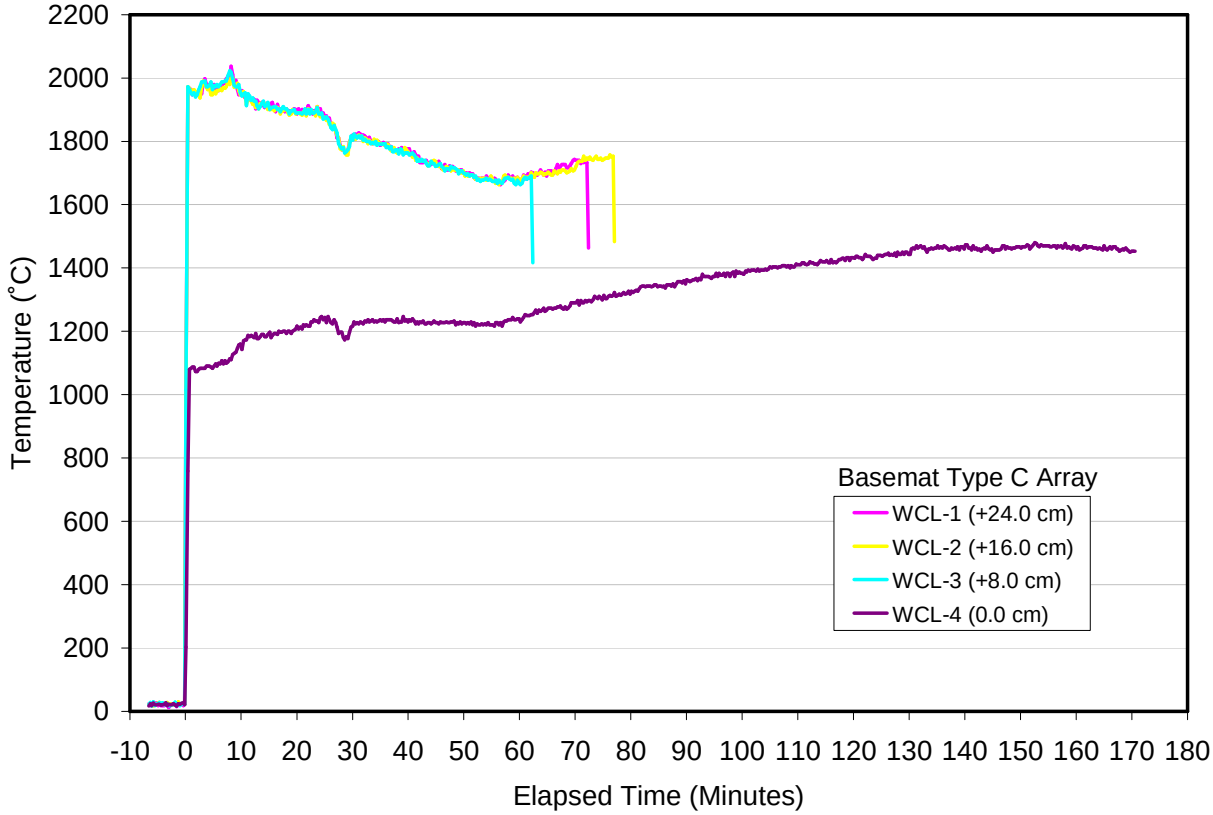

Figure C-2. Basemat Type C 'WCL' Thermocouple Array.

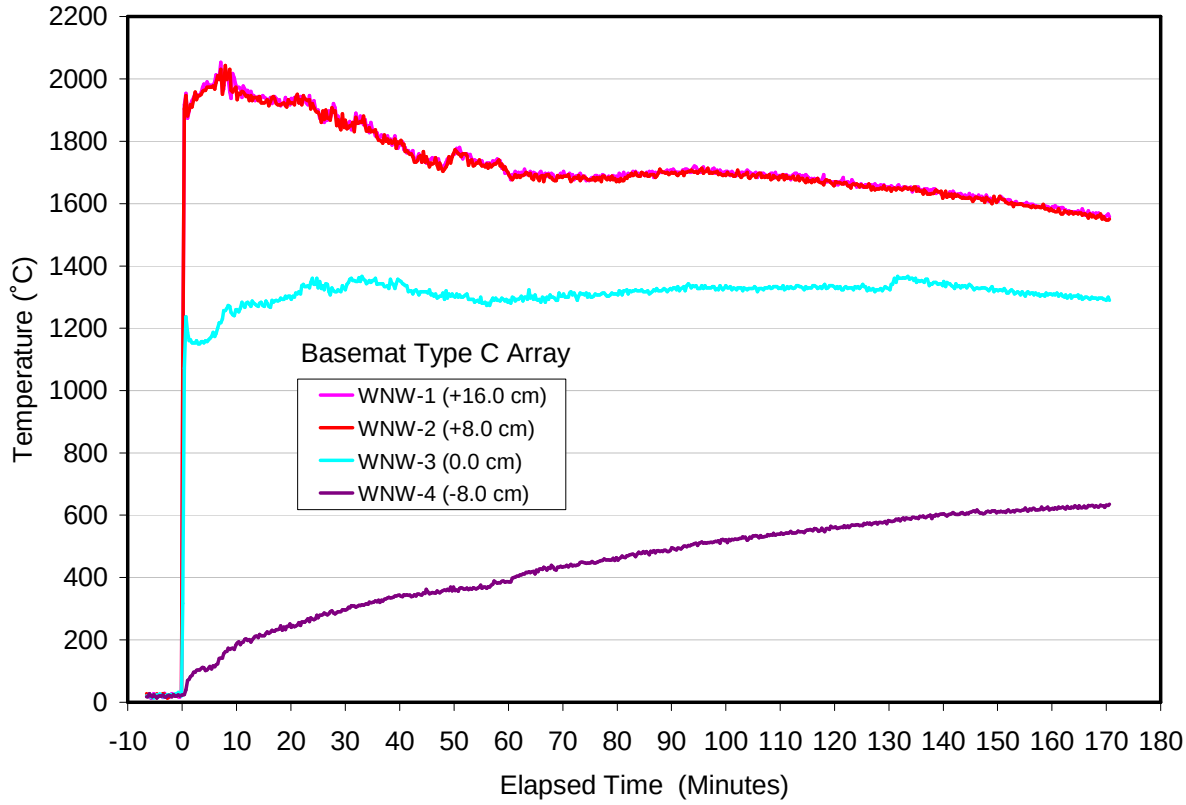

Figure C-3. Basemat Type C 'WNW' Thermocouple Array.

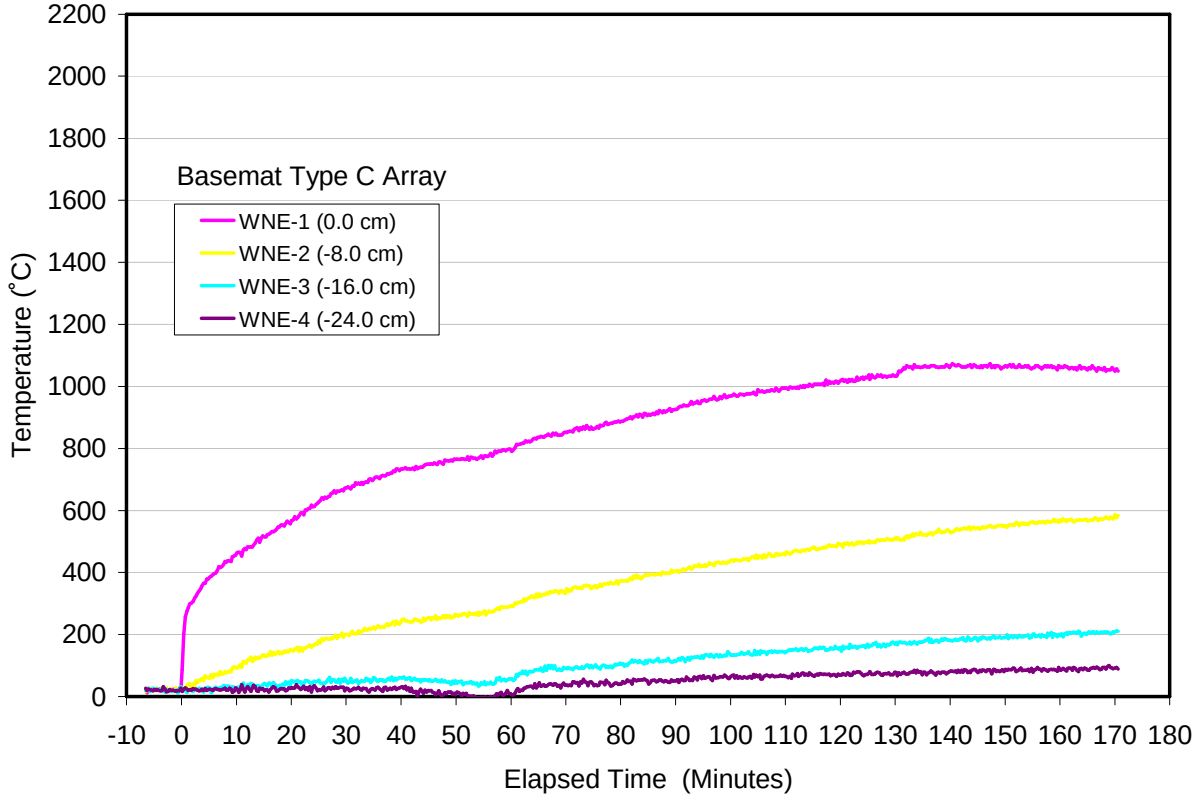

Figure C-4. Basemat Type C 'WNE' Thermocouple Array.

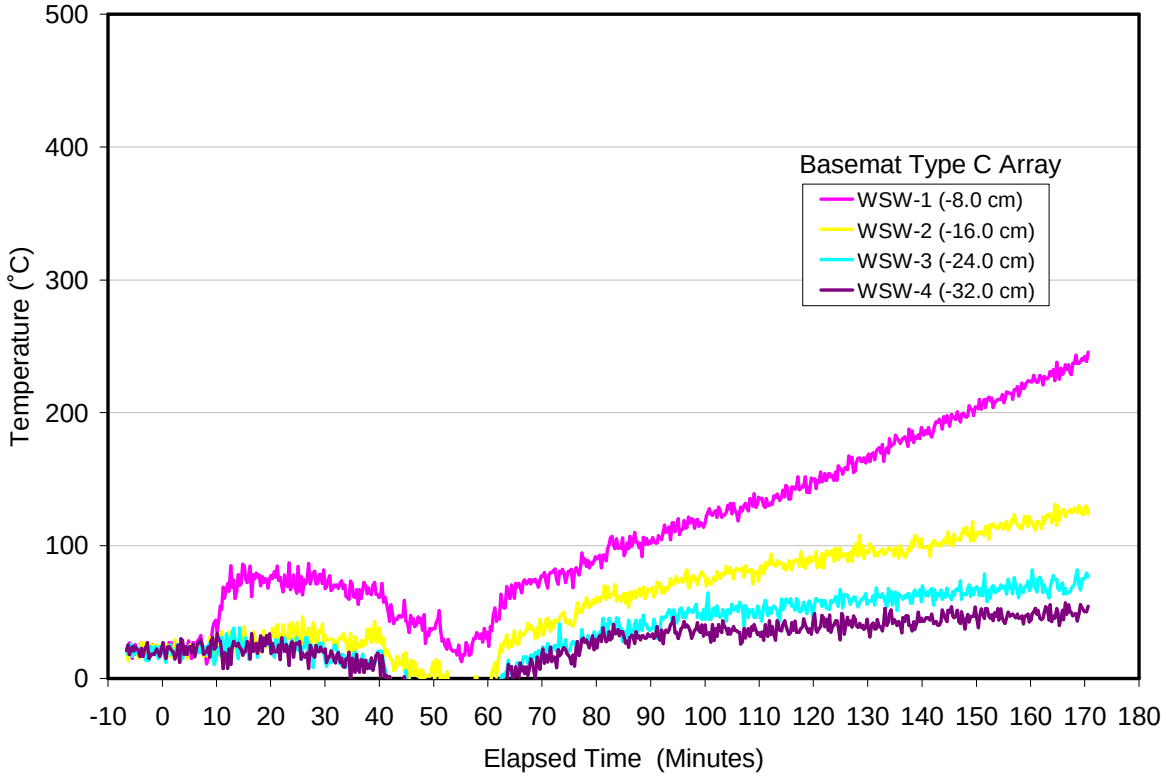

Figure C-5. Basemat Type C 'WSW' Thermocouple Array.

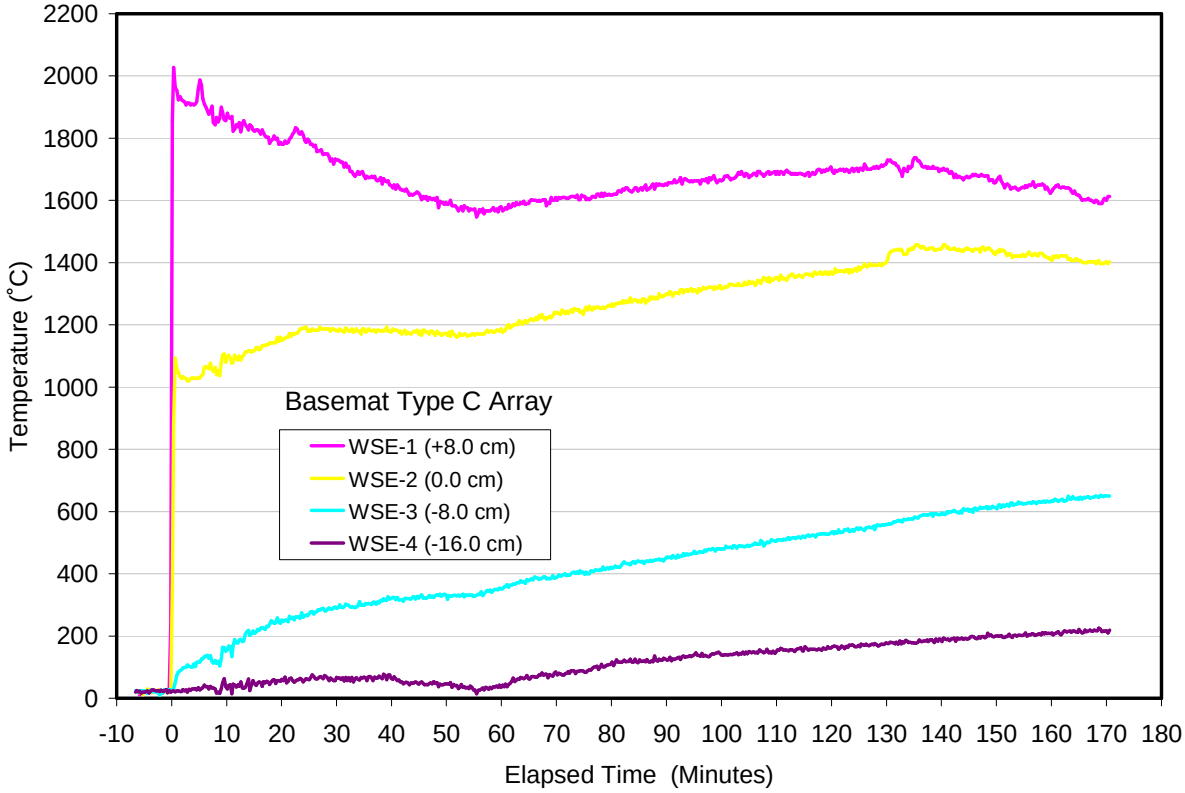

Figure C-6. Basemat Type C 'WSW' Thermocouple Array.

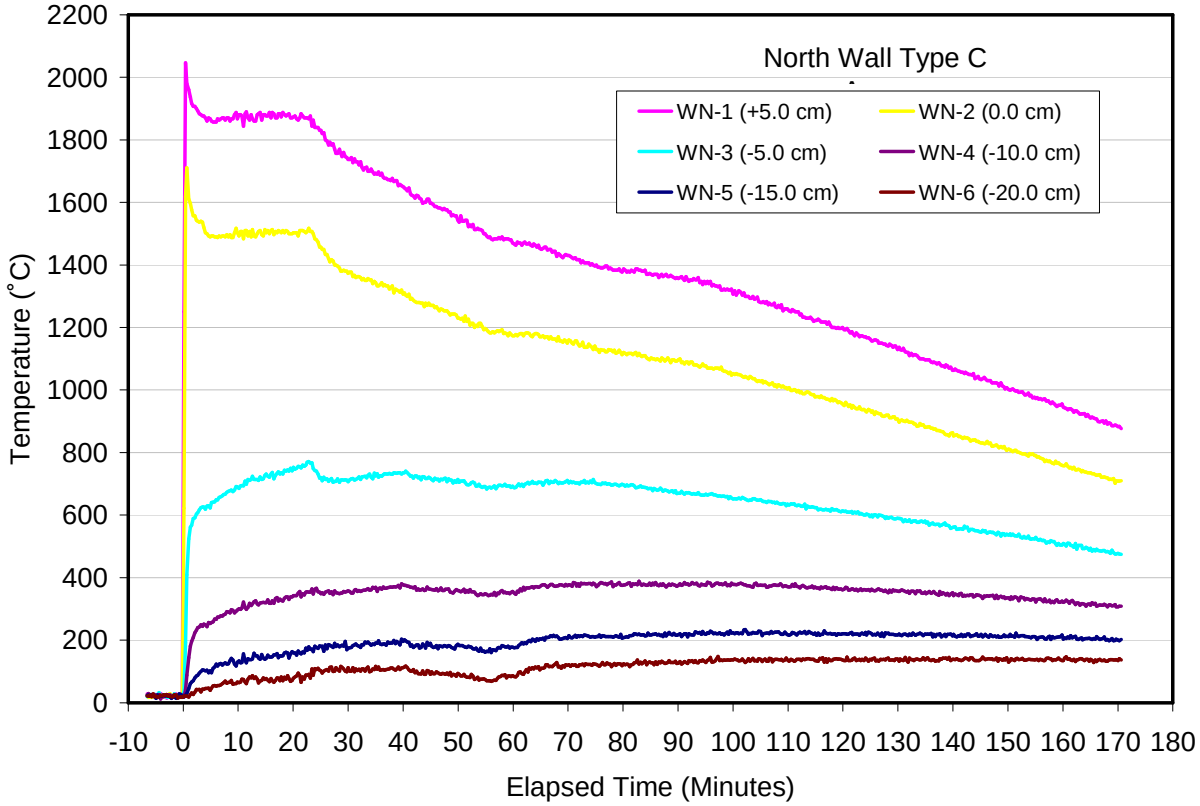

Figure C-7. North Sidewall Type C 'WN' Thermocouple Array.

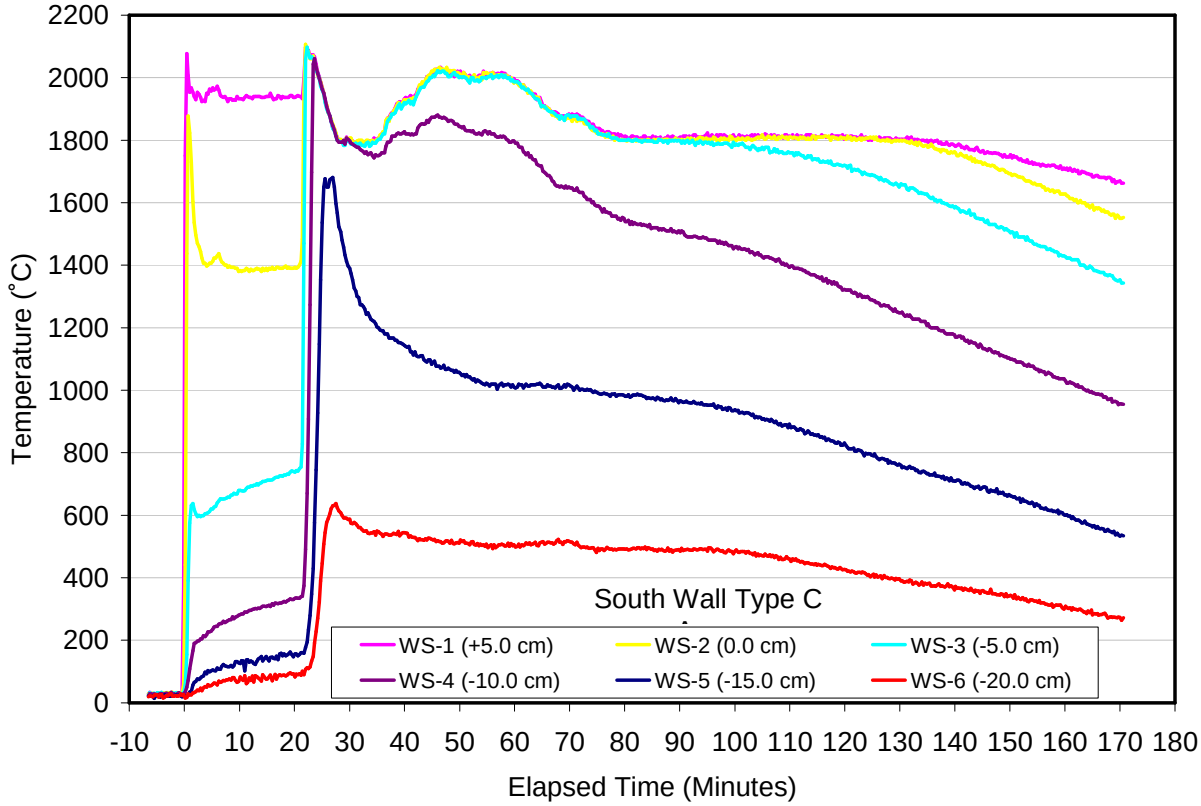

Figure C-8. South Sidewall Type C 'WS' Thermocouple Array.

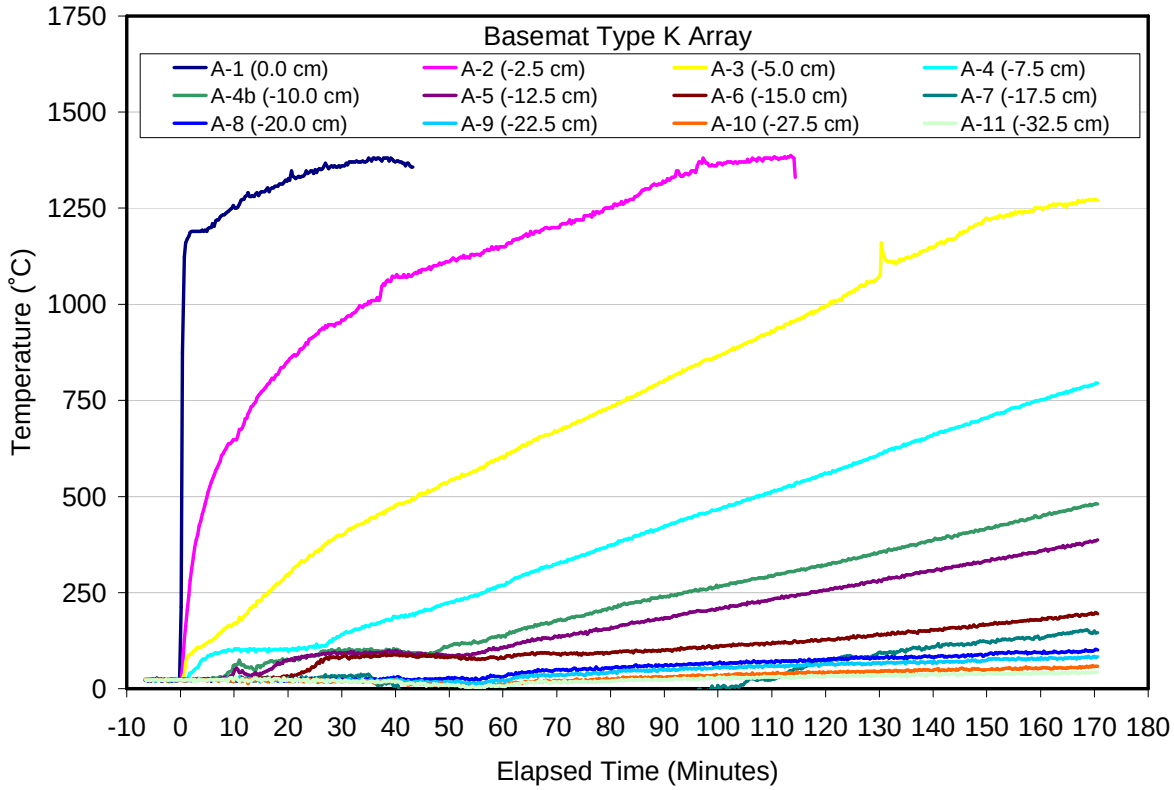

Figure C-9. Basemat Centerline Type K 'A' Thermocouple Array.

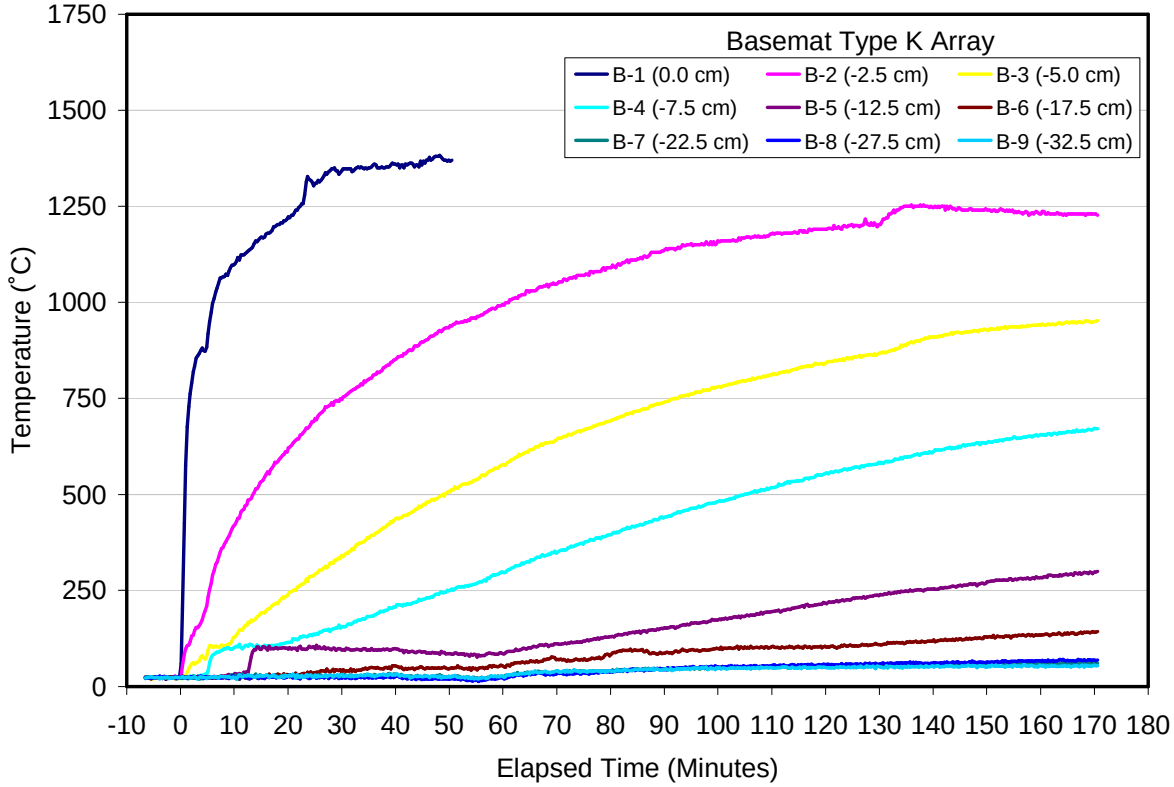

Figure C-10. Basemat Centerline Type K 'B' Thermocouple Array.

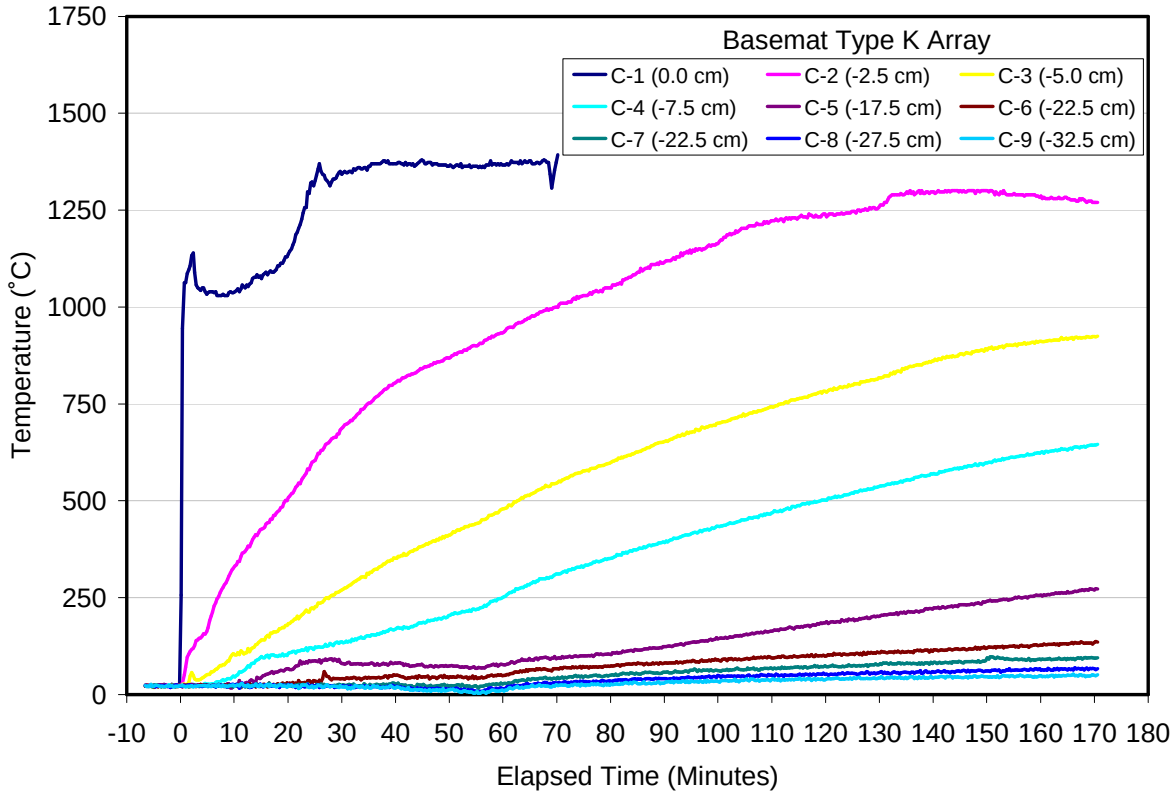

Figure C-11. Basemat Centerline Type K 'C' Thermocouple Array.

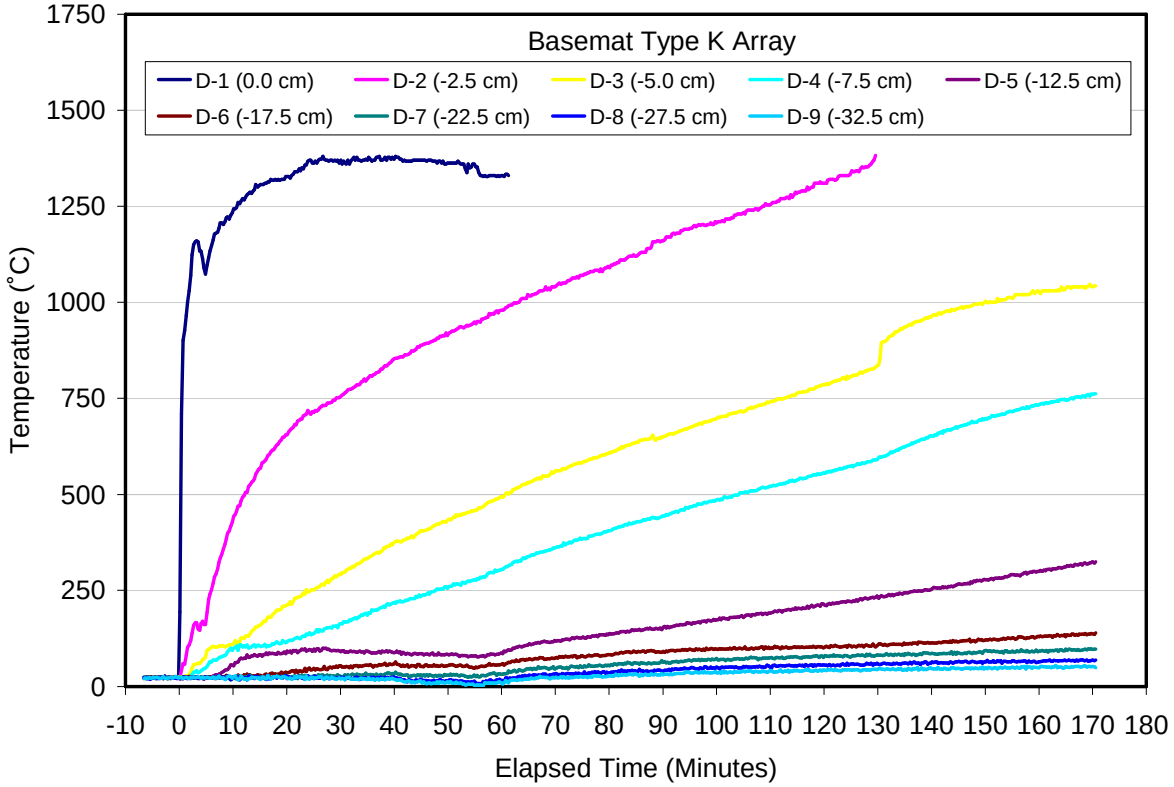

Figure C-12. Basemat Centerline Type K 'D' Thermocouple Array.

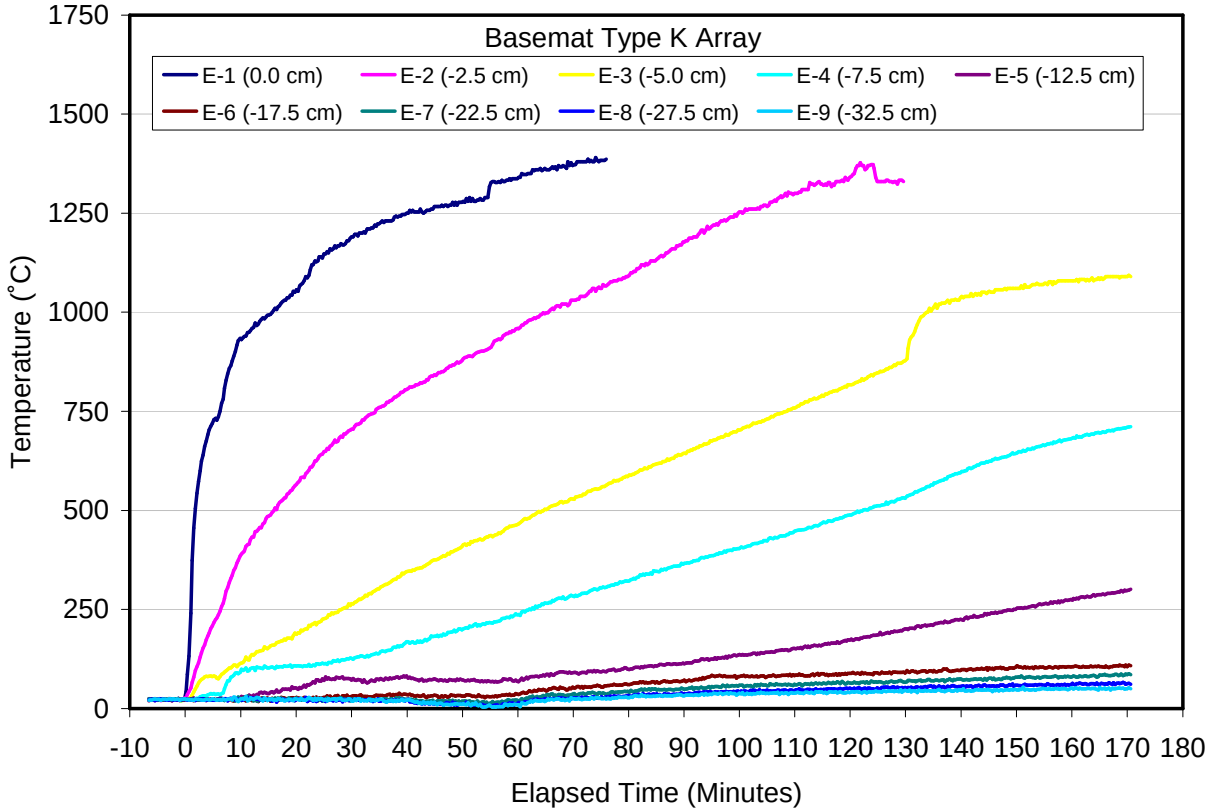

Figure C-13. Basemat Centerline Type K 'E' Thermocouple Array.

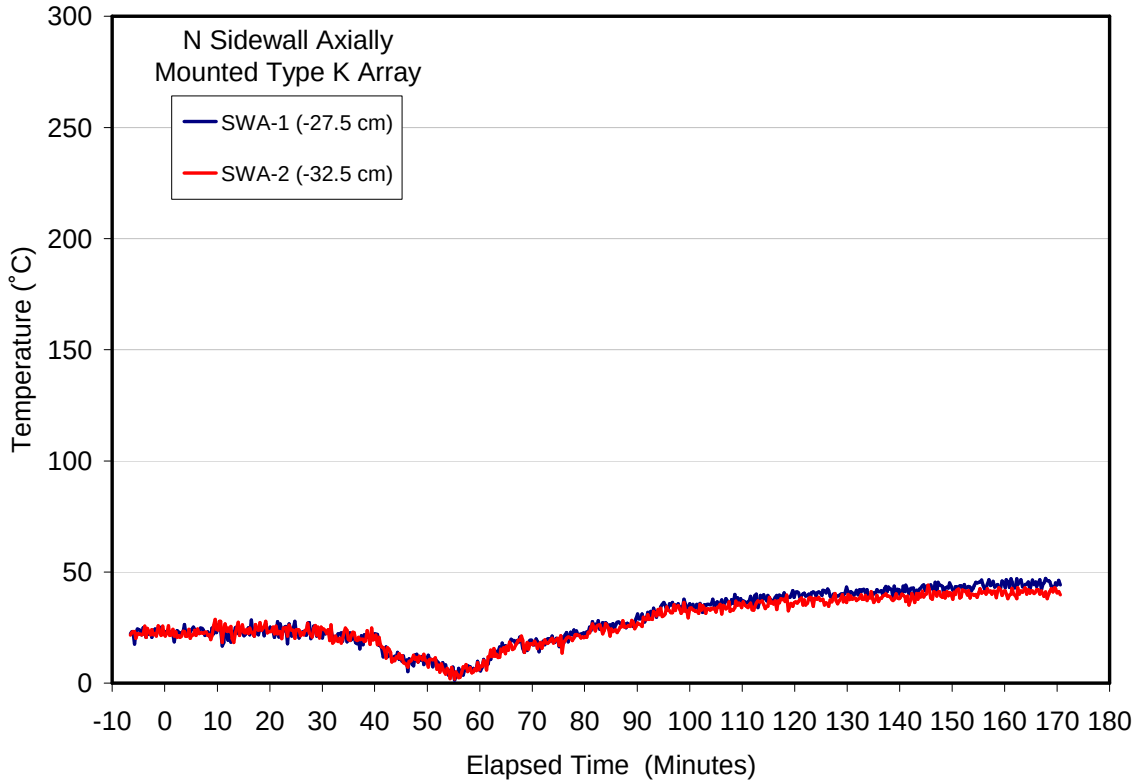

Figure C-14. North Sidewall Axially Mounted Type K 'SWA' Thermocouple Array.

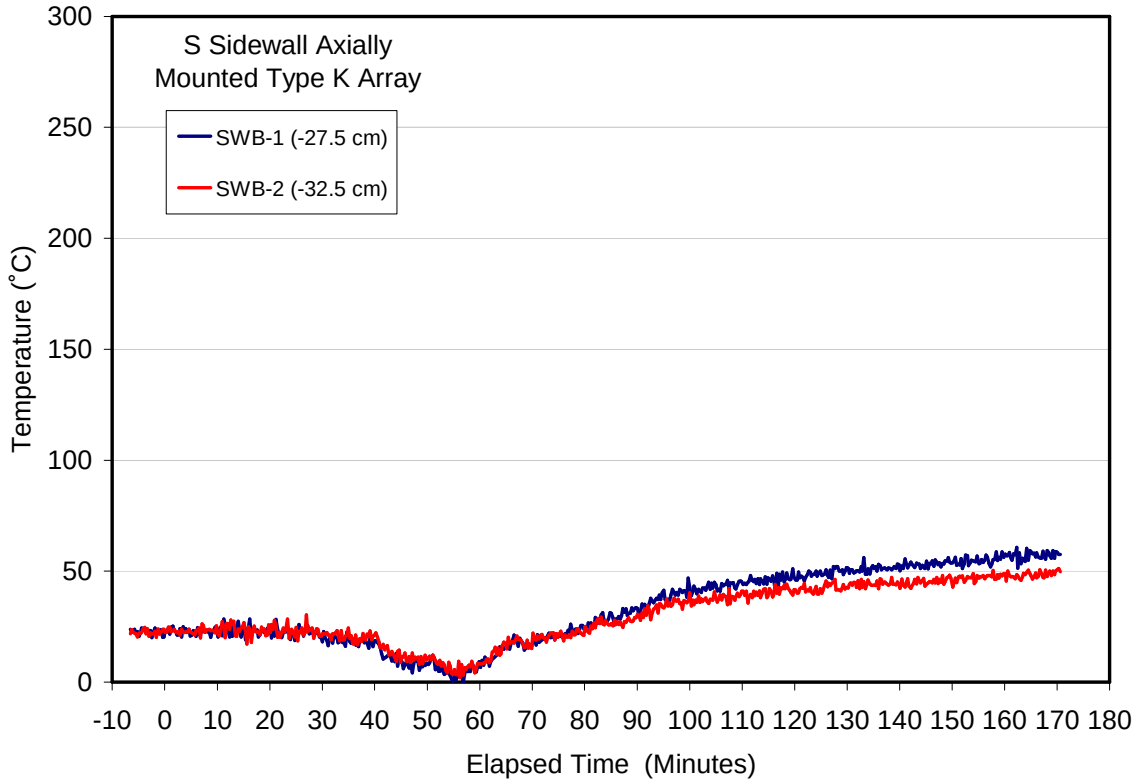

Figure C-15. South Sidewall Axially Mounted Type K 'SWB' Thermocouple Array.

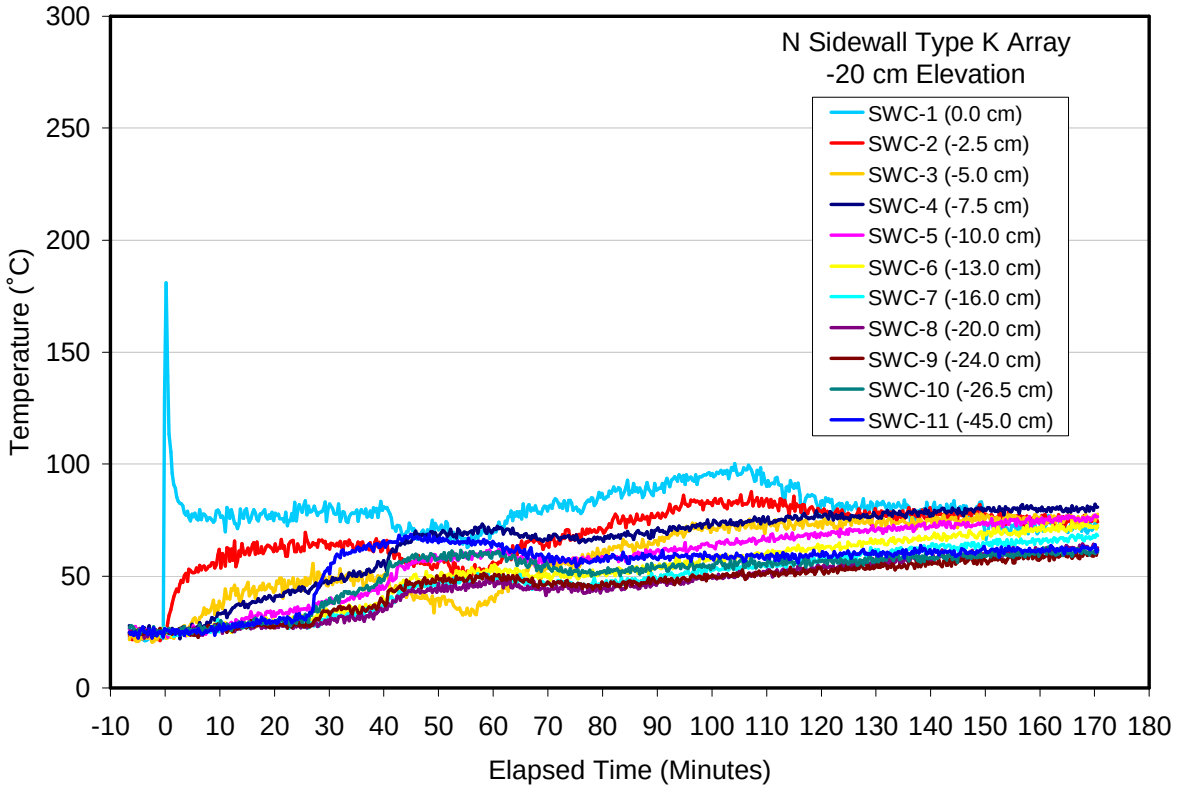

Figure C-16. North Sidewall Type K 'SWC' Thermocouple Array.

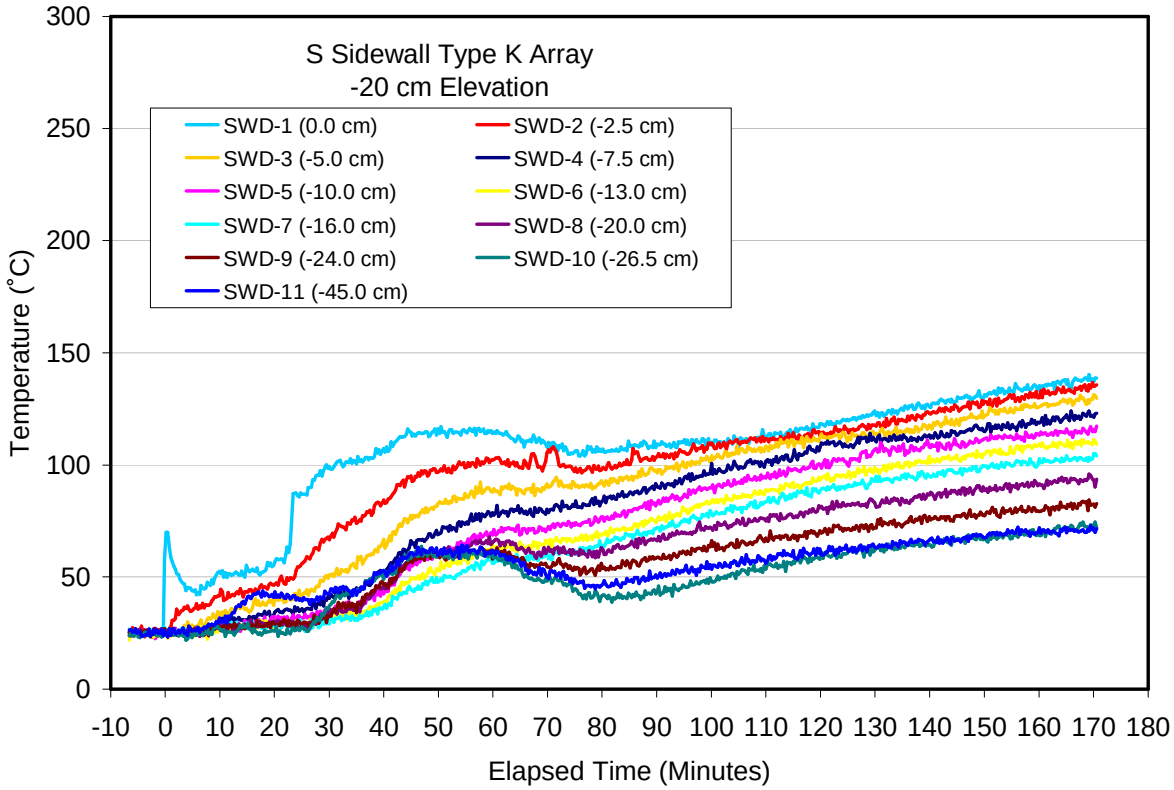

Figure C-17. South Sidewall Type K 'SWD' Thermocouple Array.

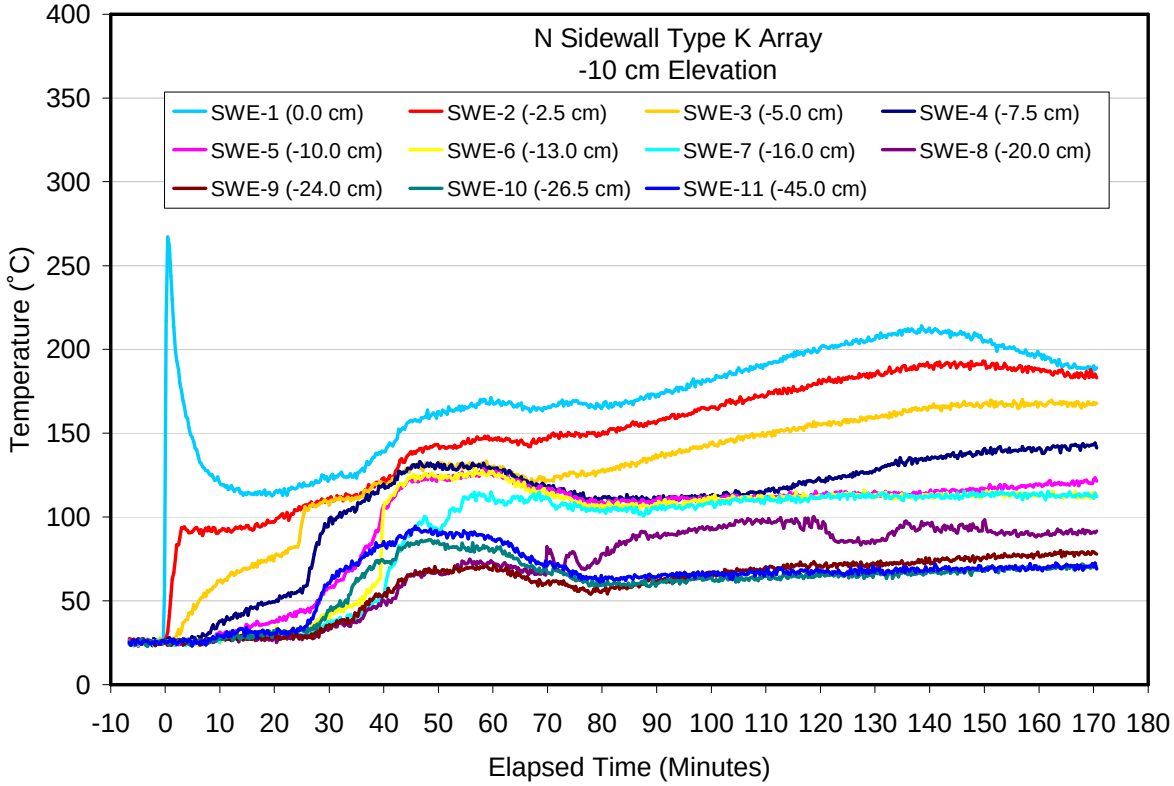

Figure C-18. North Sidewall Type K 'SWE' Thermocouple Array.

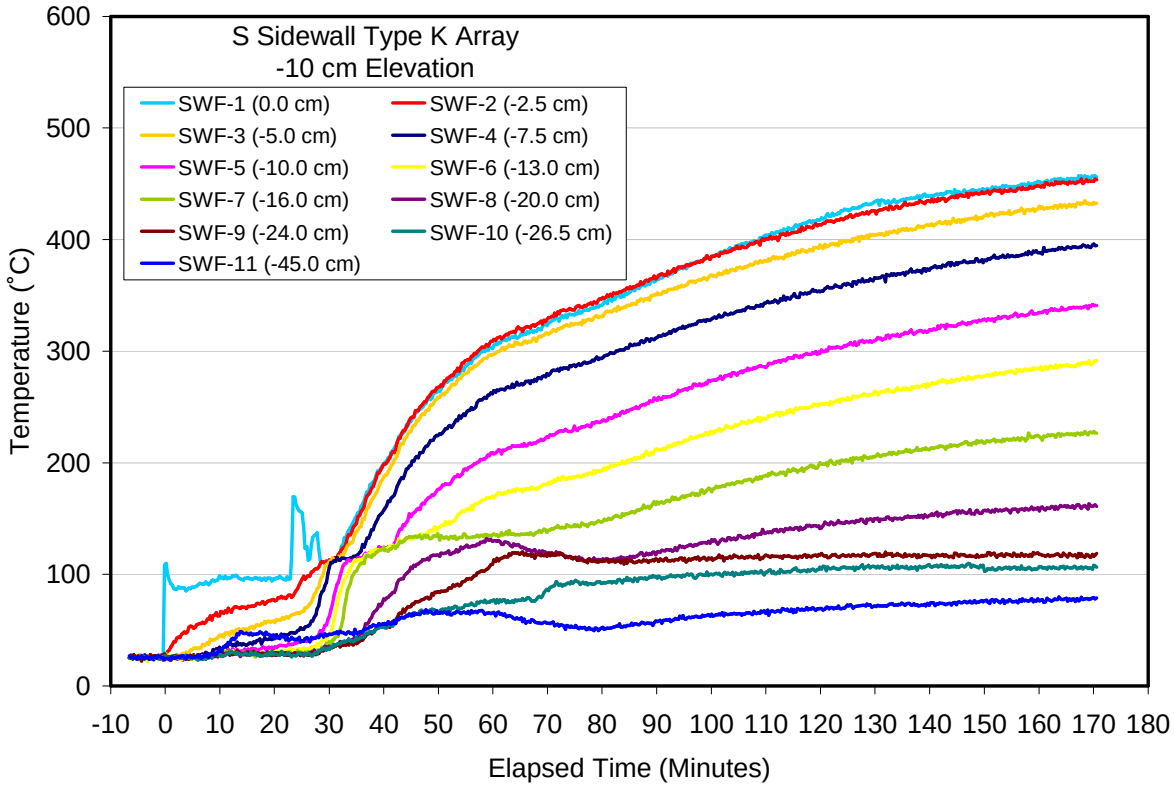

Figure C-19. South Sidewall Type K 'SWF' Thermocouple Array.

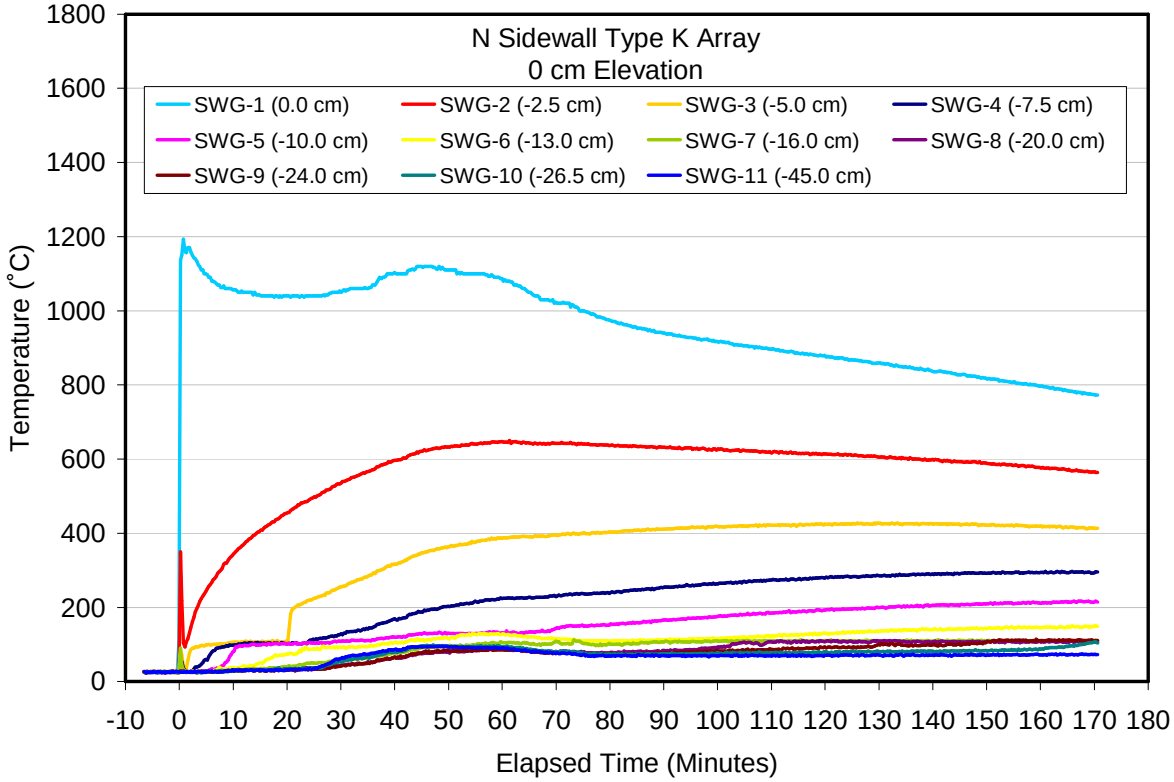

Figure C-20. North Sidewall Type K 'SWG' Thermocouple Array.

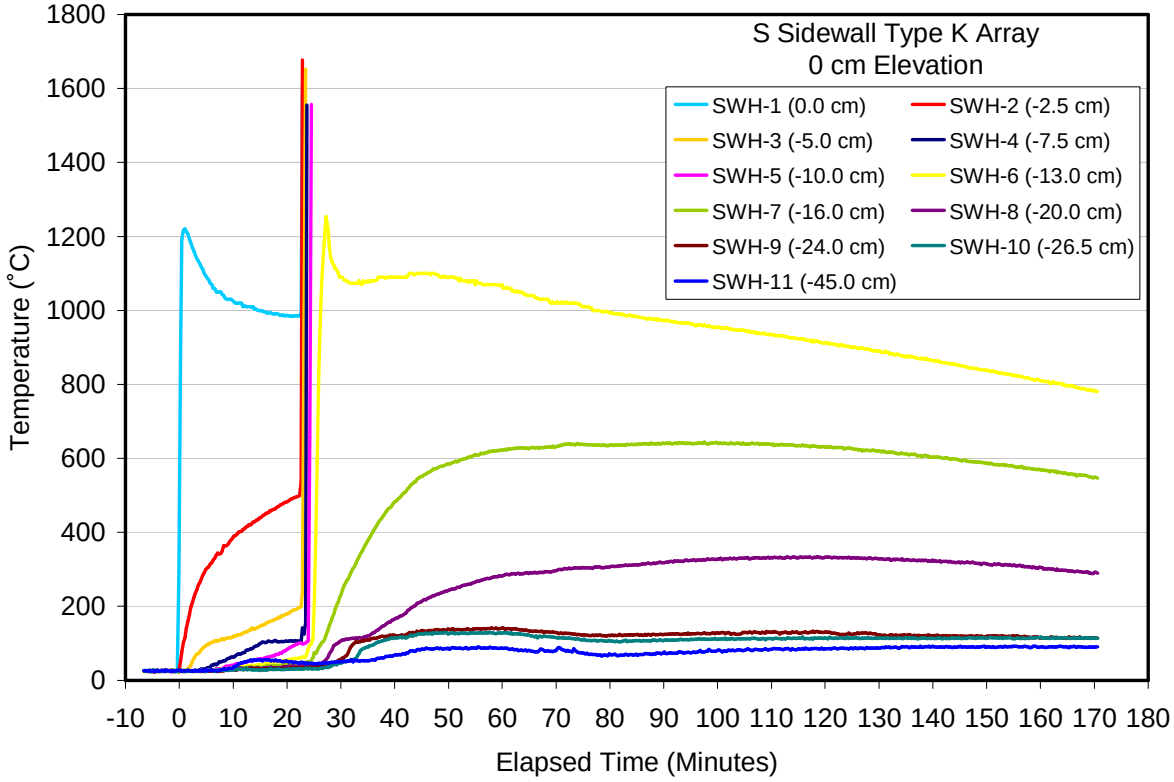

Figure C-21. South Sidewall Type K 'SWH' Thermocouple Array.

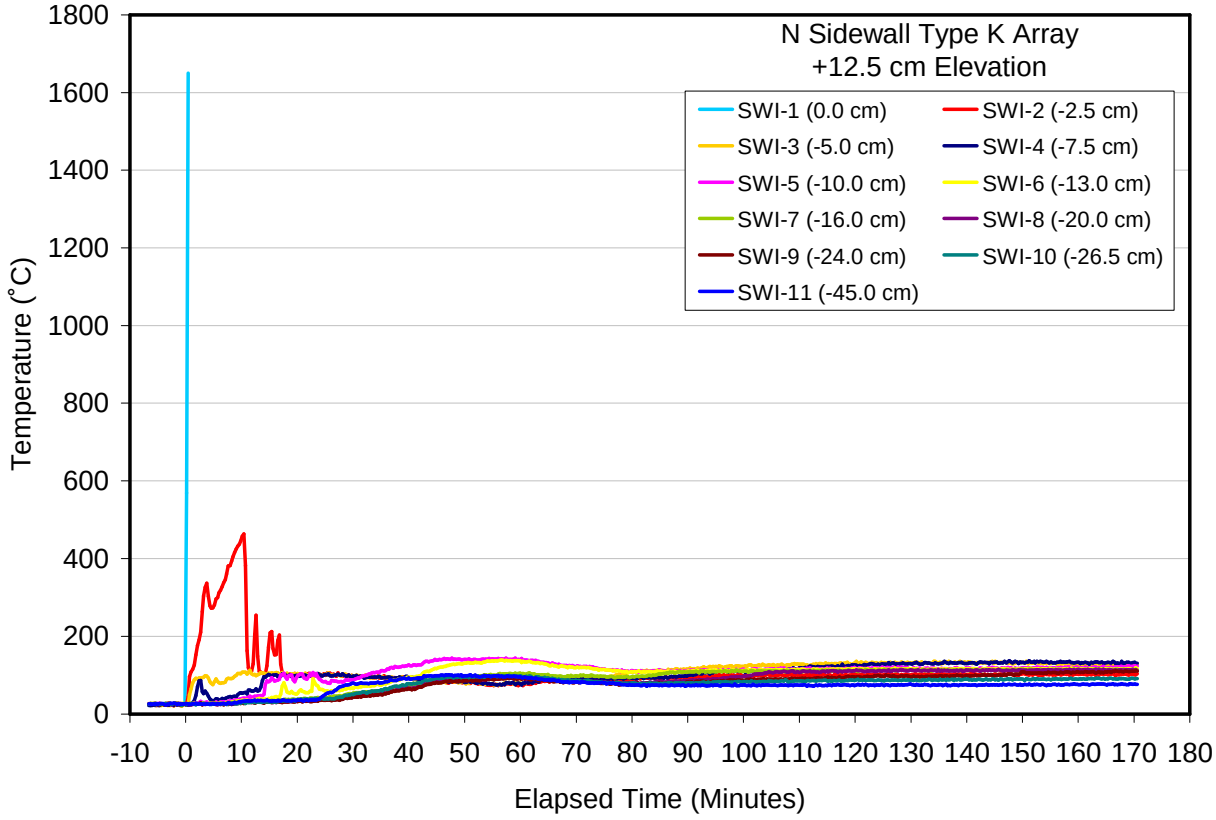

Figure C-22. North Sidewall Type K 'SWI' Thermocouple Array.

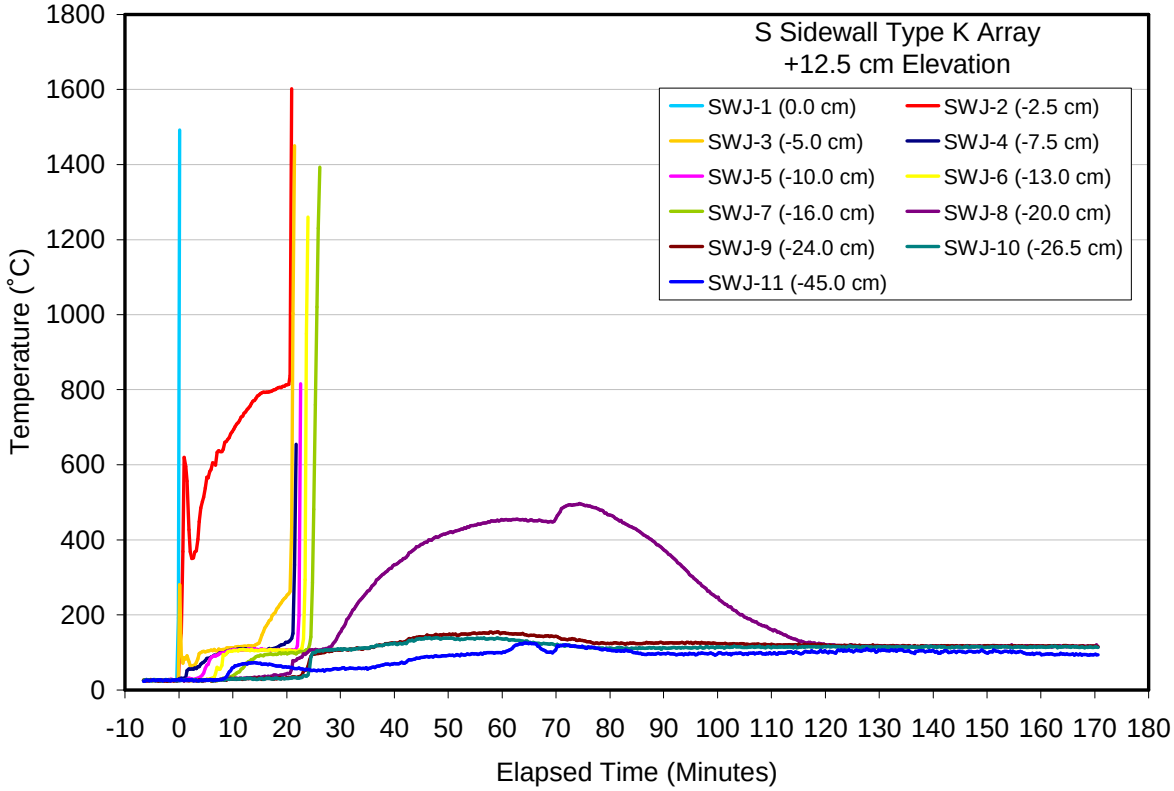

Figure C-23. South Sidewall Type K 'SWJ' Thermocouple Array.

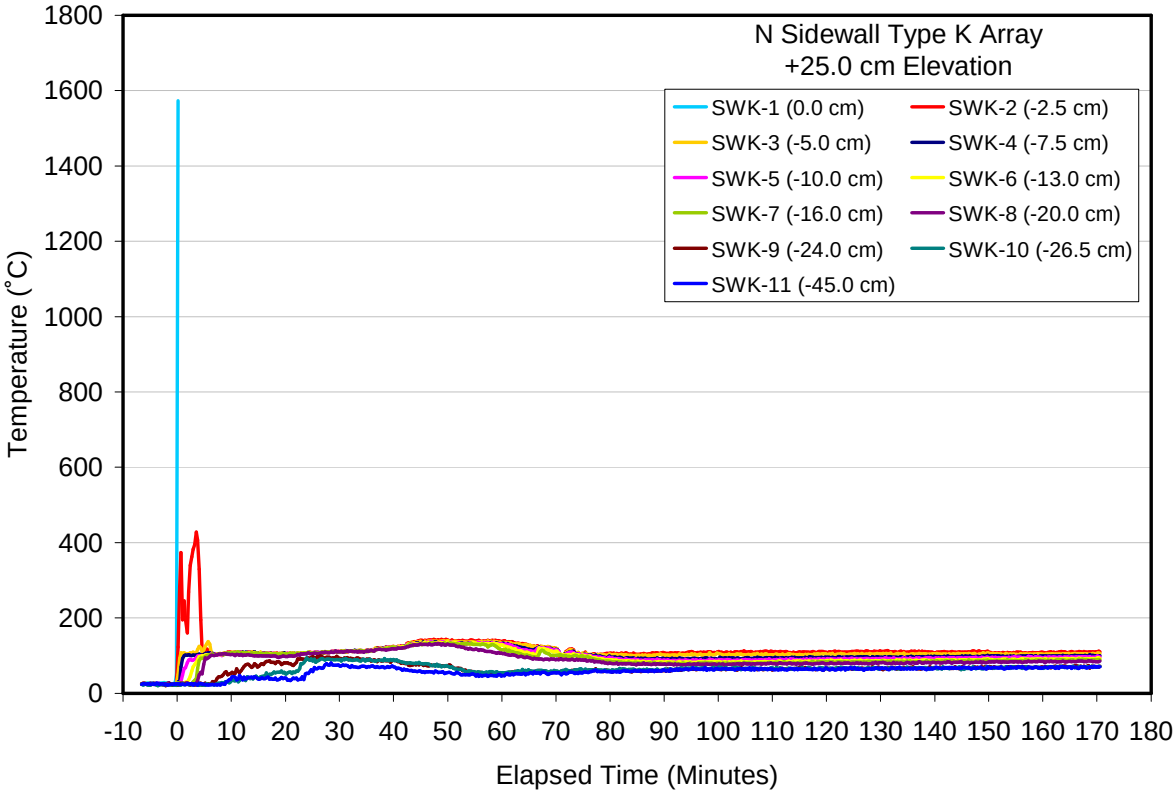

Figure C-24. North Sidewall Type K 'SWK' Thermocouple Array.

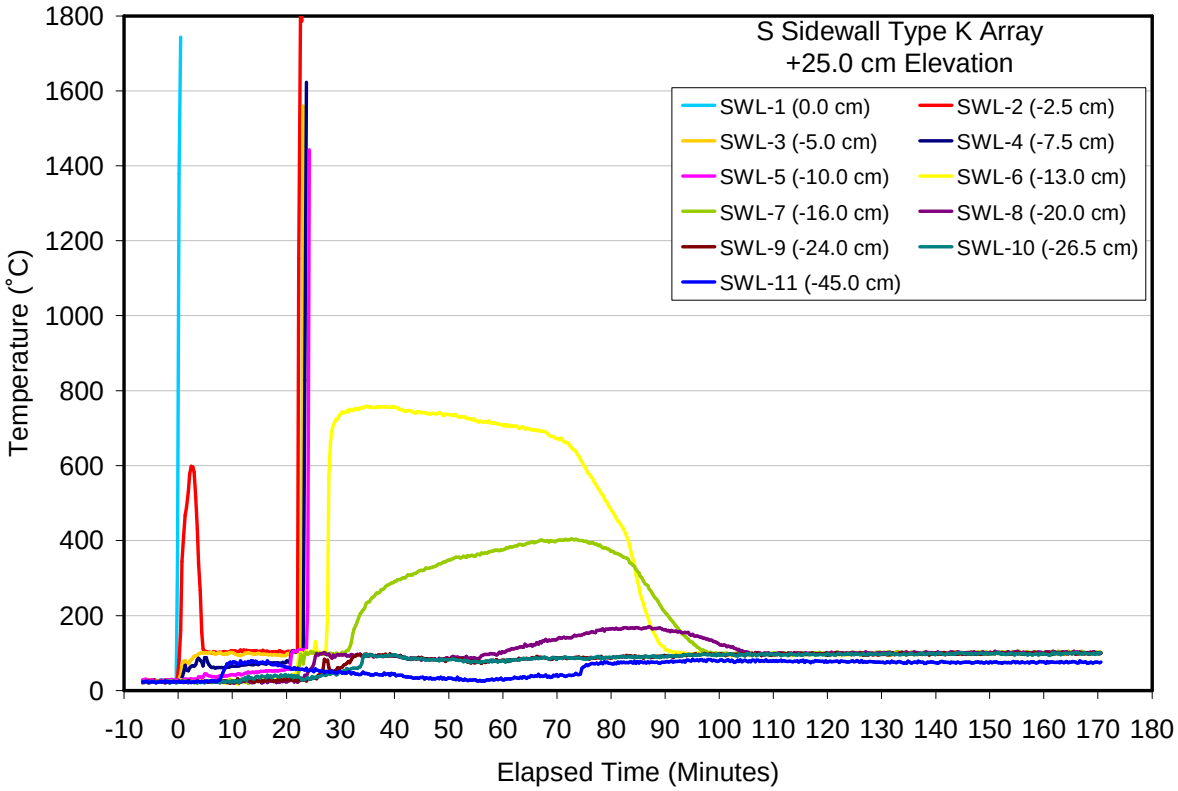

Figure C-25. South Sidewall Type K 'SWL' Thermocouple Array.

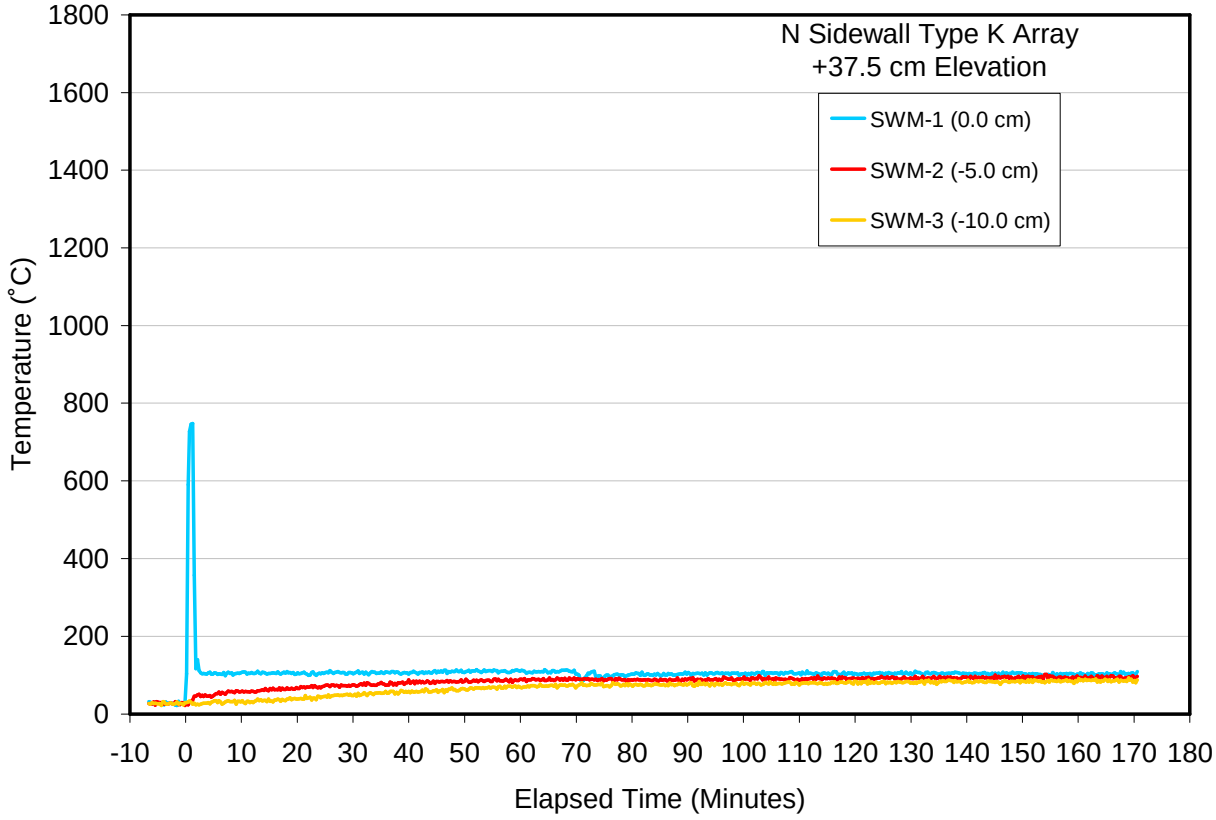

Figure C-26. North Sidewall Type K 'SWM' Thermocouple Array.

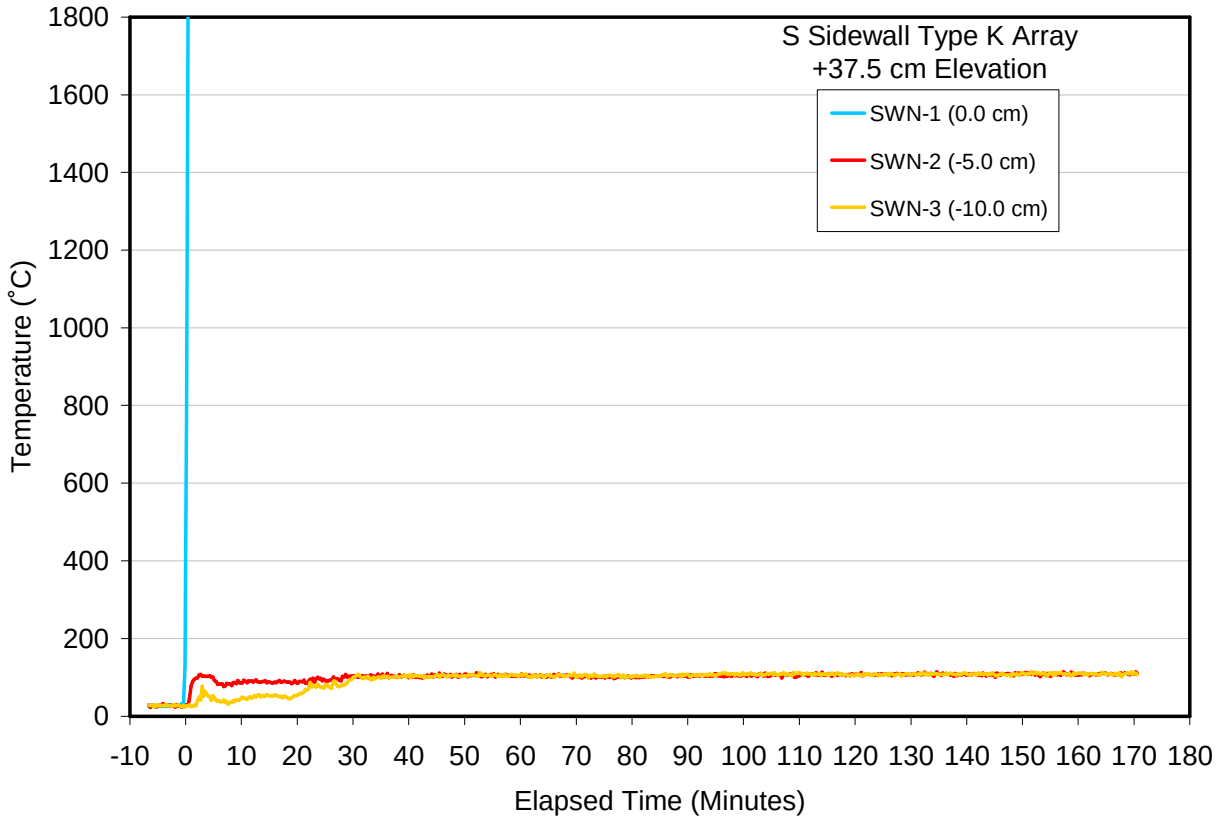

Figure C-27. South Sidewall Type K 'SWN' Thermocouple Array.

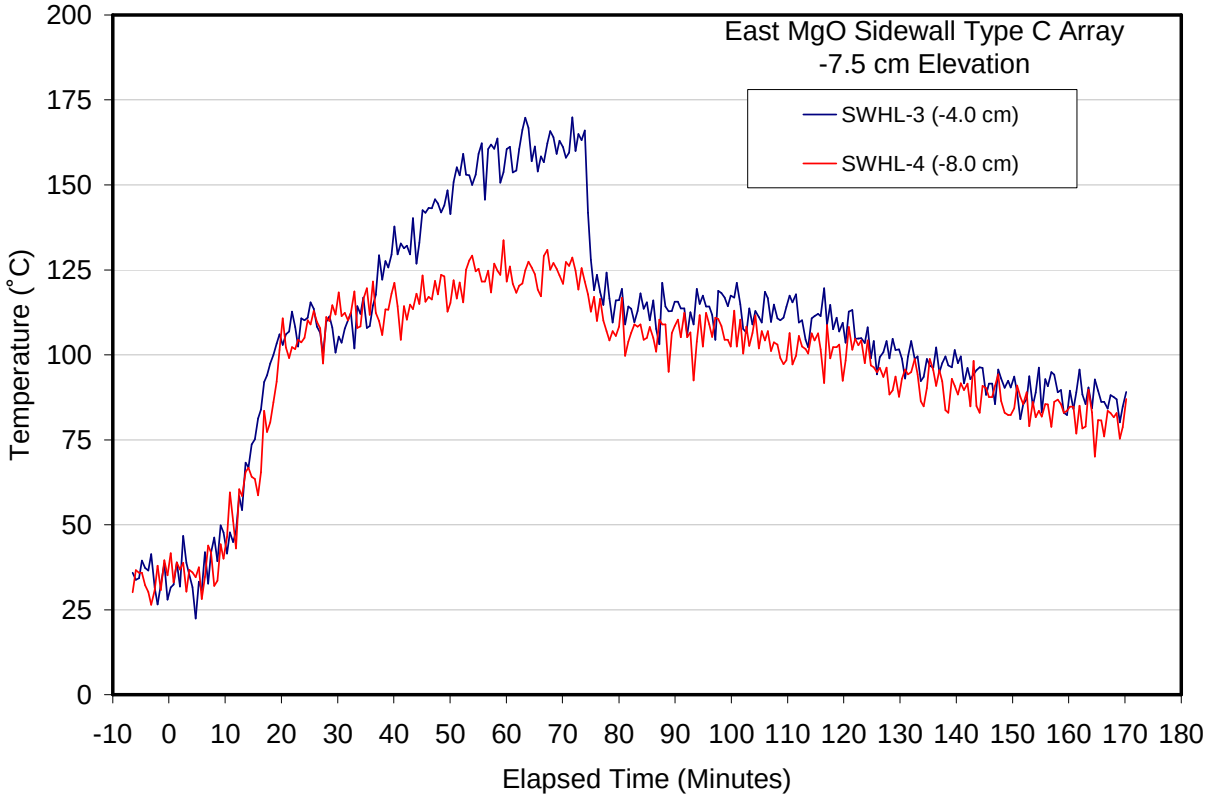

Figure C-28. East MgO Sidewall Type C 'SWHL' Thermocouple Array.

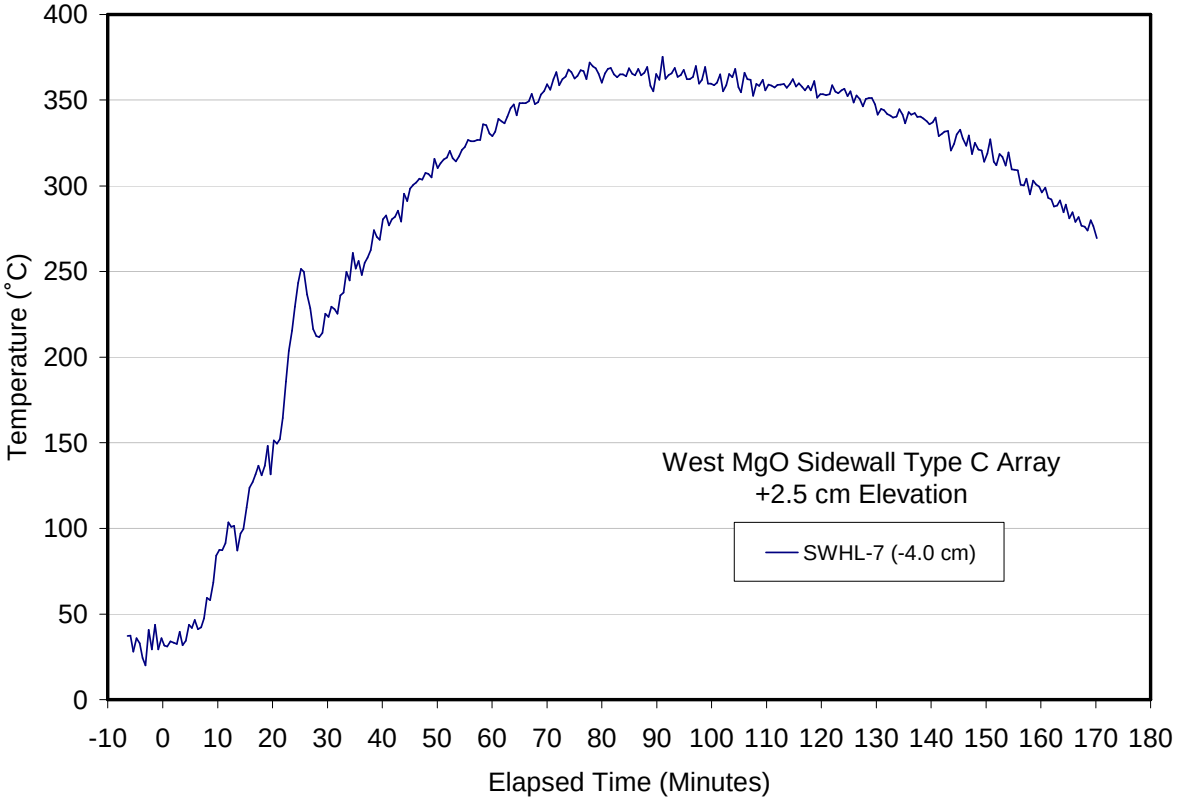

Figure C-29. West MgO Sidewall Type C 'SWHL' Thermocouple (1/2).

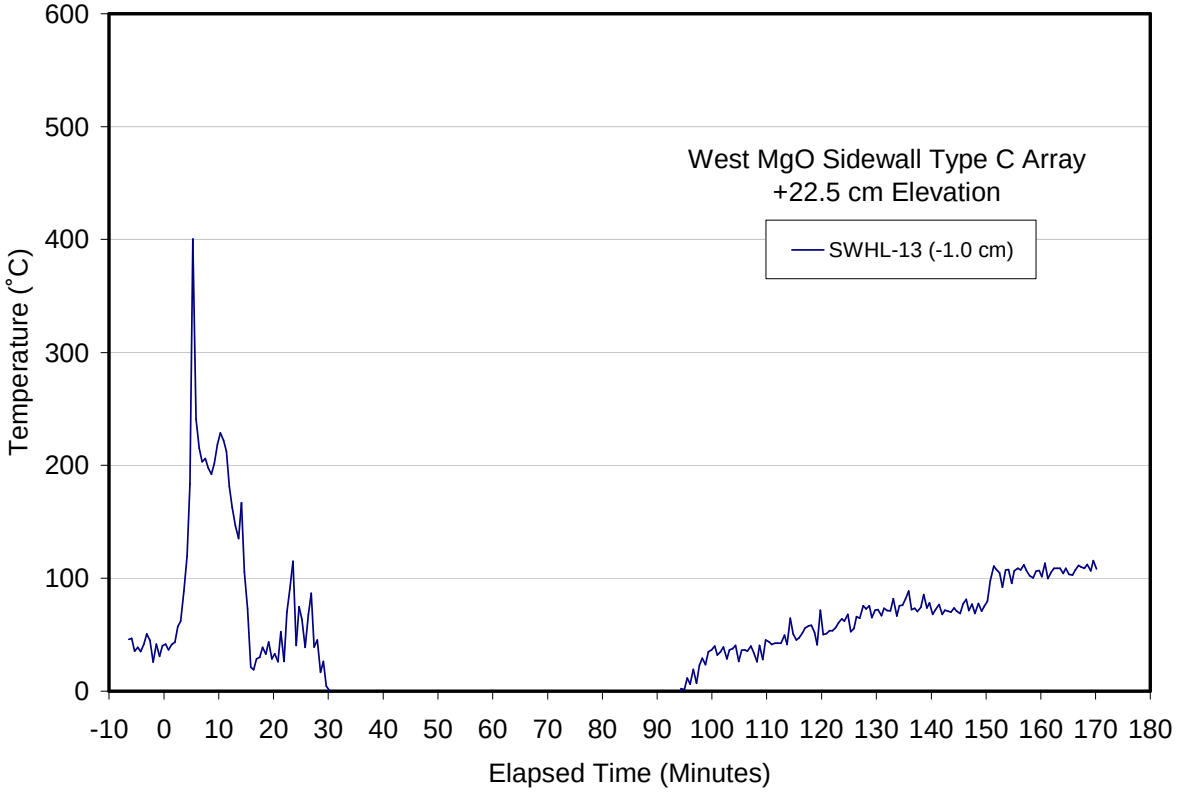

Figure C-30. West MgO Sidewall Type C 'SWHL' Thermocouple (2/2).

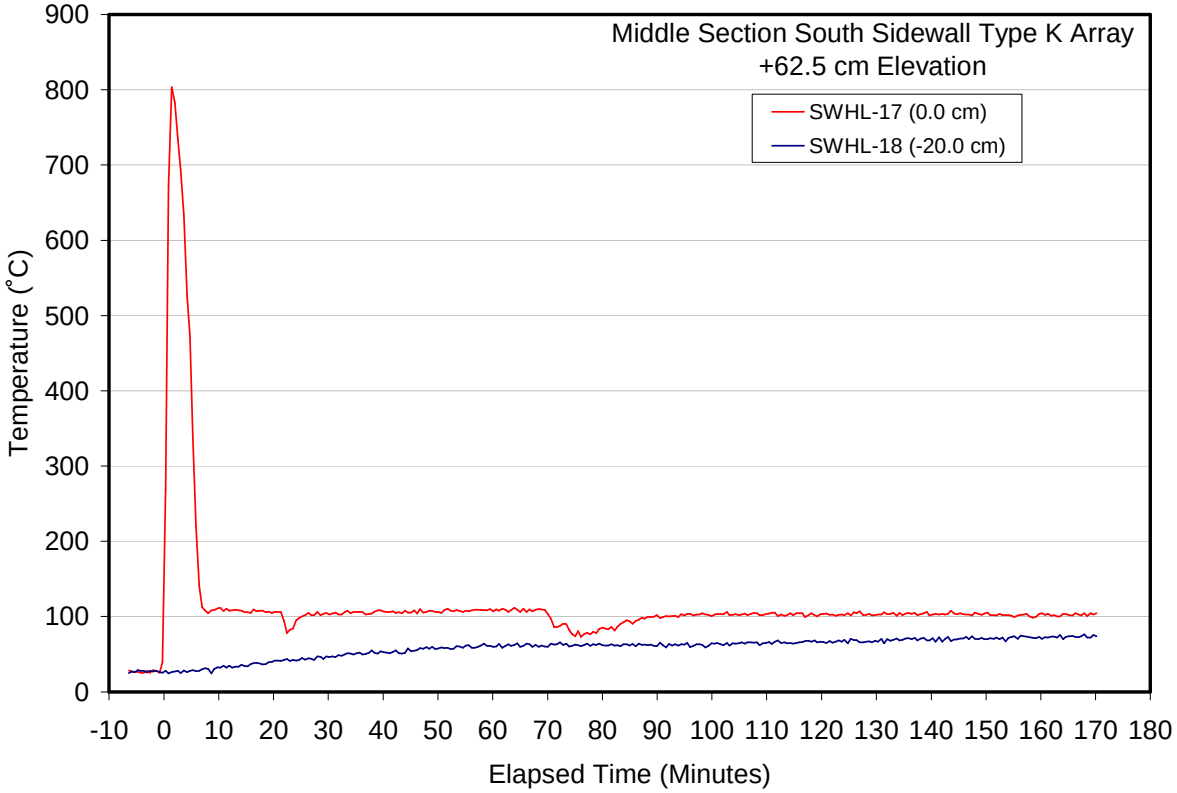

Figure C-31. Middle Section South Wall Type K 'SWHL' Thermocouple Array (1/2).

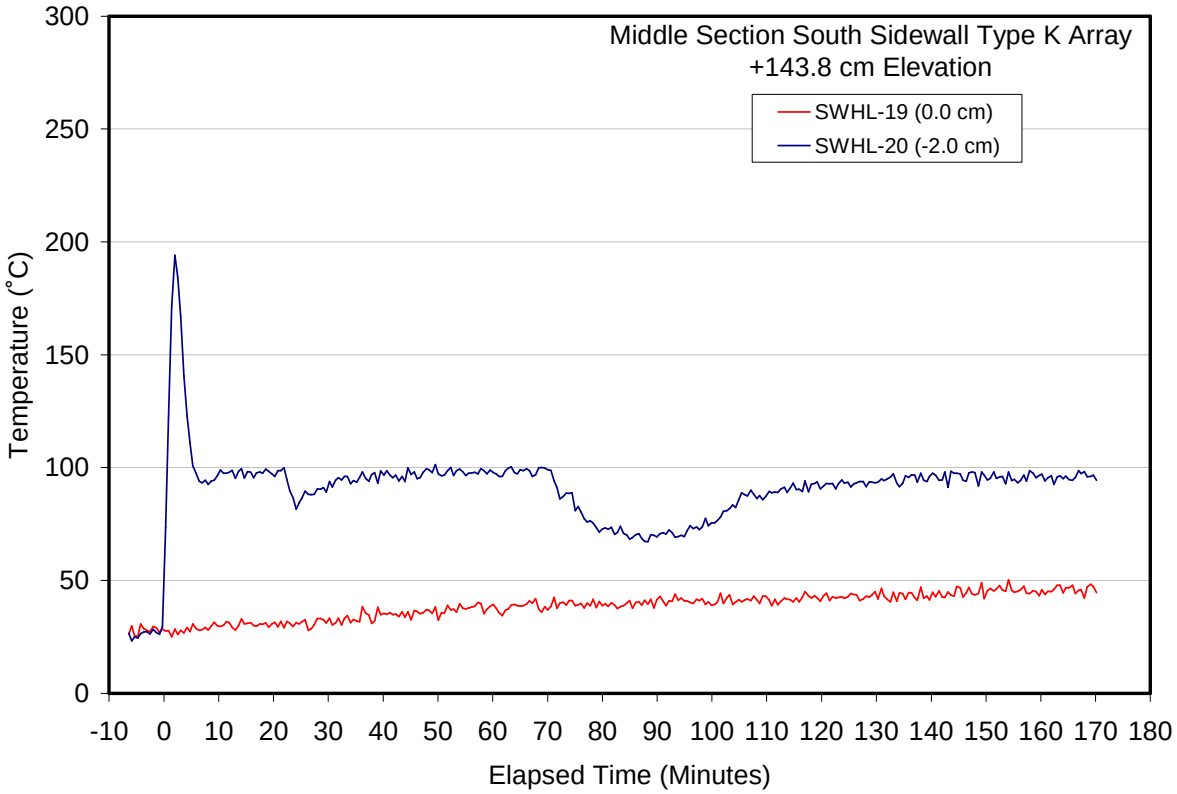

Figure C-32. Middle Section South Wall Type K 'SWHL' Thermocouple Array (2/2).

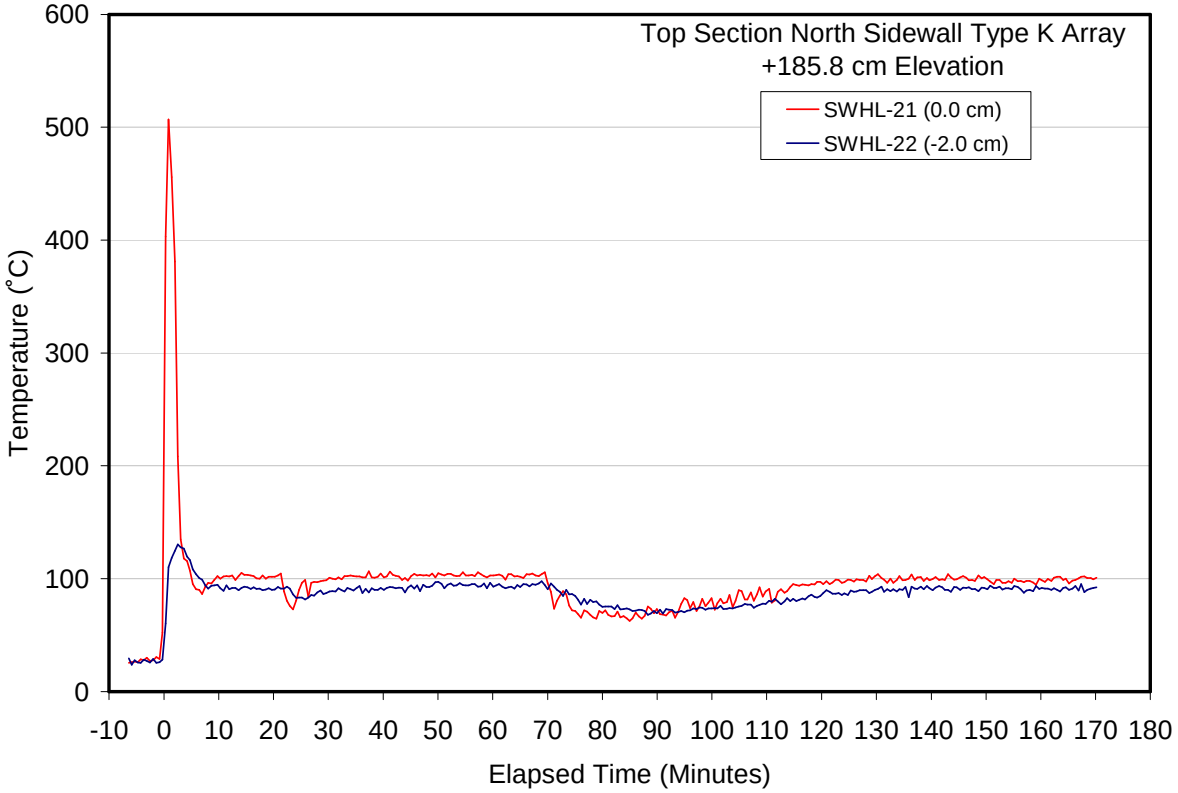

Figure C-33. Top Section North Wall Type K 'SWHL' Thermocouple Array.

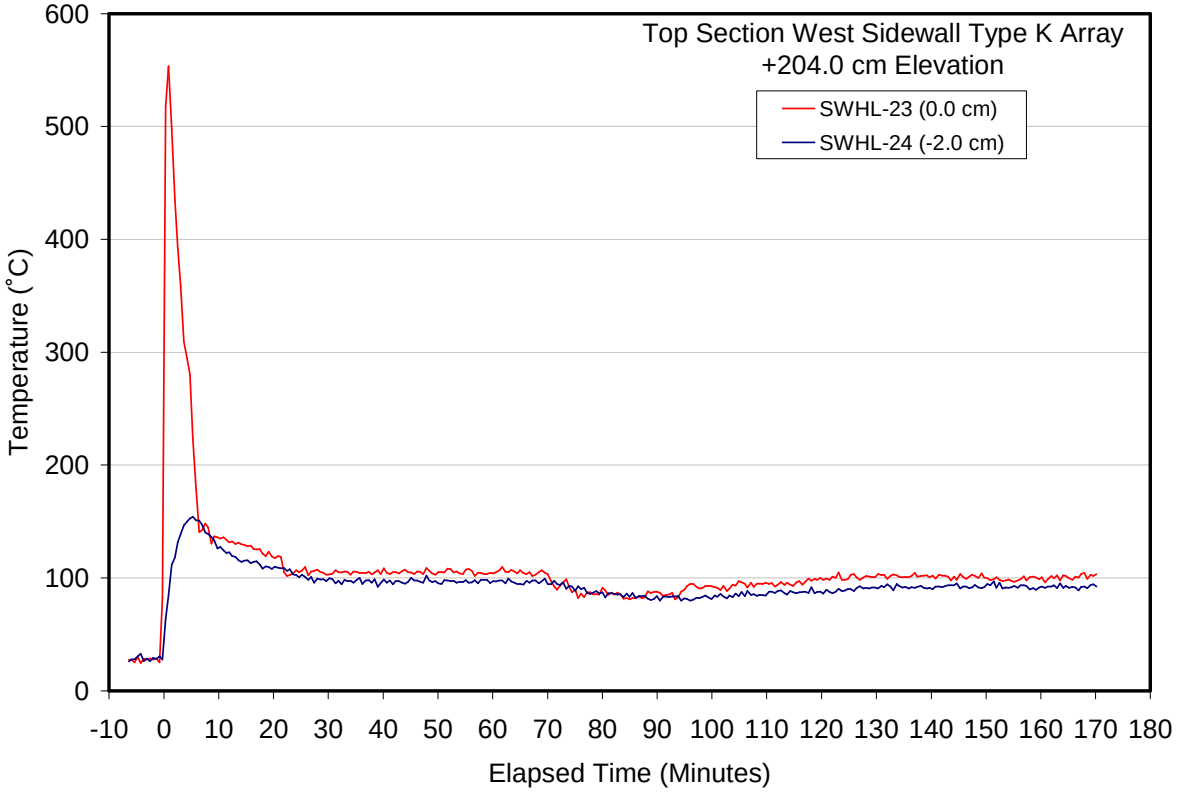

Figure C-34. Top Section West Wall Type K 'SWHL' Thermocouple Array.

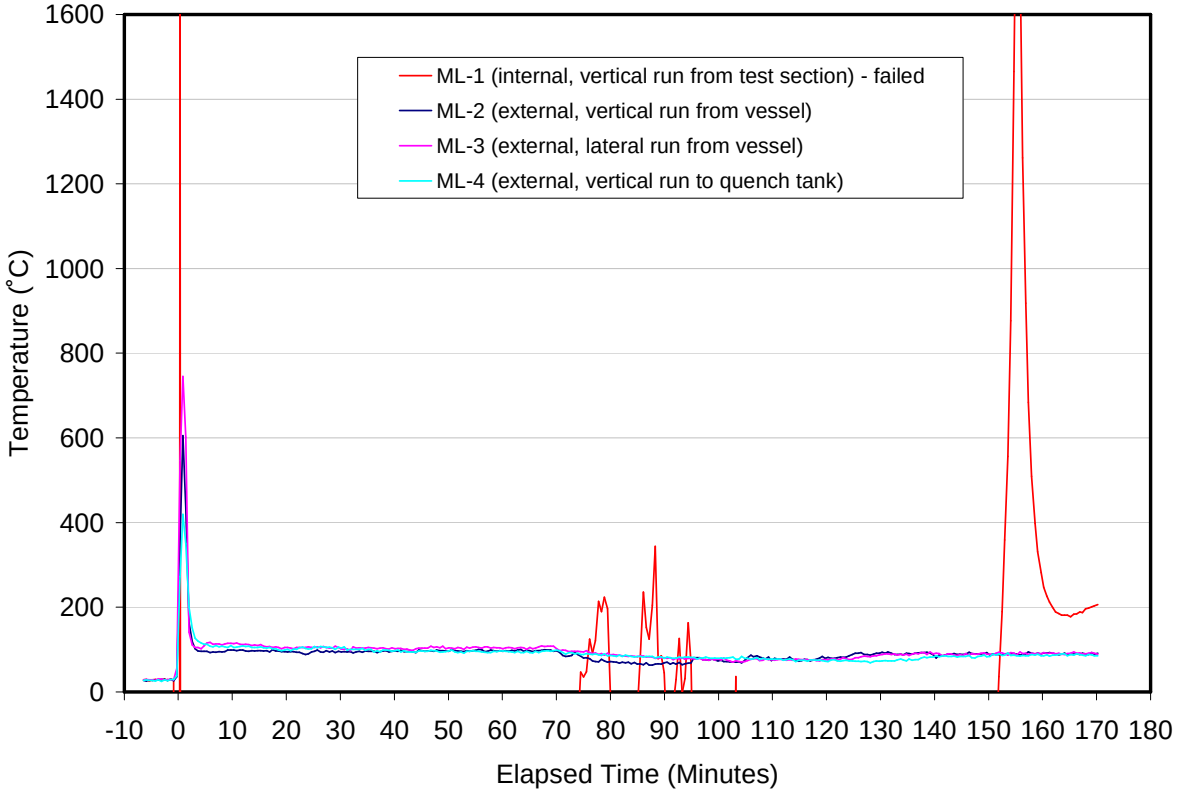

Figure C-35. Main Steamline Thermocouples.

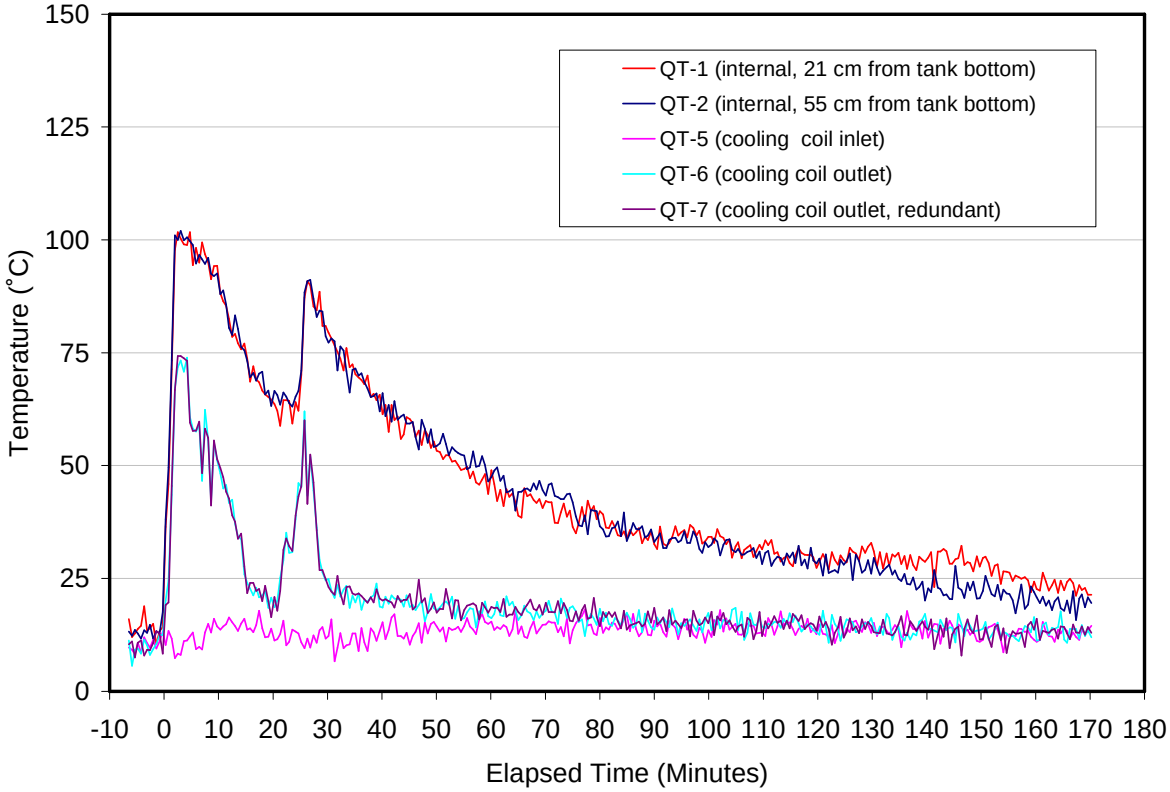

Figure C-36. Quench Tank Thermocouples.

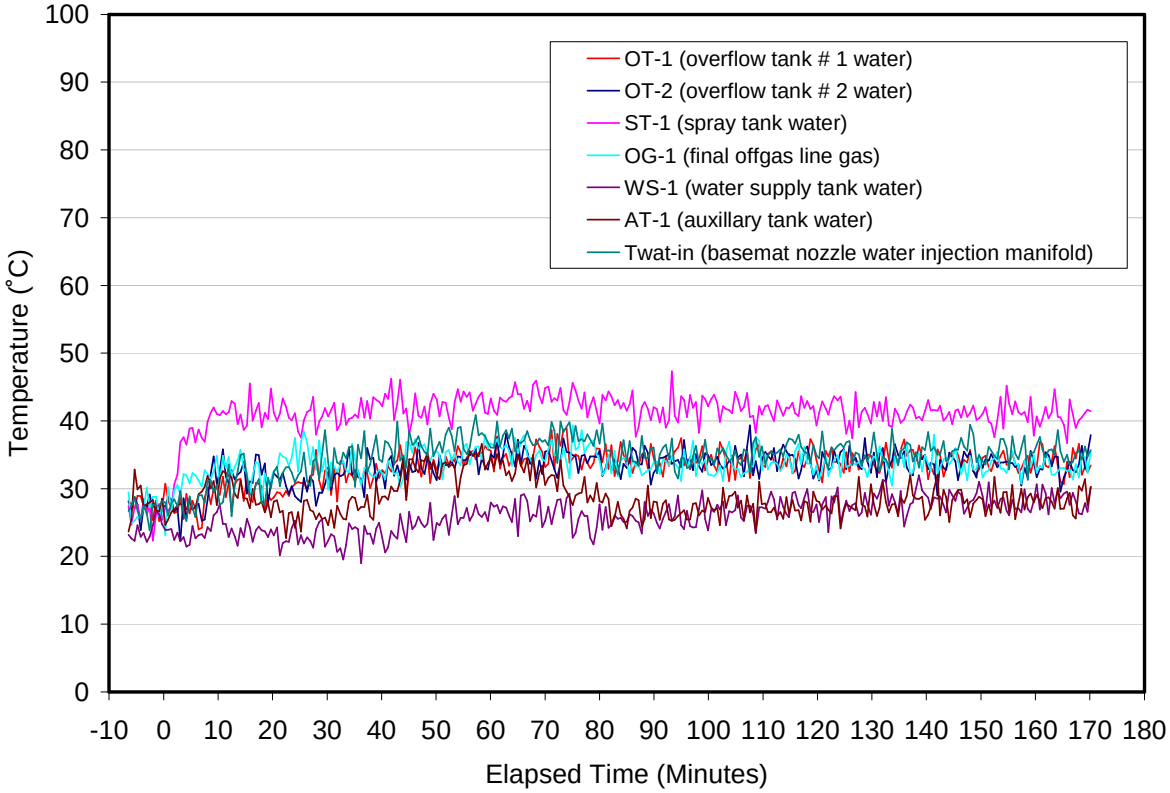

Figure C-37. Miscellaneous Quench System Thermocouples.

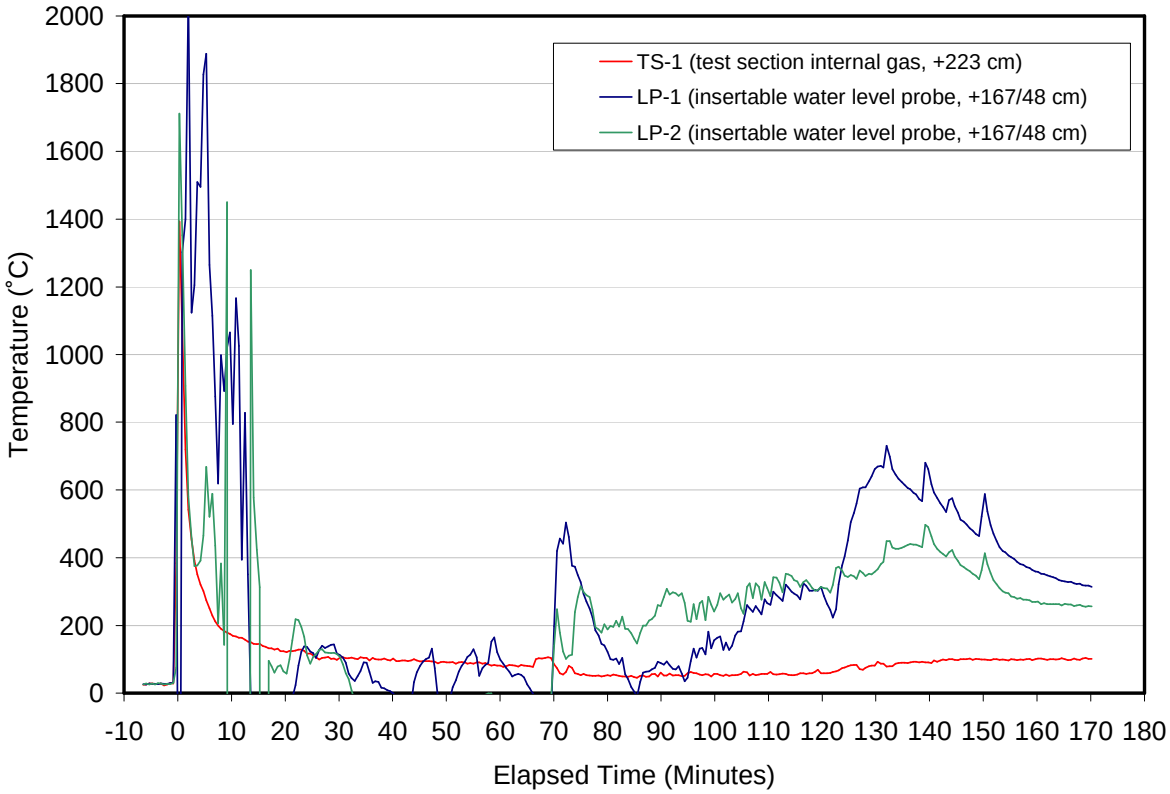

Figure C-38. Test Section Internal Gas Temperature Thermocouples.

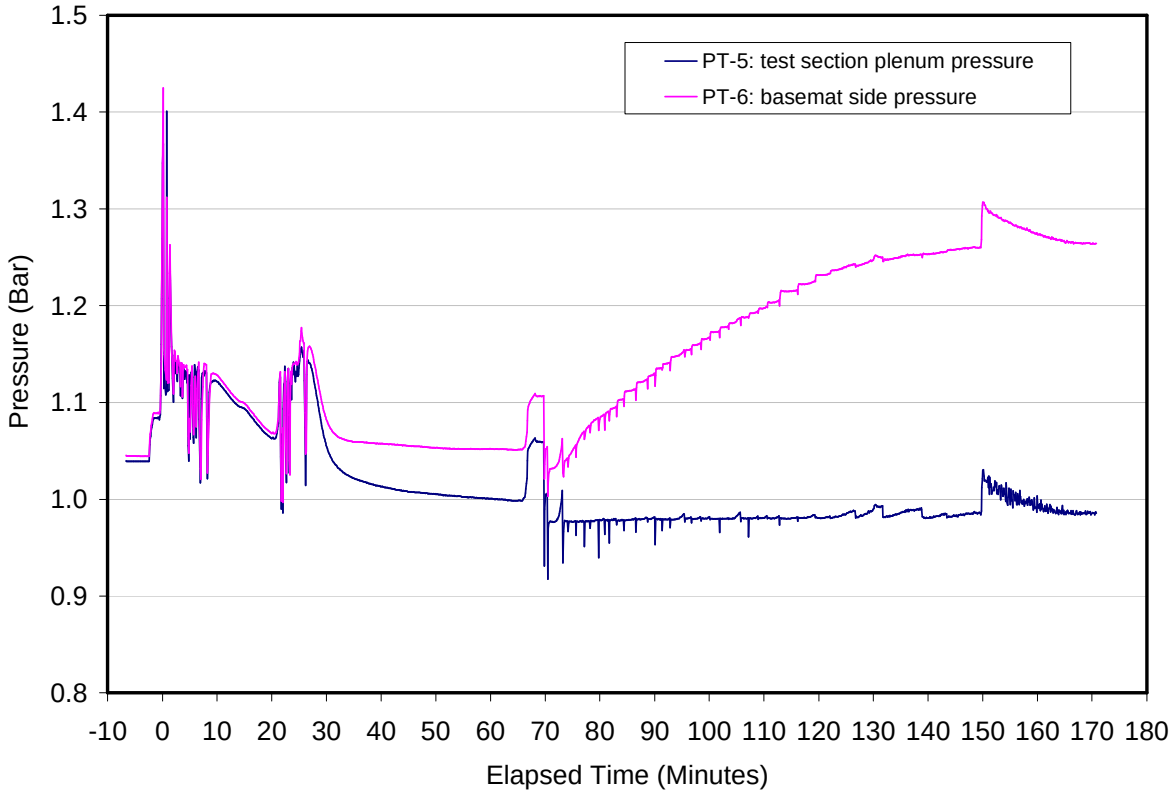

Figure C-39. Test Section Pressures.

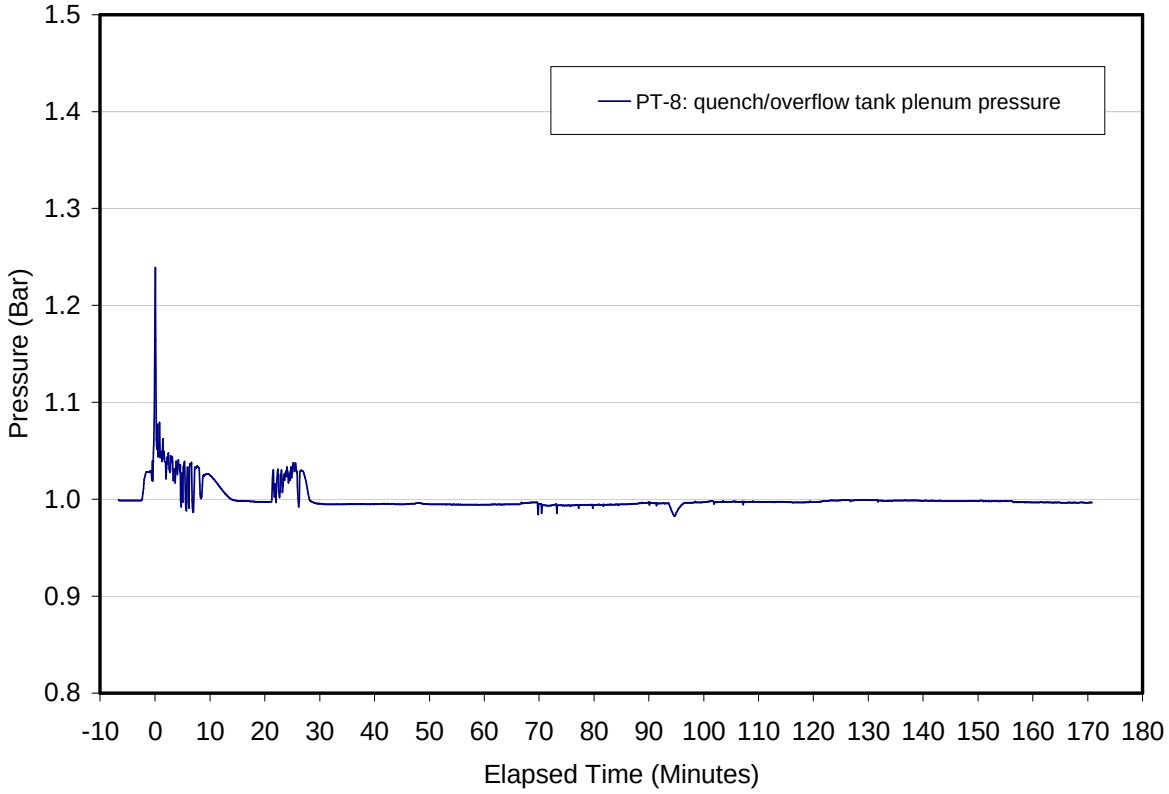

Figure C-40. Quench/Overflow Tank Plenum Pressure.

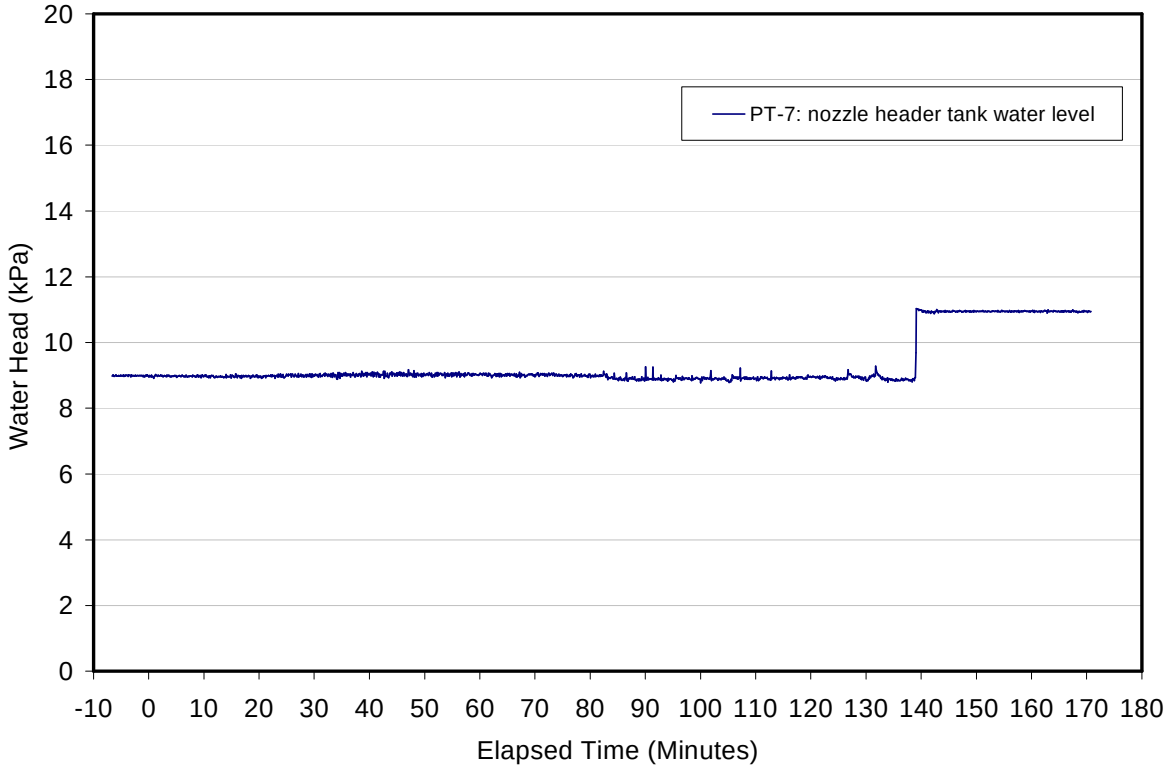

Figure C-41. Basemat Water Nozzle Supply Tank Head.

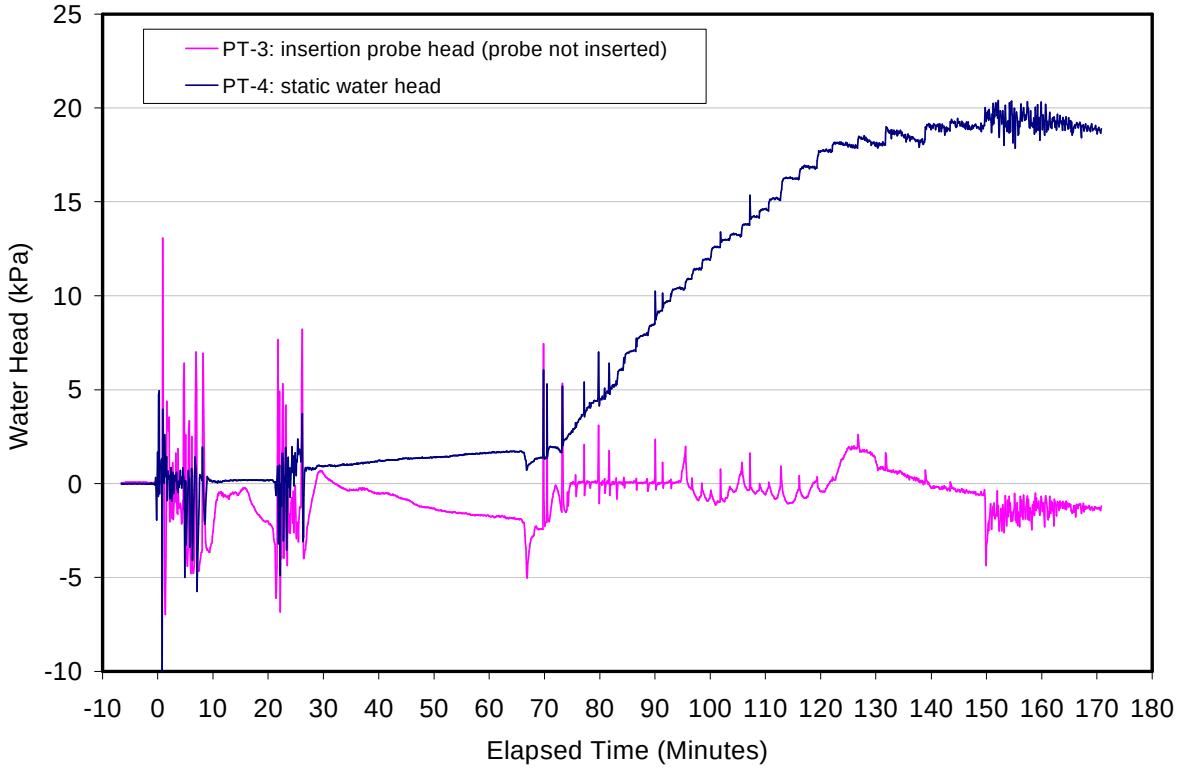

Figure C-42. Quench/Overflow Tank Plenum Pressure.

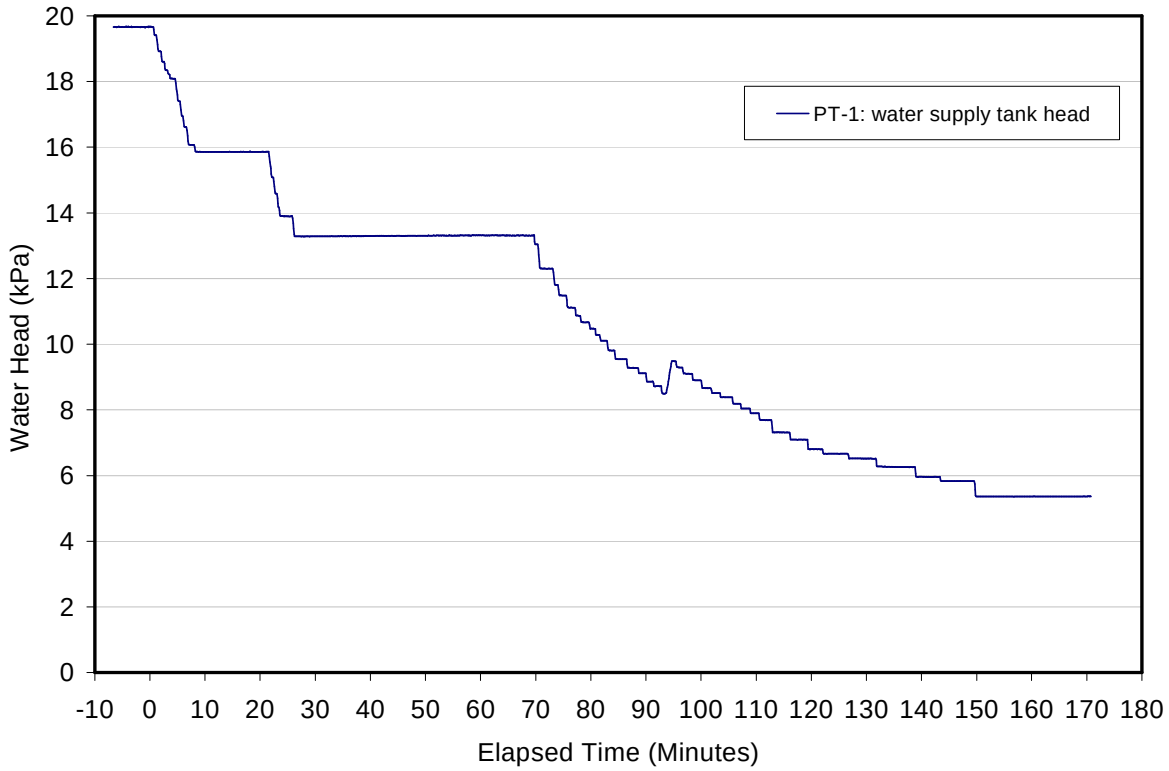

Figure C-43. Water Supply Tank Head.

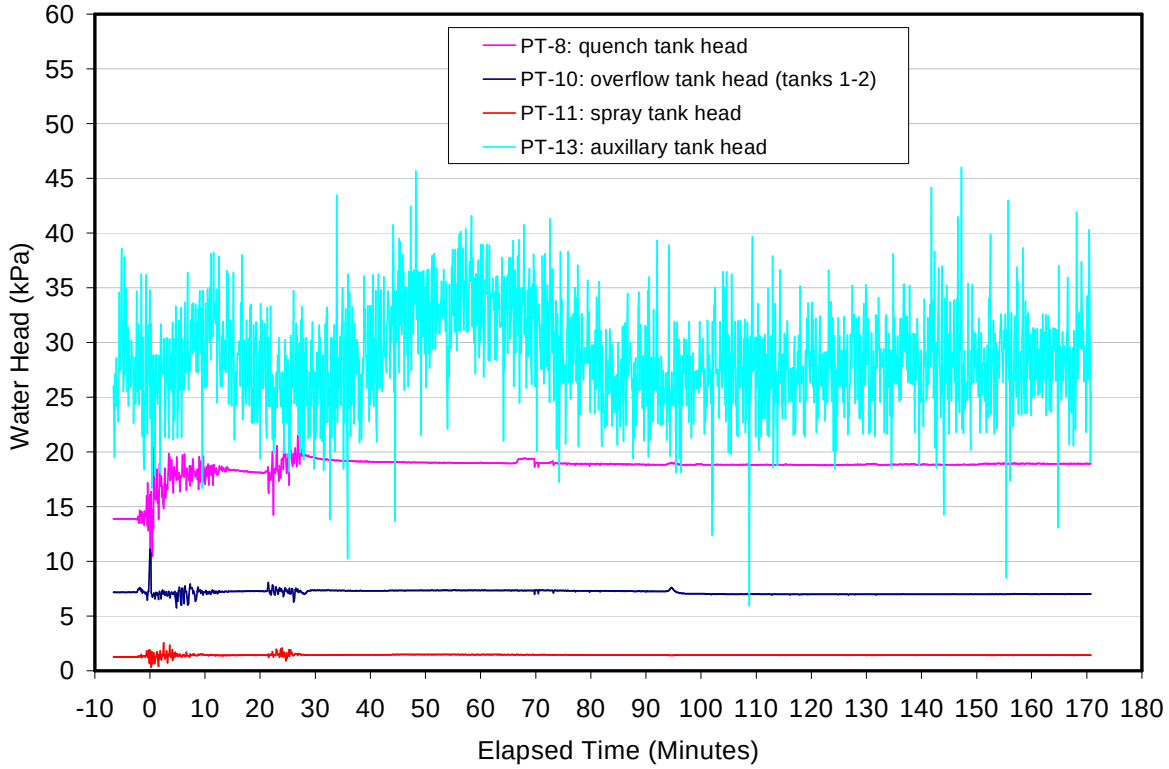

Figure C-44. Quench System Tank Water Heads.

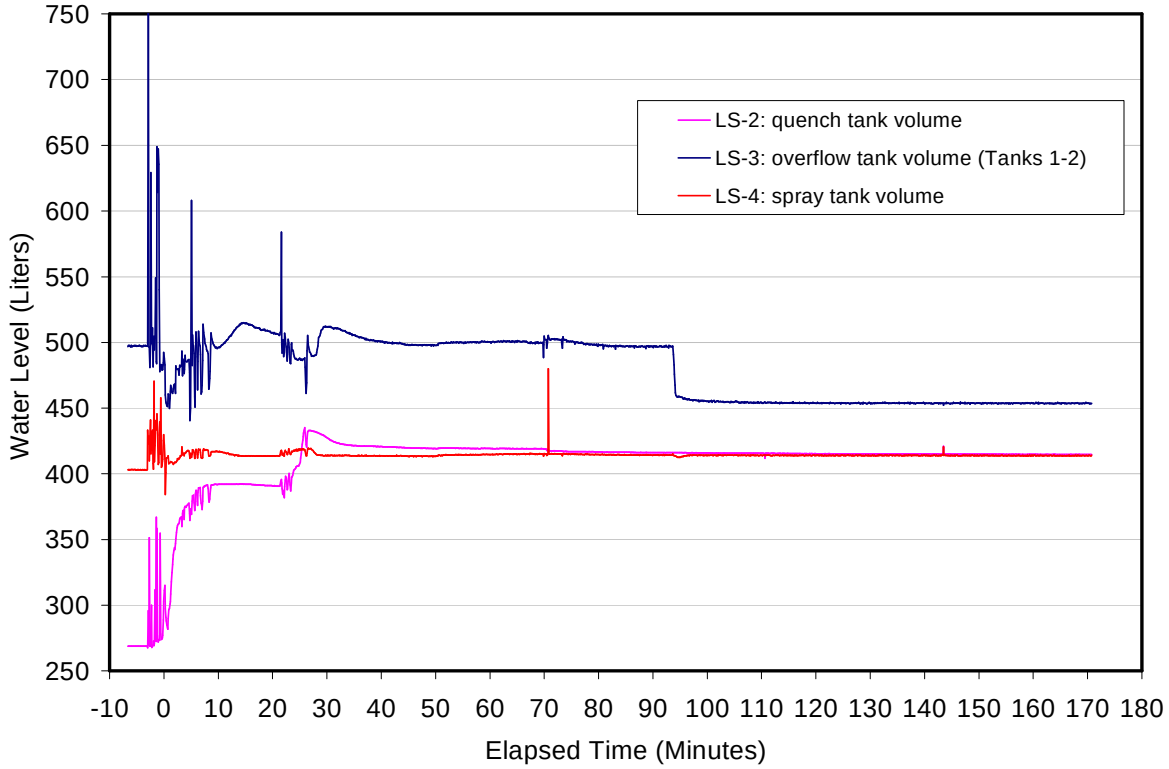

Figure C-45. Quench System Tank Water Levels.

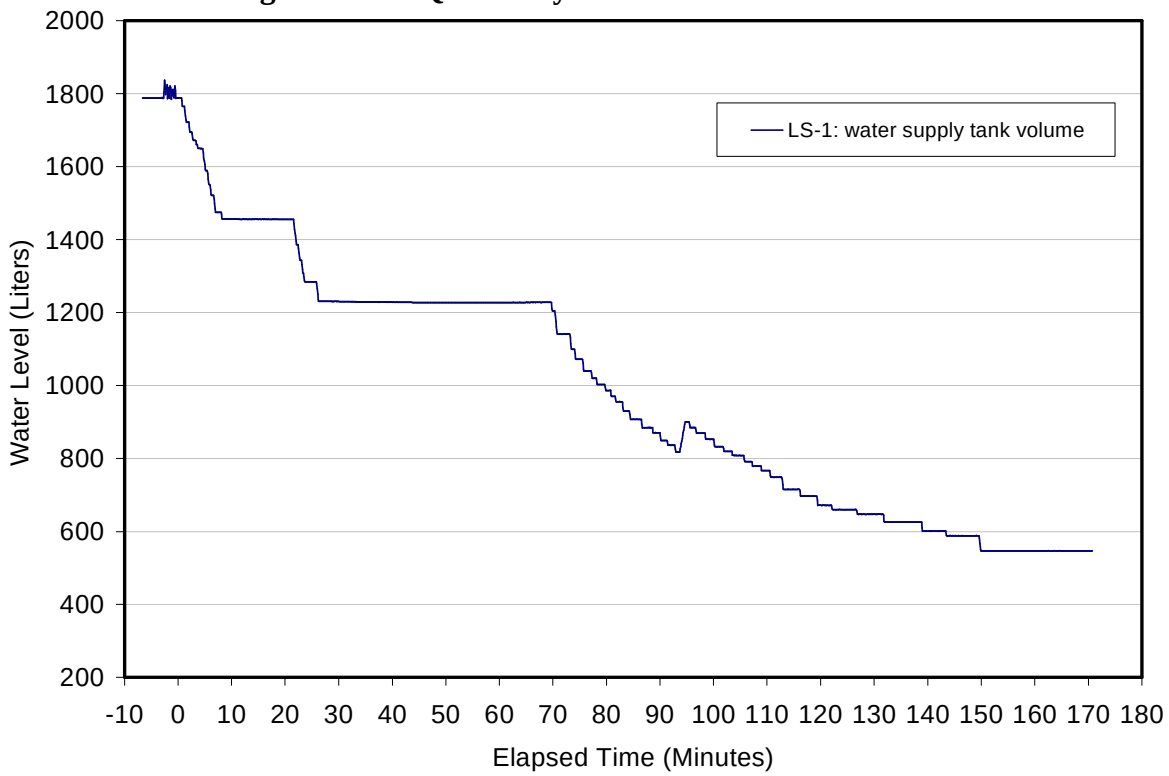

Figure C-46. Water Supply Tank Level.

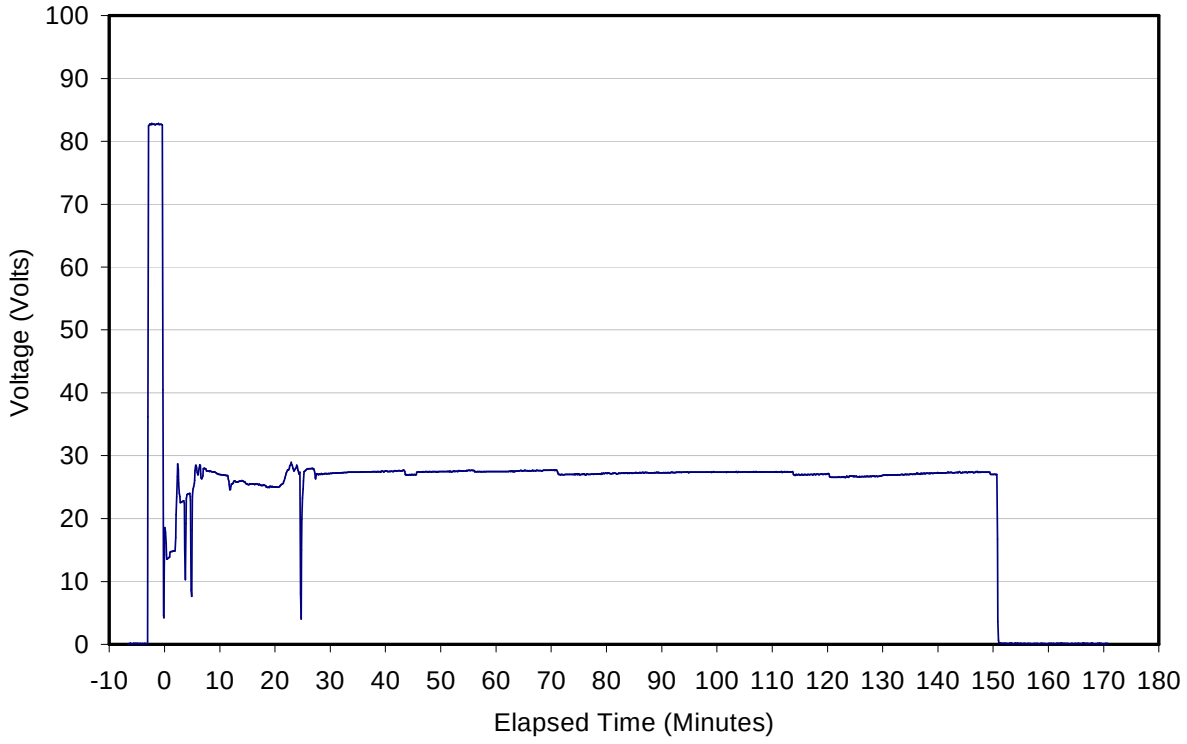

Figure C-47. DEH Power Supply Voltage.

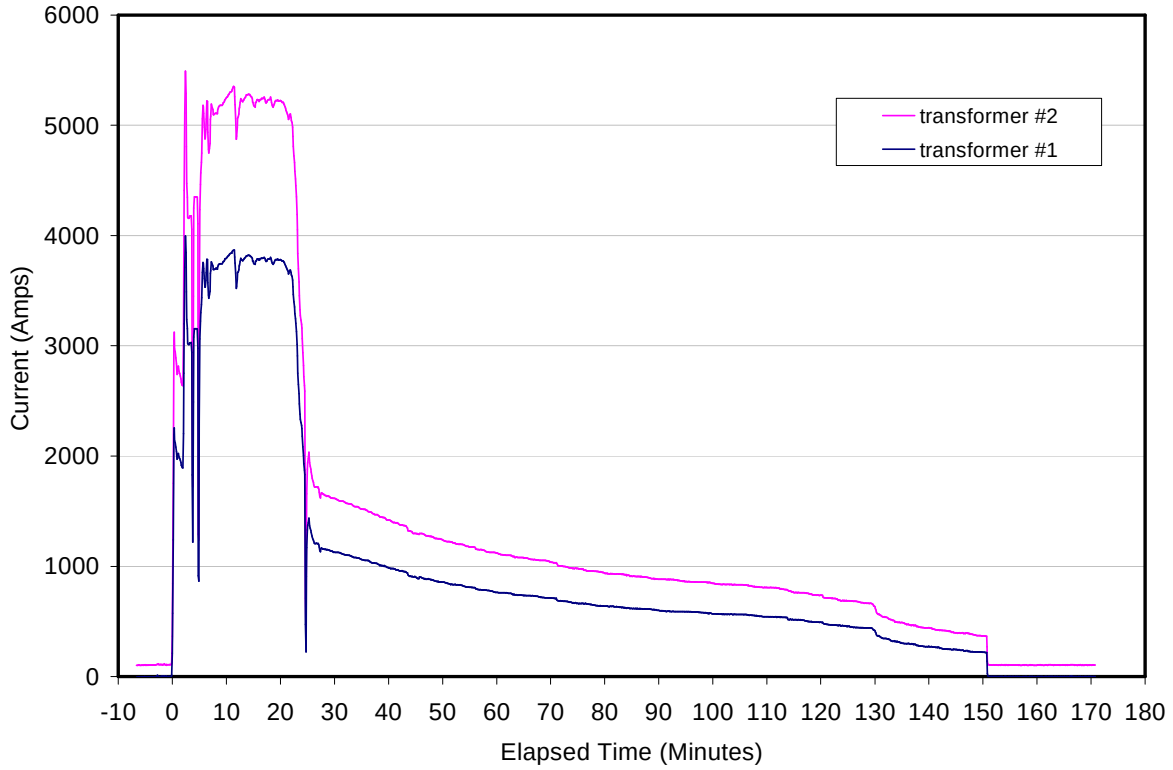

Figure C-48. DEH Power Supply Current Transformers.

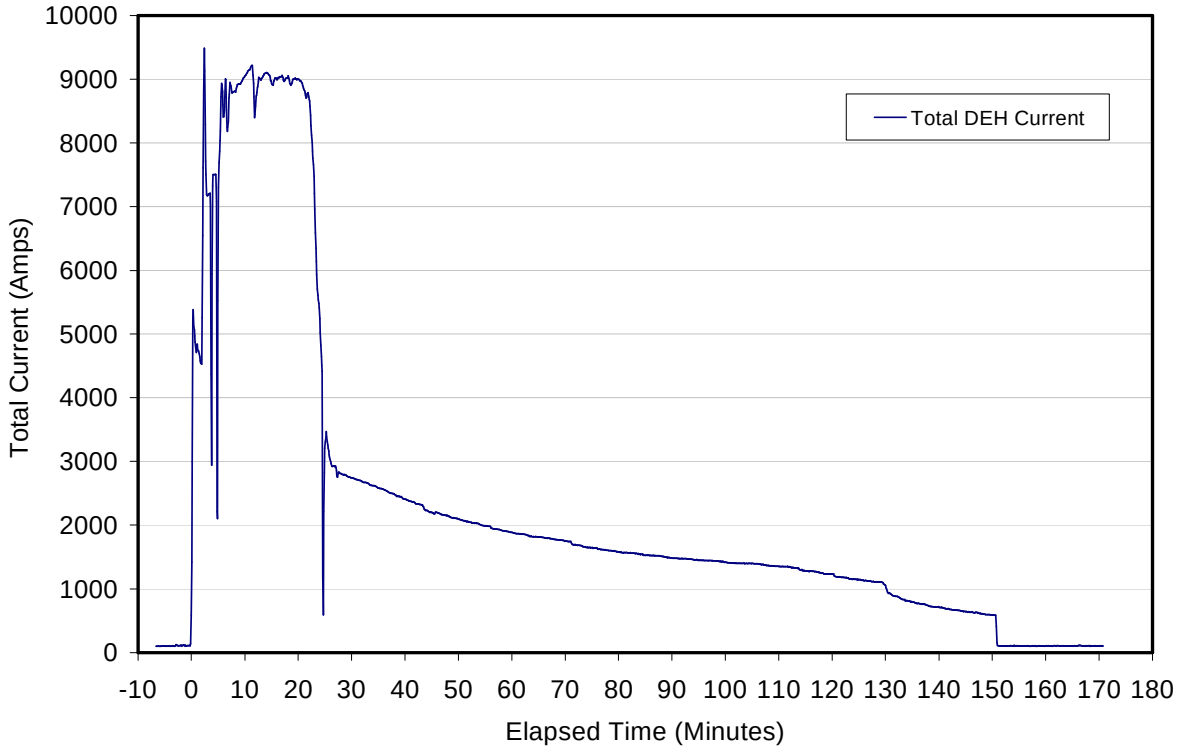

Figure C-49. Total DEH Power Supply Current.

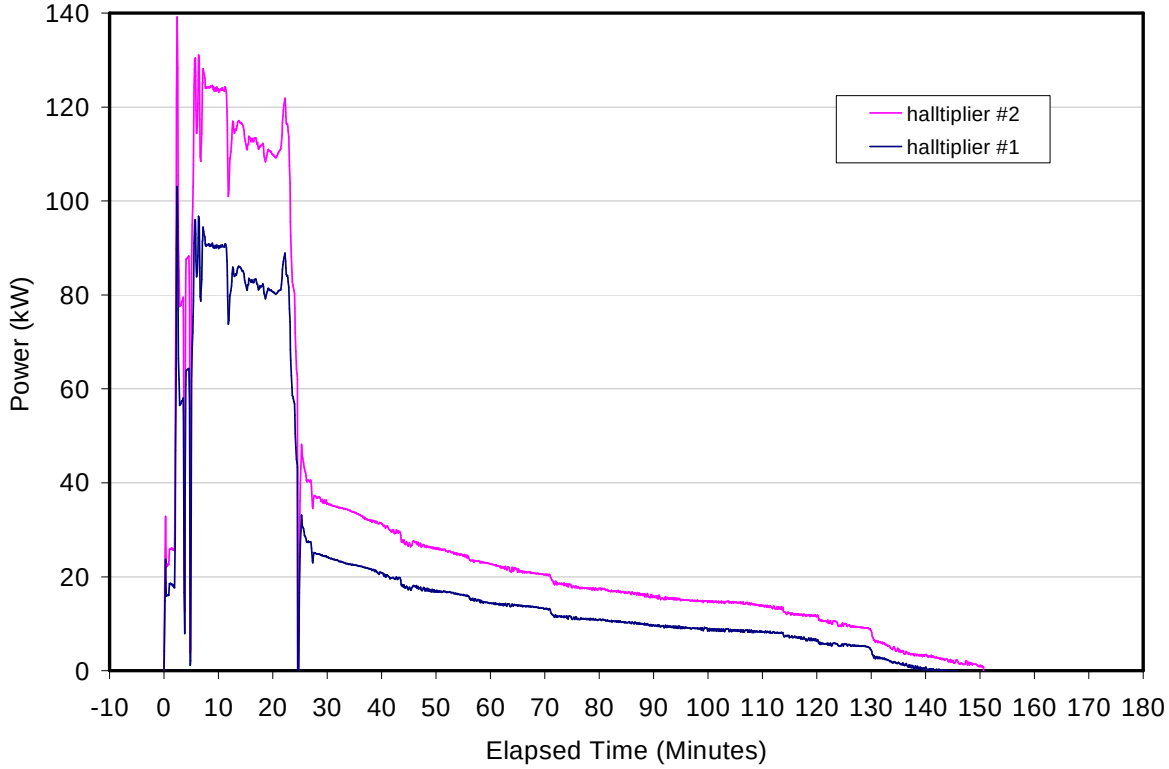

Figure C-50. DEH Power Supply Halltiplier Data.

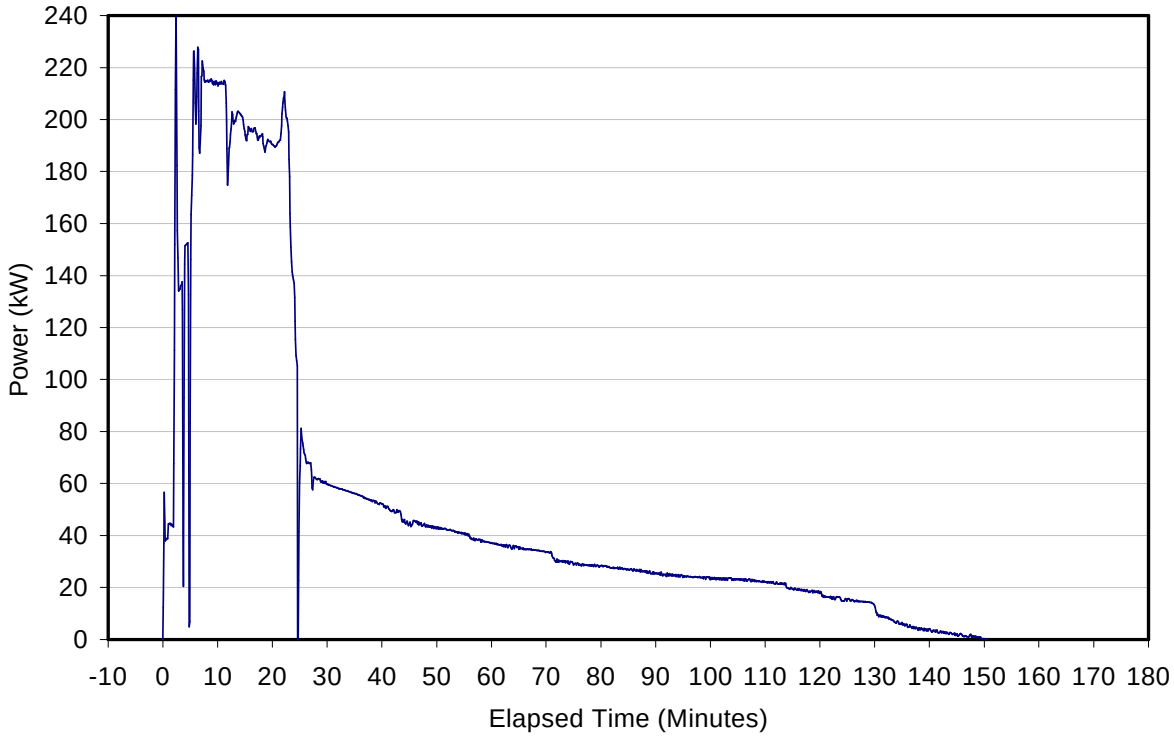

Figure C-51. Gross DEH Input Power.

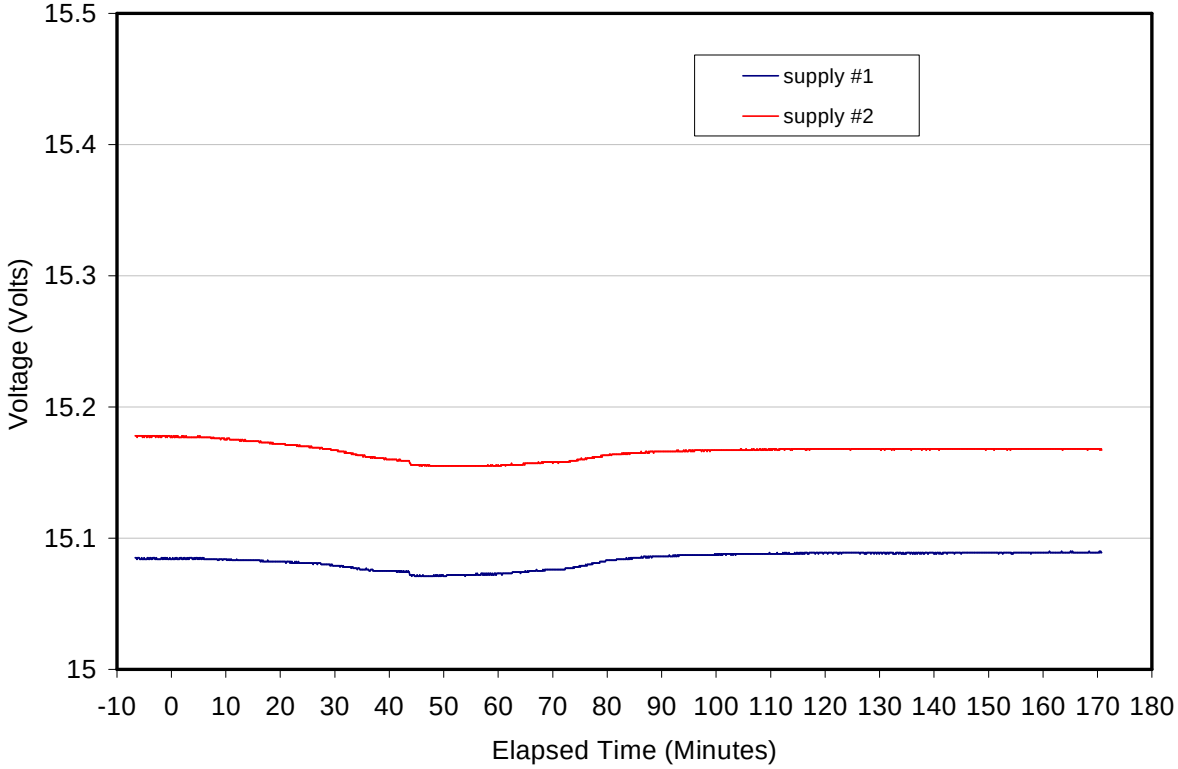

Figure C-52. Pressure Transducer Power Supply Voltages.

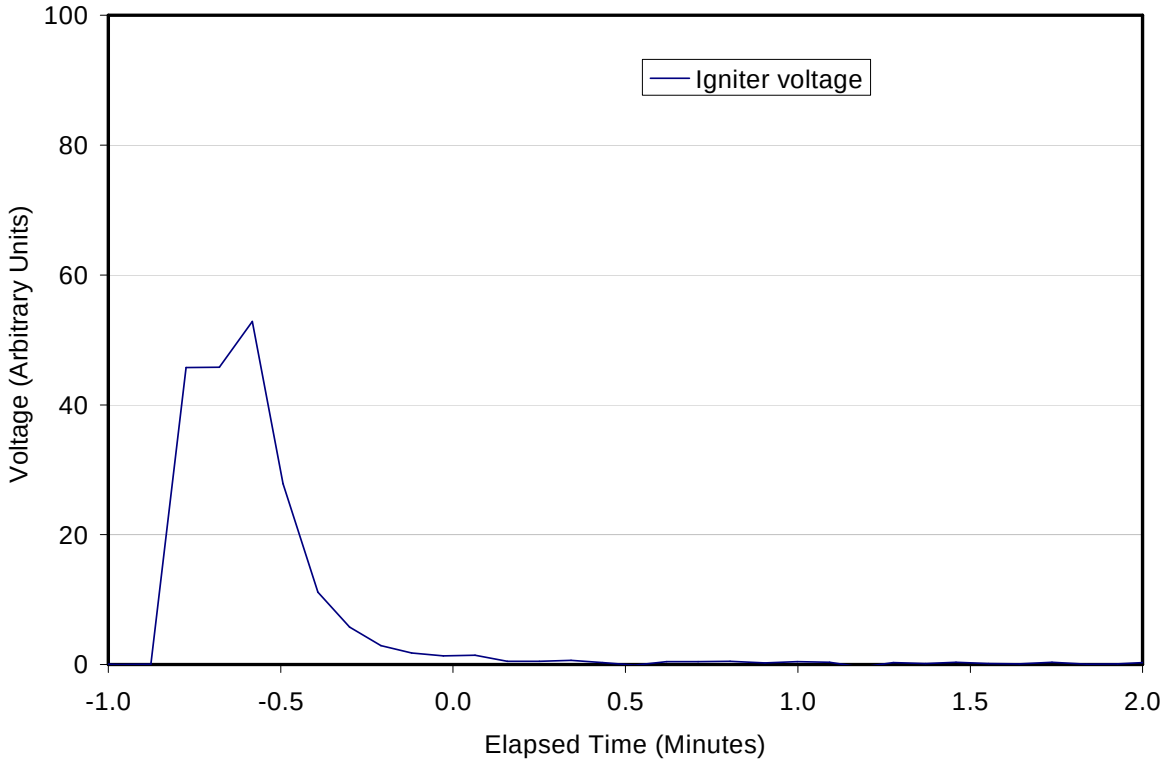

Figure C-53. DEH Power Supply Halltiplier Data.

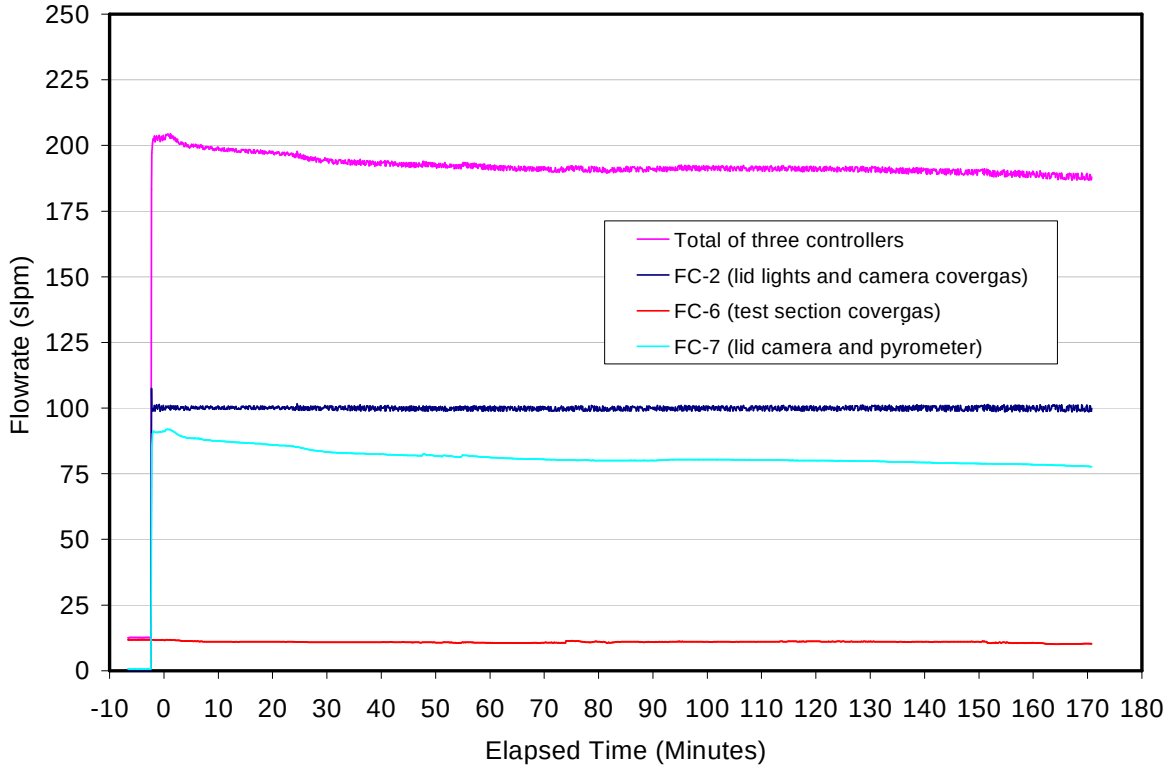

Figure C-54. Test Section Covergas Flowrates.

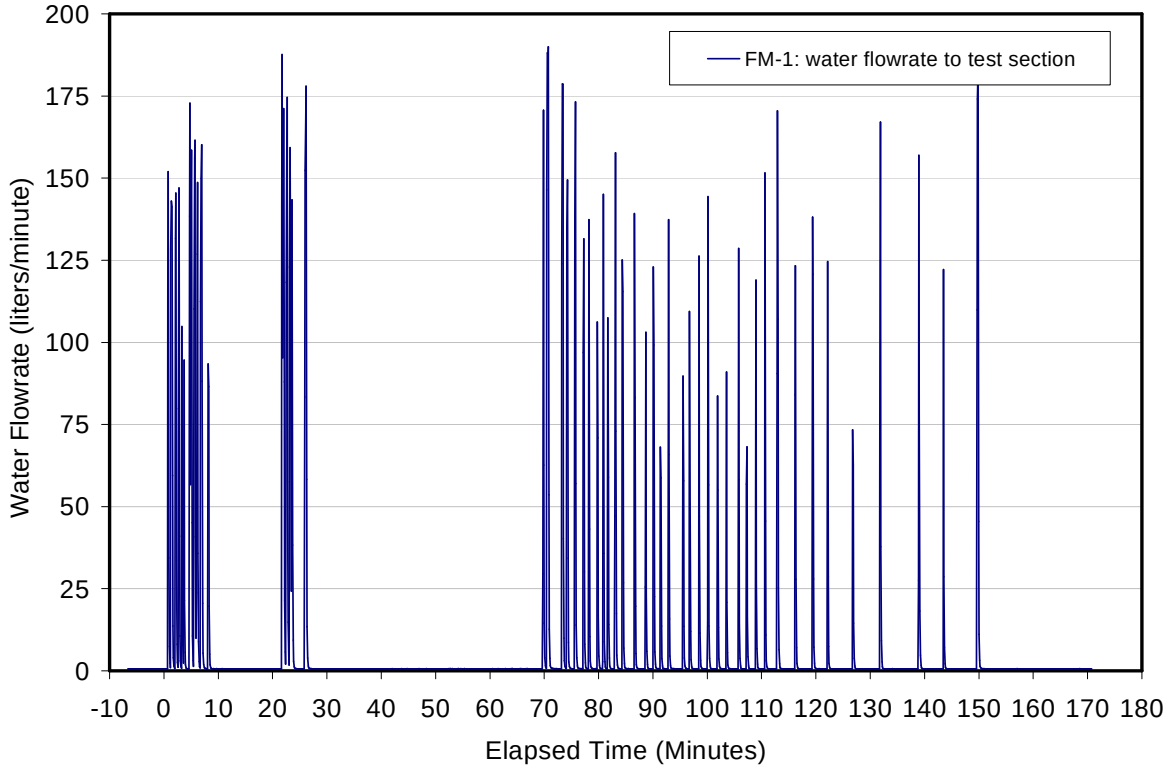

Figure C-55. Test Section Top Flooding Water Supply Flowrate.

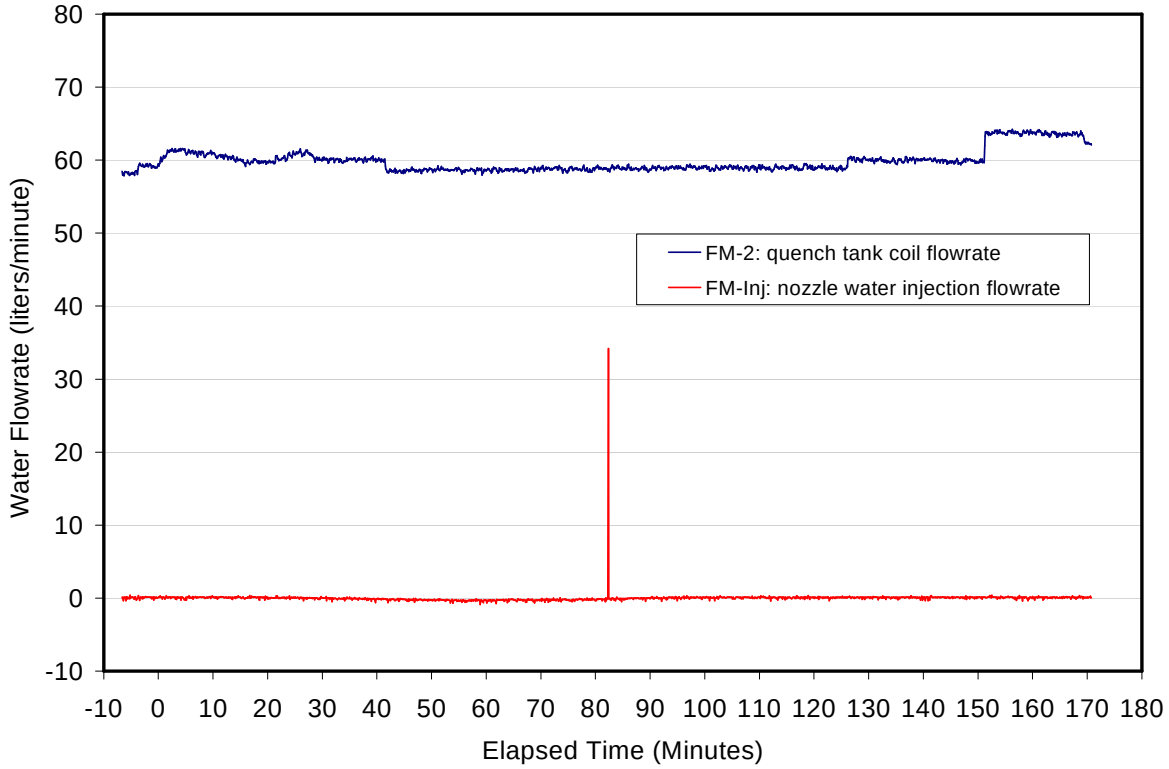

Figure C-56. Quench Tank Coil and Nozzle Bottom Injection Water Flowrates.

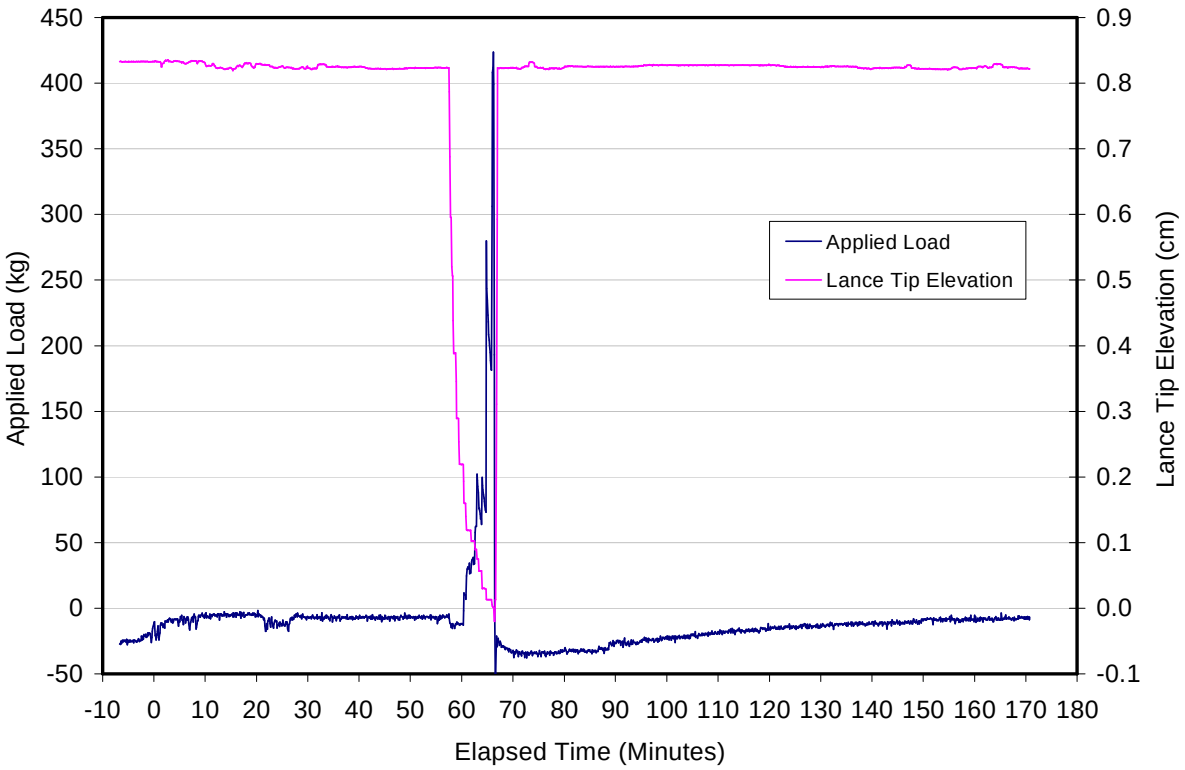

Figure C-57. Lance Insertion Probe Tip Load and Elevation.

APPENDIX D
Evaluation of Debris-Water Heat Flux

Normally, all steam from the test section is condensed within instrumented quench system tanks. The debris-water heat flux can then be readily deduced from the steam condensation rate in these tanks. However, failure of the main steamline meant that part of the steam was vented directly into the cell atmosphere, and other methods (instruments) had to be used to evaluate the debris cooling rate during the test. As the photographs in Figure D-1 illustrate, two holes formed in the main steamline during the thermite burn. The first was a fairly large (~ 6 cm^2) hole in the mainline Tee that sat on top of test section, while a second, smaller hole (~0.2 cm^2) formed in a bellows that was downstream from the Tee. This Appendix documents the extra steps that were required to evaluate the steaming rate from the test section given the fact that the steamline melted through during the test.

(a) **(b)**

Figure D-1. Photographs of Holes in the Main Steamline at (a) the Test Section Tee, and (b) Bellows Downstream of the Tee.

The general approach for evaluating the steaming rate was as follows. The water volume in all system tanks was known during the test, and so the volume of water added to the test section, as well as that condensed in the quench system tanks, was known at any time. Due to continued water addition to the test section, a direct measurement of water level in the test section became available at 73 minutes by virtue of the side-mounted differential pressure transducer tap PT-4; see Figure 2-24 for a drawing that shows the location and type of all test section pressure transducers. The PT-4 water head data is shown in Figure D-2. Given the water volumes in the tanks as well as the known water level in the test section at 73 minutes, it was then possible to determine the steam mass lost out the vent hole up to that point in time. The total steam production rate from the test section up to 73 minutes was then found from the sum of that lost out of the hole (methodology described below), plus the steam condensed in the quench system tanks. After 73 minutes, the steaming rate from the test section was then determined directly from the (derivative of the) difference of the mass added to the test section minus the mass remaining in the test section.

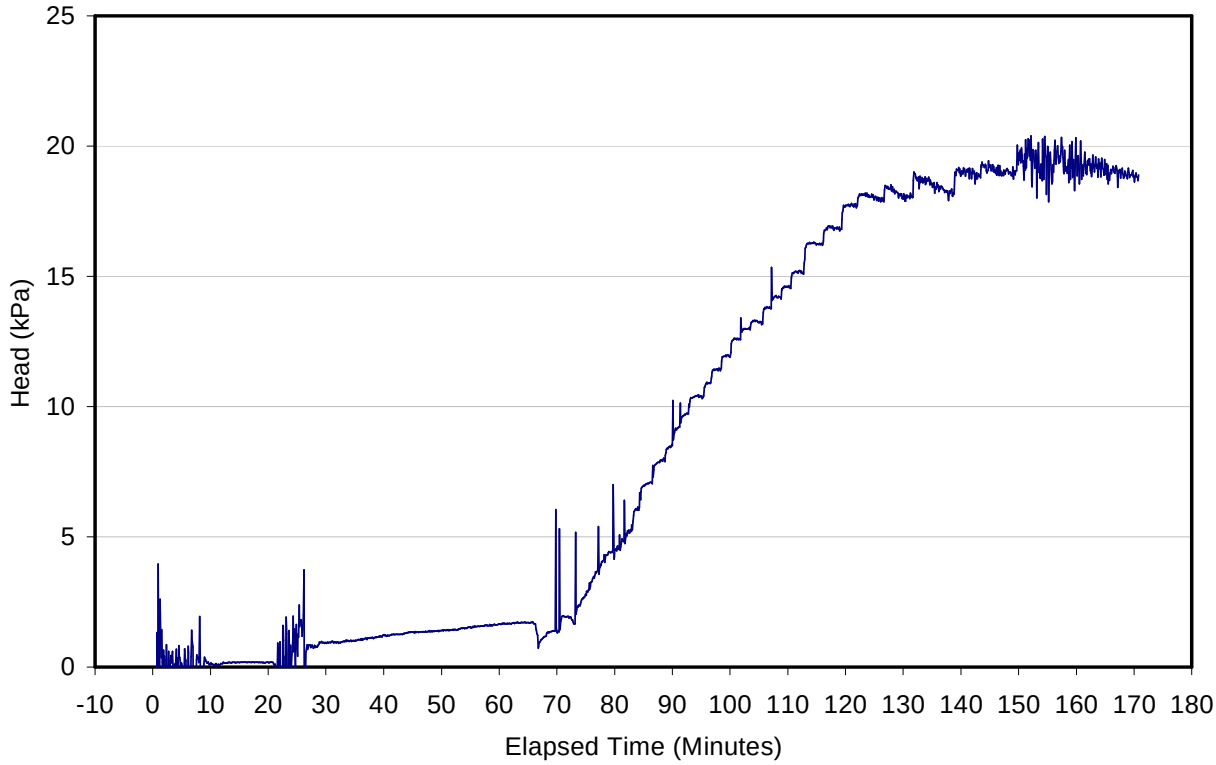

Figure D-2. Data from Test Section Side-Mounted Differential Pressure Transducer PT-4.

Test section plenum pressure was measured by transducer PT-5 (see Figure 2-24) located on the test section lid; data are shown in Figure D-3. Thus, the steam flow out of the hole in the line could be evaluated by modeling the hole as an orifice. Under this assumption, the relationship between pressure drop across the hole and the corresponding flow velocity through the hole is given by Bernoulli's equation; i.e.,

$$\Delta P = \frac{1}{2} K_{loss} \rho U^2 \Rightarrow U = \sqrt{\frac{2\Delta P}{K_{loss}\rho}} \tag{D-1}$$

where K_{loss} is the loss coefficient and ρ is gas density. The corresponding mass flow through the hole is evaluated from the conservation of mass equation:

$$\dot{m} = \rho U A_{hole} \tag{D-2}$$

In this expression, the flow area of the hole is assumed to be the previously stated value of A_{hole} = 6 cm^2 for the large hole on the test section Tee; flow out of the smaller hole downstream of the Tee is neglected.

To first approximation, the gas flow through the hole can be assumed to consist of pure saturated steam, for which the density at atmospheric pressure is $\rho = \rho_s = 0.6$ kg/m^3. However, the question arises as to what effect the helium covergas flow would have on the assessment of the steam mass flux. To address this question, the above equations were solved for a steam-

helium gas mixture in which the helium flowrate through the hole is specified. The resultant expression for the steam flow velocity is found as:

$$U_S = \frac{1}{2}\sqrt{\frac{8\Delta P}{K_{loss}\rho_s} + U_{He}\left(1-\frac{\rho_{He}}{\rho_s}\right)^2} - \frac{U_{He}}{2}\left(1+\frac{\rho_{He}}{\rho_s}\right) \qquad \text{(D-3)}$$

The total helium covergas flowrate is shown in Figure D-4. The flow velocity for this gas through the hole in the above expression was evaluated from Eq. D-2 along with the data in Figure D-4 using a density of ρ_{He} = 0.13 kg/m^3 (viz. corresponding He density at water saturation temperature).

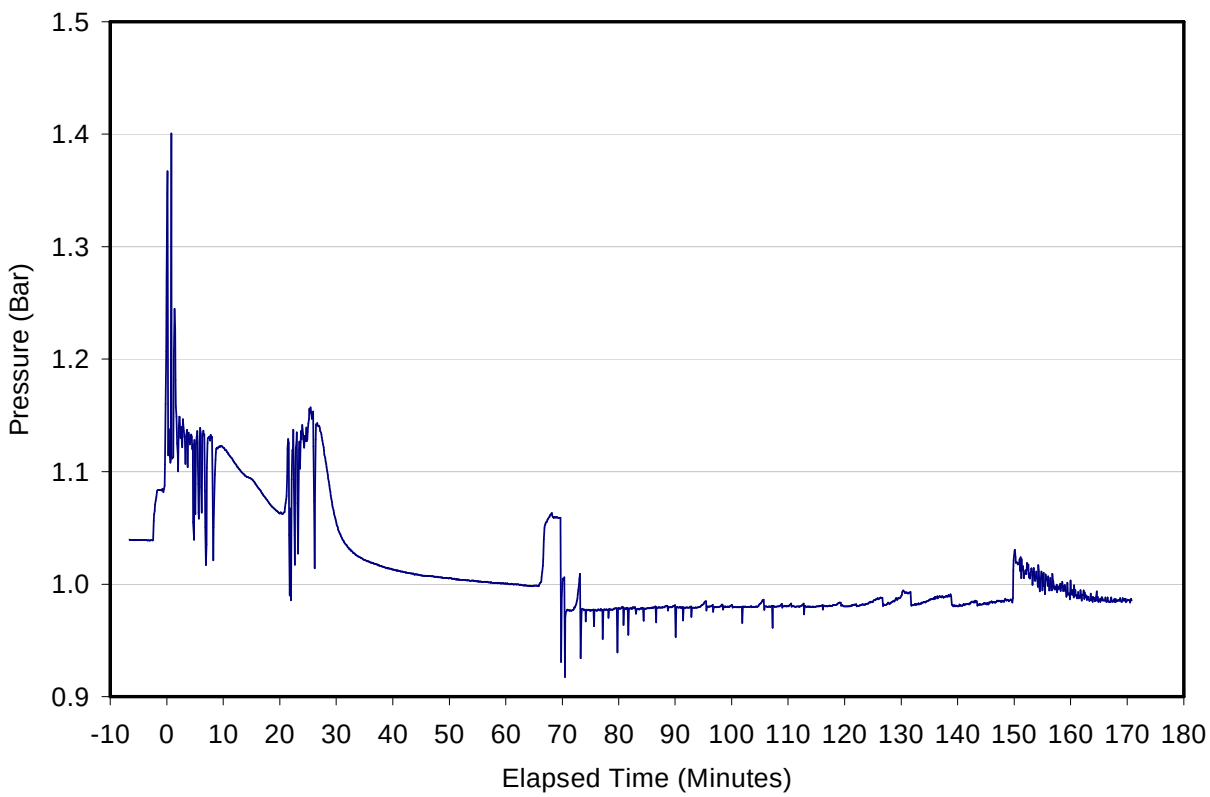

Figure D-3. Test Section Plenum Pressure (PT-5 data).

In terms of the mass balance at 73 minutes, the total free volume in the test section below the PT-4 tap was determined to be 229 l, which accounts for the structure of the large test section components as well as the presence of the corium, electrodes, and UO_2 pellets and U_3O_8 powders used as lining material on both the electrode and non-electrode sidewalls. Moreover, the total water volume added to the test section at this time from the supply tank amounted to 647 l (see Figure D-5). Finally, during the first 30 minutes of the experiment, a significant mass of steam was also condensed in the primary quench tank and secondary spray tank; this amounted to a 150 l (see Figure D-6). Thus, the total condensed steam volume lost out the vent hole by 73 minutes was 647 – 229 – 150 = 268 l. This constitutes the total (integrated) volume that one should

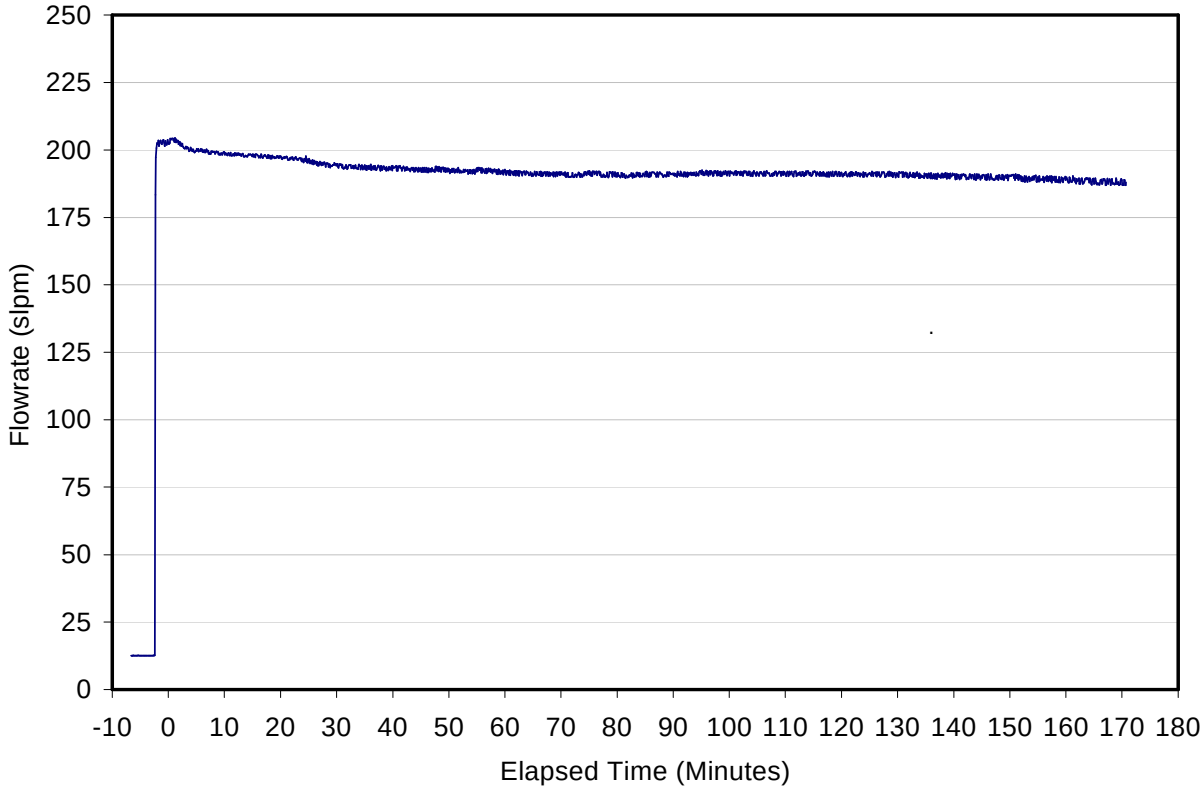

Figure D-4. Test Section Helium Covergas Flowrate.

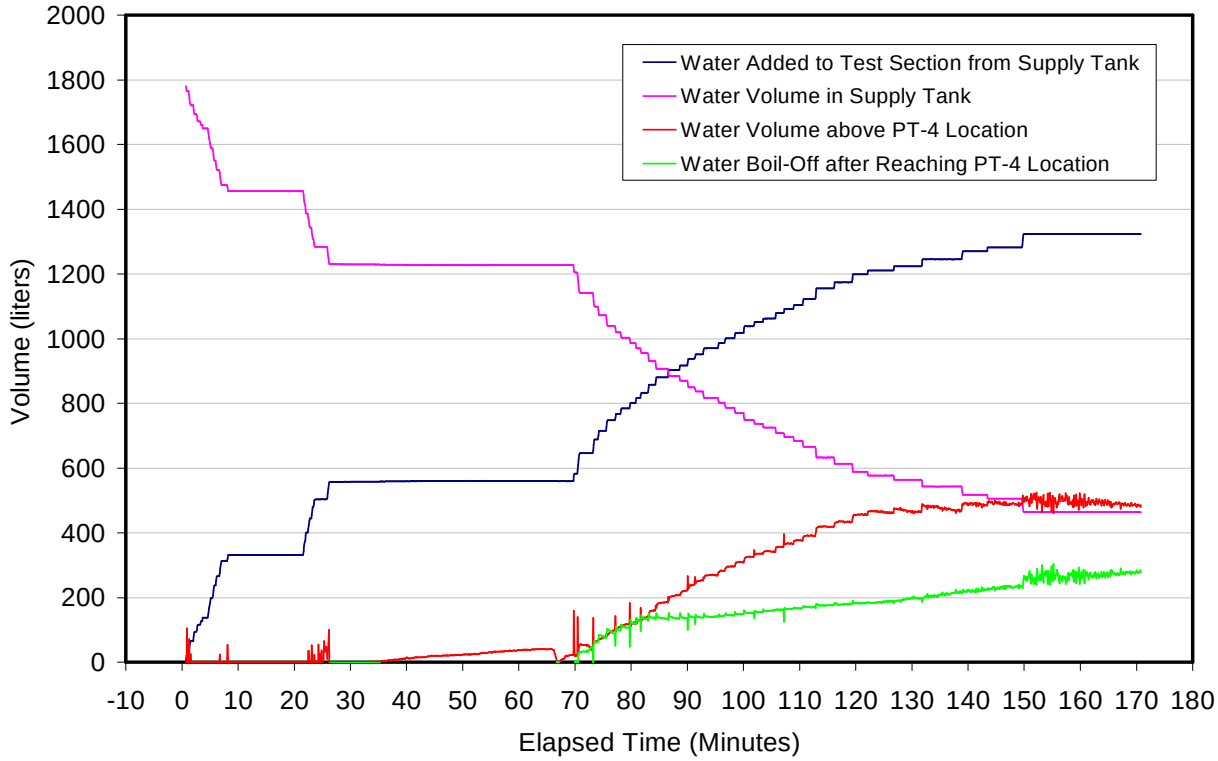

Figure D-5. Test Section Water Mass Balance Data.

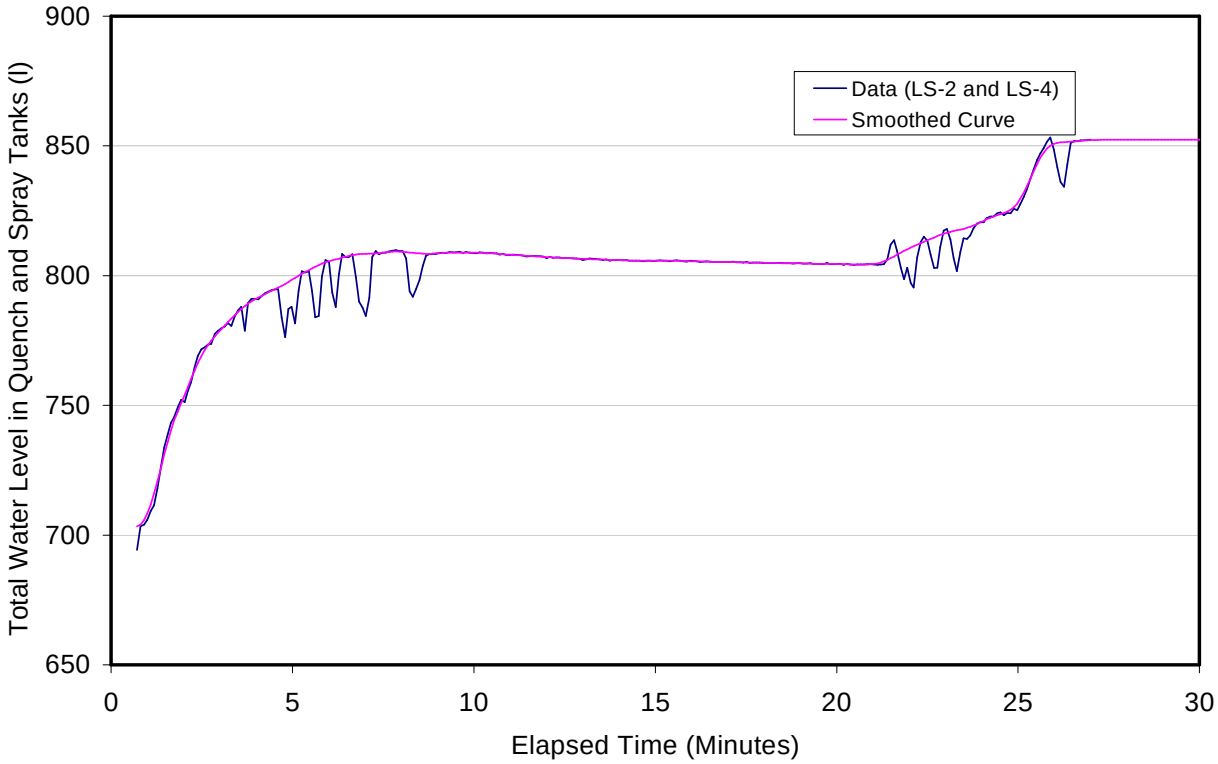

Figure D-6. Quench and Spray Tank combined Water Volumes.

obtain by integration of Eq. D-3 from the time of water addition at 0.7 minutes out to 73 minutes when the mass lost is known. The one parameter that remains to be specified as part of this calculation is the orifice loss coefficient, K_{loss}. This parameter was adjusted until the integrated condensate loss out of the vent hole up to 73 minutes equals the actual value of 268 l, using Eq. D-3 as the basis for the fit. The results of this integration are shown in Figure D-7 for the case of a loss coefficient of 0.51 which was found to best match the data. The differential pressure was calculated using the plenum pressure data (Figure 4-3) given the barometric pressure of 0.99 bar the day of the test. As is evident from Figure D-7, the presence of the helium gas flow had only a minor effect on the prediction of overall steam production. The corresponding steam mass flowrate through the vent hole, calculated from Eqs. D-2 and D-3, is shown in Figure D-8. The other component to the overall steaming rate from the test section for the first 73 minutes is that condensed in the quench and spray tanks. The steaming rate from this component (found by numerically differentiating the smoothed level data shown in Figure D-6) is also provided in Figure D-8.

As noted earlier, after 73 minutes the steaming rate from the test section was determined directly from the (derivative of the) difference of the mass added to the test section minus the mass remaining in the test section. The mass balance data for this stage of the test is shown in Figure D-5. The net steaming rate found by fitting a curve to this boil-off data and then differentiating the result is also shown in Figure D-8 (curve denoted 'LS-1 and PT-4 basis'). The total steaming rate from the core-concrete interaction was then found as the sum of the three components shown in this figure; the result is shown in Figure D-9. This data constitutes the necessary information for evaluating the debris-water heat flux that is presented in Section 4.5.

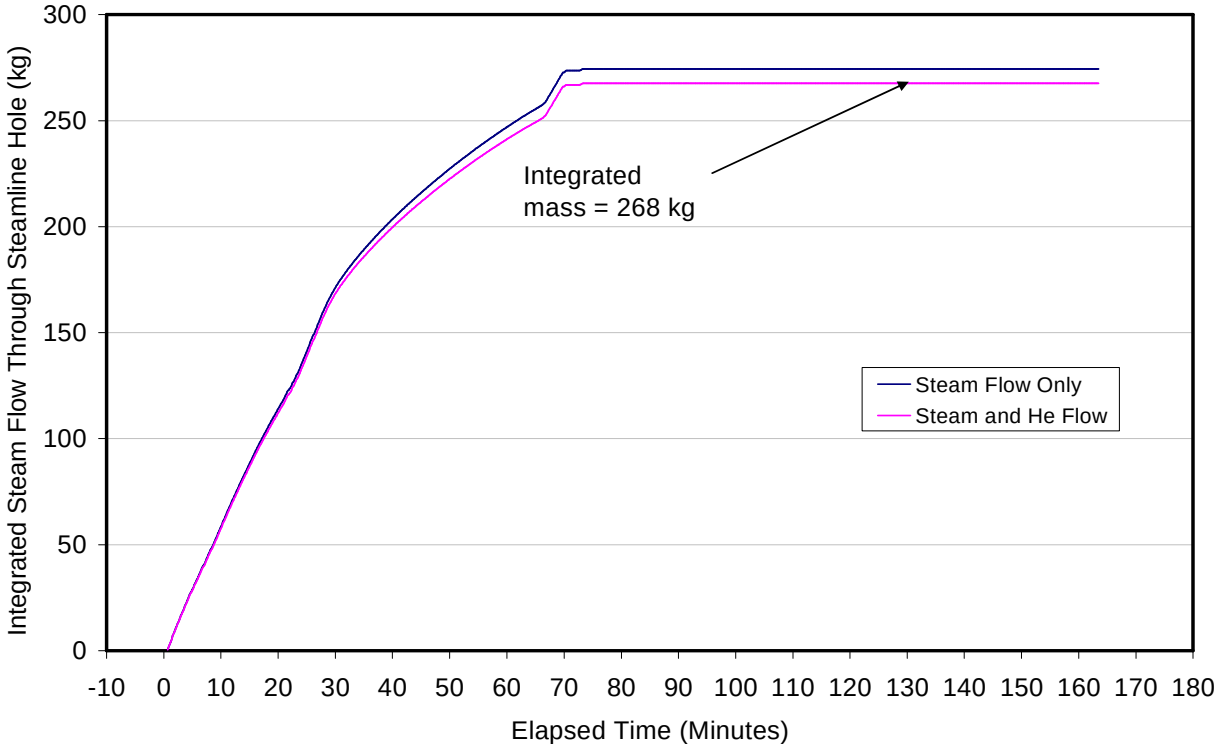

Figure D-7. Calculated Integral Steam Loss Through Hole in Test Section Tee Assuming an Orifice Loss Coefficient of 0.51.

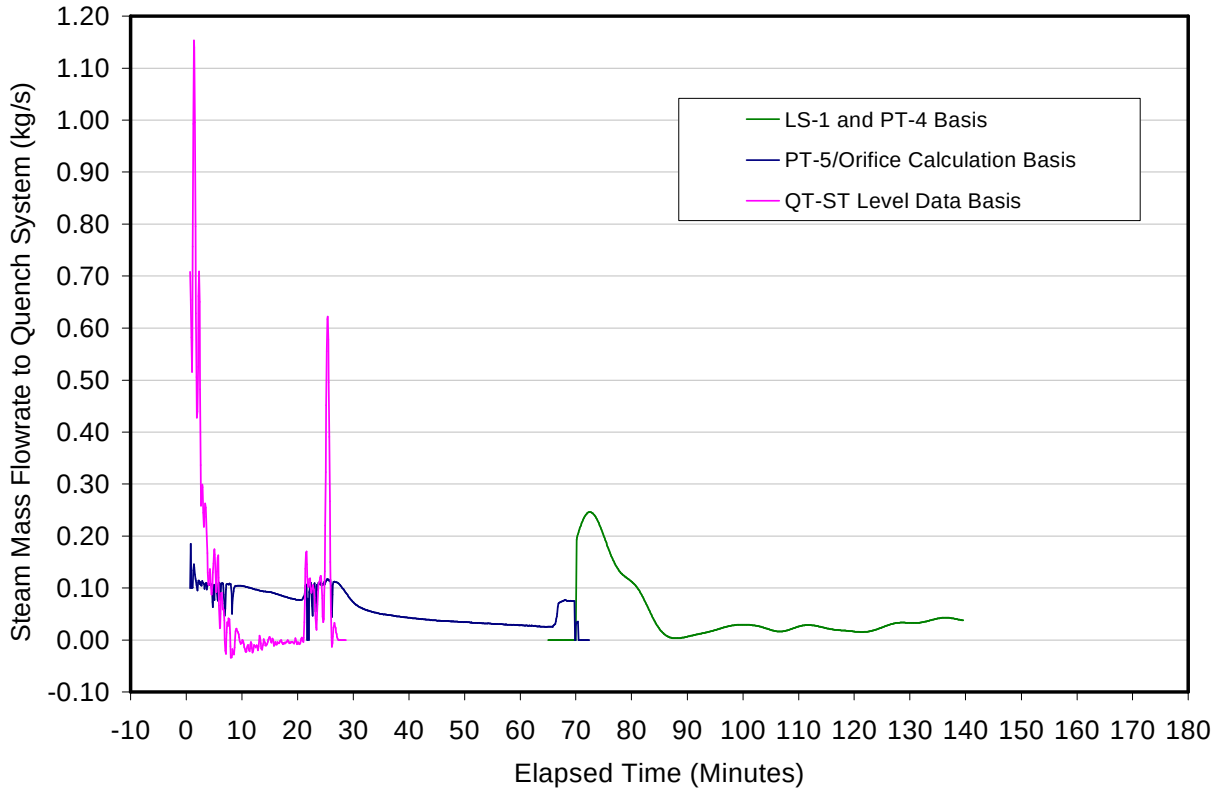

Figure D-8. Steam Mass Flowrates Calculated from Various Sources.

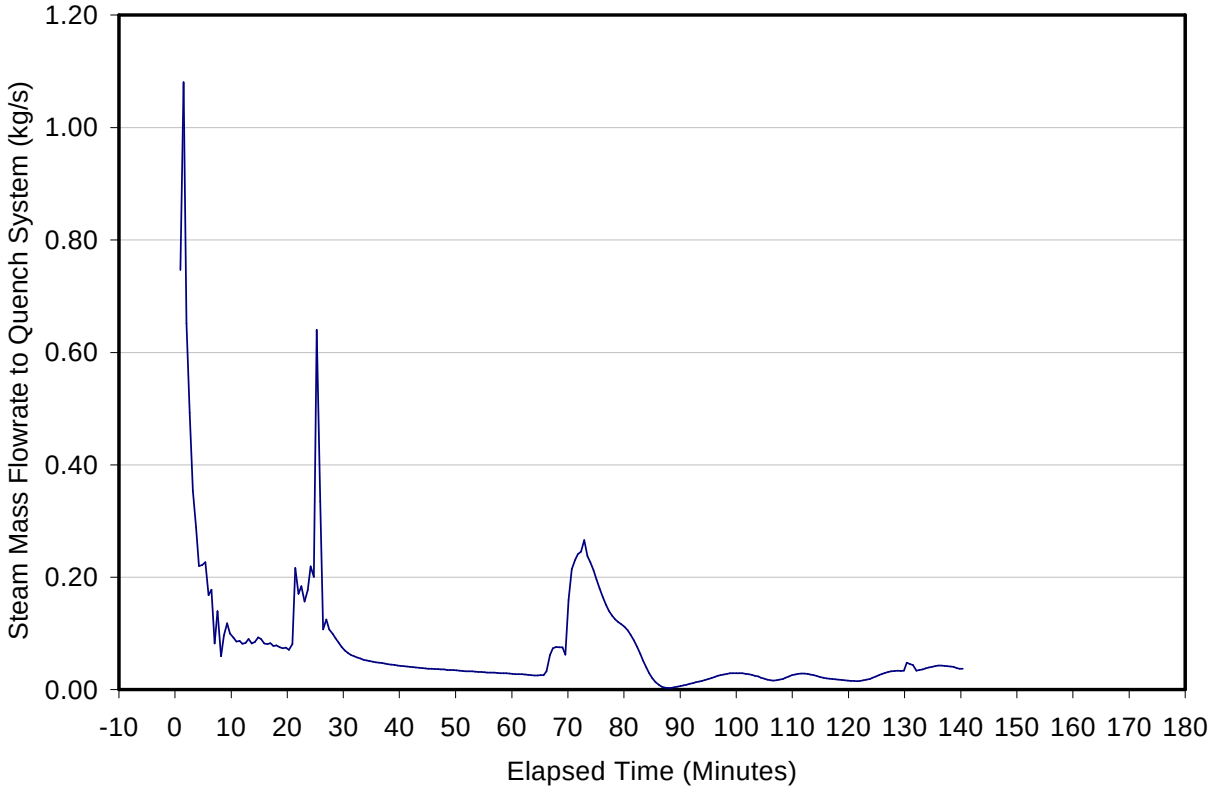

Figure D-9. Cumulative Steam Flowrate from Debris-Water Interaction.